Experimental and Kinetic Investigation of the Influence of OH Groups on NO_X Formation

Dissertation by

Myles Dungan Bohon

In Partial Fulfillment of the Requirements

For the Degree of

Doctor of Philosophy in Mechanical Engineering

King Abdullah University of Science and Technology, Thuwal,

Kingdom of Saudi Arabia

The dissertation of Myles Dungan Bohon is approved by the examination committee

Committee Chairperson: Dr. William L. Roberts

Committee Member: Dr. Sukho Chung

Committee Member: Dr. S. Mani Sarathy

Committee Member: Dr. Assaad Masri

ABSTRACT

Experimental and Kinetic Investigation of the Influence of OH Groups on NO_X Formation

Myles D. Bohon

This work investigates the influence of one or more OH groups present on the fuel molecule and the resultant formation of NO_X emissions. Combustion of oxygenated fuels has been increasing globally and such fuels offer significant potential in the reduction of pollutant emissions. One such emission class is the oxides of nitrogen, which typically form through a combination of two regimes: the thermal and non-thermal mechanisms. While thermal NO formation can be reduced by lowering the combustion temperature, non-thermal NO formation is coupled to the fuel chemistry.

An experimental and computational investigation of NO_X formation in three different burner configurations and under a range of equivalence ratios and temperature regimes explored the differences in NO formation. Measurements of temperature profiles and in-flame species concentrations, utilizing both probed and non-intrusive laser based techniques, allowed for the investigation of NO formation through non-thermal pathways and the differences that exist between fuels with varying numbers of OH groups.

The first burner configuration was composed of a high swirl liquid spray burner with insulted combustion chamber walls designed specifically for the combustion of low energy density fuels. In this system the combustion of alcohols and glycerol

(the largest by-product of biodiesel production), along with other fuels with multiple hydroxyl groups, was studied. Measurements of the mean flame temperature and exhaust gas measurements of NO_X showed significant reductions in non-thermal NO concentrations with increasing numbers of OH groups. An accompanying modeling study and detailed reaction path analysis showed that fuel decomposition pathways through formaldehyde were shown a preference due to the presence of the OH groups which resulted in reduced contributions to the hydrocarbon radical pools subsequent reductions to the Prompt NO mechanism.

Two burner configurations with reduced dimensionality facilitated measurements in premixed flames for temperature and species in high and low temperature flames. These measurements included probed thermocouple temperature measurements, extractive gas sampling for NO and intermediate hydrocarbon species, and planar Laser Induced Fluorescence (LIF) measurements for 2λOH-LIF thermometry, semi-quantitative CH_2O LIF, and quantitative NO LIF. Additionally, the simplified nature of the burner geometries allowed for the modeling of the flames incorporating detailed reaction kinetics for fuel decomposition and NO_X formation. Significant reductions in NO formation were observed in comparisons of alcohol and alkane flames, resulting in up to 50% reductions in the pollutant. Computational analyses and nitrogen flux accounting allowed for the identification of the reduction in NO formation through all the known NO_X formation pathways. It was observed that all of the known pathways exhibited reductions in contributions to NO formation in the presence of OH functional groups, indicating a complex coupling of fuel and NO_X chemistry.

ACKNOWLEDGEMENTS

I would begin by thanking my adviser Prof. William Roberts, whose continual guidance and support has carried me through seven years and four continents. He has served to challenge and inspire, always to higher ambitions, and none of the following would be possible without his mentorship.

Thank you as well to my committee for their investment in me and their instruction, who have set aside time to help me grow as a researcher.

Additionally, this work was only achievable with the help of Dr. Mariam Al Rashidi and Dr. Thibault Guiberti who have contributed their expertise and selflessly invested in me, enduring an unending string of questions. Together with Dr. Deanna Lacoste and Dr. Ayman Elbaz, I owe a debt of gratitude for their help and friendship and I look forward to many years of collaboration.

I would also like to thank many more people than I can name here. This work couldn't exist in a vacuum, and so thank you to the long list of friends and colleagues who contributed in many small ways, or who simply humored me in boring conversations.

Finally, thank you to my family, whose love and encouragement have always been a lifeline and a beacon. I strive to make you proud, to live as a man of faith you raised, and to live up to the character and principles you instilled. Thank you for your unfailing support, everything I am is due to you.

TABLE OF CONTENTS

LIST OF SYMBOLS

M_R	Air to liquid mass ratio
μ_A	Dynamic viscosity of air
μ_L	Dynamic viscosity of liquid
ρ_A	Density of air
ρ_L	Density of liquid
σ_L	Surface tension of liquid
U_A	Velocity of atomizing air
U_R	Relative velocity of air to liquid
C_{opt}	Optical collection and calibration coefficient
$D_{3,2}$	Sauter Mean Diameter (diameter of droplet with equivalent volume/surface area ratio)
D_O	Liquid orifice diameter
D_{v10}	Cumulative undersize distribution diameter below 10%
D_{v50}	Cumulative undersize distribution diameter below 50%
D_{v90}	Cumulative undersize distribution diameter below 90%
A_{21}	Einstein coefficient of spontaneous emission
B_{12}	Einstein coefficient of absorption
Q_{21}	Collisional quenching rate
f_b	Boltzmann population fraction in the ground state
Φ	Fluorescent yield

Γ	Laser line overlap integral
HC	Hydrocarbon radical, C_iH_j
I_L	Total spectral laser irradiance
M_O	Mass percentage of oxygen in molecule
n°_{NO}	Number density of target species
NO_X	Oxides of nitrogen (typically NO and NO_2)
ϕ	Local equivalence ratio
ϕ_g	Global equivalence ratio
S_g	Geometric swirl number
$\dot{Q}_T$	Total air flow
$\dot{Q}_\theta$	Tangential component of air flow in the swirl burner
$\dot{Q}_A$	Axial component of air flow in the swirl burner
$\dot{Q}_N$	Atomizing air component of air flow in the swirl burner
$\dot{Q}_f$	Volumetric flow rate of fuel
$\dot{m}_f$	Mass flow rate of fuel
T_f	Fuel preheat temperature
τ_λ	Transmissivity of collection optics

LIST OF FIGURES

LIST OF TABLES

Chapter 1

Introduction

This work initially set out to answer a simple question: can crude, waste glycerin derived from biodiesel production be used as an alternative combustion fuel and if so what are the characteristics unique to its combustion? As with many simple questions, this one has evolved over time, growing and shifting in focus. While still rooted in the same initial premise, this work seeks to answer a more fundamental question spawned in the early stages of studying glycerin combustion. This shift in focus was caused by a series of experiments in which extremely low NO_X emissions were measured in glycerol flames; emission levels much lower than expected or could easily be explained. And since NO_X emissions are among the pollutants governed under increasingly strict environmental regulations, it is important to understand if there are opportunities to reduce these emissions in other applications.

Glycerol, the primary component of the biodiesel waste stream, and also colloquially termed glycerin, is a member of a family of molecules called polyols. This family is characterized by the presence of multiple hydroxyl groups, and along with alcohols can generically be termed poly-alcohols. The glycerol molecule is a three carbon structure containing three hydroxyl groups as shown in Fig. 1.1. It is upon this glycerol backbone that all triglyceride esters are based, and it is the objective of the transesterification process – central to biodiesel production – to break apart the triglyceride molecule and separate the three fatty acids from the glycerol backbone.

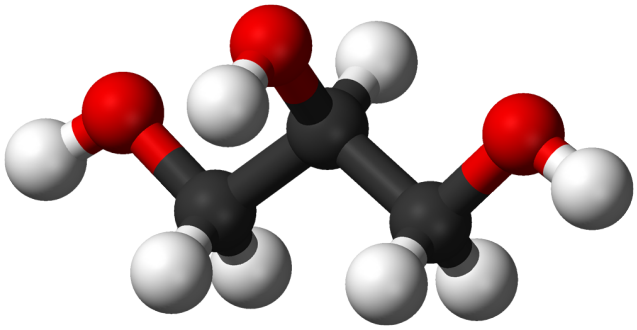

Figure 1.1: Ball and stick model of the glycerol molecule.

One consequence of this process, as well as the significant increase in biodiesel production over the past decade, is the huge production of crude glycerin far in excess of demand. While typically a waste product, potential remains to utilize this waste product as a low cost, carbon neutral energy source, particularly for use locally in the biodiesel production process.

Clearly, the structure of the glycerol molecule plays a significant role is the fuel's properties. Compared with the three carbon gaseous alkane propane, the addition of three hydroxyl groups transforms the compound into a viscous, colorless, sweet liquid with a wide range of uses from the food industry to commodity chemicals to nitroglycerin. It is less clear exactly what role the molecular structure plays in the formation of NO_X however. Additionally, there is a great deal of interest in bio-derived alcohol fuels, particularly ethanol and butanol, which exhibit similar molecular structures and combustion characteristics.

This revised focus resides at the intersection of two long standing fields of combustion research: the combustion chemistry of alcohol fuels and the formation of oxides of nitrogen. Ultimately, the question at the heart of this work is: What role does the hydroxyl group play in NO_X formation?

1.1 Formation of oxides of nitrogen

At the time of publishing for one of the most highly cited review papers on NO_X formation by Miller and Bowman in 1989 [2], the formation of combustion produced nitrogen compounds had already been studied for more than 50 years. Combustion produced NO_X emissions present significant risks to both health and the environment. The health concerns due to NO_X stem from concerns over the formation of small particles from reaction with ammonia, moisture, and other compounds, which when inhaled into sensitive lung tissues and those with asthema can aggravate lung diseases [3]. Environmental concerns over NO_X are due to the formation of tropospheric ozone and acid rain through reaction in the atmosphere [4].

While some of the atmospheric NO_X produced is biogenic or naturally caused by lightning strikes (approx. 10%), the vast majority is caused by combustion sources [4]. These pathways can broadly be grouped into one of four primary mechanisms:

1. Thermal Mechanism – controlled primarily by the elevated temperatures in the flame, this is the oldest NO_X sub-mechanism.

2. Prompt Mechanism – also known as the Fenimore mechanism, this pathway is regulated by interaction of nitrogen and hydrocarbon radicals.

3. Fuel Mechanism – limited to situations in which nitrogen is present in the fuel molecule, this sub-mechanism is similar to the prompt and can be significant in relatively unclean fuels.

4. Minor Mechanisms – a collection of several relatively newly discovered NO_X mechanisms, these pathways can be of varying importance depending on conditions.

A more detailed summary of important contributions to the understanding of each of these mechanisms, as well as the structure of the mechanism, will follow in the

next few sections. These reactions have been studied for many years, and a huge body of literature for experimental measurements of rate parameters and emissions, investigations of mechanism pathways, and computational investigations of rates of production has been developed. Therefore, the following sections cannot possibly cover every known investigation or contribution, but an effort is made to capture the significant contributions and developments in order to provide context for the remainder of this work.

1.1.1 Thermal mechanism

Often called the Zel'dovich mechanism, Yakov Borisovich Zel'dovich was the first to describe the Thermal mechanism in 1947 [5]. This seminal work in the kinetics of NO_X formation is often credited as being the most significant pathway at high temperature, thus the 'Thermal' nomenclature. The mechanism itself is a relatively simple group of three reactions:

$$N_2 + O \rightleftharpoons NO + N \tag{1.1}$$

$$N + O_2 \rightleftharpoons NO + O \tag{1.2}$$

$$N + OH \rightleftharpoons NO + H \tag{1.3}$$

This mechanism is limited by reaction 1.1 and its relatively low reaction rate caused due to the high activation energy of the nitrogen triple bond. As such, high temperatures are required in order to increase the reaction rate significantly and typically this mechanism is considered unimportant at temperatures below 1800 K [6]. After the initial reaction yields NO and N, the remaining nitrogen atom proceeds through reactions 1.2 and 1.3 to form additional NO.

In a general sense, because the chemistry of the Thermal mechanism is relatively slow when compared with the fuel oxidation reactions, the Thermal mechanism can

be considered as decoupled from the fuel oxidation [2]. This allows for the estimation of the rate of NO formation as

$$\frac{d[NO]}{dt} = 2k_{\mathrm{F}(1.1)}[O][N_2] \tag{1.4}$$

where O atom concentration must be approximated as being in partial equilibrium, rather than equilibrium, due to flame front super-equilibrium concentrations of O [7]. Therefore, Thermal NO_X formation is controlled by the forward reaction rate F(1.1) and the availability of O atoms.

Rates for reactions 1.1 to 1.3 are typically taken from a relatively limited data set, with rates compiled by Baulch et al. [8]. However, there is some indication that these rates may be too high, over-predicting rates of Thermal NO_X production and additional effort may be warranted to improve measurements of these rates [9].

1.1.2 Prompt mechanism

The Prompt mechanism may be the most investigated and most complex mechanism considered here due to the considerable coupling of the mechanism with the fuel oxidiation. This mechanism was first identified by Fenimore in the 1970's [10, 11], however there was some skepticism over the existence of such a mechanism [12]. The name 'Prompt' was attached to the mechanism due to the rapid rate at which NO was formed in the flame zone of premixed flames, rates much faster than the slow Thermal mechanism. This mechanism has also be called the Fenimore mechanism in honor of its discoverer.

The formation of Prompt NO is considered to be initiated through a rapid sequence of reactions resulting in the fixation of nitrogen by hydrocarbon radicals, HC. Many studies from the 1970's and 1980's have investigated these nitrogen fixing reactions and the associated HC radicals, proposing CH, CH_2, C_2, C_2H, and C, among others,

as the potentially contributing species [2, 10, 11, 13, 14]. Ultimately, Blauwens has shown that CH and CH_2 are likely the primary initiating species [13].

Until about 2000, the principle Prompt reactions were considered to be:

$$CH + N_2 \rightleftharpoons HCN + N \tag{1.5}$$

$$CH_2 + N_2 \rightleftharpoons HCN + NH \tag{1.6}$$

$$CH_2 + N_2 \rightleftharpoons H_2CN + N \tag{1.7}$$

$$C + N_2 \rightleftharpoons CN + N \tag{1.8}$$

of which, reaction 1.5 was considered to be the most important with reactions 1.6-1.8 considered to provide lesser contributions to Prompt NO [15]. However, from early on it has been recognized that reaction 1.5 is spin forbidden [16], requiring that the reaction cross potential energy surfaces from a doublet to a quartet surface, a relatively slow process [14].

Instead, Moskaleva and Lin showed in 2000 [17] that a better Prompt initiating reaction, that conserves spin, is the reaction

$$CH + N_2 \rightleftharpoons NCN + H \tag{1.9}$$

The resultant NCN then directly forms NO through [18]

$$NCN + O \rightleftharpoons CN + NO \tag{1.10}$$

$$NCN + OH \rightleftharpoons HCN + NO \tag{1.11}$$

$$NCN + H \rightleftharpoons HCN + NO \tag{1.12}$$

$$NCN + O_2 \rightleftharpoons NCO + NO \tag{1.13}$$

while the products of NCN, particularly HCN, behave as previously understood and

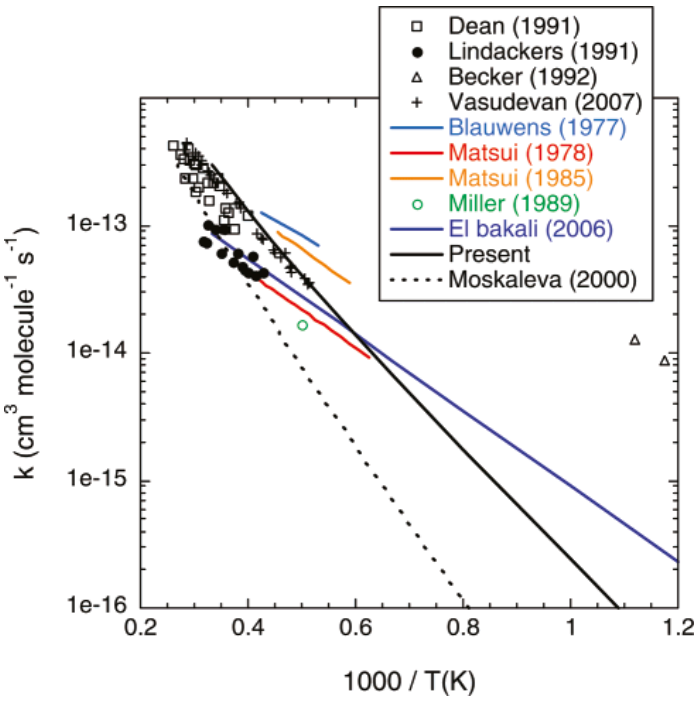

Figure 1.2: Experimental and theoretical rates for $CH + N_2 \rightarrow NCN + H$. The black symbols denote experimental measurements, which the colored lines denote modeling results. Solid and dashed black lines indicate theoretical predictions. Adapted from Harding et al. [24]

proceed to form NO in their own right [19, 20].

Experimental measurements of NCN in the flame are limited, however Smith was able to demonstrate the presence of NCN in low pressure methane flames [21] using detection by LIF. Measurements of the rate constant for reaction 1.9, have been continually improving from the initial theoretical predictions of Moskaleva and Lin [17]. Estimations from El Bakali [22] and shock tube measurements by Vasudevan at temperatures greater than 2000 K [23] improved these rates. Harding then further improved the estimate of this rate for temperatures below 2000 K [24]. A comparison of a number of studies on these rates is shown in Fig. 1.2

Additionally, accurate predictions of CH radicals are necessary for an accurate estimate of Prompt NO formation. Typically, CH is formed from methylene (CH_2), however pathways can vary depending on the fuel. Methylene is typically formed from one of two sources: methyl radical (CH_3) or acetylene (C_2H_2). At less than very

rich conditions, the dominant pathway is through methyl radical via:

$$CH_3 + OH \rightleftharpoons CH_2 + H_2O \tag{1.14}$$

$$CH_3 + H \rightleftharpoons CH_2 + H_2 \tag{1.15}$$

Once the Prompt sub-mechanism has been initiated, conversion of the remaining nitrogen-fixed species, such as HCN, NCO, CN, and N proceeds to rapidly produce NO via

$$HCN + O \rightleftharpoons NCO + H \tag{1.16}$$

$$CN + OH \rightleftharpoons NCO + H \tag{1.17}$$

$$NCO + H \rightleftharpoons NH + H \tag{1.18}$$

$$NH + H \rightleftharpoons N + H_2 \tag{1.19}$$

$$N + OH \rightleftharpoons NO + H \tag{1.20}$$

Miller [2] provides a nice summary of the three controlling issues in the Prompt sub-mechanism as follows:

1. the CH concentration and how it is established,
2. the rate of molecular nitrogen fixation (formation of HCN via $CH + N_2$; while this would now be update to NCN, the outcome is the same), and
3. the rates of interconversion among fixed nitrogen fragments.

Each of these points is significantly impacted by the fuel chemistry, far more so than the Thermal sub-mechanism. Additionally, the Prompt sub-mechanism is a significant contributor, if not the dominant mechanism, under many practical combustion conditions, necessitating the inclusion and consideration of this sub-mechanism in any detailed study of NO_X formation. A recent study of modeling of NO formation

in low pressure premixed flames showed an improved ability to predict NO formation through the NCN pathway, however additional experimental measurements of key species would help to improve the accuracy [25].

1.1.3 Fuel mechanism

In real fuels, it is not uncommon for nitrogen to be molecularly bound to the fuel molecule. This can be especially true for coal combustion, in which the coal may contain as much as 2% nitrogen by weight [2]. By the incorporation of nitrogen into the fuel molecule, the nitrogen-fixation reactions required for the Prompt sub-mechanism are effectively subverted, and the formation of NO through this fuel-bound nitrogen is considered largely independent of the initial fuel and is more dependent on the combustion environment. Conversion to NO typically occurs through either HCN or NH_3 pathways, with the pathway selection dependent on the nature of the inclusion of nitrogen in the fuel molecule, i.e. HCN is the principle pathway when the nitrogen is in an aromatic ring and NH_3 is the principle pathway when the nitrogen is in the form of an amine [11, 26].

Because the fuels used in this study are expected to contain little to no fuel-bound nitrogen, little consideration will be given to this sub-mechanism. However, it should be noted that both pathways to Fuel NO_X formation, either through HCN or NH_3, are members of the other NO_X mechanisms included in this analysis. As a result, the Fuel NO_X sub-mechanism is not completely without consideration.

1.1.4 Minor mechanisms: NO-HCN-Reburn

The term minor in this and the following mechanisms, simply indicates that these mechanisms may or may not have significant contributions to NO_X formation. Generally, these mechanism can be significant, or even dominant, under certain combustion conditions and negligible at others. The first of these mechanisms considered

here is the NO-HCN-Reburn mechanism. While naturally occurring under many flame conditions, this mechanism was originally pursued as a NO_X reduction strategy through staged combustion. The mechanism involves the recycling of NO back to HCN through reactions with HC radicals, at which time the fate of HCN is determined by the radical environment and is converted to either N_2 or back to NO.

This NO_X mitigation strategy was originally investigated by several groups in the 1970's [27, 28], and was often comprised of the segmented addition of fuel in multiple stages. The majority of the fuel is burned in the first stage, typically at relatively high temperatures with significant NO formation. In the next stage, additional fuel such as methane is injected into the combustion products of the first stage. The result is a fuel-rich region containing many HC radicals which are free to react with NO to form HCN. The last stage controls the conversion of HCN back N_2 and NO.

Determination of the specific HC radicals involved in the formation of HCN from NO has been studied by a number of people [19, 29–32], and the following reactions have been identified as the most important:

$$HCCO + NO \rightleftharpoons HCNO + CO \tag{1.21}$$

$$HCCO + NO \rightleftharpoons HCN + CO_2 \tag{1.22}$$

$$CH_3 + NO \rightleftharpoons HCN + H_2O \tag{1.23}$$

$$CH_3 + NO \rightleftharpoons H_2CN + OH \tag{1.24}$$

$$CH + NO \rightleftharpoons HCN + O \tag{1.25}$$

$$C + NO \rightleftharpoons CN + O \tag{1.26}$$

The prominence of a given initiating NO removal radical is typically condition dependent: under radical-rich conditions, NO is more likely to be removed by the smaller radicals such as CH and C, however, under less radical-rich conditions HCCO and CH_3 can be more prominent. Under most conditions however, HCCO typically plays

the most important role [33, 34].

The fate of HCN, similar to the Prompt sub-mechanism, is controlled through O atom [35], and the conversion back to N_2 follows the procession below:

$$HCN + O \rightleftharpoons HCN + H_2O \tag{1.27}$$

$$HCN + O \rightleftharpoons NH + CO \tag{1.28}$$

$$NCO + H \rightleftharpoons NH + CO \tag{1.29}$$

$$NH + H \rightleftharpoons N + H_2 \tag{1.30}$$

$$N + NO \rightleftharpoons N_2 + O \tag{1.31}$$

with the net result of the removal of a total of two NO molecules through this mechanism.

1.1.5 Minor mechanisms: NO_2

The other primary component of NO_X, NO_2 has been observed to be present in significant quantities in the flame front [36–38]. The formation of NO_2 is driven by the presence of hydroperoxyl radical in the flame front through the reaction

$$NO + HO_2 \rightleftharpoons NO_2 + OH \tag{1.32}$$

The NO involved in the above equation is typically formed via other mechanisms in higher temperature regions of the flame and transported to the cooler regions of the flame with significant HO_2 concentrations. Usually, NO_2 is rapidly converted back to NO through

$$NO_2 + H \rightleftharpoons NO + OH \tag{1.33}$$

$$NO_2 + O \rightleftharpoons NO + O2 \tag{1.34}$$

as it transits through the high temperature regions of the flame.

1.1.6 Minor mechanisms: N_2O

Under lean conditions, in which the formation of Prompt NO is low (due to low availability of CH) and the Thermal contribution is low (due to lower temperatures), one of the remaining primary NO pathways is through the N_2O mechanism [2, 7]. This mechanism is initiated by the formation of nitrous oxide (N_2O) through the three body reaction 1.35 and subsequent reaction to form NO in reaction 1.36.

$$N_2 + O + M \rightleftharpoons N_2O + M \tag{1.35}$$

$$N_2O + O \rightleftharpoons NO + NO \tag{1.36}$$

Additionally, reaction 1.35 is enhanced at elevated pressure, and as a result, this mechanism can be significant at the lean premixed temperatures and pressures of gas turbines [39].

1.1.7 Minor mechanisms: NNH

The role of NNH was first proposed by Miller et al. [40] as a participant in the Thermal $DeNO_X$ process for NO removal via non-catalytic reduction of NO by NH_3 [14, 41–44]. While not a particular focus of this work, the Thermal $DeNO_X$ process is an interesting application in which ammonia is injected under very specific temperature and oxygen conditions resulting in a self-sustaining reaction leading to the removal of NO through reaction with NH_2.

Through the investigations of the potential products of this reaction, NNH was identified as one such potential product. Later, an additional NO formation pathway through reaction of NNH with O atom was proposed by Bozzelli and Dean [45] with additional evidence for NO formation linked with NNH provided by Harrington et

al. [46]. This pathway to NO formation proceeds through reaction 1.37.

$$NNH + O \rightleftharpoons NH + NO \tag{1.37}$$

Additionally, another potential product of the $NNH + O$ reaction is N_2O. Combined with the N_2O mechanism above and the paired oxidation through amine radicals, the contribution of this mechanism can be significant under the right conditions, particularly at temperatures below the limit for the Thermal mechanism. A more recent study of Klippenstein et al. [47] provides a detailed summary of the H/N/O reactions subset and is incorporated in the NO_X mechanism in this work.

1.2 Alcohol combustion chemistry

The study of the combustion of alcohols dates back at least as far as 1953 [48], in which many early combustion researchers were investigating the combustion of liquid fuels and liquid fuel droplets [49–52]. The primary objective of these early studies was to investigate the physics of vaporizing droplets, particularly of more complicated liquid fuels such as kerosene, gasoline, diesel, and benzene and simple, easily vaporized fuels such as methanol and ethanol were often convenient to include in their studies. However, the primary focus would not shift toward the alcohol combustion chemistry until the late 1970's and early 1980's.

At this time, increasing interest in the use of alcohols as alternative fuels, as well as fuel additives, prompted the beginning of a focus on developing a detailed understanding of the combustion chemistry in the 1990's [53]. These studies focused on the measurement of laminar burning velocities and predictive models for methanol and ethanol [53–58]. As pointed out by Sarathy et al. [59], after 2003, a huge surge in research in alcohol combustion chemistry was observed, particularly with regard to ethanol (due to its significant use in transportation fuels) and the addition of

interest in the butanol isomers (due to their higher energy densities, relative ease of use experimentally, and the potential of significant levels of production through several new biofuel production processes).

It is simply beyond the scope of this work to discuss all of the studies, either experimental or kinetic, that have been conducted even within the past 15 years. Fortunately, the excellent review paper of Sarathy et al. [59] on the current state of alcohol combustion chemistry renders such a discussion redundant and unnecessary. Rather, the focus of this section will be more limited in scope, focusing instead on summarizing the characteristics unique to the combustion chemistry of the fuels used in this study.

It is helpful to first consider the unique characteristics common to all alcohols, before discussing the individual characteristics of the fuels in this study. The definitive feature of the alcohol molecule in comparison with its alkane cousin is the presence of the -OH, or hydroxyl, moiety located on the carbon chain. This hydroxyl group causes the phase to condense, and as a result all alcohols are liquid at room temperature whereas the alkane cousins remain in the gas phase until the carbon number increases to certain pentane isomers. Additionally, the hydroxyl group typically lowers the energy density, an effect which is more pronounced the smaller the molecule becomes. Along with the lower energy density, the presence of the hydroxyl group induces a polarity to the molecule, increasing the miscibility of the fuel with water.

Molecularly, the presence of the hydroxyl moiety results in weaker C-H bond dissociation energies (BDE) on the carbon bound to the hydroxyl group (α-C site) [60]. Additionally, the C-C bonds adjacent to the hydroxyl group also experience a weakening of their bond strengths while the C_2-C_3 bonds and C-H bonds on the C_2 (β-C site)are strengthened. The presence of this hydroxyl group is typically influential up to the third carbon adjacent to the hydroxyl group (γ-C site) [61]. Beyond the γ-C site, the rest of the molecule behaves similarly to those in alkanes. Finally, the

O-H bonds in the alcohol are quite strong and as such it is difficult to abstract the hydrogen from these sites.

1.2.1 Methanol combustion chemistry

The fate of methanol during decomposition is the simplest of the alcohols, is significantly different from that of its cousin methane, and occasionally is observed through the recombination of methyl and hydroxyl radicals in the combustion of hydrocarbons. The primary decomposition products of methanol are through:

$$CH_3OH \rightleftharpoons CH_3 + OH \tag{1.38}$$

$$CH_3OH\ (+H/OH/HO_2) \rightleftharpoons CH_2OH + (H/H_2/H_2O/H_2O_2) \tag{1.39}$$

$$CH_3OH\ (+H/OH/HO_2) \rightleftharpoons CH_3O + (H_2/H_2O/H_2O_2) \tag{1.40}$$

where pathways leading to CH_2OH are the most significant (approx. 75%) [58]. Consumption of methanol by OH radicals yielding CH_2OH is typically the primary consumption pathway under lean and stoichiometric conditions while reaction with H radicals yielding both CH_2OH and CH_3O are increasingly important under rich conditions [62]. The formation of CH_3, through initial decomposition reactions or through other pathways, is typically extremely low [58]. It should also be noted that while hydroperoxyl radical is primarily formed through

$$H + O_2 + M \rightleftharpoons HO_2 + M \tag{1.41}$$

in hydrocarbon flames, significant contributions to HO_2 can also occur through reaction of CH_2OH and O_2 yielding formaldehyde and hydroperoxyl radical [56, 57].

Meanwhile, the hydroxymethyl radical (CH_2OH) and methoxy radical (CH_3O) share similar fates in consumption through thermal decomposition into formaldehyde

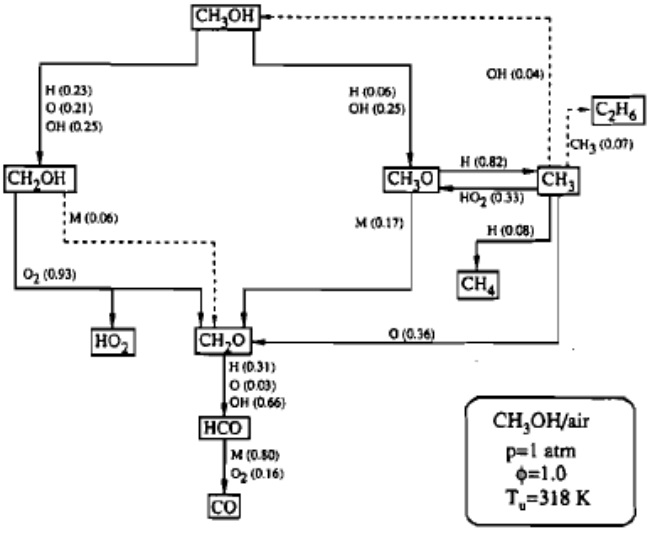

Figure 1.3: Example methanol decomposition pathway for a stoichiometric methanol/air flame. Adapted from Egolfopoulos et al. [58]

(CH_2O). While the methoxy radical is primarily consumed through the thermal decomposition pathway, a portion may proceed through reaction with H to form CH_3 under stoichiometric conditions due to the abundance of H atoms [58]. These pathways are summarized in Fig. 1.3, where clearly, nearly all decomposition pathways ultimately lead through to the formation of formaldehyde and subsequent oxidation through HCO and CO. The net result of these rather limited set of decomposition pathways is concentrations of formaldehyde and hydroperoxyl radical of 15 and 4 times that of methane with greatly reduced concentrations of hydrocarbon radicals.

1.2.2 Ethanol combustion chemistry

Ethanol has received a great degree of attention from researchers due to its common use in transportation fuels (approx. 0.88 mboe/day in the US in 2014 [63]. The chemistry of ethanol oxidation is more complicated than either methanol or its alkane cousin ethane due to the reaction pathways common to both alkane and alcohol – dehydrogenation (H-abstraction) or decomposition – as well as the additional potential for dehydration (water elimination) reactions [57]. The net result of ethanol

decomposition also contains a wider mix of both oxygenated and non-oxygenated intermediates, further increasing the complexity.

Sarathy et al. [59] delineates the decomposition pathways and the resultant products into the various reaction classes. The first pathway is the unimolecular decomposition, primarily through the following two pathways:

$$C_2H_5OH \rightleftharpoons C_2H_4 + H_2O \tag{1.42}$$

$$C_2H_5OH \rightleftharpoons CH_3 + CH_2OH \tag{1.43}$$

with reaction 1.42 favored at low temperature (less than 1400 K) and with reaction 1.43 increasing to be of comparable importance around 2000 K [64]. However, the most important reactions in ethanol decomposition in flames proceed through H-abstraction:

$$C_2H_5OH + (H/OH/HO_2) \rightleftharpoons C_2H_5O + (H_2/H_2O/H_2O_2) \tag{1.44}$$

$$C_2H_5OH + (H/OH/HO_2) \rightleftharpoons CH_3CHOH + (H_2/H_2O/H_2O_2) \tag{1.45}$$

$$C_2H_5OH + (H/OH/HO_2) \rightleftharpoons CH_2CH_2OH + (H_2/H_2O/H_2O_2) \tag{1.46}$$

with abstraction by OH radical being the most important. Typically, abstraction from the hydroxyl group (reaction 1.44) is limited due to the high bond strength in comparison to the other C-H abstraction sites, so reactions 1.45 and 1.46 are the more predominant products [65].

The resultant fuel radicals, C_2H_5O, CH_3CHOH and CH_2CH_2OH, are then consumed through either thermal decomposition or isomerization reactions. Several researchers have investigated the possible pathways for the decomposition of these ethyoxy and hydroxyethyl radicals [66, 67], and the resultant predominant pathways for

C_2H_5O are:

$$C_2H_5OH \rightleftharpoons CH_2O + CH_3 \tag{1.47}$$

$$C_2H_5OH \rightleftharpoons CH_3CHO + H \tag{1.48}$$

while CH_3CHOH proceeds through:

$$CH_3CHOH \rightleftharpoons CH_3CHO + H \tag{1.49}$$

$$CH_3CHOH \rightleftharpoons C_2H_3OH + H \tag{1.50}$$

$$CH_3CHOH + O_2 \rightleftharpoons CH_3CHO + HO_2 \tag{1.51}$$

and CH_2CH_2OH through

$$CH_2CH_2OH \rightleftharpoons C_2H_4 + OH \tag{1.52}$$

$$CH_2CH_2OH \rightleftharpoons C_2H_3OH + H \tag{1.53}$$

$$CH_2CH_2OH + O_2 \rightleftharpoons 2CH_2O + HO_2 \tag{1.54}$$

Ultimately, most of the C_2H5O undergoes reaction 1.47, with about 25% through reaction 1.48 under combustion conditions. All three reactions 1.49–1.51 are important pathways in the decomposition of CH_3CHOH, with a preference for the formation of acetaldehyde (CH_3CHO). Meanwhile, CH_2CH_2OH primarily proceeds through reaction 1.52 (approx. 90%) with the remainder through reactions 1.53 and 1.54.

Adapted from the review paper of Sarathy et al. [59], Fig. 1.4 provides a general reaction diagram for the decomposition of ethanol. As can be seen in the figure, decomposition of ethanol ultimately results in the formation of one of several stable intermediate species: ethylene (through H-abstraction from the β-C site), acetaldehyde (through H-abstraction from the α-C site), ethenol (also through H-abstraction from the α-C site), and formaldehyde (through H-abstraction from the hydroxyl and

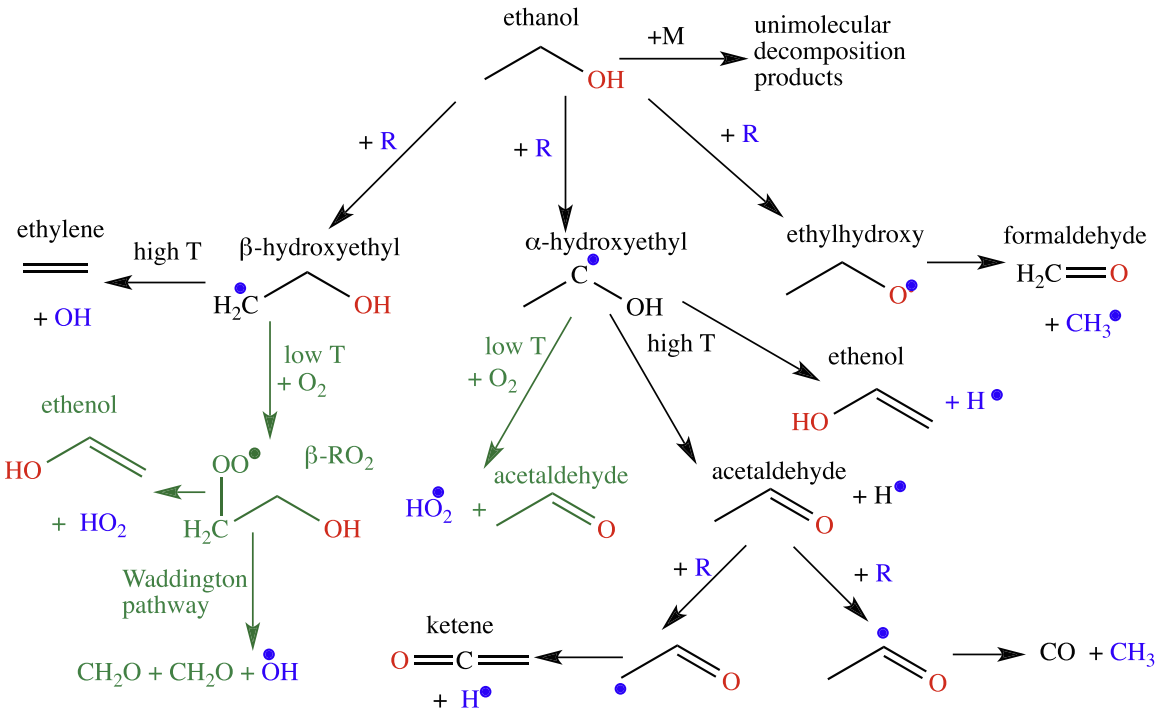

Figure 1.4: Example ethanol decomposition pathway diagram for ethanol decomposition, also showing low-temperature pathways. Adapted from Sarathy et al. [59]

through thermal decomposition of ethanol). The primary pathway is through the formation and destruction of acetaldehyde, proceeding through H-abstraction from the oxygen adjacent carbon, ultimately yielding CO and CH_3, while a minor pathway proceeds to form ketene.

1.2.3 Propanol combustion chemistry

Despite being the smallest alcohol to exist in isomeric forms, propanol has received relatively little research focus, especially in comparison to methanol, ethanol, or the butanol isomers. Along with a smaller subset of experimental and reaction rate measurements [68–73], the primary propanol kinetic models currently utilized [74–76] heavily employ estimation of reaction rates determined through analogy with the ethanol and butanol chemistry [77].

Qualitatively, the propanol isomers proceed through similar reaction paths as

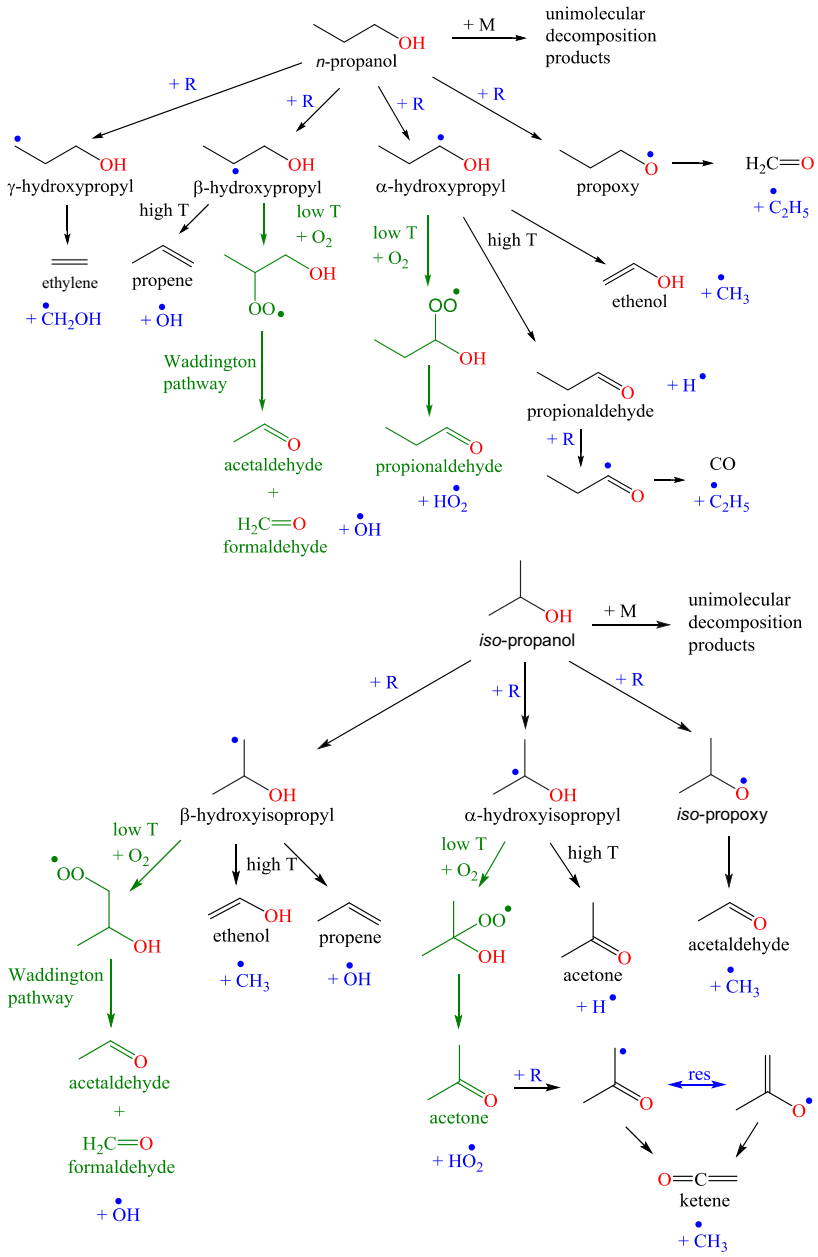

Figure 1.5: Example n-propanol and i-propanol decomposition pathway diagrams, also showing low-temperature pathways. Adapted from Sarathy et al. [59]

ethanol, proceeding through a combination of unimolecular dissociation reactions, water elimination reactions, C-C scissions, and H-abstractions. In the propanol sub-mechanism proposed by Sarathy et al. [59], rates for the unimolecular dissociations reactions are estimated from analogy. Important at high temperatures, the water elimination reactions as well as the C-C scission reactions are estimated by analogy to butanol isomers. A limited subset of H-abstraction by OH rate data is avaiable [78] with the remainder being estimate by analogy.

Figure 1.5 illustrates the generalized reaction path diagram for the propanol isomers. Decomposition for n-propanol proceeds primarily through the H-abstraction pathways, with abstraction from the α-C site favored over the other sites due to the reduced bond dissociation energy associated with the proximity of the hydroxyl group. The resultant α-hydroxypropyl radicals then form propionaldehyde (propanal), and under high temperature conditions, ethenol and methyl radical can form as well. Propanal then decomposes to form CO and ethyl radical. Products by abstraction of the other two carbon sites yield propene (from β-hydroxypropyl radical) and ethene and hydroxymethyl radical (from γ-hydroxypropyl radical). While not as major of an H-abstraction site, products from the abstraction of the oxygen adjacent hydrogen yield formaldehyde and ethyl radical.

Decomposition of i-propanol proceeds through only two C-H-abstraction sites due to the symmetry of the molecule. Abstraction from the α-C site yields acetone as an intermediate for both high and low temperature conditions. Abstraction from the β-C site yields both ethenol (and methyl radical) and propene. The resultant decomposition products of both acetone and ethenol are resonantly stable species, which combined with the greater concentrations of acetone in the i-propanol reaction path, compared with greater concentrations of propanal in the n-propanol reaction path, result in an ultimately less reactive isomer [57]. Lastly, the only pathway resulting in the formation of acetaldehyde in the i-propanol chemistry is through H-

abstraction from the oxygen, so concentrations of this pollutant are typically lower for i-propanol than for n-propanol.

1.2.4 Poly-alcohol combustion

Most of the work on the combustion of poly-alcohols (also interchangeably known as polyols or hydroxylated fuels) is motivated by interest in the use of bio-fuel derived glycerol and waste glycerin in cogeneration or combined heat and power [79]. While most poly-alcohols are relatively high-cost, low volume commodity chemicals, glycerol has recently experienced a huge surge in supply as a consequence of biodiesel production [80] followed by the expected drop in prices and a search for alternative uses [81]. An obvious application is the combustion of the waste glycerol stream, typically done locally or even on-site to the biodiesel production with direct interfacing to the production process [82].

Historical uses for glycerol are many and varied, however the demand typically required by these applications has been relatively small [80]. Due to continually increasing biodiesel production over the past decade, the annual global production of glycerol has risen to an estimated 1.5 million metric tons in 2011 from 0.9 million metric tons in 2005 [81]. Conventional uses for glycerol (and the other polyols studied in this work) include conversion to other commodity chemicals, food and pharmaceuticals, applications in biological sciences, conversion into oxygenated diesel fuel additives, and use in particle synthesis formulations [79–81, 83–87].

However, the most discussed potential use for the excess glycerol is combustion and utilization as an alternative, carbon neutral energy source. Unfortunately, the combustion of glycerol is typically a non-trivial endeavor, requiring careful consideration of the glycerol feedstock source and fuel processing, specific combustion apparatus, and potentially post-combustion treatment.

The first major endeavor to characterize the combustion of glycerol was under-

taken in 2007 by Patzer et al. [88]. Previously, researchers had considered glycerol in the context of droplet studies (due to its high viscosity and boiling point) [89], however use of glycerol as a practical alternative fuel was not researched until Patzer investigated glycerol combustion in an unmodified package boiler. Due to difficulties in stabilizing a pure glycerol flame, glycerol was co-fired with yellow grease. Significant concerns over the formation of ash, particulation matter, residual material, and fuel handling difficulties were noted as limiting concerns.

The next major endeavor to study the combustion of various crude waste glycerin streams was undertaken by the author in 2011 [90, 91]. This work built from an initial study by Metzger [92] and investigated glycerin combustion in two experimental apparatus. The first apparatus is a 7 kW laboratory scale refractory burner that has served as the basis for further experiments described in later chapters and details of the burner design is described in greater detail in Chapter 2. The second apparatus is an 82 kW laboratory scale refractory-lined furnace equipped with an International Flame Research Foundation (IFRF) movable-block, variable-air swirl burner incorporated with an air-atomizing nozzle. Additional details on the laboratory furnace are available in Ref. [93, 94]. Both systems were composed of essentially similar design, including refractory insulation of the combustion chamber, adjustable swirl numbers for flame stabilization, and air-assisted atomization for viscous fluids. Additionally, the operation of each burner was also functionally similar, whereby the apparatus was preheated using a traditional gaseous fuel (propane in the 7 kW and natural gas in the 82 kW burners) before switching to the glycerol fuel. Experiments in the 7 kW burner were conducted with a pure, USP grade glycerol fuel, while the 82 kW furnace employed two formulations of crude glycerin (with and without the methanol remnant of the transesterification reaction).

Emissions measurements of common emissions such as CO, CO_2, O_2, and NO_X as well as particulate matter and carbonyl emissions measurements were conducted.

With the exception of NO_X, both combustors produced gas-phase emissions similar to natural gas and distillate fuel oils, indicating low total hydrocarbon emissions and efficient combustion. Interestingly, NO_X emissions from the prototype burner were a factor of 20 times lower than those from the comparison fuels. Particulate matter emissions from the crude glycerol formations were observed to be extremely high (2200-3400 mg/m^3) due to the large sodium catalyst residual in the fuel, requiring any practical application to address this issue with ash mitigation/post treatment or precondition the fuel before combustion. Measurements of carbonyl compounds were conducted. One of the initial fears of the combustion of glycerol is the potential for excess emissions of carbonyl compounds (particularly acrolein), however measurements indicated only a slightly increase in these species over traditional fuels.

Additional work done by Steinmetz et al. [95] measured particulate matter, oxygenated pollutant emissions (such as aldehydes and ketones), and other volatile organic carbon emissions in the same 82 kW furnace used by Bohon [91]. Analysis of the fly ash indicated extremely large concentrations of ash in the furnace and compositional analysis revealed a predominantly alkali and alkaline earth elemental composition. This metallic content originates in the crude waste stream through the sodium hydroxide catalyst used in the transesterification reaction. Measurements using XRF did indeed indicate very high concentrations of sodium carbonate, sodium sulfate, and sodium phosphate in the collected ash samples. Steinmetz showed that much of this ash forms through nucleation and particle growth (coagulation and condensation) of vaporized metallic content in the flame. Additionally, Steinmetz measured VOC concentrations in the stack gases, with a focus on acrolein. Reported concentrations of acrolein where slightly elevated in the glycerol stack emissions, however the concentrations were still relatively low in comparison with natural gas (20.7 and 13.3 ppbv, respectively).

Several studies of the combustion of viscous fuels utilizing an air-assisted atomiz-

ing technique known as effervescent atomization have investigated glycerol combustion [96–98]. These studies focused on establishing glycerol spray flames in swirling configurations, with and without methane co-firing, and have conducted several species measurements for NO, CO, droplet size distribution and temperature in the post gases and flame region. The results from these studies are comparable with those discussed in the author's previous work [91] as well as work discussed in the following chapters [99, 100].

McNeil et al. [101] reports using straight technical grade glycerol (98%, biodiesel derived) in a 4 cylinder direct injection turbocharged diesel engine. Measurements of common emissions of near full load are shown to be lower than from diesel fuel, and the indicated efficiency is up to 2% higher. They report low concentrations of aldehydes, however it is unclear how these measurements were conducted as there are few method details reported and whether the reported concentrations are above the minimum detectable limit.

Eaton et al. [102] investigated emulsions of glycerol in diesel fuel powering a single cylinder diesel engine, with emulsions of 10% and 20% glycerol in diesel. Addition of glycerol was observed to retard ignition combustion initiation, but measurements of NO_X concentrations were observed to decrease between 5-15% while particulate matter emissions decreased up to 50%. However, unburned hydrocarbon emissions increased significantly.

1.3 NO_X formation in hydroxylated fuels

A few studies have investigated NO_X formation in the combustion of hydroxylated fuels, however not as much work has been done in this area as one might expect. Most of this work has been focused exclusively on NO_X formation in the combustion of alcohols.

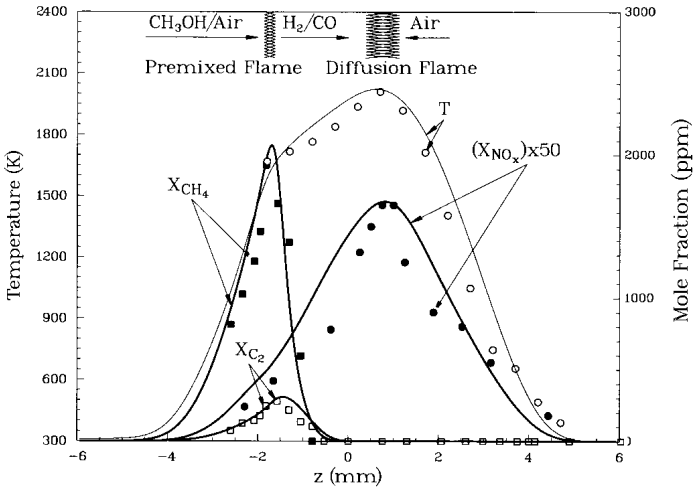

Figure 1.6: Profiles of temperature and mole fractions of CH_4, $C_2H_{i=2,4,6}$, and NO_X in a two-stage methanol-air flame with an equivalence ratio of 2.4 and a strain rate of 50 s^{-1}. Adapted from Li et al. [103]

William's group has conducted several studies on NO_X formation in methanol and ethanol flames. The first of these works by Li et al. [103] examined the combustion of methanol in an atmospheric pressure laminar, two-stage premixed flame and a counterflow two-stage flame with three different methanol kinetic mechanisms (184 reactions with 45 species, as well as a 6-step and 1-step mechanism) including a relatively simple NO_X mechanism (52 reactions, 13 species). Only a relatively small set of experimental extracted gas sample measurements for NO concentrations were reported. Comparisons of measurements with model predictions showed good agreement for both the premixed and diffusion flames as shown in Fig. 1.6.

Li attributes most of the NO formation to the Thermal mechanism, reasoning that predicted concentrations of CH are very low in comparison with methane and the resultant Prompt contribution is expected to be low as well. Li et al. [104] also studied the addition of water, N_2, CO_2, and Ar and observed subsequent reductions in NO formation through the Thermal mechanism via suppression of the temperature.

Saxena et al. [105] later extended the methanol mechanism of Li for use with ethanol and a validation study was conducted. Measurements of NO concentrations

were very limited however, presenting a single set of measurements in a partially-premixed ($\phi = 2.3$) ethanol-air flame. A detailed investigation of NO_X contributions was not conducted, rather predicted concentrations of NO were attributed primarily to formation through the Thermal mechanism. Contributions through the Prompt mechanism were predicted to be greater than that in the methanol flames however still lower than hydrocarbon flames due to predicted peak CH concentrations of approximately 50% of comparable alkane flames.

Marques et al. [106] studied NO in ethanol flames with laser saturated fluorescence (LSF) with the primary objective of using OH^* and CH^* chemiluminescence to correlate NO concentrations. They report a predominance of thermal NO in stoichiometric flames and prompt NO in rich flames. They observe a strong correlation of CH^* chemiluminescence with NO formation under fuel-rich conditions, however they ultimately recommend a ratio of the chemiluminescence of CH^* to OH^* as a better correlation to NO formation.

The only other work to conduct a direct comparison of NO concentrations between alcohol and alkane fuels was Chung et al. [107]. The fuels of interest were butane and butanol isomers. In this work, measurements of NO concentrations were conducted by planar laser induced fluorescence (PLIF) measurements in stagnating premixed flames. Simulations of these flames were conducted using the butanol chemistry of Sarathy et al. [77, 108] with a NO_X sub-mechanism for methane combustion from El bakali et al. [22]. Chung showed that for most butanol isomers lower levels of NO were formed, except for iso-butanol, and asserts that consistently lower NO was formed through both Prompt and Thermal mechanisms.

1.4 Objectives and contributions

In the most general sense, the endeavor of this work was to gain a better understanding of the role that the presence of one or more hydroxyl groups on the fuel molecule plays in the formation of NO_X emissions. Initial work published by the author [90, 91] indicates the potential for significantly reduced NO_X emissions in the combustion of glycerol, a fuel characterized by the presence of three hydroxyl groups on the fuel molecule. In pursuit of this goal, a high swirl burner apparatus was designed expressly to address the unique difficulties inherent in the combustion of the poly-alcohol fuels (such as glycerol). Additionally, a vaporization system was developed to provide the steady vaporization and premixing of alcohols to allow for more fundamental studies in configurations with better defined boundary conditions than the swirl burner. Detailed chemical kinetic modeling under a number of configurations was also conducted, with a focus on exploring the different contributions from NO_X formation sub-mechanisms. These objectives are summarized below:

- Construct and characterize a high swirl, insulated liquid spray burner apparatus for the combustion of low energy density, high viscosity, difficult to burn fuels.
- Understand the atomization characteristics of the viscous fuels and the impact of atomization quality on flame dynamics.
- Characterize the variations in both thermal and non-thermal contributions to NO_X formation in the combustion of polyols through both experimental and kinetic modeling means.
- Investigate the fuel decomposition pathways of poly-alcohols and the influence of varying molecular structure on decomposition pathways and intermediate species distributions.
- Design a vaporization system for the premixing of alcohol and other liquid fuels

(with a reasonable volatility) to be integrated with canonical burner configurations.

- Experimentally investigate temperature and species concentrations in a canonical flame with reduced dimensionality for comparisons with flame simulations.

- Non-intrusively probe canonical premixed flames with in-situ planar Laser Induced Fluorescence techniques for temperature, NO, and formaldehyde concentrations.

- Conduct a nitrogen flux accounting study to determine contributions from non-thermal NO_X sub-mechanisms and the influence that fuel decomposition pathways have on relative formation of NO through these pathways.

Chapter 3 describes the development of the high swirl burner for low energy density, high viscosity fuels. This work includes a parameter study of the effect of the global equivalence ratio and atomizing air flow rate under fixed firing rate and swirl number conditions for glycerol and diesel spray flames. Measurements of exhaust gas temperature and composition were conducted as well as a limited set of measurements of droplet size distributions for both fuels. This work was originally published in 2013 [99].

Chapters 4–5 conduct a detailed investigation of the atomization characteristics of the C_1-C_3 poly-alcohols and investigate the mean temperature distribution and NO_X emissions. Utilizing the available controls, the operating conditions are carefully controlled to yield matching temperature distributions, thus allowing for a direct comparison of non-thermal NO_X contributions for these difficult to burn fuels. Chapter 6 then compares fuel decomposition pathways through a detailed reaction path analysis of perfectly stirred reactor simulations under burner typical temperatures and equivalence ratios. The work contained in these chapters was originally published in 2015 [100].

Chapter 7 then conducts measurements of the temperature distribution in premixed alcohol flame flames stabilized on a porous plug McKenna burner. The temperature was measured with the combined techniques of probed thermocouple measurements and 2λ-OH PLIF thermometry. This temperature was then imposed as the predefined temperature in simulations of these flat flames. Comparisons of measured and predicted concentrations of NO in the post flame were conducted. Lastly, the contributions from the various NO_X formation pathways to the total NO formation was investigated through a nitrogen flux accounting. The work contained in this chapter has been accepted for presentation in 2016 [109].

Chapter 8 presents an investigation of non-intrusive NO concentration measurements in premixed burner stabilized and bunsen conical flame configurations. Quantitative NO PLIF measurements were conducted, allowing for investigations of both the thermal and non-thermal contributions for both alkanes and alcohols under a range of equivalence ratios. The work contained in this chapter is currently under preparation for submissions.

Finally, Chapter 9 presents an investigation of the concentrations of formaldehyde concentrations in alcohol and alkane bunsen conical premixed flames. Formaldehyde is a key intermediate species in the decomposition pathways of alcohols (and polyalcohols), and represents a decomposition pathway with limited contribution to nitrogen fixing carbon species. Relative concentration measurements of formaldehyde in the flame front was conducted via semi-quantitative PLIF measurements under a range of equivalence ratios. The work contained in this chapter is also currently under preparation for submission.

Chapter 2

Experimental apparatus, techniques, and methods

This chapter provides a detailed description of the different burner apparatus and diagnostic techniques utilized throughout this text. While each chapter includes a brief description of the apparatus, conditions, and/or techniques specific to that chapter, it is in this section that the details of the design, operation, or experimental considerations for all of the equipment and tools used in the following work will be discussed.

Among the burners used in this study are three different configurations. In Section 2.1 the high swirl burner will be presented. The other two burners utilize a prevaporization system described in Section 2.2 accompanied by descriptions of the McKenna and Bunsen burners in Sections 2.2.1 and 2.2.2, respectively.

The following sections will discuss the various diagnostic techniques used through this work. Section 2.3 will provide an introduction to Laser Induced Fluorescence (LIF) techniques in general, followed by specific considerations for 2λ-OH LIF thermometry, CH_2O LIF, and NO LIF. Sections 2.4, 2.5,and 2.6 will then present the technique for probed thermocouple measurements, extractive gas sampling for species concentrations, and droplet size distribution measurements, respectively.

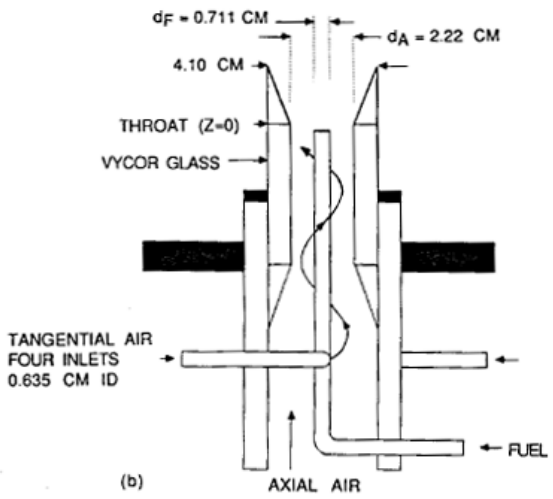

Figure 2.1: Cross-section of burner used for swirl stabilized flames. Adapted from Chen et al. [110].

2.1 Swirling spray burner

The swirl burner used in this work is based on the designs of Feikema et al. and Chen et al. [110–112]. This burner features two air inlets oriented as shown in Fig. 2.1 to allow for the control of the swirl number independently of the equivalence ratio. The first air inlet is oriented axially and enters through the bottom of the plenum and is represented as $\dot{Q}_A$. Oriented tangentially to the walls of the plenum and perpendicularly to the axial air inlet are four additional inlets that impart the swirling momentum. The sum of these four inlets is represented as $\dot{Q}_\theta$. Located axially along the centerline of the burner is a fuel tube. This fuel tube extends up through the mixing plenum and into a venturi and quarrel, the exit of the tube is aligned with the base of the quarrel. By controlling the ratio of the air flow through $\dot{Q}_A$ and $\dot{Q}_\theta$, the swirl number can be varied without necessitating a change in the flow rate of air as would be required for a fixed vane swirler.

The swirl number was defined by Ribeiro and Whitelaw [113] as:

$$S = \frac{\int_0^{d_A/2} (U_\theta r)\,(U_z 2\pi r dr)}{(d_A/2)\int_0^{d_A/2} (U_z^2 - U_\theta^2/2)\,2\pi r dr} \tag{2.1}$$

where U_θ and U_z are the tangential and axial velocities and d_A is the throat diameter. It was then shown by Claypole and Syred [114] that the swirl number was linearly proportional to the geometric swirl number, S_g. Determined by $\dot{Q}_A$ and $\dot{Q}_\theta$, the geometric swirl number provides a more convenient measure of swirl than the actual definition in equation 2.1. Claypole showed that S_g could be described as:

$$S_g = \frac{r_o \prod r_e}{A_t} \left[\frac{\text{Tangential Flow}}{\text{Total Flow}}\right]^2 \tag{2.2}$$

where r_o is the distance from the center of the burner to the center of the tangential inlets, r_e is the radius of the exits, and A_t is the total area of the tangential inlets. This can be further simplified to:

$$S_g = \frac{\pi r_o d_A}{2A_t} \left(\frac{\dot{m}_\theta}{\dot{m}_\theta + \dot{m}_A}\right)^2 \tag{2.3}$$

This relation was then used to define S_g for the remainder of the work.

While based on the burner described above, the apparatus here expanded on the design considerably. The previous burner was designed for the combustion of gaseous fuels, however the current burner needed to operate with liquid fuels, requiring the inclusion of an atomization system. Further, the atomization system had to be capable of producing a fine quality atomization of highly viscous liquids. Commercially available air atomizing nozzles from Hago and Delavan were used throughout this study, allowing for a low pressure solution to the atomization of viscous liquid. On top of need for an atomization system, many of the fuels of interest in this study were very difficult to ignite and maintain a flame due to low energy densities, high boiling

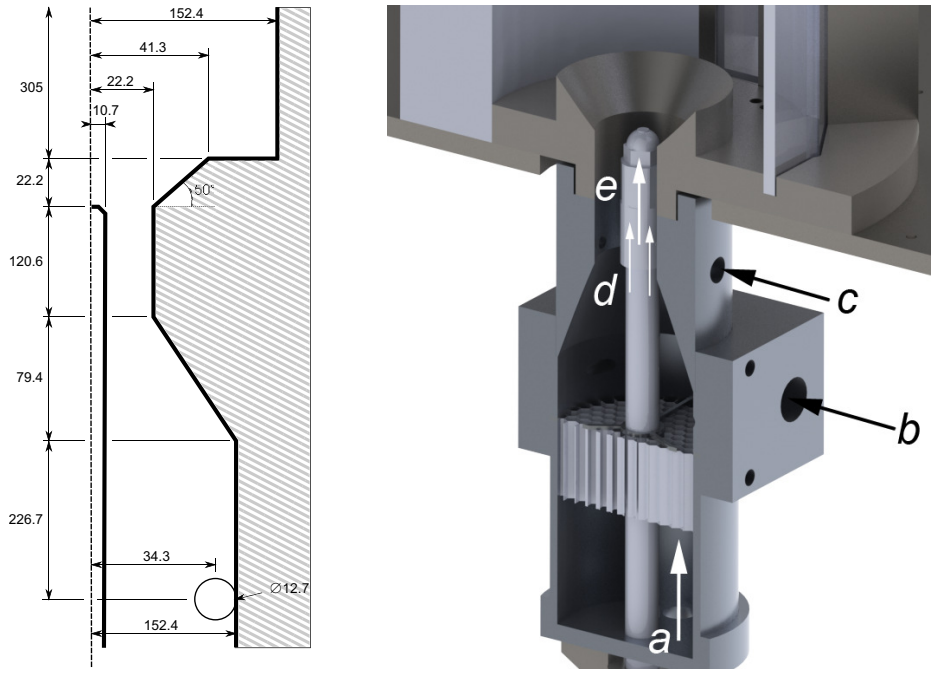

Figure 2.2: Geometry of swirl burner used in this work and a cartoon rendering of the orientation of the burner components.

points, low volatilities, and high auto-ignition temperatures. The solution was the inclusion of an insulated combustion chamber confining the flame. Figure 2.2 demonstrates the finalized geometry and cartoon rendering of the burner configurations.

Here, the axial air flow $\dot{Q}_A$ is labeled (a), and one of the four tangential inlets is labeled (b). The fuel atomization system utilizes an air-atomizing nozzle which introduces a third air inlet labeled (d). The liquid fuel exits the fuel lance with the atomizing air at the nozzle tip (e).

Due to the difficulty in burning some of the fuels as mentioned, a warm up process needs to be followed. When beginning operation, a gaseous flame is established with propane entering through the inlet labeled (c). A swirling propane flame is established and maintained for 30–45 minutes in order to allow for the combustion chamber to reach a steady temperature. When ready to switch to liquid spray flames, the flow rate of liquid fuel is increased while simultaneously the flow rate of propane is decreased. This allows for a relatively constant energy flux and for the injection of the difficult

to burn fuels directly into an existing flame.

This burner can operate up to a power of 10 kW, however operation was typically limited to the range between 7 and 9 kW. It was observed that below about 5 kW, controlling fuel flow and maintaining adequate temperature in the chamber was difficult for some fuels. And above 10 kW, spray flames would extend beyond the top of the combustion chamber.

All gaseous flow rates are controlled with Brooks Thermal Mass Flow Controllers. The liquid mass flow rates are either metered or controlled with Brooks Quantim Coriolis Mass Flow devices. Set point control was achieved through a National Instruments LabView control architecture, integrating the flow and set point control with the data acquisition hardware. Data logging of flow rates, temperatures, and pressures was recorded during sampling and was made available for monitoring during operation.

2.1.1 Reciprocating piston pump based fuel system

Because of the wide range of fluid properties, the fuel delivery system presents several hurdles which were necessary to address. Two different fuel delivery systems were designed and implemented, however the first proved to be difficult to use in practice and the second proved to be a much better system.

The first system was composed of a heated separatory funnel with stopcock and valve on the bottom of the flask. Warmed liquid was then directed to the inlet of an Eldex Optos Metering Pump. This pump uses a reciprocating piston to draw in and pump out liquid while the flow rate is controlled by the rate of the piston. However, this unsteady pump induces pressure fluctuations in the fluid stream which need to be dampened. If the pulses remain undampened, a pulsation in the flow rate of fuel at the nozzle is observed which can even extinguish the flame. The pressure fluctuations are dampened by means of a hydraulic accumulator and needle valve. A hydraulic

accumulator is a device composed of a rigid outer shell containing a bladder filled with pressurized compressible gas. When pressurized liquid enters the accumulator, the compressibility of the gas absorbs the fluctuations in the incompressible liquid. The needle valve downstream of the accumulator ensures that the pressure balance in the accumulator adequately absorbs the fluctuations. Additionally, the pressure in the gas bladder can be controlled to ensure adequate pressure for fuel delivery. When operating correctly, this system works well. However, considerable difficulty can be encountered in the ability of the piston to pump high viscosity liquids. Due to the small inlet orifice and valving, the intake of the pump can struggle to draw in even warmed viscous liquid, resulting in stalling of the pump. This is compounded by the inverse correlation in these fuels between viscosity and energy density, meaning that the fuels that are the most difficult to pump also require the highest flow rate to maintain a constant energy flux.

2.1.2 Pressurized fuel reservoir system

Therefore, the second system was developed and has shown significantly more success and is much easier to operate. This system trades off the continual operation and ability to refill the fuel reservoir of the first system for the ability to operate without a pump. The principle of operation is simple and a cartoon schematic diagram is shown in Fig. 2.3. A large cylindrical tank of liquid fuel is filled and orientated with an outlet below the liquid surface level. The top of the tank is sealed and pressurized with a dry inert gas such as N_2 or argon. The bottom of the tank is routed to the inlet of the flow rate controller, composed of either a coriolis controller or a coriolis meter and needle valve combination for manual control. The complete system is composed of 4 tanks of 3.4 L each, ganged together into two pairs of two. The pressurized gas system is connected to a high pressure gas supply and precision pressure regulator for pressures up to 35 bar as well as the laboratory vacuum system which can be

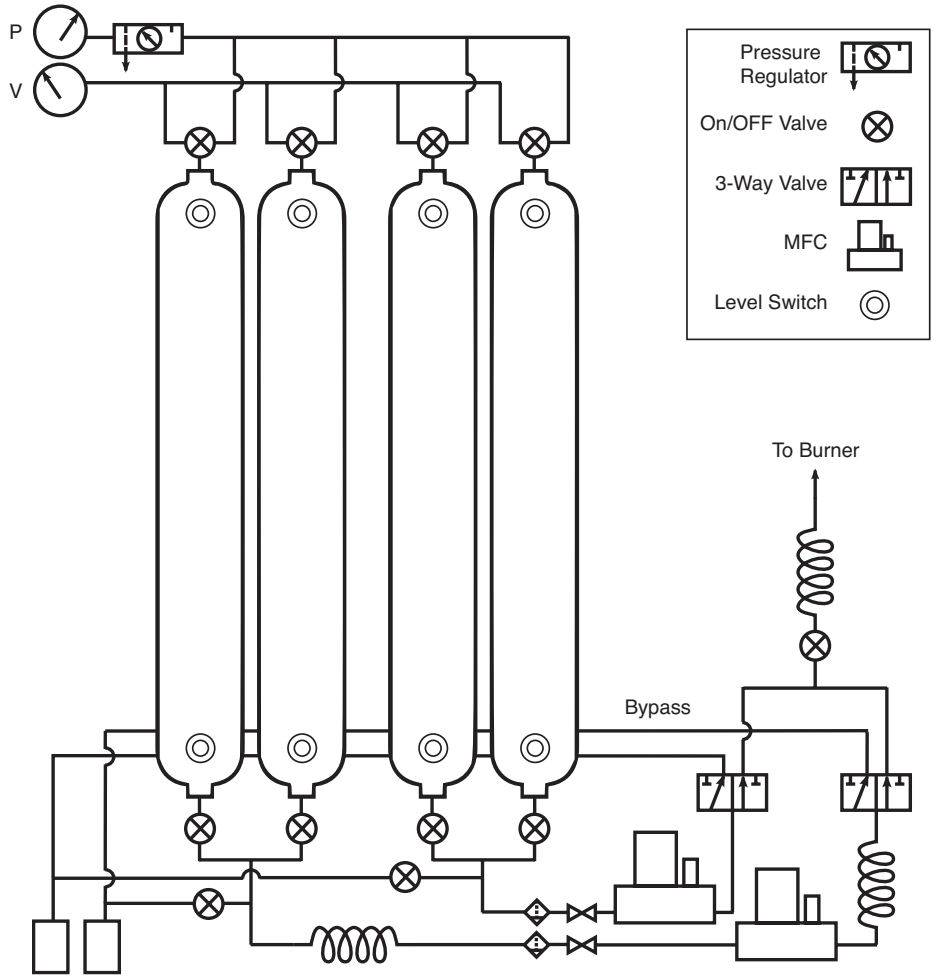

Figure 2.3: Liquid fuel delivery system.

used to refill the cylinders by reversing the process. Each cylinder is fitted with an ultrasonic level switch at the top and bottom, indicating high and low level indicators. Apart from the ends of the cylinder, the liquid filled volume is a linear function of the fill height, allowing for easy monitoring of the liquid level. The downstream fluid path from each cylinder pair includes a pneumatically controlled three way valve to supply fuel to the burner or to a bypass. This allows for the fuel preheat system to be activated and equilibrated with a flowing liquid medium before switching the flame to liquid operation.

The biggest limitation of this fuel delivery system is the limit on continual run time through the need to refill the cylinders. This is somewhat compounded through

Table 2.1: Fuel consumption rates and burn times, P=9kW

Fuel (units)	$\dot{m}_f$ (g/min)	ρ_f (g/ml)	$\dot{Q}_f$ (mL/min)	Burn Time (min/L)
Glycerol	33.61	1.261	26.65	37.5
Propylene Glycol	24.92	1.036	24.05	41.5
Ethylene Glycol	31.61	1.113	28.41	35.2
n-Propanol	17.56	0.803	21.87	45.7
Ethanol	20.10	0.789	25.48	39.3
Methanol	27.10	0.791	34.26	29.2
Propane	11.62	0.00186	6250	-

the need for a warm-up period before operation. However, Table 2.1 shows estimates of the available operating times for all the different liquid fuels in this work. Methanol shows the highest volumetric fuel consumption rate. If both available cylinders are filled, yielding 6.8 L, then the burn time available is about 3 hours and 20 minutes which is enough time to complete experiments with a concerted effort. The longest burn time is available using n-propanol at a little over 5 hours. A note of caution should be included here however. If the liquid level in the fuel reservoir completely depletes and all liquid up to the flow rate controller is purged, a catastrophic failure can occur. As the liquid is removed from the flow rate controllers, the largest pressure drop in the system is also removed which allows for the very rapid deposition of all the remaining liquid in the fuel lines between the controller and the nozzle into the combustion chamber. This results in a much larger and richer flame seeking oxygen that is not available in the combustion chamber. Therefore, the user must heed the low level indicator and quickly begin preparations to shut down the burner and refill the fuel reservoir.

2.2 Prevaporization system

The spray flames of the burner described in the previous system can be quite difficult to model with detailed chemistry due to the multiphase physics and wide range of

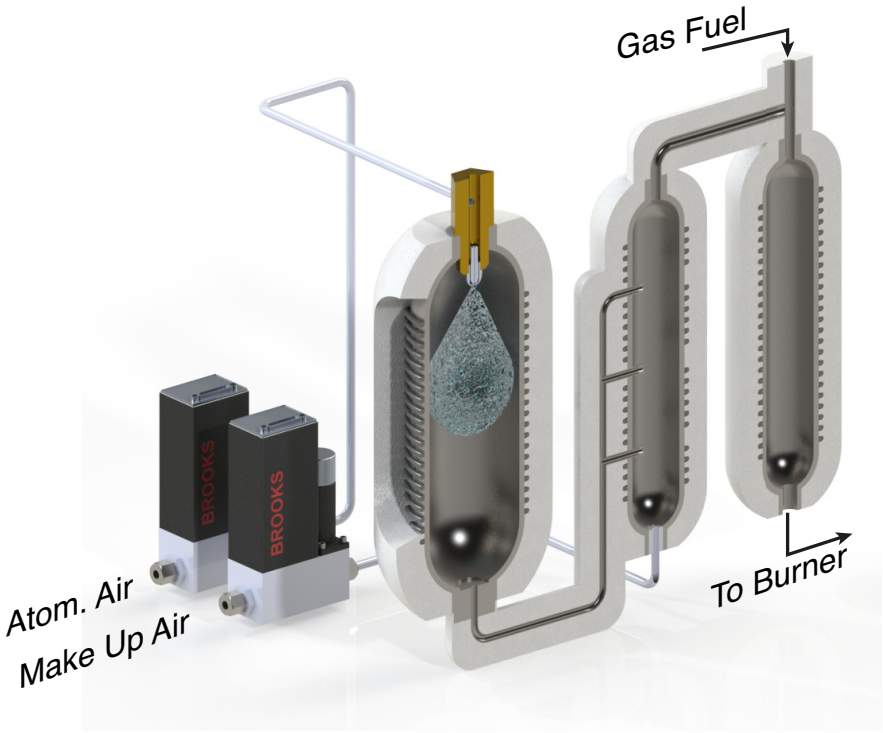

Figure 2.4: Liquid fuel vaporization and premixing system.

scales involved in accurately capturing the droplet physics. Therefore, this work is also interested in investigating more fundamental and simpler flame configurations, such as premixed flat and conical flames. However, all of the fuels of interest are liquid at room temperature, and a system designed specifically to vaporize the fuels in a reliable and consistent manner is necessary.

Thus, the prevaporization system illustrated in Fig. 2.4 was developed. This system utilizes a sequence of heated mixing chambers to vaporize and mix fuel with air over a range of equivalence ratios and mass flow rates. Here, the primary vaporization chamber is the first in a sequence of three insulated and heated chambers. Liquid fuel is atomized in this first chamber using a similar air atomizing nozzle to the swirl burner. The atomizing air is preheated before injection. Primary chamber temperatures are controllable up to 180°C, allowing for the vaporization of a fairly wide range of fuels. The extremely rich mixture of vaporized fuel and air then enters the second chamber through the three side ports of the second chamber. Make up air

also enters this chamber from the bottom, bring the mixture down to the required equivalence ratio. Mixing of the rich fuel/air mixture into the make up air by injecting through the small tubes in the side of the chamber helped to isolate the final fuel air mixture from any acoustic oscillations induced by the atomizing air nozzle. Under some conditions, it was observed that without this mixing strategy the flame could be affected. After mixing in the secondary chamber, the tertiary chamber provides one final volume to fully mix before entering the burner. Additionally, if gaseous fuels are desired, rather than liquid, the gaseous fuel can be injected into this chamber to premix. Every region and air stream is heated, insulted, and temperature controlled, allowing for final temperatures up to 120°C.

Most of the experiments in this work base the gas exit velocity on a factor of the laminar burning velocity. For the different fuels, empirical measurements were taken from literature. Vagelopoulos et al. [115] provided data for the C_1–C_3 alkanes, Gulder et al. [55] provided data for methanol and ethanol, and Veloo et al. [72] provided data for the propanol isomers. Unburned gas temperatures for these flames were typically higher than the temperatures for the flames speeds in the literature, so corrections were made for the variations in the laminar burning velocity as a function of temperature [116, 117] using the correlation:

$$S_u = S_{u,o} \left(\frac{T_u}{T_{u,o}} \right)^{\alpha} \left(\frac{P}{P_o} \right)^{\beta} \tag{2.4}$$

$$\alpha = 2.18 - 0.8(\phi - 1) \tag{2.5}$$

$$\beta = -0.16 + 0.22(\phi - 1) \tag{2.6}$$

$$\tag{2.7}$$

where $S_{u,o}$ is the laminar burning velocity at the reference conditions $T_{u,o}$ and P_o.

With the prevaporization system providing a steady and controlled supply of vaporized liquid fuel and air mixtures, several premixed burner configurations can be

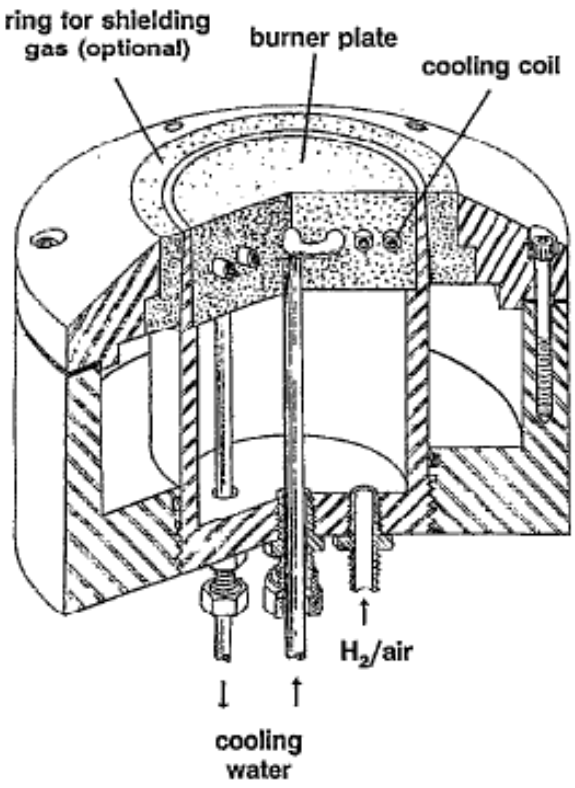

Figure 2.5: McKenna premixed flat flame burner. Adapted from Prucker et al. [118].

used easily. The two used in this work are a McKenna flat flame and Bunsen-type conical flames described in the following two sections.

2.2.1 McKenna burner

The first premixed burner used in this work is a McKenna flat flame as shown in Fig. 2.5. This burner uses a sintered stainless steel porous plug to stabilize a flat flame on the burner surface through heat loss to the porous plug. The porous plug is typically cooled with a circulating water system through the plug. However, the exit gas temperature of the conditions in this study is 100°C, so the water system was replaced with a oil recirculation system. Around the perimeter of the porous plug is equipped with an annular coflow ring of shielding gas where N_2 was injected.

Porous plug flat flame burners such as the McKenna burner have long been used

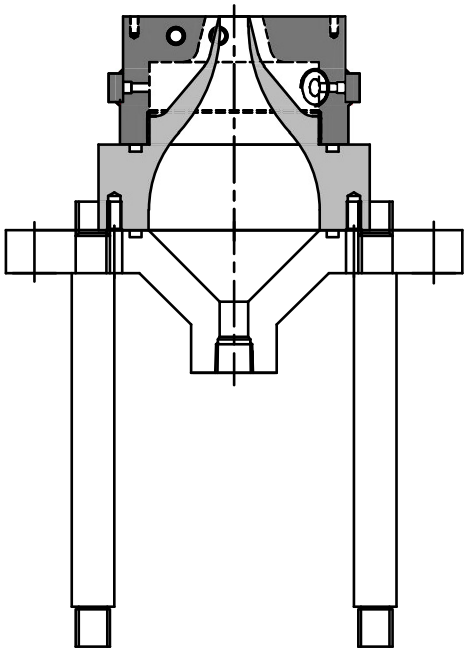

Figure 2.6: Bunsen premixed conical flame burner.

to provide reference one-dimensional flames for flame, chemistry, and laser diagnostic studies [118–123]. Their axisymmetry, one-dimensional nature, and ease of installation in low pressure configurations make them well suited to modeling studies. Care must be taken, however, to account for the significant heat loss to the porous plug due to the proximity of the flame to the burner surface either through measurements of the heat deposited into the water recirculation system or measurements of the temperature field. Lastly, due to the significant heat loss, peak temperatures in the flame can often be relatively low limiting the formation of thermal NO, which is a feature of these flames that will be exploited.

2.2.2 Bunsen conical flame burner

The second premixed burner configuration used in this work is a Bunsen-type conical flame. This flame is characterized by its conical shape. A premixed fuel and air stream enters the bottom of the burner and exits the converging section of the nozzle shown in Fig. 2.6 at velocities greater than the laminar burning velocity, where a

Figure 2.7: Bunsen-type stoichiometric methane/air premixed conical flame. Image courtesy of Dr. Deanna Lacoste.

flame is then stabilized on the rim of the nozzle. The flame stabilizes in a conical shape as shown in Fig. 2.7, where the normal component of the unburned gas velocity is equal to the laminar burning velocity. The tip of the flame experiences high stretch effects and an increase in the laminar burning velocity, thus closing the flame tip. The flame is detached from the rim of the nozzle due to heat loss and extinction of the flame near the nozzle rim.

Conical flames are another configuration which have been studied for an extremely long time. One application of this configuration is the measurement of the laminar burning velocity, which has been shown to be proportional to the uniform axial velocity at the exit of the nozzle and the sine of the cone angle [124–127]. Bunsen-type flames are also well suited to studies of Lewis number effects in premixed flames, resulting in interesting cupping and stretch effects [128–133]. Additionally, conical premixed flames are convenient flames in which to study the flame response to acoustic forcing and measurements of the flame transfer function to investigate coupling of heat release and pressure fluctuations [134–138].

2.3 Laser Induced Fluorescence

Laser Induced Fluorescence (LIF) is a species specific in-situ diagnostic for many different combustion relevant measures. Techniques have been developed to measure

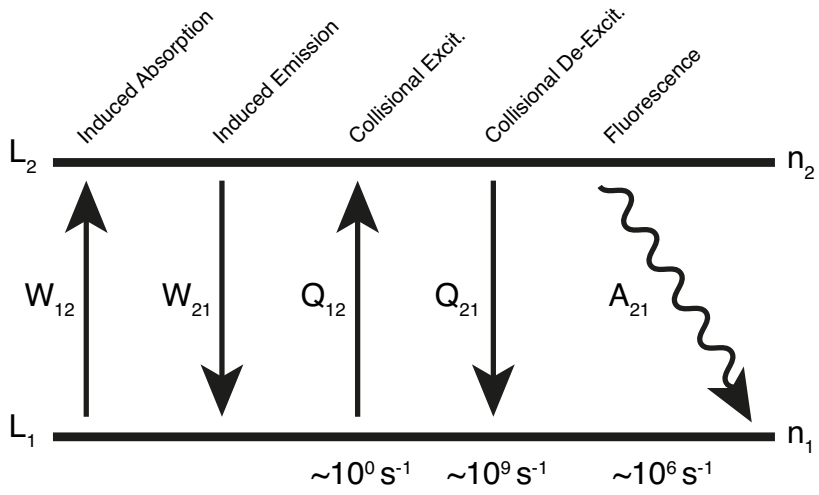

Figure 2.8: Two-level model for possible LIF transitions.

many different properties using LIF:

- n_i: number density of a target species i,
- T: temperature, either through the Boltzmann fraction or through multi-line techniques,
- X_i; concentration of species i,
- $\vec{u}$: gas velocity, measured through the Doppler shift of the absorption frequency,
- P: pressure, measured through line broadening.

A number of resources are available for the researcher stepping in to begin an experimental LIF campaign [139, 140], especially for species concentration or number density measurements of common intermediate species. While individual species involve specific considerations, the process involved in LIF diagnostics is generally consistent.

Regardless of the target property, LIF is essentially the observed spontaneous emission of a laser-excited species. If the laser source is tuned to a resonant transition of the target molecule, then the target will be excited to an unstable excited

state. Once in the excited state, photons can be emitted as the molecule returns to lower energy states. Additionally, collisions with other molecules can transition the molecule to lower or higher energy states. A simplified model for the LIF system can be seen in the two-level model shown in Fig. 2.8.

W_{12} is the rate at which molecules absorb incoming laser irradiation and transition to an excited energy level L_2 and is proportional to the Einstein coefficient of absorption B_{12}. Collisional excitation Q_{12} is typically much smaller than the other transition rates, so it can be neglected. Molecules in the excited energy state can experience one of three outcomes in this two-level model. They can be induced again to emit the absorbed energy and transition to a lower energy state, however, in the weak excitation limit, the population in the excited state (assuming equilibrium) is much less than in the ground state and

$$W_{21} \ll A_{21} + Q_{21} \tag{2.8}$$

and the rate of molecules leaving state 2 is controlled by the collisionally quenching (de-excitation) Q_{21} and spontaneous emission (fluorescence) A_{21} processes. In this weak excitation limit, the population in the excited state, n_2 can be described as:

$$n_2 = n_1 \frac{W_{12}}{A_{21} + Q_{21}} \tag{2.9}$$

A beneficial feature of this weak limit is that the fluorescence is linear with excitation rate, however, $Q_{21} \gg A_{21}$ resulting in relatively weak signals. This limit is also known as the linear regime. Operation in the limit of strong excitation is also another viable option for some species and utilizes high values of W_{12}, allowing the excited population n_2 to reach steady state, saturating the population and resulting in a fluorescence signal that is independent of the collisional quenching rate. This limit is also know as the saturation regime and is commonly known as the Laser Saturated

Fluorescence (LSF) technique. However, it can be difficult to fully saturate when not at low pressures or when Q_{21} is large. All of the experiments in this work utilize the linear regime, so the focus will remain on the LIF technique.

The spectral fluorescent radiative power $\Phi_F(\nu)$ can be expressed as [140]:

$$\Phi_F(\nu) = \epsilon h\nu \left(\frac{A_{21}}{4\pi}\right) \Omega_c \int_{V_c} n_2 \phi(\nu) dV_c \tag{2.10}$$

where ϵ is the collection optics efficiency, h is Planck's constant, ν is the transition frequency, Ω_c is the solid angle of the collection optics, $\phi(\nu)$ is the normalized spectral distribution of the fluorescence, and the integral is evaluated over the overlapping volume of the incident beam and the collection optics. Integrating through the irradiated volume, accounting for the collection optics, applying the weak excitation limit, and incorporating the Boltzmann population fraction for the ground state population, equation 2.10 can be rewritten in the more convenient form:

$$S_i = C_{opt} B_{12} I_L f_B \Gamma \Phi n_i^o \tag{2.11}$$

where C_{opt} is the combined constant for the collection optics, B_{12} is the Einstein coefficient of absorption ($\propto W_{12}$), $I_L(E_L, \Delta\nu_L)$ is the spectrally resolved laser irradiance, $f_B(T)$ is the Boltzmann population distribution, $\Gamma(\Delta\nu_L, T, P, X_k)$ is the normalize overlap integral of the incident and absorping transition frequencies, $\Phi(T, P, X_k)$ is the fluorescent yield in the weak excitation limit, and $n_i^o(T, P, X_i)$ is the number density of the target species.

Execution of the technique in this work uses a basic setup consistent to all of the target properties. A light source emits a tuned UV beam which is directed toward the measurement region through a series of UV grade fused quartz optics and wavelength specific mirrors. The objective is to form a focused laser sheet of a constant height. This is achieved using a beam expanding telescopic assembly.

The beam first encounters a concave and convex lens assembly. The collimated beam expands through the concave lens, however the focal points of the concave and convex lenses are aligned, resulting in the expanding beam exiting the convex lens collimated but magnified in diameter by a factor equal to the ratio of the focal lengths. This large diameter collimated beam is then focused through a cylindrical lens, creating a measurement region with a height approximately equal to the collimated diameter (the full height is not typically used due to the low irradiance at the top and bottom of the sheet). The width of the sheet is equal to the waist of the beam and is typically on the order of 300 μm. The width of the sheet is also not constant as the beam is focused; however, the focal length of the cylindrical lens is quite long and the variation in the width in the vicinity of the focal point is minimal over the width of the measurement region. This was confirmed with measurements of the sheet width on exposed burn paper located at the front and back of all burners and no measurable difference in sheet width was observed. Finally, because the operation of the diagnostic is in the weak excitation limit (linear regime), variations in the width of the sheet should have minimal impact on the fluorescence signal in these steady, lower dimensional flames.

However, because a circular beam is focused into a sheet, the energy distribution is not constant through the height of the sheet. Additionally, the distribution of energy through the circular cross-section of the collimated beam is also unlikely to be evenly distributed before sheet formation. Further complicating matters, the shot-to-shot variation in both the energy distribution and total energy can be significant and careful account of these fluctuations needs to be included. To accomplish this objective, a small portion (approx. 4%) of the laser beam was sampled after sheet forming using a fused quartz flat plate inserted 45° to the beam path. This sampled beam was directed to a cuvette filled with a solution of coumarin dye in ethanol solution. As each laser shot was fired, this small portion of the beam would fluoresce the dye in the couvette. A CCD camera oriented perpendicularly to the beam would

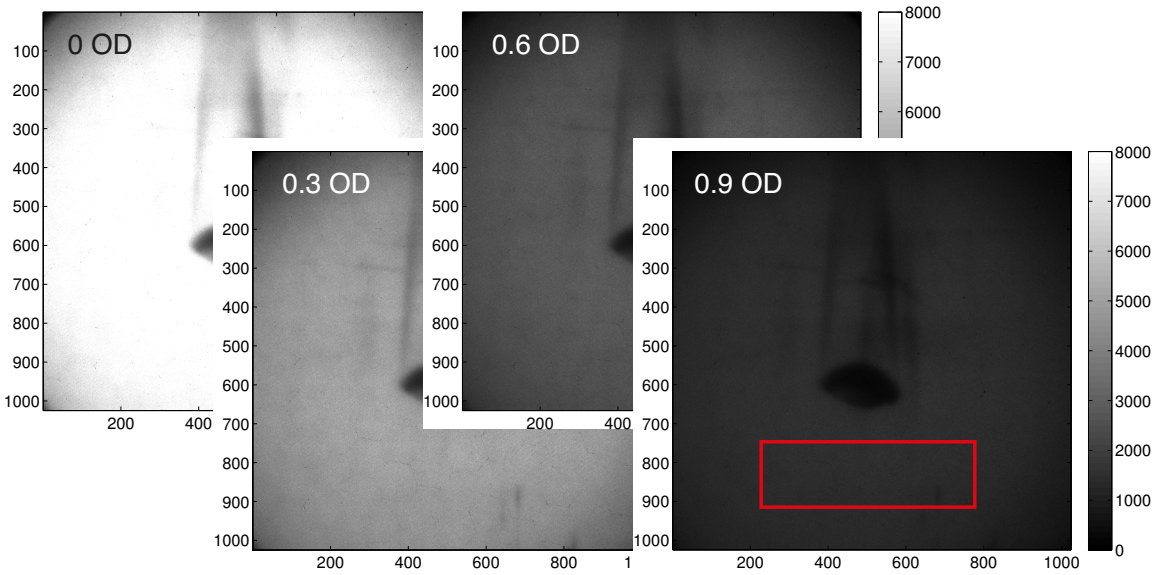

Figure 2.9: Exposures of the black body radiation with increasing neutral density filters for pixel linearity calibration.

capture the dye fluorescence. The concentration of dye was tailored to each desired wavelength to allow for optimal fluorescence signal in the dynamic range of the CCD camera. From each exposure, the energy distribution as a function of height in the beam was recorded and the total energy of the shot could be extracted from the intensity of the fluorescence.

Simultaneously, the remainder of the beam excited the target species, and the fluorescence signal was captured with a gated, blue-enhanced Princeton Instruments PI-MAX3 ICCD camera. The exposure time of the camera was limited to the lifetime of the fluorescence of the target species to reduce extraneous light impacting the sensor. Additionally, filters were used to limit the spectral distribution visible to the camera to the limited range of the target species fluorescence.

The pixel response of the ICCD to photons is sensitive to the wavelength and can be non-linear with the number of photons. Improvements have been made over the years to improve the linearity of the pixel response, however corrections for this non-linearity were conducted for these experiments. This calibration procedure used a black body radiator, set at a constant temperature (1200°C), that was imaged using

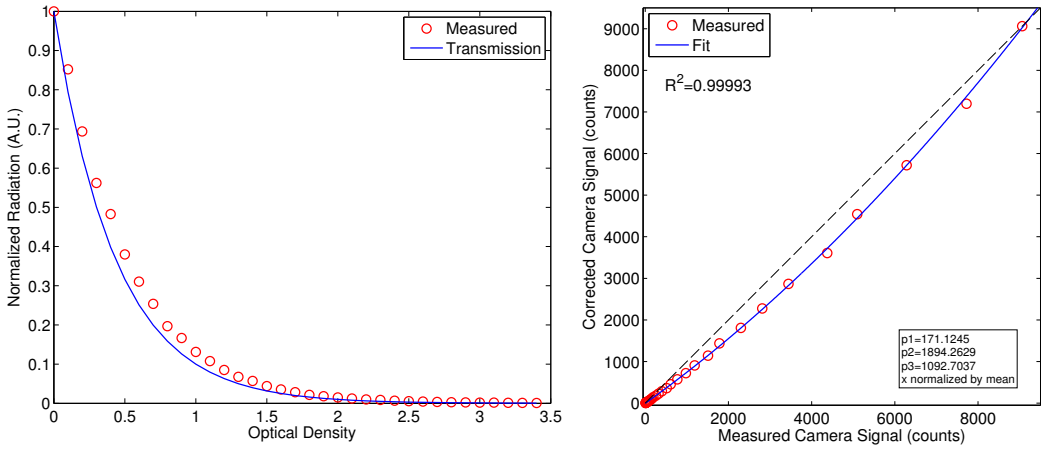

Figure 2.10: Decay in pixel intensity with increasing optical density versus expected intensities (left) and non-linear correction calibration (right). Exposures conducted with a bandpass filter centered at 310 nm used in OH-LIF.

the same filter. The pixel intensity was shown to be reliably linear as a function of exposure time (so long as exposure was longer than a few nanoseconds). Therefore, the ICCD exposure was set to provide an average pixel intensity when imaging the black body radiator approximately 20% higher than the maximum intensity in the experiment. Increasingly dense neutral density filters were included with the spectral filter to capture the sensor response to a known variation in the radiative flux. A sample of four exposures of the black body radiator with increasing optical densities up to 0.9 OD is shown in Fig. 2.9. The red bounding box shows the region in which measurements of the mean pixel response (less dark current) for each exposure were conducted.

Figure 2.10a shows the normalized average pixel response with increasing OD's up to 3.4, along with the expected transmission. It can be seen that the camera response does not perfectly follow the expected transmission, indicating a non-linear response, especially as the signal gets low. The non-linear pixel response can be mapped to the expected response as shown in Fig. 2.10b, and a calibrated intensity curve can be used to correct exposures in the LIF images.

Spatial calibrations for each experiment were also conducted using a similar method.

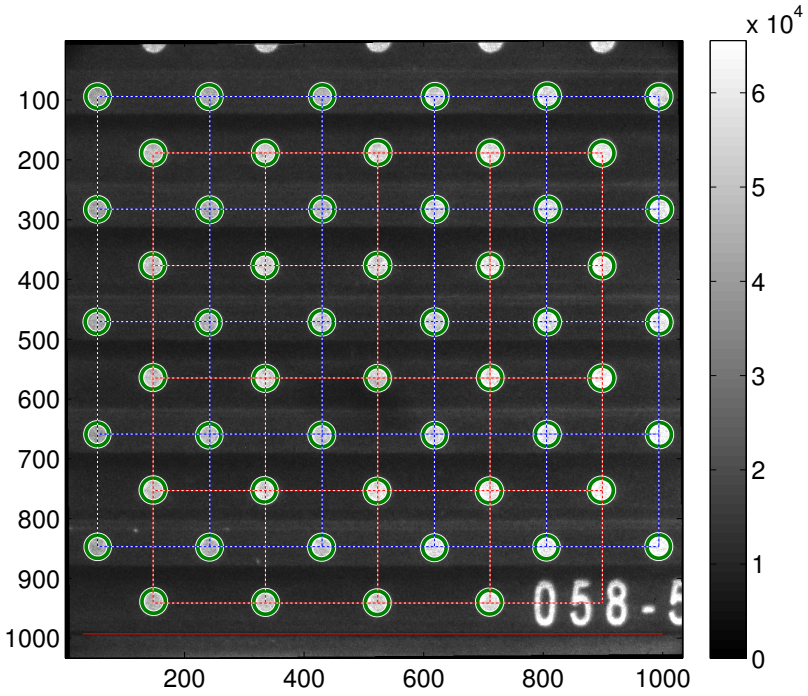

Figure 2.11: Example spatial calibration target, showing identification of grid markers, spacing, and uniformity.

A calibration target grid with markers 5 mm on center was exposed at the beginning and end of each day to ensure alignment was maintained throughout the experiment. For each day, the target grid exposure was analyzed to determine the scale in the image. Figure 2.11 shows a sample spatial calibration target. Each of the grid markers was identified and circled in green. Grids were drawn through the center of each marker allowing for the determination of the grid pixel spacing and confirmation of uniformity. With a known spacing of the grid markers, the dimensions in physical space could be determined for each experiment.

It was necessary to correlate the profile correction and ICCD images to identify common points in the beam. To do this process, a portion of the beam was blocked with a sharp edge after forming the sheet, but before sampling for the correction profiles. The location of this sharp edge was varied as shown in Fig. 2.12. This allowed the identification of the vertical pixel number for the ICCD image and the corresponding vertical pixel in the profile correction image. Then a mapping transfer

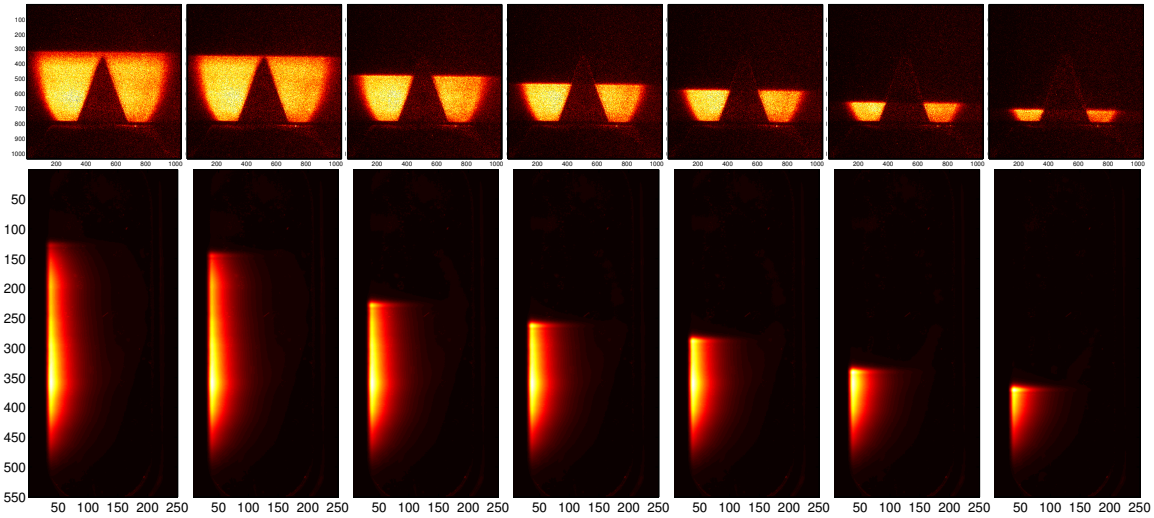

Figure 2.12: Images of LIF and corresponding profile correction images and portions of the beam were blocked.

function could be built to correlate the beam profiles observed in the correction images with the corresponding location in the flame.

For each experiment, operation in the linear regime was confirmed for both the target species and the profile correction dye solution. This process involved systematically decreasing the average pulse energy as measured by an energy meter and recording the LIF and dye fluorescence responses. The fluorescence was plotted against the laser energy and a linear trend was confirmed. Experiments were then operated at around 80% of the available energy of the laser to ensure that the experiment remained in the linear regime despite energy fluctuations.

All of these procedures were repeated for the OH, CH_2O, and NO LIF experiments in this work. In addition to the general calibrations and corrections discussed above, each experiment required unique considerations, such as the selection of the excitation transition, LIF signal calibration, and quenching quantification procedures. Each of these considerations will be discussed separately in the following subsections where applicable. It is possible to omit some of the procedures discussed above, and this can be a perfectly acceptable approach under the right conditions. However, if any significant discussion of relative species concentrations, especially as they relate to

differences in fuels under a wide range of conditions and measured at different times, the above represents a minimum scope of corrections necessary to adequately capture these trends.

2.3.1 2λ OH thermometry

The first LIF experiment in this work is actually a two-rotational line technique for measuring temperature. LIF thermometry has been developed for use with a number of target species, both naturally occuring such as OH, and seeded into the flow such as NO. Introductions to the use of two excitation wavelengths for thermometry are included among Ref. [141–146]. In general, the principle is to measure the ratio between two broadband LIF images excited at a pair of carefully selected rotational transitions. Following equation 2.11, the ratio R of the LIF images can be written as:

$$R = \frac{(C_{opt}B_{12}I)_1}{(C_{opt}B_{12}I)_2}\frac{\Gamma_1}{\Gamma_2}\frac{f_1(T)}{f_2(T)}\frac{\Phi_1(T)}{\Phi_2(T)} \tag{2.12}$$

The first convenient feature of this approach is that the ratio is independent of the target species concentration. For both NO and OH target species, the ratios of Γ_1/Γ_2 and Φ_1/Φ_2 have been shown to be negligibly temperature dependent given careful selection of transitions [144, 147]. The result is that the only temperature dependence in equation 2.12 comes through the population distribution. If thermal equilibrium is assumed, the population fraction follows Boltzmann statistics, and the ratio can be simplified as:

$$R = C\frac{I_1}{I_2}\exp\left(-\Delta\varepsilon_{12}/kT\right) \tag{2.13}$$

where C is an in-situ experimental calibration and $\Delta\varepsilon_{12}$ is the energy difference between the two transitions. Equation 2.14 can be rewritten to solve for the temperature

as a function of the ratio of LIF images as:

$$T = \frac{-\Delta\varepsilon_{12}/k}{ln(R/C) - ln(I_1/I_2)} \tag{2.14}$$

Transition selection requires careful consideration of the conditions expected in the flame. The work here uses transitions selected from the $A^2\Sigma^+ \leftarrow X^2\Pi(1,0)$ OH band. Transitions in this band are easily accessed with a 10-Hz Nd:YAG pumped, frequency doubled, Rhodamine-dye laser. Several criteria for transition pair selection include rotational lines with high enough populations and strong enough line strengths to yield good signal. Additionally, the selected lines need to be isolated from other rotational lines. Typically, the transition pair would be chosen from different ground states with a common excited state, which would eliminate variations in the fluorescent yield Φ. However, it is difficult to find transitions meeting the above criteria and common upper states while also having a $\Delta\varepsilon_{12}$ large enough to provide sensitivity at flame temperatures [144]. Therefore, transitions with common ground states and differing excited states were chosen; however calibration at each experimental condition helps to relieve the effect of differing quenching environments.

The transitions selected for this work are a pair recommended by Seitzman et al. [144]. The $P_1(7)$ and $Q_2(11)$ transition pair were selected, with a line separation energy $\Delta\varepsilon_{12}/k$ of 2046 K. This pair provides good temperature sensitivity over the temperature range 1200–2000 K. Background subtractions were conducted by removing a background image with the laser off from the LIF image. Off-line background images showed no measurable background interference.

Ensuring that the laser is tuned properly to the expected transition is important to account for differences in the dye laser stated wavelength and the actual output wavelength. It is possible (and likely) that the two have shifted due a litany of unexpected and uncontrollable variables in the laboratory environment. Therefore it is

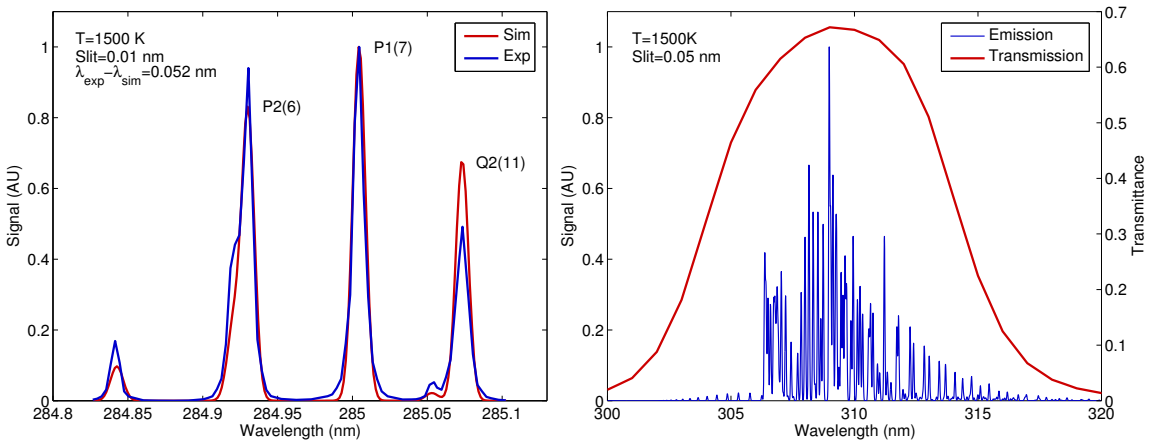

Figure 2.13: Wavelength scan of OH rotational lines and simulation of transitions identifying the $P_1(7)$ and $Q_2(11)$ transition pair used for thermometry (left) and OH emission spectra and transmittance of 310 nm bandpass filter (right).

necessary to ensure that the stated wavelength is properly calibrated to the expected output. This is achieved by conducting a wavelength scan around the expected transition wavelength. The OH fluorescence emitted in the post flame of a stoichiometric propane flame imaged on an ICCD is averaged in a region of interest over 50 shots. This mean fluorescence is then plotted over a range of wavelengths and compared with a calculated spectrum encompassing the desired transitions as calculated by LIFBASE [148]. Figure 2.13 shows a comparison of the normalized measured and simulated spectra, with a baseline shift. The measured spectra is then shifted 0.052 nm to match the calculated spectra to ensure the optimal transitions were selected. This process was repeated at the beginning of each day to account for day-to-day shifts in calibration after system shut-down. Figure 2.13 also shows the OH emission spectra near 310 nm. A 310 bandpass filter with 10 nm FWHM was used to filter out extraneous light and eliminate scatter of the excitation beam at 285 nm.

As mentioned previously, fluctuations in the shot-to-shot spatial distribution of laser energy and total irradiance are present in the laser system. Corrections for these shot-to-shot fluctuations are required to improve the quality of the temperature measurement. Figure 2.14 shows the typical fluctuation in total energy and the nor-

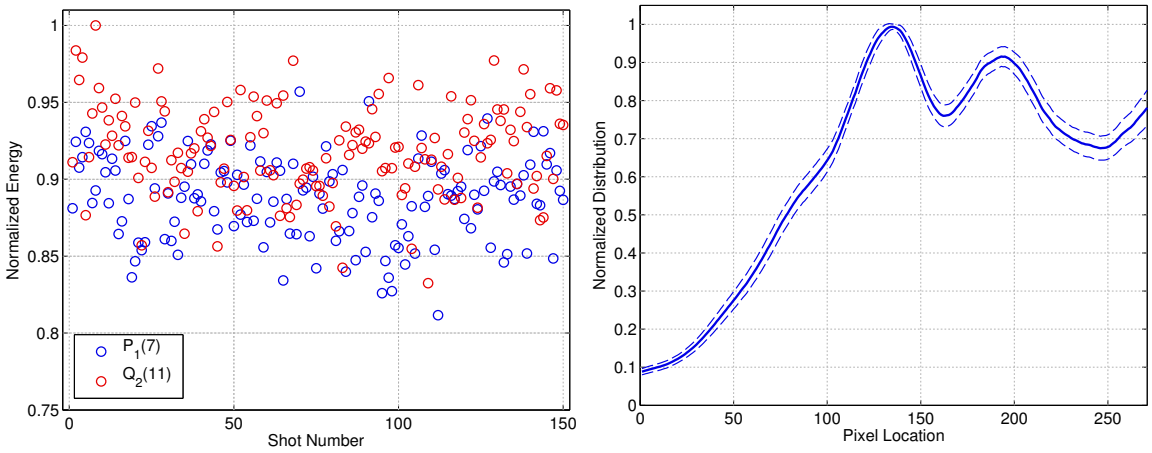

Figure 2.14: Shot-to-shot fluctuations in total energy and energy distribution at 285 nm.

malized energy distribution in a single experiment run. Average laser pulse energies were approximately 18 mJ/pulse. The fluctuation in total energy varies by approximately 5% from shot to shot, while significant variations in the distribution of energy through the vertical profile of the beam can be seen.

An algorithm was developed for extracting the energy profile and total energy fluctuations from the profile correction images. This algorithm is demonstrated in Fig. 2.15. Here, an example single shot image is shown in (b). Subfigure (a) shows the distribution of energy, which is calculated by dividing each vertical column in the image by the maximum in that column and averaging the results. This yields a very consistent normalized distribution while still accounting for absorption through the dye solution. The image can then be corrected by dividing by the profile, which yields (c) and a one dimensional distribution of energy. The total energy is calculated by taking the sum of pixel intensities in each column in (b) and normalizing to a reference standard of known energy. This normalized pixel intensity is plotted in (d), where the absorption through the beam path is clearly seen. The ratio of the two absorption curves are plotted in (g), and it can be seen that the energy in this example shot is approximately 73% of that of the reference shot. The spatially corrected profile

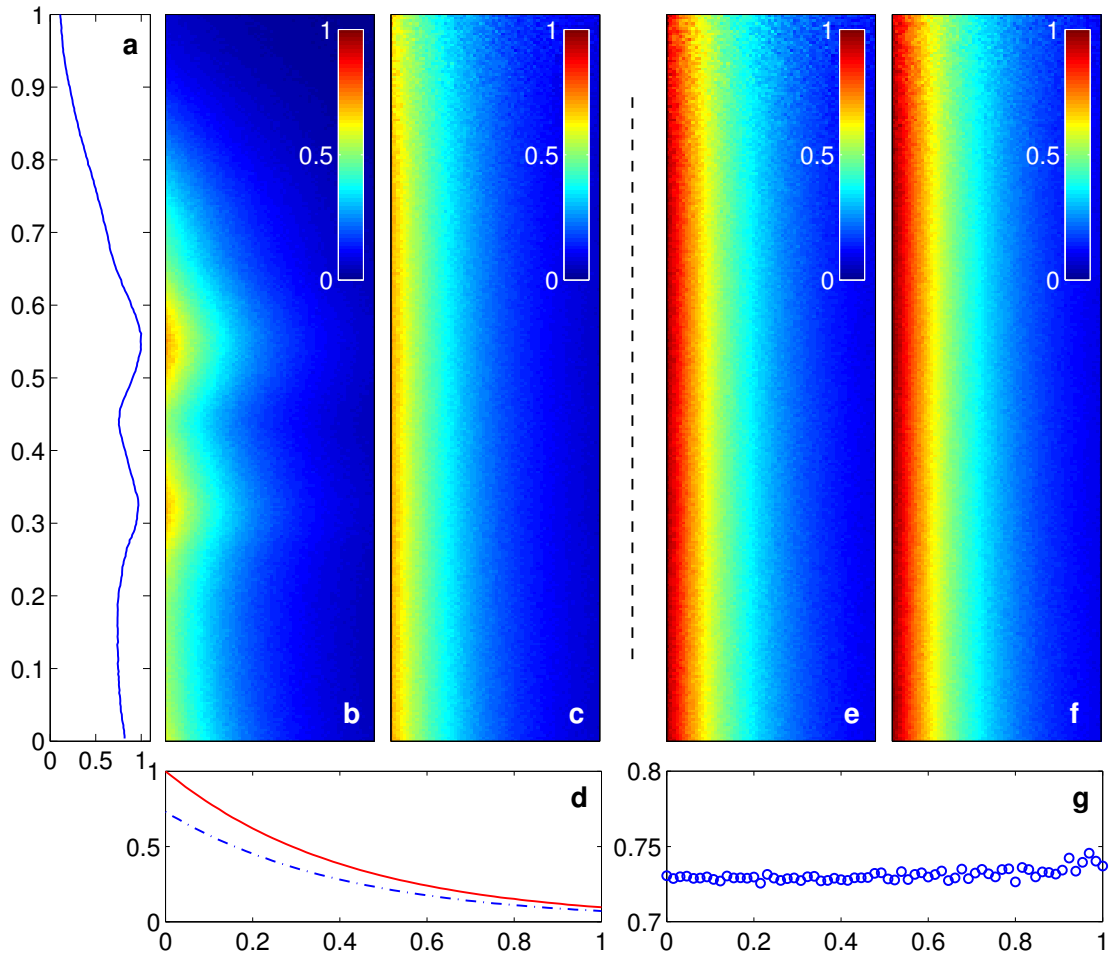

Figure 2.15: Process for quantifying shot-to-shot fluctuations in laser energy and energy distribution.

in (c) and then be corrected for energy fluctuation and is shown in (e). Comparing with the reference shot in (f), this algorithm does a good job of extracting the spatial and total energy information from the dye fluorescence and correcting to a common standard.

2.3.2 Formaldehyde LIF

LIF studies of formaldehyde are another common application of the LIF technique. Often, formaldehyde LIF will be used in conjunction with OH LIF. In such studies the heat release rate can be approximated by the formyl radcial (HCO), however

concentration of HCO are typically very low, yielding low measurement signals. Alternatively, the fact that formyl radical is formed through the combination of CH_2O and OH in the flame yields an easier measure of the heat release rate through the product of the LIF signals of both species [149].

Additionally, CH_2O can be fairly easily accessed using excitation of the strong vibronic $A^2A_1 \leftarrow X_1A^1\ 4_0^1$ band between 330 and 370 nm [150–155]. Popular transitions around 339 nm and 352 nm are often used with tunable light sources, however it also very common to use the frequency-tripled output of an Nd:YAG around 355 nm to excite the weak end of the 4_0^1 band. While the transitions at 355 nm are weak, the high energy and ease of use of a non-tunable frequency-tripled laser make this a common transition and is the method selected for this work. Pulse energies of approximately 500 mJ/pulse were used.

Broadband emission of CH_2O LIF was observed between 400–500 nm through a set of long and short pass filters. Harrington and Smyth [151] showed that PAH fluorescence could be observed in this spectral range. However, the PAH LIF saturated at very low laser energies and it was possible to successfully limit the PAH background with high laser energies. CH_2O LIF avoided saturation at large incident energies due to rapid transfer of rotational energy while in the excited state. Background subtract with the laser off was also applied.

While determination of the quenching environment for correction of LIF signal to number density is the goal, this objective has proven difficult. The quenching rate can be described in terms of the collisional cross-section σ_i as:

$$Q_{21} = \sum_i n_i \sigma_i v_i \tag{2.15}$$

where n_i is the number density of the collision partner and v_i is the relative velocity of the colliders. However, direct measurements of the collision cross-sections for excited

CH_2O are limited. Yamasaki and Tezaki [154] provide collisional quenching rates of a few bath gas species (He, N_2, CO_2, DME, and O_2) at 295 K, however temperature dependent rates were only available for N_2 and only one rate for O_2 was available.

Rather, researchers typically take the approach of Paul and Najm [149], in which a temperature dependence of:

$$\sigma \sim T^{\beta},\ -0.5 < \beta < 0 \tag{2.16}$$

and since $n_i v_i$ scales as $T^{-0.5}$, the total quenching rate $Q_{21} \sim T^{\alpha}$ with $-1 < \alpha < -0.5$.

Finally, the population fraction of the ground state can be described as [156]:

$$f = f_{ele} f_{vib} f_{rot} \tag{2.17}$$

$$f_{ele} = 1 \tag{2.18}$$

$$f_{vib} = (1 - e^{-1680.5/T}) \tag{2.19}$$

$$f_{rot} = \frac{40.1969 e^{-740/T}}{(1 + 0.134/T + 0.037/T^2)^{3/2}} \tag{2.20}$$

2.3.3 NO LIF

The last LIF scheme used in this work is for the measurement of NO. A fantastic three part review of strategies for NO LIF is available in Ref. [157–159]. In these works, different excitation schemes are presented and a review of the available transitions is covered. A number of different schemes and transitions are available, but only the technique used in this work will be covered.

NO in the flame was excited at a wavelength near 226 nm. This wavelength was achieved using a mixing after doubling scheme, in which a 10-Hz Continuum Nd:YAG laser at 1064 was doubled to 532 and used to pump a Rhodamine dye laser yielding 572 nm. This was then frequency-doubled to 286 nm. Finally, this 286 nm beam was mixed with the fundamental at 1064, to yield a fourth beam at 226 nm. All

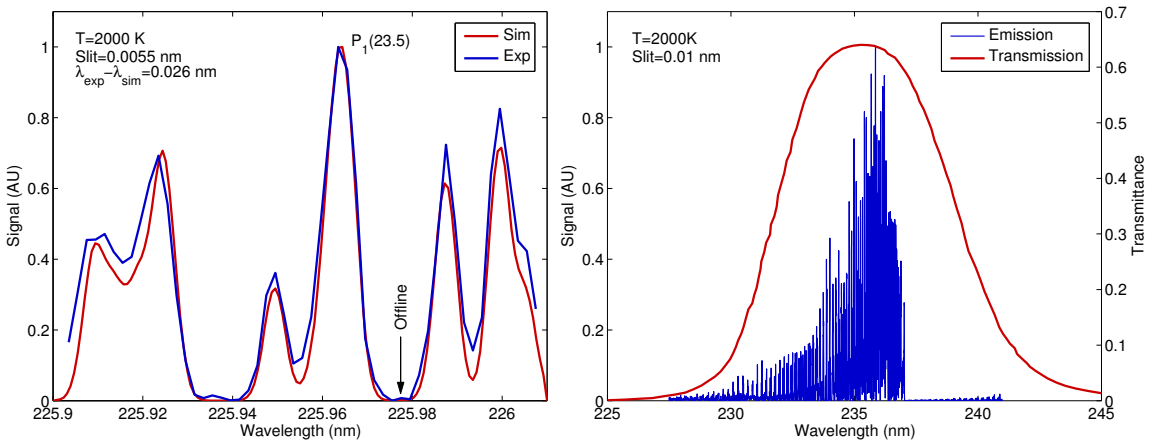

Figure 2.16: Wavelength scan of NO rotational lines and simulation of transitions identifying the $P_1(23.5)$ and off-line transitions (left) and NO emission spectra and transmittance of 236 nm bandpass filter (right).

four beams (1064, 572, 286, and 226 nm) were dispersed in a Pellin-Broca prism and the 226 nm beam was used to excite the $A - X(0, 0)$ band of NO. Pulse energies of approximately 1.4 mJ/pulse were possible, however pulses around 1 mJ/pulse was the target energy.

A review of the available transitions in the viscinity of 226 nm has shown a number of popular transitions [121, 160–163]. This work uses the $P_1(23.5)$, Q_1+$P_1(14.5)$, Q_2+$R_{12}(20.5)$ transition at 225.963 nm (226.03 nm in vacuum) proposed by DiRosa et al. [161]. This transition was selected because it shows the best performance with regard to minimal O_2 interference and maximum NO signal strength [157]. NO LIF emission was observed in the $A - X(0, 1)$ band centered near 236 nm.

Similarly to the OH spectra, a scan of the rotational spectrum was conducted each day to ensure proper spectral alignment and transition selection. An example scan is shown in Fig. 2.16 with indicators for the $P_1(23.5)$ transition and the off-line background discussed below. Also shown in Fig. 2.16 is the simulated emission spectra and the transmissivity curve for a custom made 236 nm bandpass filter with a 7.5 nm FWHM.

Unfortunately, interference O_2 LIF background emission is unavoidable in all of the

desired transitions, and a strategy must be employed to correct for this background emission. Following the approach of Refs. [121, 161, 164], measurements of NO LIF for both on- and off-line resonance was observed. Additionally, the dark current in the ICCD sensor was also measured. Background corrected LIF signals were then calculated as:

$$S_{NO} = (S_{\text{online}} - S_{\text{dark}}) - (S_{\text{offline}} - S_{\text{dark}}) \tag{2.21}$$

It should be noted that at elevated pressure (in excess of 20 bar), the spectral density of these NO transitions becomes too high to allow for the excitation of a non-resonant line, so other background correction schemes would need to be used.

Quantification of NO number density from the LIF signal is an achievable goal using a series of quenching corrections available in the literature. Of the terms comprising equation 2.11, appropriate corrections are available for each. The experimental calibration term C_{opt}, inclusive of the optical collection efficiency, will be discussed in context in Section 8.2.2. The Einstein coefficient of absorption, B_{12}, is a constant of the selected transition. The laser irradiance is appropriately accounted for following the previously discussed scheme for fluctuations in the total energy and energy distribution. The ground state population fraction can be assumed to be in thermal equilibrium as described by Boltzmann statistics and a correlation for this term is included in Table 8.2. The laser line overlap integral Γ is a weak function of temperature, but can be shown to be close to unity at atmospheric pressure, with a negligible influence at these experimental conditions [165, 166].

Corrections for the fluorescent yield Φ require the most consideration. Settersten et al. [167] provide a very helpful work for estimating the temperature and species dependent quenching rates for NO. Following their empirical correlations for bath gas quenching rates, estimation of the collisional cross-sections and quenching rates can be made as a function of temperature as shown in Fig. 2.17. At combustion temperatures, the major quenching species are estimated to be H_2O, CO_2, N_2, O_2,

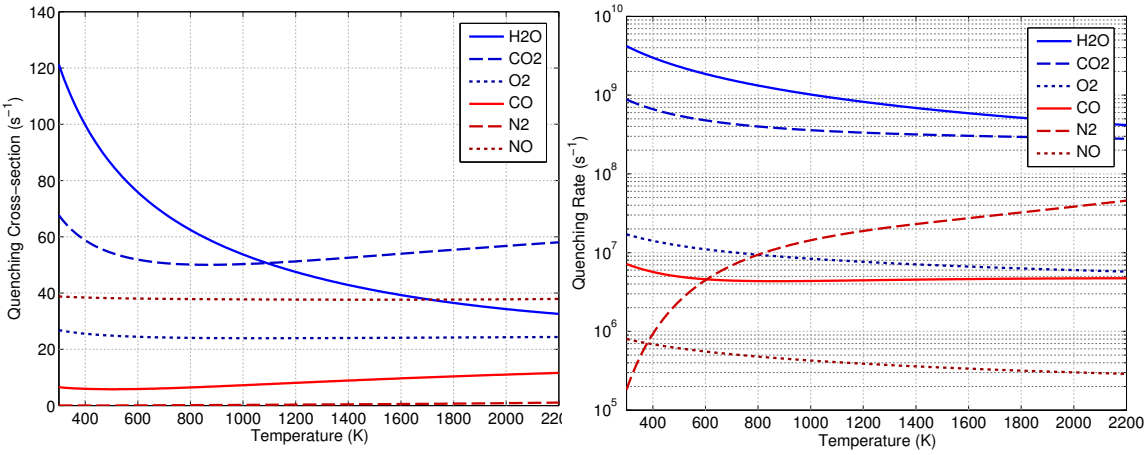

Figure 2.17: Collisional cross-sections (left) and quenching rates (right) for major bath gas species in NO LIF estimated using [167].

and CO. Application of the required quenching corrections are further discussed in context in Sections 8.2.2 and 8.3.

2.4 Thermocouple measurements

In addition to the 2λ-OH LIF thermometry technique for measuring temperature, measurements by thermocouple probes were also conducted in several configurations. Thermocouples operate by taking advantage of the Seebeck effect, in which a circuit composed of two different conductors with junctions at different temperatures results in a temperature dependent voltage across the conductors. This is known as the thermoelectric effect.

Thermocouples are categorized by conductor metals, the selection and pairing of which allow for sensitivity in different temperature ranges and stability in oxidizing or reducing environments. The most common thermocouples are type-K (chromel-alumel alloy) with a general purpose temperature range between -200°C and 1350°C. Fluid handling and preheating control in this work all utilized type-K thermocouples.

For higher temperature measurements however, thermocouples made of platinum or platinum/rhodium alloys are required. These thermocouples are more stable at

temperatures in excess of the type-K peak temperatures, however sensitivity is sacrificed. In this work, temperature measurements directly in flames used type-R thermocouples (Pt/Rh 87%/13% - Pt 100% alloy) with peak temperatures in excess of 1600°C. The thermocouples were in a bare wire form factor, encased in a two hole round ceramic insulator made of 99.8% alumina ceramic, which provides support to the fine thermocouple wire while also remaining non-reactive and stable at high temperatures.

Care must be taken in the interpretation of thermocouple measurements and account must be taken of heat transfer from the junction bead which can interfere with measurement of the gas temperature. These heat transfer considerations include: radiation from the bead to surroundings, convection in flowing gases, conduction through the thermocouple wires, catalytic surface reactions, surface soot deposition, and transient effects in response to unsteady gas temperatures [168]. A scheme for applying corrections for radiative losses and convective heat transfer is discussed in context in Section 7.1.1. Effects from conduction through the thermocouple wires can be minimized with sufficiently long leads [169]. It is difficult to correct for catalytic surface reactions, therefore it was attempted to minimize this effect through the coating of the thermcouple junction with a silica oxide coating approximately 10 μm thick. Fortunately, these studies are non-sooting flames, so soot deposition was not observed. All thermocouples exhibit a delayed response to changes in bath gas temperature known as the response time. This lag is induced through the heat transfer terms discussed above and heat capacity of the bead materials and must be considered in turbulent or unsteady temperature fields.

2.5 Extractive gas sampling

Extractive gas samples were monitored in several experimental configurations in this work. Whether samples were collected in the post flame exhaust gases or probed from the flame zone, samples were conditioned the same way. The instruments for gas analysis typically required similar sample gas conditioning before introduction into the instrument, so the most rigorous requirements were followed. Sample gases were collected through a quartz micro-probe with a drawn tip and orifice measured to be approximately 250 μm. This orifice size was small enough to allow for significant cooling of the sample gases collected in the flame through aerodynamic cooling. The probe was connected to a diaphragm vacuum sample pump pulling a vacuum through the probe. Exiting the pump, sample gases were dried with an anhydrous calcium sulfate desiccant and then finally filtered with a 4 μm filter. Depending on the application and required sample gas flow rate, dilution with argon was available in dilution ratios up to 15. Dilution and sample gas flow rates were carefully controlled, and corrections for variations in the sample gas composition on the gas correction factor in the mass flow controller was included.

Analysis of the sample composition was available through a suite of California Analytical Instruments analyzers. The first instrument measured NO/NO_2 and O_2 concentrations using chemiluminescence (CLD) and paramagnetic detectors, respectively. The second instrument measured CO/CO_2 concentrations utilizing a non-dispersive infrared detector (NDIR). Finally, measurements of unburned hydrocarbons corrected to methane concentrations were available utilizing a flame ionization detector (FID). Additionally, selected measurements of H_2, O_2, N_2, CO, CO_2, and C_1–C_5 saturated and unsaturated hydrocarbons were available utilizing an Agilent Refinery Gas Analyzer (RGA). Based on an Agilent 7890 GC, this system uses a combination of eight different gas chromatograph (GC) columns and three detectors (two thermoconductive detectors (TCD) and one FID).

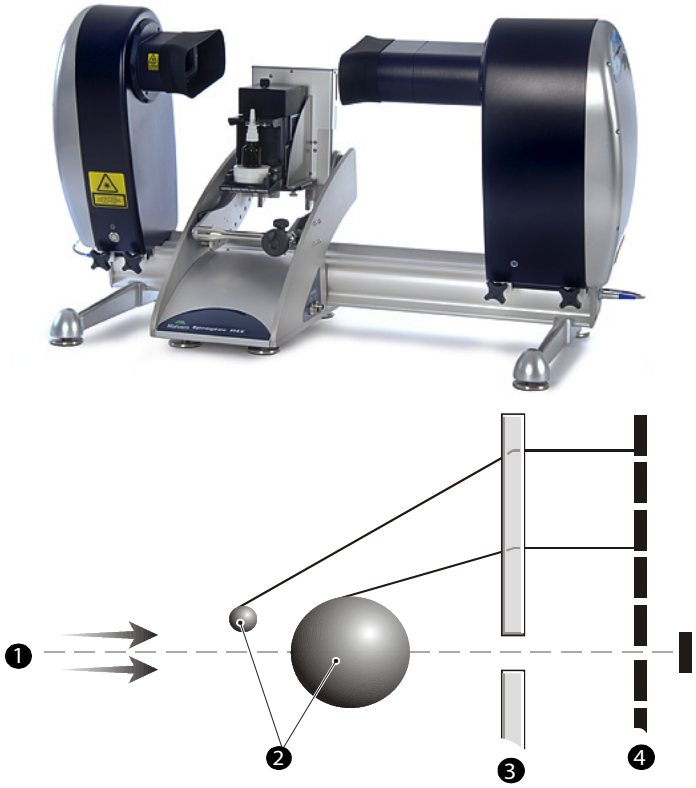

Figure 2.18: Malvern Spraytec particle and droplet size analyzer (top) and principle of laser diffraction for particle size measurements (bottom). Adapted from Spraytec user manual [170].

2.6 Spray droplet size distributions

Measurements of the spray droplet size distributions as an indicator of quality of atomization were conducted using a Malvern Spraytec particle and droplet size analyzer shown in Fig. 2.18. This device consists of a transmitter (left) and receiver (right) module with the spraying device located in between. A He-Ne laser beam (632.8 nm) is expanded and collimated into a 10 mm beam in the trasmitter module. The beam the passes through the measurement region and is scattered by the spray. The scattered light is then focused through a lens in the receiver module onto a detector array.

As shown in Fig. 2.18, the angle of diffracted light is a function of the scattering particle's size, as well as the refractive index and density. Smaller diameter particles

diffract at a greater angle than the larger diameter particles, allowing for the array of detectors to correlate to the droplet size distribution if the material properties are specified. Non-diffracted light is also focused through a pin hole and is used to determine the transmission. This technique allows for measurements of particle diameters in the range of 0.1–2000 μm.

Chapter 3

Comparison of global NO emissions in swirling glycerol and diesel spray flames

The objective of this chapter is to provide an initial analysis of the large scale differences in the formation of NO_X emissions in the combustion of glycerol when compared with a more traditional, non-oxygenated fuel, namely diesel. This chapter investigates the exhaust gas concentrations of NO_X as well as the stack gas temperature from the combustion of both fuels in the first iteration of the swirling spray burner described in Section 2.1.

Experiments are conducted for a fixed firing rate and geometric swirl number S_g while the global equivalence ratio ϕ_g and atomizing air flow rate $\dot{Q}_N$ are varied. The experimental setup and diagnostic techniques are described in Section 3.1. Measurements of the droplet size distribution for each fuel is analyzed in Section 3.2. Then the influence of the ϕ_g is described in Section 3.3, followed by observations on the flame shape in Section 3.4 and the influence of the atomizing air flow rate in Section 3.5.

3.1 Experimental setup

The combustion apparatus used in this chapter is the first iteration of the swirling spray burner described in Section 2.1 and shown in Fig. 3.1. Swirling flow is achieved through the mixing of two air streams: an axially oriented stream $\dot{Q}_A$ and 4 tangentially oriented streams $\dot{Q}_\theta$ positioned perpendicularly to the axial air flow with each port positioned offset from the axis of symmetry. The swirling flow exits the mixing plenum through a converging and then diverging section known as a venturi and quarrel, respectively. Along the axis of symmetry is positioned a fuel lance composed of a third, atomizing air stream $\dot{Q}_N$ and a liquid fuel stream. The end of the fuel lance is fitted with an air atomizing nozzle, described in greater detail in Section 2.1. The exit of the nozzle is positioned at the base of the quarrel (beginning of diverging section). Operation of the burner proceeds as described in Section 2.1, with the swirl number controlled through the distribution of combustion air through the axial and tangential inlets. Liquid fuel was delivered using the reciprocating piston pump and pressure fluctuation dampening accumulator system described in Section 2.1.1. Exhaust gas samples and stack gas emissions were collected at the exit of the combustion chamber and recorded throughout the experiments.

The range of experimental conditions used throughout this chapter are listed in Table 3.1. It was determined to hold the power of the burner constant, rather than the mass or volume flow rate of fuel, due to the significant differences in energy densities for each of the fuels. The net result is approximately a factor of 2 difference in volumetric flow rate $\dot{Q}_f$ and nearly a factor of 3 difference in mass flow rate $\dot{m}_f$. However, it was determined that given the low energy density of the primary fuel of interest, glycerol, and the necessity of maintaining a nearly constant heat loss through the refractory combustion chamber, it was better to sacrifice the differences in fuel flow rate and instead maintain a constant power in the burner. This sacrifice allows for a comparable combustion environment and burner wall temperature for each fuel.

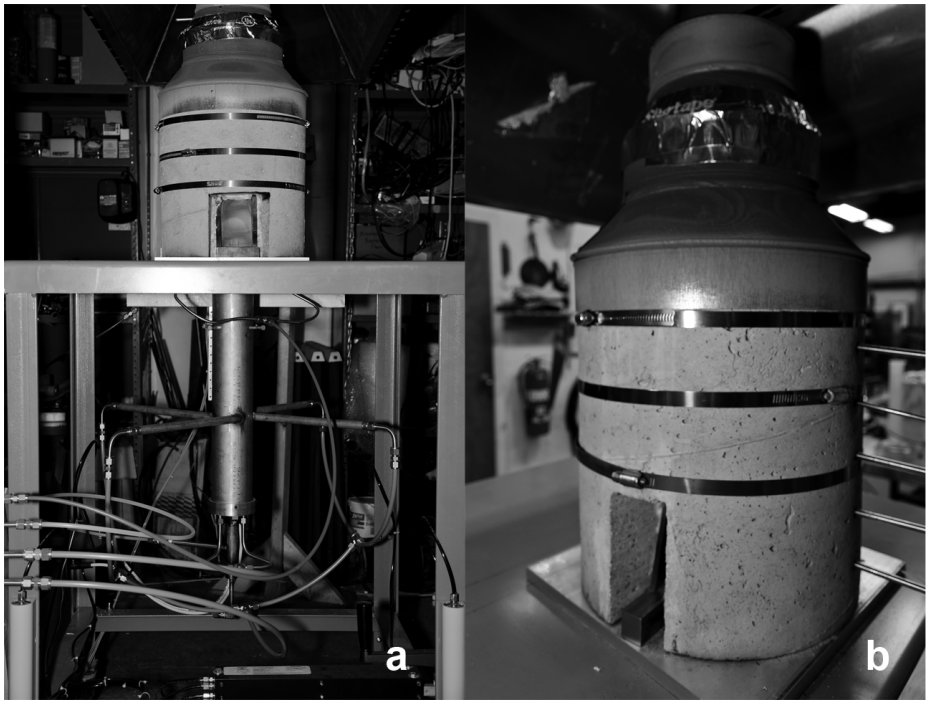

Figure 3.1: Photographs of the swirling spray burner used in this chapter. Subfigure a) illustrates the 4 tangential flow paths and the mixing plenum while subfigure b) shows a close up of the cast refractory combustion chamber and exhaust stack.

Consequences of the significant differences in fuel thermo-physical for each fuel are discussed in greater detail in Section 3.2.

One of the features of the method of inducing swirl utilized in this burner is the ability to easily vary the global equivalence ratio without significantly impacting the geometric swirl number S_g. This is achieved through changing the ratio of air introduced through the axial and tangential ports. Therefore throughout this chapter the swirl number is held fixed at an S_g=5.

The first set of experiments listed in Table 3.1 describes the conditions under which the influence of the global equivalence ratio ϕ_g is examined. In this set of experiments, a small subset of atomizing air flow rates $\dot{Q}_N$ is determined and shown in bold font in Table 3.1. For each condition, $\dot{Q}_N$ is held constant while ϕ_g is varied through the listed range by changing $\dot{Q}_T$. The second set of experiments follows a similar procedure, with a small subset of the ϕ_g selected and held fixed (and shown in bold

Table 3.1: Experimental Conditions for Glycerol and Diesel Spray Flames

	(Units)	Glycerol	Diesel
Power	(kW)	9.3	9.3
$\dot{m}_f$	(g/min)	35	12.5
$\dot{Q}_f$	(ml/min)	31	15
T	(°C)	60	25
S_g	(-)	5	5
		Experiment 1: Influence of ϕ_g	
$\dot{Q}_T$	(SLPM)	115-225	165-225
$\boldsymbol{\dot{Q}_N}$	**(SLPM)**	**8, 14, 20**	**4, 8, 14**
ϕ_g	(-)	0.62-1.37	0.64-0.99
		Experiment 2: Influence of $\dot{Q}_N$	
$\dot{Q}_T$	(SLPM)	140, 150, 165, 190, 210	165, 190, 210
$\dot{Q}_N$	(SLPM)	7-20	3-16
$\boldsymbol{\phi_g}$	**(-)**	**0.75, 0.83, 0.96, 1.05, 1.13**	**0.78, 0.87, 0.99**

font) while the $\dot{Q}_N$ is varied over the listed range. Between these two experiments, the primary parameters for the control on this swirl burner can be investigated.

Throughout the experiments in this chapter, the NO_x exhaust gas stack emissions are measured after the exit of the combustion chamber. These measurements are conducted using a quartz sampling probe with a 0.75 mm diameter orifice. The probe was positioned 30 cm downstream of the exit of the combustion chamber. Sample gases were aerodynamically cooled in the quartz probe, followed by drying using a silica get desiccant drier and filter through a 6 μm paper filter. Accompanying the exhaust gas sampling are temperature measurements of the exhaust gas temperature positioned near the tip of the sampling probe. These measurements were made using a 0.2 mm type-R thermocouple and are uncorrected for heat losses.

Flow rates of the three air streams are monitored using teledyne hasting thermal mass flow meters and are manually controlled with needle valves. Meanwhile, the liquid fuel flow rate was controlled using an Eldex Optos HPLC metering pump for both fuels as previously described. Fuel flow rate oscillations were dampened using

the pressure oscillation dampening system.

3.2 Droplet size distribution

Before exploring the influence of ϕ_g and $\dot{Q}_N$ on the emissions characteristics, it is important to gain a better understanding of the nature of the atomization of the liquid fuels. This is especially important given the significantly different thermo-physical properties of glycerol and diesel. Additionally, because the best method to atomize viscous liquids, such as glycerol, is to use an air atomizing nozzle, there can be significant consequences to the choice of atomizing conditions. Therefore, this section presents an initial investigation into the influence of $\dot{Q}_N$ on the droplet size distribution, with a more involved discussion of atomization characteristics in Chapter 4.

Table 3.2: Thermo-physical Properties

Property	(Units)	Glycerol	Diesel
Temperature	(°C)	60	25
Dynamic Viscosity	(cP)	86	1.4
Surface Tension	(N/m)	0.0605	0.0248
Energy Density	(kJ/g)	∼16	∼43
Boiling Point	(°C)	287.9	149-371
Autoignition Temperature	(°C)	370	203

Table 3.2 lists several thermo-physical properties important to the quality of atomization. Particularly important to the atomization process is viscosity and surface tension. From Table 3.2 it can be seen that glycerol has both a greater viscosity and surface tension, despite the higher initial temperature. It can be expected that this should have a profound effect on the quality of the spray and the ability of the liquid stream to break up into droplets.

In order to observe this effect, a Malvern Spraytec aerosol and spray droplet size analyzer was utilized to measure the droplet size distribution in a non-reacting spray

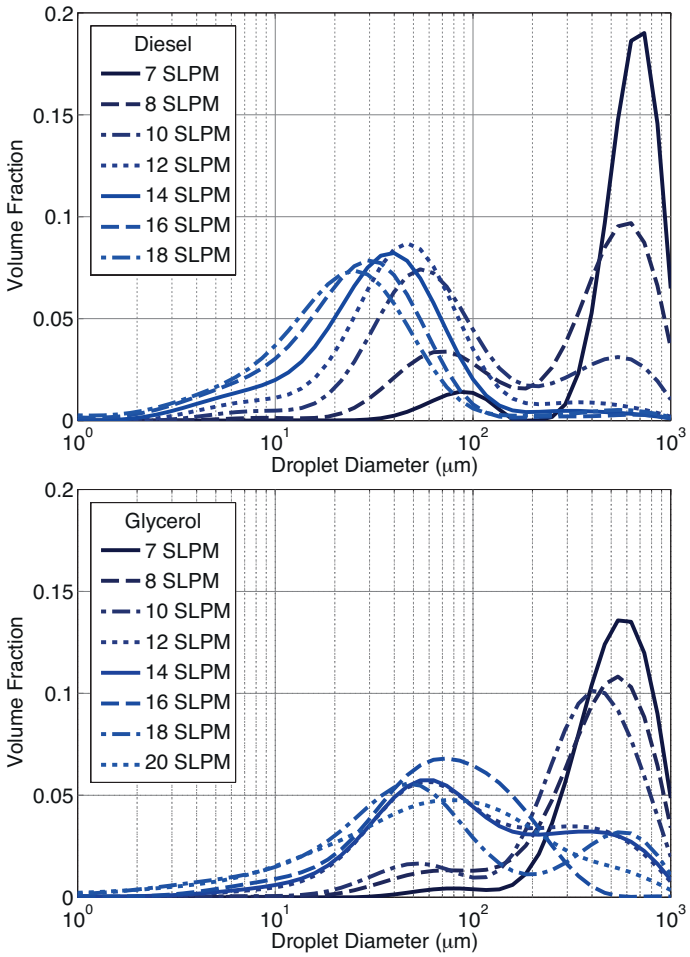

Figure 3.2: Droplet size distributions for diesel and glycerol sprays as a function of the $\dot{Q}_N$

for each fuel over a range of operational atomizing air flow rates. These measurements were conducted 2.5 cm from the tip of the nozzle. The droplet size measurement is conducted following the theory described in Section 2.6, resulting in a cylindrical measurement region, 1 cm in diameter, extending through the width of the spray. Measurements were conducted at fuel flow rates and temperatures listed in Table 3.1, while $\dot{Q}_N$ was varied through a range of 7 to 20 SLPM.

Figure 3.2 shows the measured droplet size distribution for diesel and glycerol. For both fuels at low atomizing air flow rates, the droplet size distributions are bimodal with peaks centered on 90 and 700 μm for diesel and 80 and 600 μm for glycerol at 7 SLPM. As $\dot{Q}_N$ was increased, the larger mode dramatically decreased as fewer large

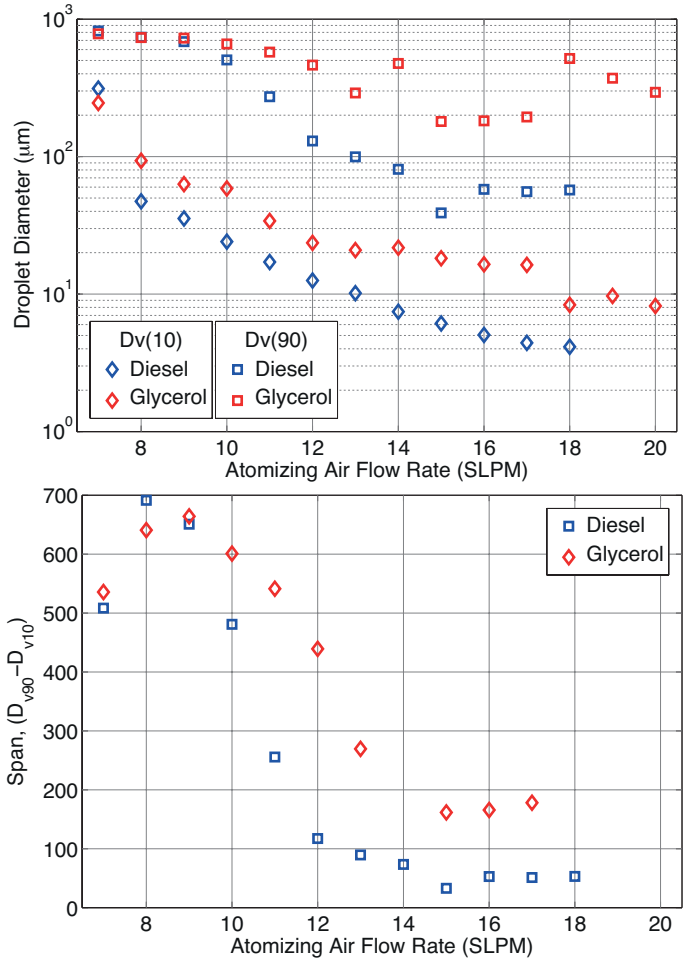

Figure 3.3: Cumulative undersize distributions below 10% and 90% and Span, (D_{v90}-D_{v10}), for diesel and glycerol sprays

droplets were formed. With increasing $\dot{Q}_N$, the diesel spray transitions to a single mode and shifts to progressively finer droplets. The glycerol spray exhibits a similar trend, however the result is an overall larger droplet size.

It can also be seen in Fig. 3.3a that both the cumulative undersize distributions D_{v10} and D_{v90} are consistently lower for diesel than for those of glycerol. As was observed in Fig. 3.2, increasing the atomizing air flow rate rapidly shifts the distribution of droplet sizes to smaller diameters. It is interesting to note that the shift to smaller diameters is accompanied by a corresponding shift in the span of the distribution as shown in Fig. 3.3b. Above approximately 10 SLPM, a rapid drop in the span was measured, corresponding with the reduction in the larger mode. It can also be seen

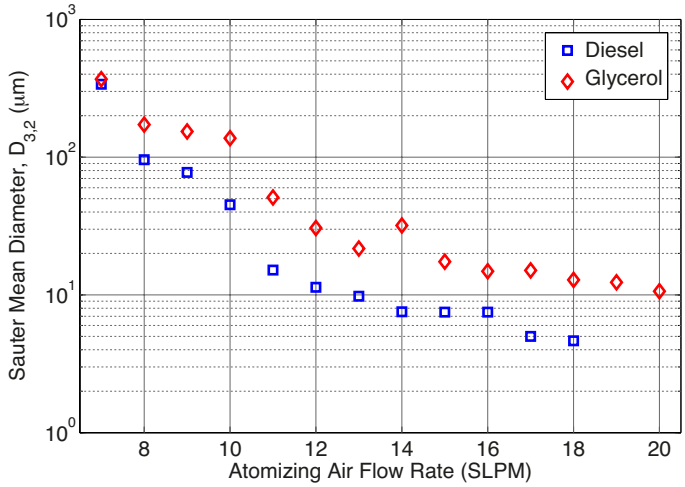

Figure 3.4: Sauter Mean Diameter, $D_{3,2}$, for diesel and glycerol sprays

that the increase in atomizing air flow rate has a stronger effect on reducing the span in the less viscous diesel spray than the glycerol spray, resulting in: a delayed initiation in the reduction of the span, slower response to further increases in the $\dot{Q}_N$, and larger span when the effectiveness of increasing $\dot{Q}_N$ diminishes.

The net result of the influence of $\dot{Q}_N$ can be seen in Fig. 3.4, which shows the Sauter Mean Diameter, $D_{3,2}$, for both sprays. $D_{3,2}$ is the diameter of a mono-disperse droplet distribution with an equivalent ratio of volume to surface area. $D_{3,2}$ is calculated as:

$$D_{3,2} = \frac{\sum_{i=1}^{N} D_i^3 v_i}{\sum_{i=1}^{N} D_i^2 v_i} \tag{3.1}$$

where D_i is the geometric mean particle diameter of a given bin i and v_i is the volume percentage of particles in bin i. Equation 3.1 serves as a single representative diameter for a poly-disperse spray in which surface area plays a dominate role, such as in evaporation and combustion [52]. A rapid reduction in the $D_{3,2}$ can be seen with initial increases in $\dot{Q}_N$, however the effectiveness is reduced as the $\dot{Q}_N$ increases. Overall, the diesel spray is composed of a smaller diameter distribution of droplets than the glycerol spray. In a general sense, the influence of the difference in droplet distributions can be inferred to include longer evaporation times and lower

Stokes number in the glycerol spray. This will result in a reduced tendency for glycerol droplets to follow the gas phase recirculation zones, with the potential for the droplets to overcome the negative velocity along the centerline (established due to the swirl induced recirculation zone) or for the droplets to be centrifuged to the walls of the combustion chamber. Both outcomes would further increase droplet evaporation time [114, 171–173]. Conversely, the smaller droplets of the diesel spray will tend toward shorter evaporation times and exist closer to the exit of the nozzle, allowing for greater entrainment in recirculation zones.

3.3 Influence of global equivalence ratio

In order to investigate the influence of the global equivalence ratio ϕ_g on NO_X formation, measurements of the stack gas emission of NO_X and the exhaust gas temperature were conducted on the conditions listed in Table 3.1 for Experiment 1. In this study, the firing rate was held constant. Additionally, S_g was held fixed. For each of the selected $\dot{Q}_N$, $\dot{Q}_T$ was varied, resulting in ϕ_g in the range of 0.64 to 0.99 for the diesel flames and 0.62 to 1.37 for the glycerol flames. A constant swirl number was achieved through the independent variation in $\dot{Q}_A$ and $\dot{Q}_\theta$ flow rates, while the relative proportion of each was maintained constant.

It was possible to operate the glycerol flame under much richer conditions than the diesel flame. This is likely attributable to the very high fuel bound oxygen in glycerol, where M_O is greater than 50%. This high M_O results in very low soot formation, as will be discussed in Section 3.4, allowing the glycerol flame to operate under rich conditions in which the soot formation in the diesel flame became prohibitive. It is also conceivable that the high M_O allows for leaner local equivalence ratios ϕ than would be common for fuels with a lower M_O.

Figure 3.5a illustrates the very significant differences in measured NO_X concen-

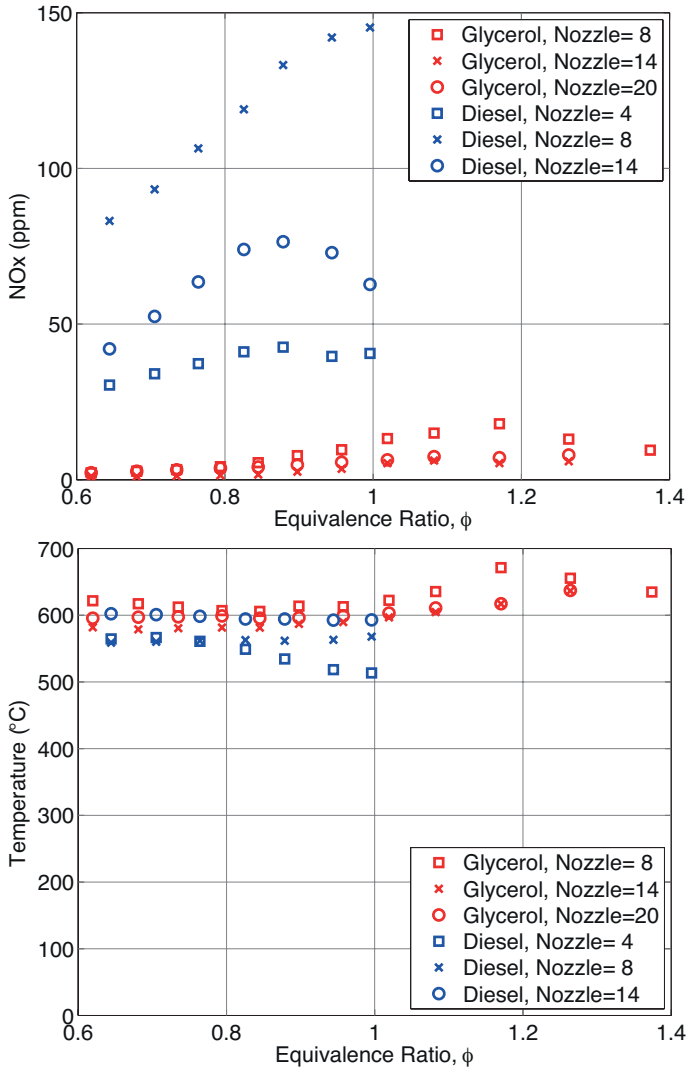

Figure 3.5: Measured a) NO_X concentrations and b) exhaust temperature as a function of ϕ_g for several $\dot{Q}_N$.

trations for the two fuels. It was previously shown [90, 91] that NO_X formation in glycerol combustion can be significantly lower than more traditional fuels, however it was unclear how NO_X formation would compare under a wider range of conditions. From Fig. 3.5a, NO_X emissions can be more than an order of magnitude lower in some cases.

Increases in NO_X emissions with increasing ϕ_g are consistent with the dual effects of increasing peak temperatures around ϕ_g=1 and the increase in prompt NO formation due to the increased availability of hydrocarbon radicals. This second effect

will be investigated in greater detail in subsequent sections. The steeper slope in NO emissions with ϕ_g observed in the diesel flames compared with those of glycerol may also indicate greater partial premixing. Such an effect would not be unexpected due to the greater vaporization rates of the diesel spray when combined with strong mixing in a swirling flame. The net result being a stronger coupling of NO_X formation to the peak flame temperature.

It can also be observed that NO_X formation in the glycerol flames peaks in the globally rich regions, hinting at the important roles of prompt NO and the availability of hydrocarbon radicals in NO_X formation for highly oxygenated fuels.

Figure 3.5b provides a comparison of the exhaust gas temperatures measured by a thermocouple positioned at the exit of the combustion chamber. It can be seen that the exhaust gas temperatures between diesel and glycerol flames were quite comparable. While this does not offer a convenient explanation for the low NO_X emissions observed in the glycerol flame, it does help to eliminate the likelihood of the lower emissions being a result of incomplete combustion. It should also be mentioned that calculated stoichiometric adiabatic flame temperatures for diesel (approximated as dodecane) and glycerol are 2413 K and 2201 K, respectively, which is not a great enough difference to account for an order of magnitude difference in NO_X formation.

Because changing ϕ_g in Fig. 3.5 requires that $\dot{Q}_T$ also changes, it is interesting to investigate the influence of $\dot{Q}_T$ on NO_X formation as shown in Fig. 3.6. Changes in $\dot{Q}_T$ will have the greatest impact on the flame structure as the relative strengths of the recirculation zones and the momentum of the spray jet are varied. Increasing $\dot{Q}_T$ at a constant $\dot{Q}_N$ will directly increase the strength of the mixing and entrainment of spray into recirculation zones. As a result, partial premixing is increased, shifting local ϕ off stoichiometric, lowering temperatures and ultimately reducing NO_X formation as seen in Fig. 3.6.

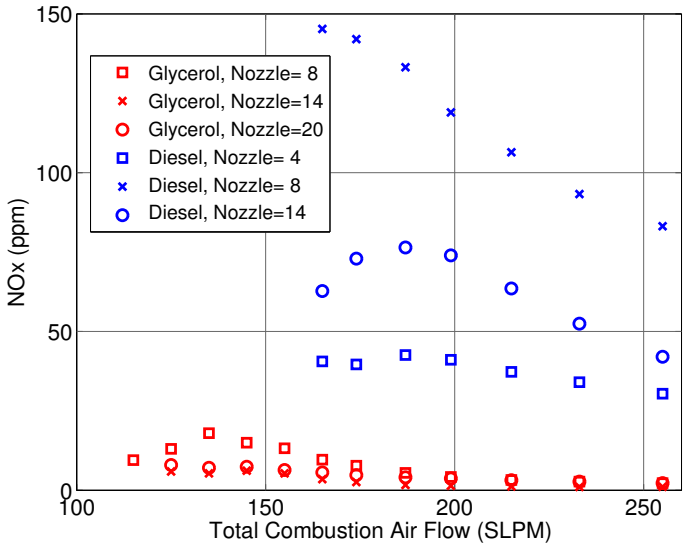

Figure 3.6: Measured NO_X concentrations as a function of $\dot{Q}_T$.

3.4 Observation on the flame shape

In order to better understand the influence of $\dot{Q}_N$ on the structure of the flame, instantaneous images of the natural luminosity for diesel and glycerol flames under varying $\dot{Q}_N$ were taken. These photographs are shown in Fig. 3.7, where the upper set of photos shows diesel flames with $\dot{Q}_N$ between 2 and 14 SLPM, and the lower set shows glycerol flames with $\dot{Q}_N$ between 8 and 20 SLPM. For both sets, S_g, firing rate, and $\dot{Q}_T$ (210 SLPM) are held constant. The resulting ϕ_g was 0.78 and 0.75 for diesel and glycerol, respectively. Exposure times and aperature values were held constant throughout and neutral density filters were used to avoid detector saturation.

It is immediately apparent that the glycerol flame is far less luminous than the diesel flame, indicating that glycerol has a much lower propensity to form soot than diesel due to its high degree of oxygenation. A second observation is that changes in the atomizing air flow rate have a significant impact on the structure of the flame. It is interesting to note that it was possible to increase the atomizing air flow rate in the glycerol flame significantly higher than 20 SLPM, much higher than it was possible to spray the diesel. At the low end of the atomizing flow rate range for both fuels,

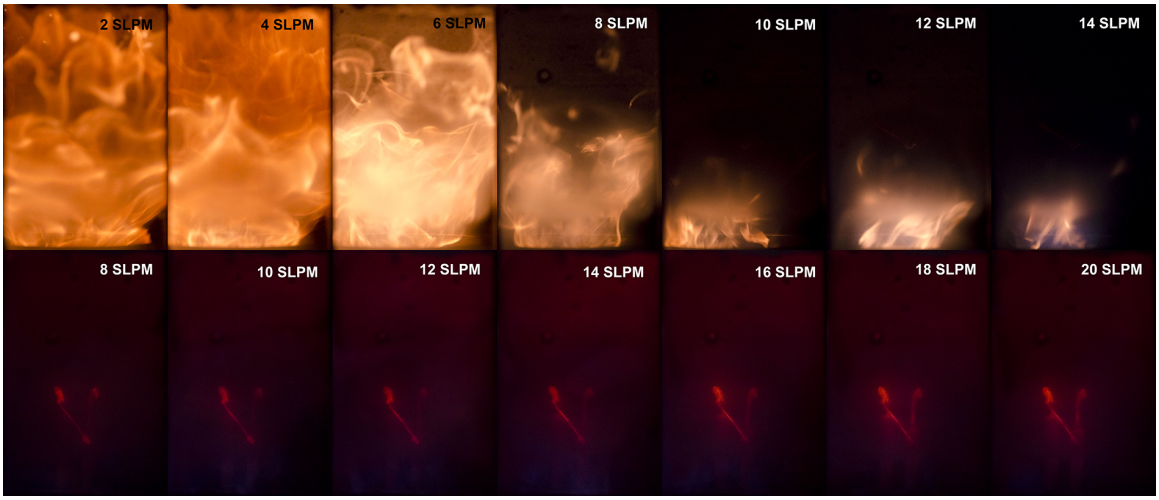

Figure 3.7: Direct photographs of diesel and glycerol flames under varying $\dot{Q}_N$.

the flame is very wrinkled and large droplets of liquid fuel are occasionally observed far from the nozzle. Lower than 5 SLPM, the diesel flame completely fills the field of view while increasing the atomizing air flow rate causes the flame to become more compact. For both fuels at high atomizing air flow rates, the flame is extremely compact and very blue, indicating significantly reduced soot formation.

There appears to be a transition in flame shape around 7 SLPM for the diesel flame and around 12 SLPM for the glycerol flame where the flame transitions from a large, wrinkled flame with significant interaction with the recirculation zone to a compact, much less luminous flame. This transition can be attributed to observations made by Chen et al. [110] when examining the influence of the fuel jet momentum on the recirculation of a swirling, non-premixed flames. More on these effects will be discussed in Chapter 5, however this transition in flame shape can be observed in Fig. 3.7 around 8 SLPM for the diesel flame, and while harder too seen, around 12 SLPM for the glycerol flame. These transition values are made for a single value of total air flow rate and swirl number and can have different transition values as the strength of the recirculation vortex changes.

3.5 Influence of the atomizing air flow rate

To further investigate the influence of the atomizing air flow rate, measurements of NO_X formation were made over a range of atomizing air flow rates while holding the global equivalence ratio ϕ_g constant. These measurements are shown in Fig. 3.8a and it can be seen that there is a large disparity in NO_X formation for glycerol compared with diesel, consistent with the previous measurements. NO_X formation peaks around 8 and 10 SLPM for diesel and glycerol, respectively.

Figure 3.8b shows just the glycerol NO_X measurements rescaled, and as expected the peak measured NO_X value increases as ϕ_g increases due to the effects discussed above. At the high end of the measured range of atomizing air flow rates, the droplet size distribution shifts to smaller droplets, which result in higher evaporation rates and greater partial premixing, shifting the flames locally off stoichiometric and thereby reducing the total NO_X formation as well as the differences in NO_X formation when comparing different global equivalence ratios. At the low end of the measured atomizing air flow rate range, the shift to larger droplets results in reduced evaporation rates, longer residence times, and lower heat release rates, ultimately reducing NO_X formation rates.

It is also likely that, particularly for extremely large glycerol droplets and high global equivalence ratios, reduced evaporation rates coupled with shorter residence times (due to lower entrainment in the recirculation zone characterized by lower Stokes numbers) could result in less than complete combustion by the time the droplet reaches the exit of the combustion chamber. In Fig. 3.8c, measurements of the exhaust gas temperatures for these conditions are shown, and despite significant differences in the NO_X emissions, not only between fuels but also with varying atomizing air flow rates, it is interesting to note that the measured exhaust gas temperature remained nearly constant.

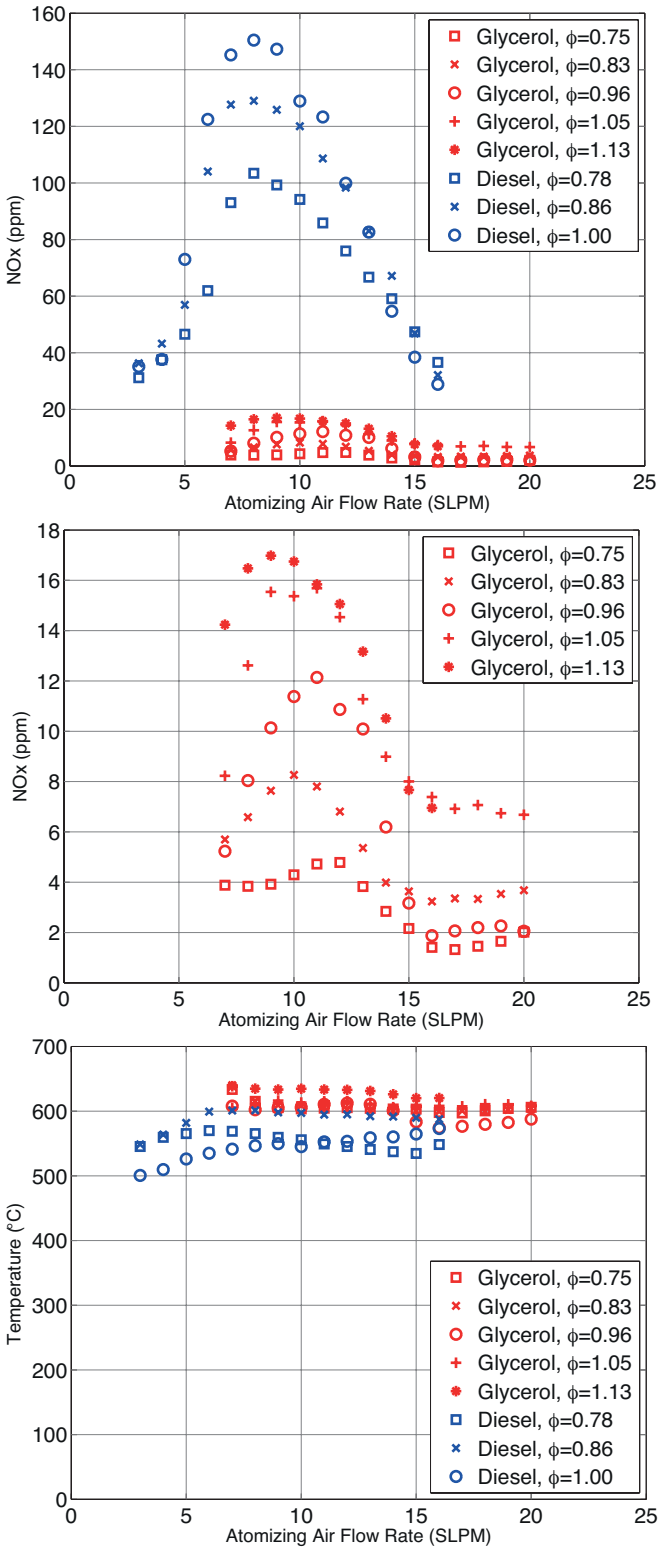

Figure 3.8: Influence of the $\dot{Q}_N$ on NO_X formation for a) diesel and glycerol, b) glycerol in detail, and c) exhaust gas temperatures.

3.6 Conclusions

The objective of this first chapter was to investigate the nature of NO_X emissions from the combustion of glycerol, and determine whether initial measurements of NO_X concentrations were systematically lower than those of a more traditional fuel. In pursuit of this objective, measurements of the spray characteristics for diesel and glycerol sprays were conducted, the structure of the flames was observed under varying $\dot{Q}_N$, and measurements of NO_X concentrations were conducted as functions of the global equivalence ratio ϕ_g, the total flow rate of air $\dot{Q}_T$, and the atomizing air flow rate $\dot{Q}_N$.

From these studies, it was possible to conclude that through the variation of the spray characteristics via the atomizing air flow rates and the global equivalence ratio, as well as the residence time through the total combustion air flow rate, that glycerol flames consistently produced up to an order of magnitude lower NO_X. In conditions in which the diesel and glycerol sprays were of similar droplet size distributions, significantly lower NO_X emissions were measured, despite consistent adiabatic flame temperature and measured exhaust gas temperatures. Therefore, a reasonably safe conclusion can be made that the observed effect of lower NO_X from the combustion of glycerol is not a burner effect, but indeed is due to the properties of glycerol as a fuel. The subsequent chapters will attempt to diagnose the specific causes of this lower NO_X formation and will broaden the scope to include the entire family of alcohol and polyalcohol fuels.

Additionally, it was shown that both the flame and NO_X emissions can be profoundly impacted by the combination of S_g, $\dot{Q}_N$, $\dot{Q}_T$, ϕ_g. Care must therefore be taken in the selection of operating conditions, however opportunity can also be found in the careful control of these parameters and design for flame characteristics.

Chapter 4

Measurements of droplet size distribution in poly-alcohol sprays

The objective of this chapter is to investigate the atomization characteristics of a wide range of hydroxylated fuels. In Chapter 3, it was shown that the thermo-physical properties of the liquid fuel can have a profound influence on the quality of atomization and droplet breakup, flame shape, and emissions. Therefore, in order to develop a deeper understanding of the influence of one or more OH functional group on NO formation, it is necessary to conduct a deeper investigation of atomization characteristics of the wide range of fuels to be used in Chapter 5.

Here, experiments will be conducted utilizing a Malvern Spraytec laser diffraction spray particle and droplet sizer. The theory of laser diffraction is discussed in greater detail in Section 2.6. An explanation of the experimental setup is included in Section 4.1. A visual study of the variations in spray angle and quality of atomization is conducted in Section 4.2. An investigation of the influence of the atomizing air flow rate and the initial fuel temperature is discussed in Sections 4.3.2 and 4.3.3, respectively.

4.1 Experimental setup

The experimental apparatus used in this chapter is composed of two components: 1) the nozzle and fuel conditioning system and 2) a spray capture system. Atomization is achieved using the Hago air atomizing nozzles used in conjunction with the swirling liquid spray burner and described in Section 2.1. Liquid flow rates and temperatures were controlled using the pressurized reservoir fuel delivery system discussed in Section 2.1.2. Fuel flow rates were controlled with a Brooks Quantim coriolis mass flow meter.

Due to the high flow rate of air necessary to atomize using this technique, aerosolized droplets will tend to disperse throughout the lab. Therefore, it was necessary to implement a system to capture the spray before dispersion. This was achieved through the device shown in Fig. 4.1 in which a high flow rate of air is drawn through a series of metal wire mesh screens. The nozzle is positioned such that the spray impinges on, and is drawn through, the mesh screens. As the spray impinges on the screens, the droplets coalesce and are collected in a drip pan in the bottom of the capture

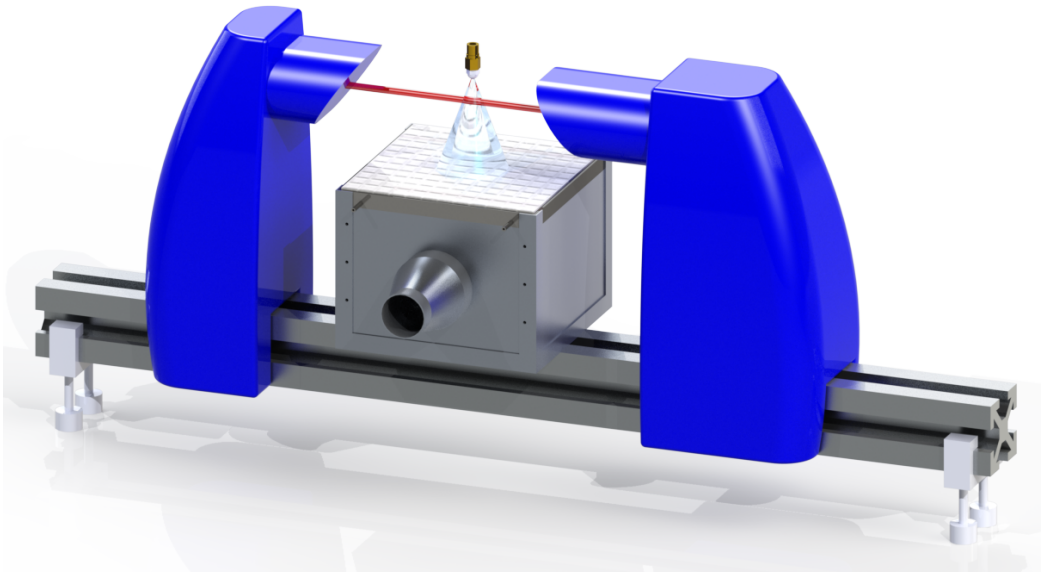

Figure 4.1: Diagram of spray capture device, illustrating position of transmitter, receiver, beam path, and spray positioning.

Table 4.1: Atomization parameters for droplet size distribution study

Property	(Units)	Conditions
Nozzle		
Part	(#)	SN609-2, SN609-3
Nominal Flow Rate	(cm^3/min)	12.6, 18.9
Temperature	(°C)	20-80
Firing Rate	(kW)	9, 10
Atomizing Air Flow Rate, $\dot{Q}_N$	(SLPM)	4-20
Fuel Mass Flow Rate at 9 kW	(g/min)	
Methanol	-	27.1
Ethanol	-	20.1
n-Propanol	-	16.1
Ethylene Glycol	-	31.6
1,2-Propylene Glycol	-	24.9
Glycerol	-	33.5
Refractive Index	(n/a)	
Methanol	-	1.33
Ethanol	-	1.36
n-Propanol	-	1.39
Ethylene Glycol	-	1.44
1,2-Propylene Glycol	-	1.43
Glycerol	-	1.47

box. This system avoids dispersion of fuel droplets into the environment, while also reducing the overspray that can disperse into the beam path of the particle sizer, which would interfere with the measurements.

Droplet size distributions were measured using the Malvern Spraytec aerosol and spray droplet size analyzer, previously used in Section 3.2, the operation of which is described in Section 2.6. For these experiments, the center of the 10 mm beam path was positioned 2.5 cm from the tip of the nozzle. The spray was positioned at the midpoint between the transmitter and detector modules of the Spraytec using the 750 mm focal length lens, allowing for droplet detection in the range of 2 to 2000 μm. The parameters investigated in this study are shown in Table 4.1

Due to the large disparity in liquid mass flow rates at a constant firing rate, and limited turn-down ratios for the nozzles, it was decided to investigate which nozzle

size would provide the best atomization over the wide range of conditions intended for the following chapter. Additionally, because the liquid viscosity, surface tension, and density are all strong functions of the temperature, a wide range of liquid preheating temperatures were investigated for the low volatility fuels. Also shown to have a profound impact on the quality of atomization in Section 3.2, the atomizing air flow rate $\dot{Q}_N$ was investigated.

4.2 Photographs of spray shape

The first objective was to visualize the spray shape for several conditions to gain a qualitative understanding of the influence of the atomizing air flow rate and fuel preheat temperature on the spray structure. Direct photographs using a Nikon D700 CMOS camera and strobe were taken for several glycerol sprays and are shown in Fig. 4.2. Figure 4.2a begins with a low fuel preheat temperature and low $\dot{Q}_N$. In this image, it is clear that the quality of the atomization is very poor. Many large droplets can be observed throughout the spray. It can also be seen that the spray angle is relatively wide. Because many of the fuels used in this study have relatively poor combustion characteristics, such as low energy densities and high autoignition temperatures, poor atomization can yield disastrous consequences. A droplet distribution that skews toward few, large diameter droplets will exhibit much longer vaporization times. As a result, droplet lifetimes can become sufficient to exit primary reaction zones, and migrate to lower temperature regions of the combustion chamber and possibly even survive throughout the entire combustion chamber. Additionally, shifts in droplet distributions toward larger sizes reduces the proportion of energy released through the rapid combustion of the small diameter droplets. Such droplets are vital for the stabilization and anchoring of the flame. Consequentially, poorly atomized sprays are easily blown off.

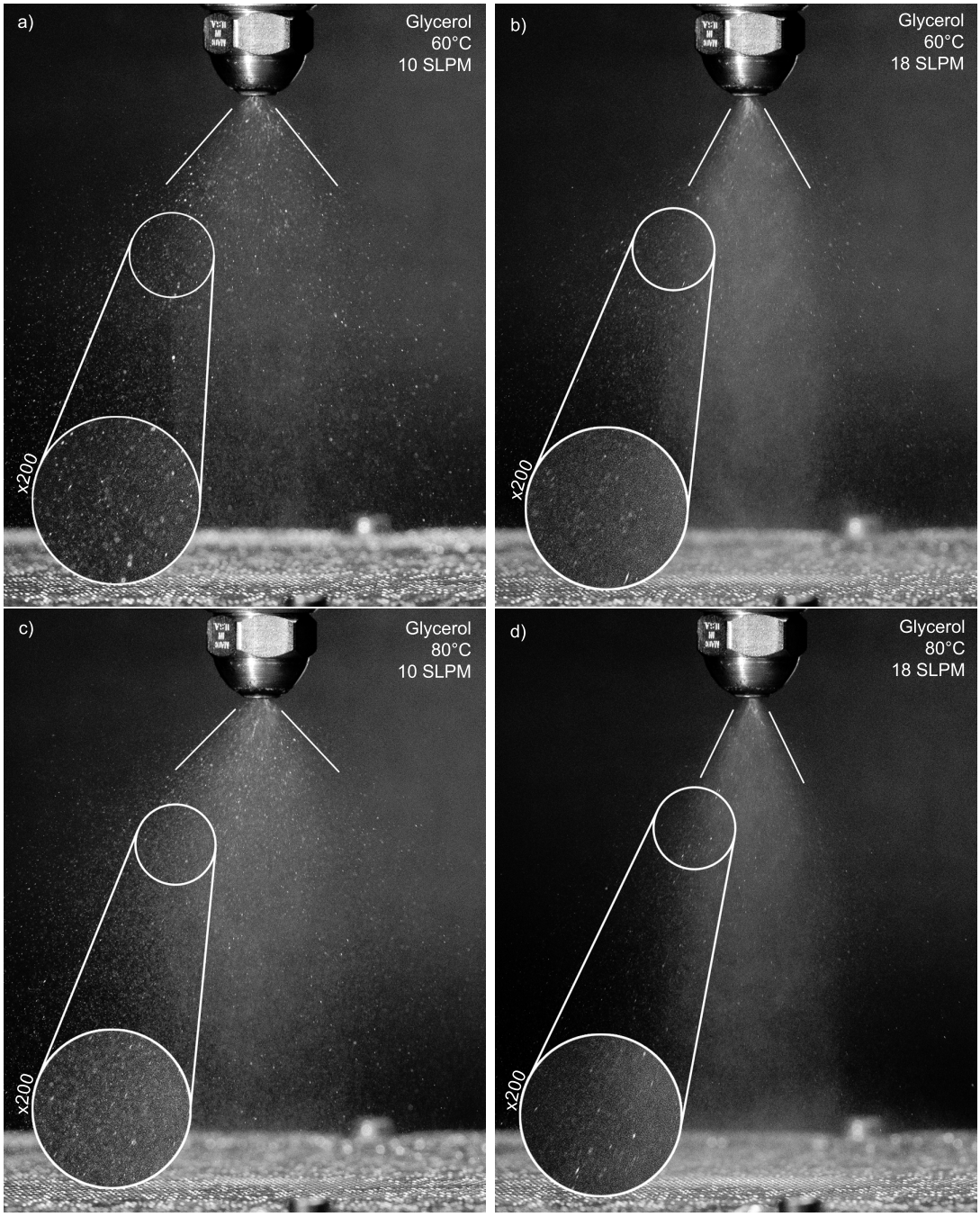

Figure 4.2: Influence of temperature and atomizing air flow rate on spray: a) low fuel preheat temperature and low atomizing air flow rate, b) low fuel preheat temperature and high atomizing air flow rate, c) high fuel preheat temperature and low atomizing air flow rate, and d) high fuel preheat temperature and high atomizing air flow rate.

Two parameters can be easily controlled to modify the quality of atomization. The first is to increase $\dot{Q}_N$ as shown in Fig. 4.2b. Here, the spray angle narrows due to the higher velocity air stream. It can also be seen that the occurrence of large, single droplets is reduced and the mist of fine droplets is increased. The fuel preheat temperature is another parameter that is easily controlled. Increasing preheat temperature as shown in Fig. 4.2c, it can be seen that the spray angle is relatively unaffected. However, the occurrence of large droplets does appear to be reduced and the mist of fine droplets increased. Finally, by combining a high fuel preheat temperature with high $\dot{Q}_N$, the spray angle is narrowed and the presence of large droplets is greatly reduced, yielding a greatly improved quality of atomization from Fig. 4.2a.

Throughout the following sections, a more quantitative investigation of these parameters is discussed. The objective is to achieve the finest quality spray possible for a given fuel and combustion condition. However, it should be noted that the best atomization condition is not necessarily to use the highest possible $\dot{Q}_N$ with the highest possible fuel preheat temperature. As will be shown in much greater detail in Chapter 5, and was hinted at in Section 3.4, the quality of atomization and the velocity of the atomizing air and droplet stream can have a profound influence on the flame shape and combustion properties. Therefore, a thorough understanding of the atomization parameters listed in Table 4.1 is necessary to adequately control and optimize the conditions for Chapter 5.

4.3 Droplet size distributions

In the following sections, quantitative measurements of droplet size distributions were conducted using the Malvern Spraytec as described in Sections 2.6 and 4.1. Each measurement began with the establishment of a continuous, steady spray at one

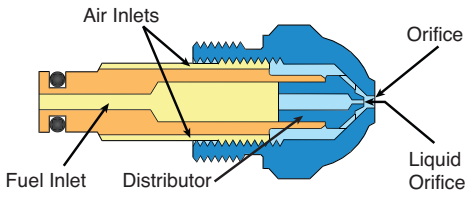

Figure 4.3: Schematic diagram of air atomizing siphon nozzle, illustrating the fuel and air inlets, along with the liquid orifice and the external orifice.

of the conditions listed in Table 4.1. The Spraytec as manually triggered to begin laser diffraction measurements over the span of 30 seconds, capturing distributions every second. The resultant 30 measurements were then averaged to provide the mean, steady state droplet size distribution located 2.5 cm from the nozzle tip. The parameters of interest are as follows: 1) nozzle size, 2) atomizing air flow rate, 3) liquid preheat temperature, and 4) liquid thermo-physical properties.

4.3.1 Influence of nozzle size and turndown ratio

The first parameter of interest is the influence of the nozzle size, or nominal flow rate. The nozzles used in this study are commercially available Hago-Danfoss air atomizing siphon nozzles. For the sake of this study, two different sizes are selected: SN609-3 and SN609-2 with nominal $\dot{Q}_f$ of 0.3 and 0.2 gallons per hour (18.9 and 12.6 cm^3/min), respectively. Relative to the majority of commercially available nozzles, these two are among the smallest available.

A cartoon of the inner structure of the air atomizing nozzle is shown in Fig. 4.3. The fuel and air delivery is via a co-annular tube, with the liquid and air streams in the center and outer sections, respectively. At the interface with the nozzle stem, an o-ring seals the liquid channel, while the air stream is separated into 4 channels cut up the nozzle stem and below the external nozzle cap. The distributor has a series of vanes cut into the air path, imparting a swirl to the air stream to enhance internal mixing. The distributor also has a finely machined liquid orifice.

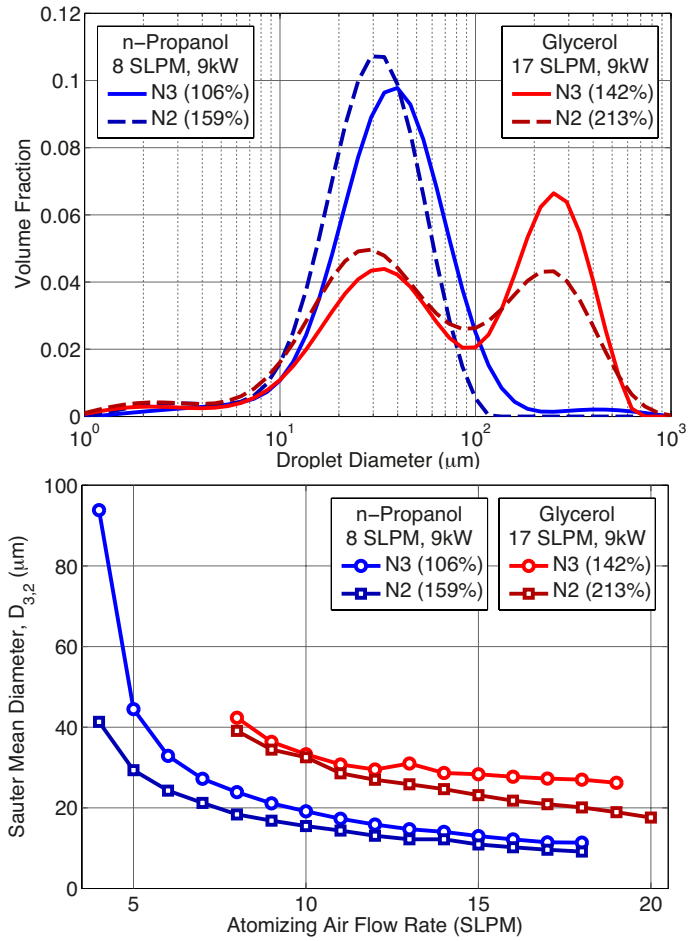

Figure 4.4: Influence of nozzle size and $\dot{Q}_f$ relative to nominal nozzle size

Two different size Hago-Danfoss air atomizing nozzles (part numbers SN609-3 and -2) were examined for low and high viscosity fuels, n-propanol and glycerol. The mass flow rate was maintained at 9 kW, which is the specified firing rating of the swirl burner. This firing rate places the SN609-3 as the optimally sized nozzle for the $\dot{Q}_f$ of n-propanol at approximately 106% of nominal flow rate. Due to the low energy density of the more highly oxygenated fuels, this value increases to approximately 140% of nominal flow rate for glycerol at 40°C.

It was interesting to see if the quality or atomization could be improved through the variation of the nozzle size. Initial experiments with changing the nozzle size in the swirl burner showed that attempting to increase the nominal flow rate of the nozzle

resulted in unsteady combustion for the low flow rate fuels. For this experiment, an SN609-4 nozzle was used with a nominal flow rate of 0.4 gallons per hour (25.2 cm^3/min). This unsteady combustion was due to operating too far below the nominal flow rate. The design of these nozzles is such that, for low viscosity liquids, a fuel delivery system (such as a pump, pressure chamber, or gravity feed) is unnecessary due to the siphoning effect of the high velocity stream of air across the liquid orifice in the distributor. Additionally, increasing the air flow rate directly increases the lift of the siphon system, allowing for a higher firing rate. However, in the system used here it is necessary to precisely control the flow rate of both low and high viscosity fuels, and to do so independently of the atomizing air flow rate. Because the fuel delivery system is closed, when the nozzle is oversized, the siphon effect can draw fuel through the liquid orifice at a rate greater than the rate defined by the delivery system. The result is an unsteady flow rate of liquid fuel, where a burst of excess fuel is atomized followed by a period of low flow rate of liquid as the cavity is refilled. Therefore, due to the unsteady atomization, droplet size distribution measurements where not conducted with the SN609-4.

On the other hand, decreasing the nozzle size below the firing rate showed minor improvements in the quality of atomization. This effect can be seen in Fig. 4.4. Decreasing the nozzle size results in a $\dot{Q}_f$ of n-propanol of about 160% of the nominal flow rate. As can be seen in Fig. 4.4a, both nozzle create high quality atomization at 8 SLPM, with a primarily mono-modal distribution. Decreasing the nozzle size has a slight shift in the median droplet diameter and a slightly higher proportion of the distribution in smaller droplets. On the other hand, the higher viscosity glycerol spray shows a bi-modal distribution for both nozzles. Decreasing the nozzle size has a similar effect to that observed in the n-propanol spray, such that the smaller nozzle shifts to an overall smaller diameter distribution. The large diameter mode is significantly reduced, however the center of the mode is not significantly shifted.

Meanwhile, the smaller diameter mode is both shifted to a smaller size and to a slightly greater proportion of the volume distribution.

Examining $D_{3,2}$, this same shift in quality of atomization can be observed over a greater range of $\dot{Q}_N$ in Fig. 4.4b. For both fuels, $D_{3,2}$ is consistently lower for the smaller nozzle. For n-propanol, increasing $\dot{Q}_N$ results in a reduction in the difference between the two nozzles. The opposite appears to be true for the glycerol sprays, however $D_{3,2}$ is more sensitive to errors in the measurement of volume fraction of droplets in larger diameter bins, where relatively few large droplets can compose a significant volume fraction while only representing a minuscule proportion of the number distribution.

While numerous styles of air atomizing nozzle configurations are available, they generally fall under one of two classifications: pre-filming and plain-jet. Pre-filming atomizers often involve the impingement of a liquid stream onto a pre-filming surface in which the surface area of the liquid can be increased into a thin liquid film. This sheet can then be sheared off of a pre-filming lip by a high velocity air stream on both sides of the liquid film. One such configuration can be seen in the work of Rizkalla et al. [174, 175]. The atomization achieves the greatest success when the liquid film has a uniform thickness, is as thin a possible and contacts the highest possible air velocity on both sides. The plain-jet configuration, is a relatively simpler geometry, composed of a centrally located liquid jet with an annular air stream. Such configurations have been examined by Kim and Marshall [176], Lorenzetto and Lefebvre [177], and Tsai and Viers [178]. The nozzle of Kim and Marshall also featured the ability to include a secondary air nozzle along the centerline of the fuel stream, creating an annular liquid sheet between two air streams which has been shown by Lefebvre to be capable of fine atomization [179]. The commercially available nozzles used in this study exhibit characteristics of both nozzle configurations, characterized by a swirling air stream and internal mixing.

In the study of Lorenzetto, the authors examined a range of liquid orifice diameters, along with a range of external orifice (or throat) diameters, allowing for the independent study of the fuel orifice diameter separate from the air/liquid mass ratio and air/liquid velocity ratio. They showed that for low viscosity liquids, the liquid orifice diameter, D_O, was relatively inconsequential to the droplet size distribution. For high viscosity fluids, $D_{3,2}$ was shown to be proportional to ${D_O}^{0.5}$. Therefore, it can be concluded that the greatest proportion of the reduction in $D_{3,2}$ observed in Fig. 4.4 can be attributed to an increase in the air/liquid velocity ratio for the n-propanol spray and and a combination of air/liquid velocity ratio and smaller D_O.

4.3.2 Influence of atomizing air flow rate

Apart from the thermo-physical properties of either the liquid or air stream, the most important parameter affecting quality of atomization is the flow of atomizing air. It is intuitive that the air velocity would have a significant impact on the quality of atomization. Additionally, both the mass ratio, M_R, and the relative velocity, U_R, of atomizing air to liquid affect the quality of atomization. In a fixed nozzle geometry, it is difficult to individually investigate the three parameters, so for the following section, they will be grouped together under the influence of $\dot{Q}_N$. Fortunately, the three parameters generally have similar effects on the quality of atomization.

Figure 4.5 shows the powerful influence of $\dot{Q}_N$ on droplet size distributions. In Fig. 4.5a, sprays of 1,2-propylene glycol are measured. Propylene glycol was selected due to its moderately high viscosity, lower only than glycerol in this study, but relatively low mass flow rate of fuel due to its relatively high energy density (second only to n-propanol). Here, the liquid is slightly pre-heated to 60°C. Starting at an $\dot{Q}_N$ of 7 SLPM, the distribution is very broad and exhibits a significant large diameter mode. However, increasing $\dot{Q}_N$ up to 15 SLPM rapidly improves the quality of the atomization. The large diameter mode is reduced in proportion with this a significant

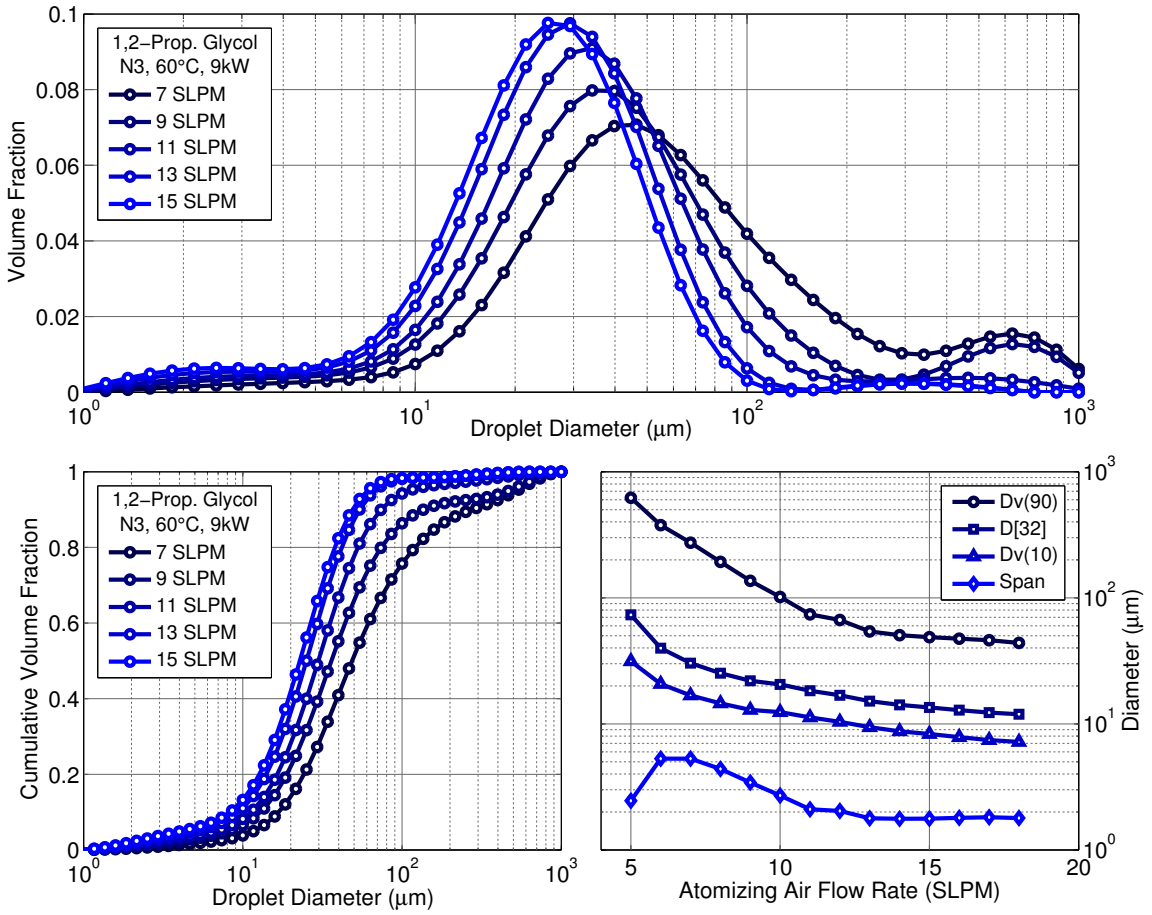

Figure 4.5: Influence of atomizing air flow rate on droplet size distribution, cumulative volume fraction, and cumulative undersize distributions

shift in the diameter of the mode, while the the primary mode exhibits a shift in both the diameter of this mode to smaller diameter droplets, but also an increase in the proportion of the spray in this primary mode.

The cumulative volume distribution in Fig. 4.5b demonstates this shift well. The lower $\dot{Q}_N$ sprays exhibit a less steep rise in the distribution along with a slight shelf at larger diameters before the large mode becomes prominent, accounting for as much as 10% of the volume of the spray. Increasing the atomizing air flow rate results in a much steep rise through the 10-50 μm range and a lower proportion of the spray in the larger diameter mode.

The derived parameters plotted in Fig. 4.5c quantify this effect. Here, the cumula-

tive undersize distributions of 10 and 90% show the rapid improvement in the quality of the spray. The rapid reduction in the D_{v90} at low atomizing air flow rates illustrate the reduction in the large diameter mode. Nearly an order of magnitude reduction in the D_{v90} diameter is observed over the range of the $\dot{Q}_N$. While not as rapid, a significant reduction in the D_{v10} is also observed. Examining the Span in Fig. 4.5, it can be seen that at the low flow rates, increasing $\dot{Q}_N$ results in a reduction of the Span, indicating a narrowing of the distribution. However, above approximately 11 SLPM, the Span remains relatively constant, indicating that the distribution is relatively constant in shape. This helps to describe the effect observed in Fig. 4.5a, in that the primary mode only exhibits an increase in the proportion of the spray contained in that mode while also observing a reduction in the diameter of the mode with increases in $\dot{Q}_N$ in the low range. This effect was not observed in the high range of $\dot{Q}_N$. Lastly, Fig. 4.5c also plots $D_{3,2}$. Similarly to the Span, initial increases in $\dot{Q}_N$ result in a rapid reduction in $D_{3,2}$, however increasing beyond approximately 9-10 SLPM the droplet size distribution does not exhibit as significant an improvement in the quality of the spray.

These effects have been studied in significant detail in many works, however Lefebvre provides a rigorous overview of early experimental correlations in [179]. In this work, Lefebvre details several studies using various nozzle configurations and catalogues a number of different empirical correlations. Results for pre-filming atomizers are more consistent than those of the plain-jet, however some general trends can be observed among the various correlations. Lefebvre notes that $D_{3,2}$ can be correlated to the sum of two terms. The first is dominated by inertial forces of the air stream. When viscous forces are of lower importance, the inertial and surface tension terms dominate, indicating that this first term is governed by the Weber number (defined as the ratio of the inertial to surface tension forces). This can be expressed in the

relation below:

$$\frac{\mathrm{SMD}_1}{D} \propto \frac{\text{Surface Tension Forces}}{\text{Inertial Forces}} \propto (We)^{-x} \propto \left(\frac{\sigma_L}{\rho_A \mathrm{U_R}^2 D}\right)^{0.5} \tag{4.1}$$

where D is the characteristic length of the atomizer (typically the liquid jet diameter). The exponent $x = 0.5$ is derived from fitting to experimental data.

As the viscosity is increased, a second term must be considered. This term is proportional to what has become known as the Ohnesorge number which characterizes viscous forces in relation to the square root of the inertial and surface tension forces. This yields the relationship below:

$$\frac{\mathrm{SMD}_2}{D} \propto \frac{\text{Viscous Forces}}{\sqrt{\text{Inertial} \cdot \text{Surface Tension Forces}}} \propto Oh \propto \frac{\sqrt{We}}{Re} \propto \frac{\left({U_A}^2 D \rho_L / \sigma_L\right)^{0.5}}{\left(\mathrm{U_R} D \rho_L / \mu_L\right)} \tag{4.2}$$

Wigg [180] showed that to conserve momentum between the liquid and air interaction, the relative velocity $\mathrm{U_R}$ and be written as:

$$\mathrm{U_R} = U_A / \left(1 + 1/\mathrm{M_R}\right) \tag{4.3}$$

Finally, a general expression for the droplet size distribution can be written as:

$$\frac{\mathrm{SMD}}{D} \propto \frac{\mathrm{SMD}_1 + \mathrm{SMD}_2}{D} \propto \left[\left(\frac{\sigma_L}{\rho_A {U_A}^2 D}\right)^{0.5} + \left(\frac{{\mu_L}^2}{\sigma_L \rho_L D}\right)^{0.5}\right]\left(1 + \frac{1}{\mathrm{M_R}}\right) \tag{4.4}$$

The important take away from this general analysis with regard to the influence of atomizing air flow rate is through the first order term U_A. Various researchers have empirically found this term to have a power dependence on the order of 1-1.4, however it is consistently the dominate term. Experimentally, the strong influence of $\dot{Q}_N$ on droplet size distribution is shown in Fig. 4.5. However, from the viewpoint of optimization, there is a limit to the effectiveness of $\dot{Q}_N$ on both improvement in

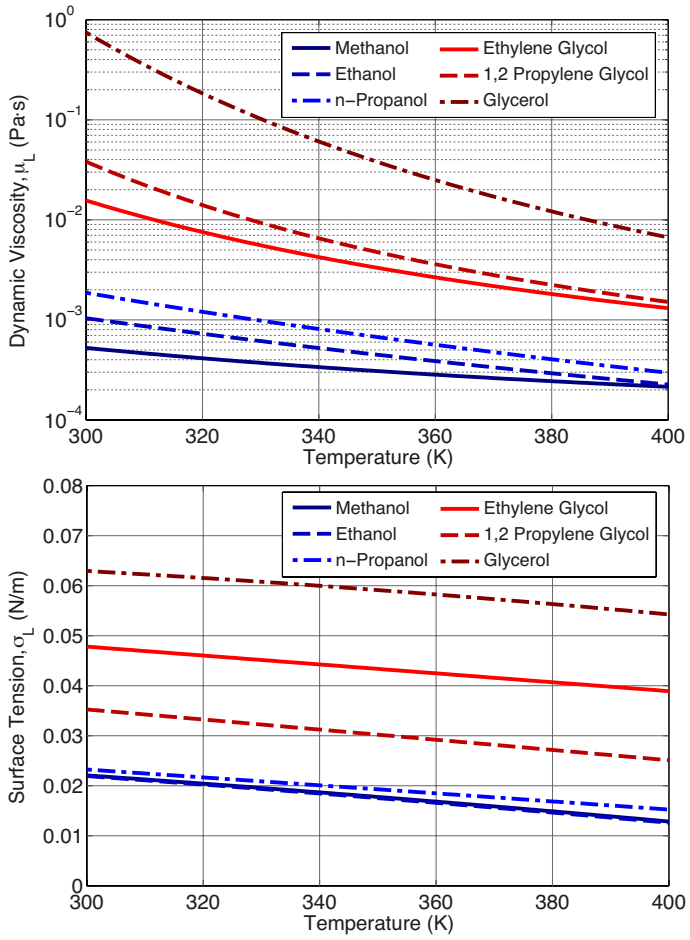

Figure 4.6: Influence of fuel preheat temperature, T_f, on dynamic viscosity, μ_L.

quality of atomization as well as the global flame structure as the spray velocity increases. This effect will be investigated in more detail in Section 5.2.1, however at this point, it will suffice to acknowledge that the highest achievable atomizing air flow rate is not necessarily the optimal rate.

4.3.3 Influence of liquid temperature

In addition to improvements through $\dot{Q}_N$, quality of atomization can be greatly influenced by several thermo-physical properties of the fuel. As can be seen in Equation 4.4, an approximate first order dependence on dynamic viscosity, μ_L, can be expected. Dynamic viscosity is most strongly influenced by the fuel preheat temper-

ature, T_f. This dependence can be seen in Fig. 4.6a. Clearly, increasing T_f results in a rapid reduction in μ_L, with the expected corresponding improvement in quality of atomization. Additionally, increasing T_f also exhibits a corresponding decreasing in surface tension, σ_L, however with a weaker dependence on T_f. Rizkalla and Lefebvre [175] note that in sprays of liquids with relatively low viscosity, when the first term of Equation 4.4 dominates, droplet sizes are primarily controlled through U_A and σ_L. However, with increasing σ_L, the second term in Equation 4.4 renders the first less significant. As a result, surface tension is generally less important in sprays of highly viscous liquids. Lastly, Lefebvre [179] notes that liquid density generally has little effect on the mean droplet size.

Care must be taken in the selection and control of T_f. The swirling combustion apparatus described in Section 2.1 is capable of heating the liquid fuel up to approximately 100°C, allowing for a degree of control of over the thermo-physical properties of a wide range of fuels. This is especially important due to the wide range of viscosities present in the fuels of interest, spanning three orders of magnitude. The influence of T_f will therefore be investigated in this section to better understand these effects.

Figure 4.7 illustrates the effect of T_f for two different $\dot{Q}_N$ in 1,2-propylene glycol sprays. Here, T_f varies between 20-60°C. In Fig. 4.7a, it can be seen that increasing T_f generally improves the quality of atomization. However, where increasing $\dot{Q}_N$ generally improves quality of atomization by shifting the distribution to smaller diameters, increasing T_f improves the atomization by narrowing the primary mode. This effect can be observed quite strongly in the reduction in the proportion of the sprays contained in the range between 70 and 120 μm and the corresponding increases in the distribution peaks at approximately 35 and 18 μm for the 9 and 15 SLPM sprays, respectively. This effect can be attributed to the ability of waves to propagate through the liquid, forming ligaments, and ultimately forming droplets. As the liquid viscosity increases, the amplitude of these propagating waves is dampened by viscous

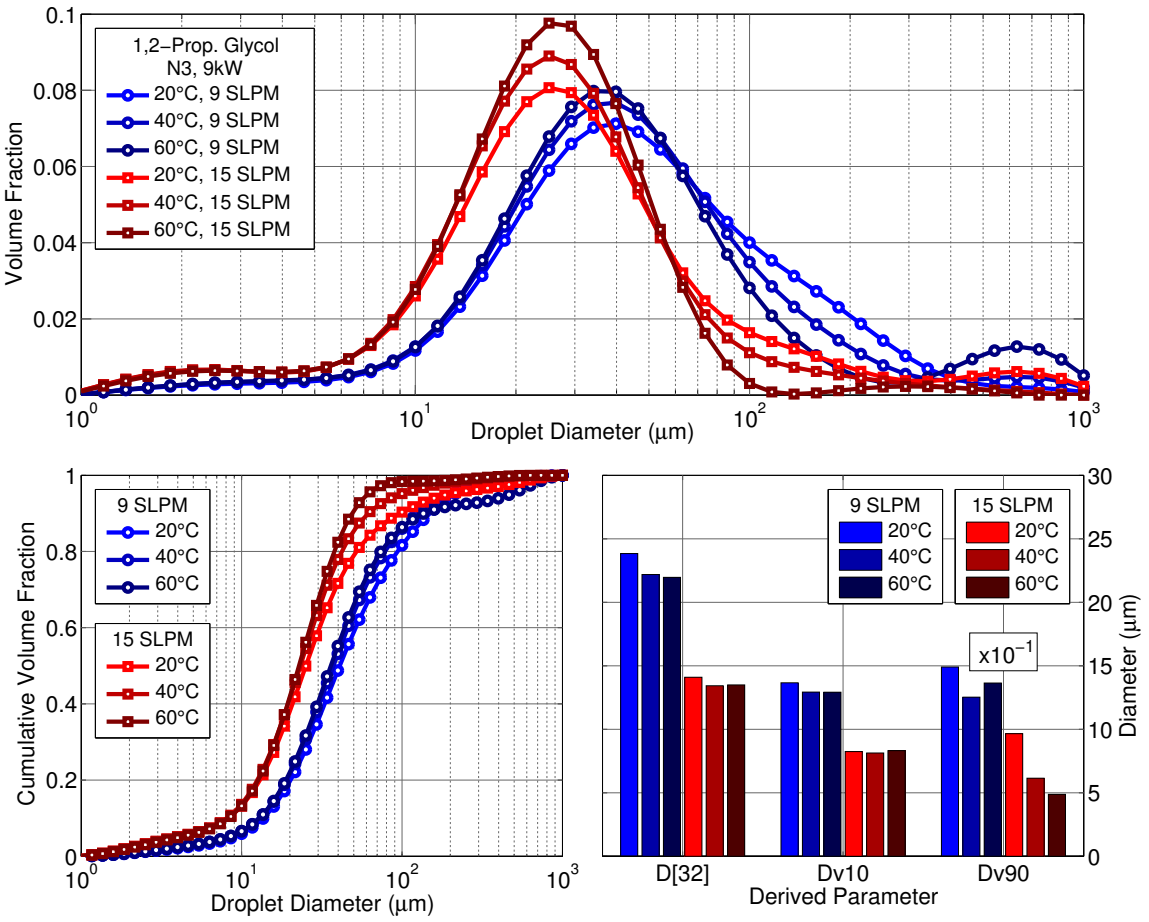

Figure 4.7: Influence of fuel preheat temperature, T_f, on dynamic viscosity, μ_L.

forces [178]. As a result, ligaments take longer to form, shifting the region in which ligaments fragment into droplets further downstream into lower velocity regions [179].

While easy to identify in Fig. 4.7a, it is easier to discern the impact of T_f in Figs. 4.7b and c. It can be seen in Fig. 4.7b that the largest influence of T_f occurs in the larger droplets. D_{v50}, i.e. the median droplet size or the size below which 50% of the spray is contained, is relatively unmoved between the different T_f. However, the distributions above D_{v50} show a definite narrowing of the distribution through a reduction in the prevalence of large droplets, especially under higher $\dot{Q}_N$ flow rates. This effect can be seen more clearly in the bar graphs of Fig. 4.7c. Here, the $D_{3,2}$ only very slightly decreases with increasing temperature (as discussed above, $D_{3,2}$ is a stronger function of U_A than T_f). Additionally, D_{v10} remains practically unchanged.

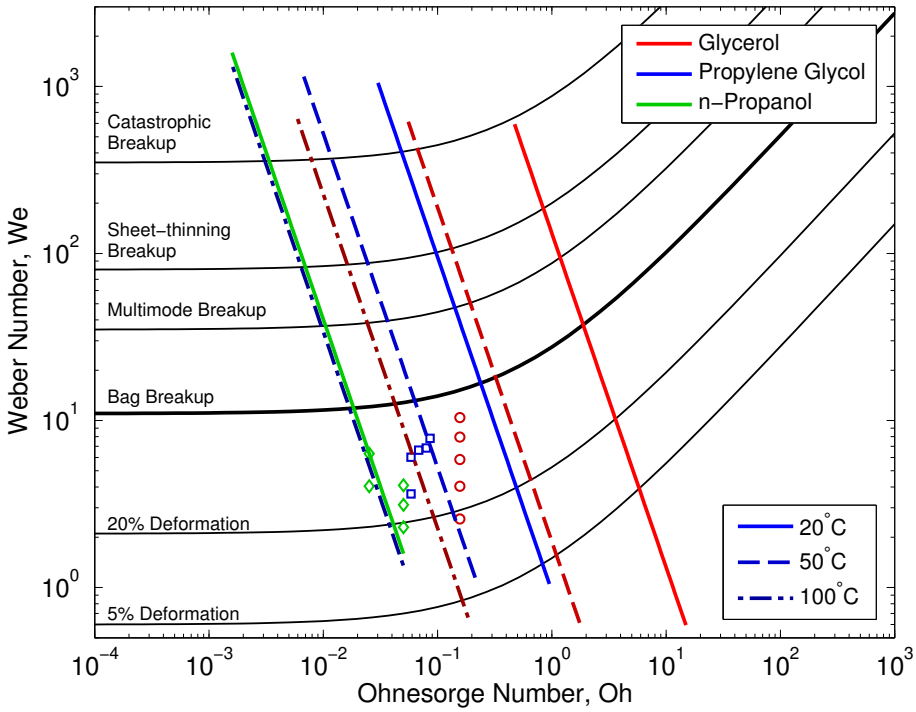

Figure 4.8: Regime diagram of secondary atomization modes, illustrating influence of fuel preheat temperature (lines) and regime locations for large diameter modes (markers).

However, D_{v90} shows a rapid decline, reducing the number of large droplets and narrowing the span.

Analysis of the secondary atomization and breakup modes can be seen in Fig. 4.8. As could also be seen in both Figs. 4.5 and 4.7, a large diameter mode can occur under relatively poor atomization conditions with a mode diameter around 600 μm. These large diameter droplets (or possibly ligaments) may proceed to breakup further in additional secondary atomization modes. These breakup modes occur at different Oh and We numbers as plotted in Fig. 4.8. Orientation in this regime can be simply described with respect to each non-dimensional number. A higher We number indicates greater aerodynamic forces compared with the droplet surface tension forces, therefore a greater likelihood of breakup and fragmentation. A higher Oh number, meanwhile, indicates a greater ratio of viscous forces to surface tension forces, resulting in a reduced chance of breakup with increasing Oh. Therefore, Fig. 4.8 can be

interpreted as droplets in the northwest corner having the greatest tendency toward secondary breakup, whereas those in the southeast corner will have the lowest tendency toward secondary breakup and are likely to combust without further breakup.

It is difficult to define a specific transition between different breakup modes, but those plotted in this figure simply show the regions near which transitions occur [181, 182], with correlations based on those of Gelfand [183]. The first major breakup mode is the Bag breakup plotted in the thicker black line, below which further breakup is either unlikely or can proceed through the vibrational modes, producing only a few additional droplets with diameters on the order of the parent [182].

The colored lines in Fig. 4.8 indicate lines of constant temperature at different droplet diameters between 100 μm and 5 mm for the C_3 fuels. Larger droplets will have a correspondingly higher We, than smaller diameter droplets. Increasing T_f results in significant shifts to lower Oh, however it can be seen that at $Oh < 1$ breakup transitions become primarily determined by the We.

Estimating Oh and We for the large diameter modes for the C_3 fuels, and plotting the location in the regime diagram (markers) shows the potential for the droplets contained in these large diameter modes to further breakup. The markers are plotted over a range of atomizing air flow rates, with higher flow rates yielding greater relative velocities between the droplet and gas streams and correspondingly higher We. It appears unlikely that the droplets in these large diameter modes will experience further breakup beyond the measurement region. Firstly, all of these large modes are below the bag breakup mode, so any secondary atomization is limited to the vibrational modes and fragmentation into only a few droplets with diameters of near the same order. Secondly, with $Oh \sim 1$, increasingly the T_f shifts to lower Oh but only slightly increases the We. In this region, transitions in breakup modes are largely independent of Oh. A much more effective technique for minimizing the impact of the large mode is to increase the relative velocity of the droplet and increase the

We. Thirdly, increasing the atomizing air flow rate reduces the proportion of the fuel contained in the large mode and shifts toward the primary mode. The net result of all these effects is that in the following combustion experiments, the large mode is a relatively small proportion of the total fuel and that the large droplets which are formed are not likely to further breakup into smaller droplets, but rather combust at their measured sizes.

4.4 Conclusions

The objective of this chapter was to investigate the characteristics of the liquid spray under a range of operating conditions and assess the impact of changing these parameters on the droplet size distribution. In the pursuit of this objective, an experimental apparatus was constructed to capture the cold flow spray and conduct measurements of droplet size distributions via a Malvern Spraytec aerosol and particle size analyzer. The impact of the nozzle size and turndown ratio of two commercially available air atomizing nozzles was examined, followed by the influence of the atomizing air flow rate $\dot{Q}_N$, and the liquid preheat temperature T_f.

Each of these parameters demonstrated a unique influence on the spray. Decreasing the fuel flow below the nominal flow rate of the nozzle greatly reduced the quality of the atomization due to unsteady siphoning effects. Meanwhile increasing above the nominal flow rate resulted in minor improvements in the quality of atomization while eliminating the unsteady siphoning effect. The greatest impact on quality of atomization was clearly achieved through increases in $\dot{Q}_N$. While there is a limit to the effectiveness of increasing $\dot{Q}_N$, in the typical range of flow rates expected for these experiments, significant improvements to the droplet size distribution were achieved through the narrowing of the distribution, a shift to subsequently smaller droplet diameter modes, and reductions in the presence of larger droplets. However, care

must be taken to limit $\dot{Q}_N$ to values below those which would lift off or blow out the swirling flame under experimental conditions. Lastly, the influence of the fuel preheat temperature T_f was observed. While less pronounced than $\dot{Q}_N$, increasing T_f does exhibit the beneficial effect of reducing the prevalence of larger diameter droplets without needing to continue to increase $\dot{Q}_N$.

The objective of the following chapter will be to utilize the knowledge of the effects of these atomization parameters to influence the rate of fuel vaporization of a wide range of liquid fuels. When coupled with the control of the mixing characteristics of the swirling flame, isolation of unique fuel effects can be achieved and will be presented in the following chapter.

Chapter 5

Experimental measurements of mean flame temperatures and global NO emissions in swirling spray flames of poly-alcohol fuels

With an understanding of the influence of atomizing air flow rate, $\dot{Q}_N$, and fuel preheat temperature, T_f, on droplet size distributions for the wide range of conditions and fuels explored in the previous chapter, the next objective is to explore how these and other parameters can be used to control the flame shape and formation of NO_X emissions in the swirling liquid spray burner. This burner was introduced in Section 2.1 and was the basis for the emissions experiments of Chapter 3. It should be noted that, from an experimental stand point, the combustion of some of these fuels (particularly the diols and triol) is non-trivial. Attempting to convert these fuels into the gaseous phase in a stable and well-characterized manner is extremely difficult due to very low vapor pressures, coupled with high boiling points and low smoke point temperatures. Therefore it becomes necessary to atomize the fuel directly into the flame. This precludes the use of most simple, well-characterized burner geometries

which would be preferable to the more complicated combustion physics inherent in a swirling spray flame. However, with careful control of the boundary conditions it is possible to gain some qualitative insight into the fuel effects. Chapters 7–9 will be devoted to experiments in more canonical premixed flame configurations utilizing fuels which are more readily vaporized.

In this chapter, experiments will be conducted to explore the influence of various boundary conditions on the mean flame temperature profiles throughout the primary combustion region, along with corresponding measurements of global NO_X formation. Sections 5.2.1 and 5.2.2 will investigate the influence of $\dot{Q}_N$ and S_g on flame shape and maximum mean temperatures. Section 5.3 will then attempt to match the flame temperature profiles of all the fuels. Comparisons of NO formation in these matched temperature profiles will allow for a qualitative comparison of non-thermal differences in NO_X formation between each of the fuels.

5.1 Experimental setup

The fuels of interest in this work are the one to three carbon alcohols: methanol, ethanol, and n-propanol, respectively; two diols: ethylene glycol (ethane-1,2-diol) and propylene glycol (propane-1,2-diol) with two and three carbon atoms, respectively; and one triol: glycerol (propane-1,2,3-triol). This matrix allows for the variation of the structure of the molecule from 1-3 carbons and from 1-3 hydroxyl groups. A consequence of such varied molecular structure is the wide variability is thermo-physical properties of these fuels. Table 5.1 shows a number of thermo-physical properties taken from the Design Institute for Physical Properties (DIPPR) Project 801 database of thermo-physical and environmental properties, maintained by the American Institute of Chemical Engineers (AIChE) [1]. As can be seen from the table, the fuel-bound oxygen concentration varies from 26% to over 50% by mass.

Table 5.1: Thermo-physical properties of fuels from DIPPR database [1]

Properties	Units	Methanol	Ethanol	n-Propanol
Carbon Atoms	#	1	2	3
Hydrogen Atoms	#	4	6	8
Oxygen Atoms	#	1	1	1
Molecular Weight	g/mole	32	46	60
Fuel-Bound Oxygen (mass)	%	50	34.8	26.7
OH/C Ratio	-	1	0.5	0.33
A/F_{ST}	-	6.44	8.95	10.30
Energy Density	kJ/g	19.9	26.8	33.6
Boiling Point	°C	64.6	78.3	96.5
Autoignition Temperature	°C	463.9	422.9	413.0
Density (25°C)	g/mL	0.791	0.789	0.803
Dynamic Viscosity (25°C)	cP	0.538	1.077	1.950
Surface Tension (25°C)	N/m	0.0222	0.0221	0.0234
Properties	Units	Ethylene Glycol	Propylene Glycol	Glycerol
Carbon Atoms	#	2	3	3
Hydrogen Atoms	#	6	8	8
Oxygen Atoms	#	2	2	3
Molecular Weight	g/mole	62	76	92
Fuel-Bound Oxygen (mass)	%	51.6	42.1	52.2
OH/C Ratio	-	1	0.66	1
A/F_{ST}	-	5.54	7.23	5.22
Energy Density	kJ/g	17.1	21.7	16.1
Boiling Point	°C	197.0	186.1	287.9
Autoignition Temperature	°C	400	420.9	370
Density (25°C)	g/mL	1.113	1.036	1.261
Dynamic Viscosity (25°C)	cP	16.868	42.48	866.3
Surface Tension (25°C)	N/m	0.0480	0.0355	0.0631

Additionally, the ratio of hydroxyl groups to carbon atoms (OH/C ratio) varies from 1/3 to 1/1. It is also interesting to note that the energy densities for the fuels can be relatively low and vary greatly between the fuels. Lastly, it is important to note the significant differences in boiling point, viscosity, and surface tension for each of these fuels as these properties greatly affect the droplet size distribution and vaporization.

Throughout this chapter, several parameters are held constant across all the experiments. Table 5.2 lists these parameters. There are several considerations from this table which deserve further discussion. As can be seen in Table 5.1, there can be significant variability in the energy density due to the changing fuel-bound oxygen concentrations (16.0-30.7 MJ/kg). It was therefore deemed better to hold the firing rate constant and vary the fuel mass flow rate, $\dot{m}_f$, to compensate for the difference in energy densities. This results in approximately a factor of 2 difference in mass flow

Table 5.2: Constant Conditions for Poly-Alcohol Swirling Spray Flames

	(Units)	Conditions
Firing Rate	(kW)	9
ϕ_g	(-)	0.8
Nozzle	(#)	SN609-3
$\dot{m}_f$ at 9 kW	(g/min)	
Methanol	-	27.1
Ethanol	-	20.1
n-Propanol	-	16.1
Ethylene Glycol	-	31.6
1,2-Propylene Glycol	-	24.9
Glycerol	-	33.5

rates from the lowest (n-propanol) to the highest (glycerol). The global equivalence ratio was also held at a constant value of $\phi_g = 0.8$. This equivalence ratio was chosen as a globally lean flame to allow for complete combustion to occur and to avoid nearing the differing lean blowout limits for each fuel. It should be recognized however, that while globally lean, combustion throughout the chamber will occur under a wider range of local equivalence ratios due to variable vaporization rates and mixing conditions. However, through the control of the swirl number, atomizing air flow rate, and initial fuel temperature while allowing for difference in the thermo-physical properties of each fuel (i.e. volatility, surface tension, viscosity, etc.), one can exert a modicum of control over of the shape and temperatures of the flame.

Sections 5.2.1 and 5.2.2 will investigate two of the primary means of control through $\dot{Q}_N$ and S_g. Table 5.3 summarizes the conditions over which the influence of each parameter will be investigated. Exp.1 will examine increasing $\dot{Q}_N$ under both a

Table 5.3: Conditions for Investigations of Mean Temperature Profiles

Variable	Exp. 1a	Exp. 1b	Exp. 2
Fuel	Propylene Glycol	Glycerol	Propylene Glycol
T_f	60°C	80°C	60°C
$\dot{Q}_N$	**6-10 SLPM**	**14-18 SLPM**	9 SLPM
S_g	1.5	3.8	**1.40-1.55**

Figure 5.1: Diagram of translating thermocouple rake and positioning relative to the combustion chamber.

relatively low and high flow conditions and constant S_g. Exp.2 will then examine the influence of S_g while maintaining a constant $\dot{Q}_N$.

5.1.1 In-flame thermocouple measurements

Temperature measurements were made using a rake of size 0.125 mm diameter bare wire type-R thermocouples (Pt-Pt/Rh 13%), spaced 12.7 mm apart as shown in Fig. 5.1. Due to the high interior wall temperatures, the measured temperatures were left uncorrected for radiative losses. A 0.125 mm diameter thermocouple is too large to allow for temporal resolution of high frequency temperature fluctuations, however the objective is simply to evaluate the spatial variations of the mean temperature profile. For most of the flames of interest, the total combustion air flow rates, $\dot{Q}_T$, and temperatures are very close; therefore it is reasonable to assume differences in the fluctuations in measured temperature due to turbulent fluctuations and mixing of the flame with cooler surrounding gases between each of the flames of differing fuels at

similar conditions to be relatively small, allowing for a relatively slow measurement of the mean temperature.

This rake of thermocouples is mounted on a linear translation stage, capable of 72 mm of radial translation from the centerline. The axial position can also be translated 6.35 mm, allowing for a measurement window of 72 mm×70 mm. This measurement region begins 22 mm downstream of the tip of the fuel nozzle and is assumed axisymmetric.

5.1.2 Global species concentration measurements

Exhaust gas emissions were measured using a bank of California Analytical Instruments analyzers as described in Section 2.5. All sample gases were collected through a quartz probe positioned downstream of the exit of the combustion chamber using a diagram sample pump. Sample gases were cooled, dried, and filtered before analysis. NO/NO_2 analysis was conducted using a CAI Model 650 chemiluminescent detector (CLD) while CO/CO_2 analysis was conducted using a CAI Model 603 non-dispersive infrared detector (NDIR).

5.2 Control of flame shape

As previously mentioned, the objective of this section is to gain insight into the effects of variations of $\dot{Q}_N$ and S_g on the overall flame shape, and more particularly, on the temperature profile throughout the combustion region. Intuitively, these two parameters will tend to have opposing effects on the recirculation and mixing within the combustion region. Chen et al. [110] investigated a series of swirl stabilized flames with an axially oriented fuel jet positioned on the centerline. They observed a transition in flame shape as the ratio between the fuel jet momentum to the momentum of the centerline reverse flow, which is due to the toroidal recirculation vortex, increased.

This transition occurs between what the authors describe as "strongly recirculating flames" and "fuel-jet dominated flames".

While their work focused on gaseous fuel jets only, similar transitions were observed in the current work due to the high axial velocity of the atomizing air stream. Here, a trade off must be made between the improved quality of atomization achieved through increasing $\dot{Q}_N$ and the inevitable transition away from strongly recirculating flames. In the case of the more volatile fuels, such as n-propanol, a clearly strongly recirculating flame was easily achievable through the combination of low $\dot{Q}_N$ and high S_g. However, as the volatility of the fuel decreases (through a combination of higher boiling point temperature or higher viscosity), the $\dot{Q}_N$ necessary to achieve satisfactory atomization increases. Consequently, the fuel-jet momentum increases (generally coupled in these fuels with a corresponding increase in fuel mass flux). Therefore, to maintain a consistent flame shape, S_g must increase as well. However, S_g is limited by the geometry of the burner. The net result of these competing mechanisms is a complex interplay of effects which will be investigated further in the following sections.

5.2.1 Effect of atomizing air flow rate

In Fig. 5.2, the influence of increasing $\dot{Q}_N$ can be seen in a propylene glycol flame. In these figures, the swirl number is held constant at $S_g = 1.5$ while the atomizing air flow rate is increased from 6 to 10 SLPM. Recall from Fig. 4.5, at the low range of $\dot{Q}_N$, much of the fuel flow is shifted toward larger droplets, with subsequently larger Stokes numbers where the Stokes number is defined as:

$$Stk = \frac{\rho_L d_d^2 u_0}{18 \mu_g D} \tag{5.1}$$

where d_d is the droplet diameter, u_0 and μ_g are the local gas velocity and dynamic viscosity, respectively, and D is the characteristic length scale of the burner quarrel exit.

Droplets with higher Stokes numbers can more easily detach from the air flow; subsequently, larger droplets can more readily pass through recirculation zones, and not be entrained, or be centrifuged to the outer edges of the combustor [173, 184]. As a consequence, much of the fuel is not entrained in the lower, fuel-driven vortex as described by Feikema and Chen [110–112] as seen in the upper portion of Fig. 5.2. The temperature distribution in this figure shows that much of the heat release occurs relatively far downstream due to the weak entrainment of the droplets and slow vaprorization.

Increasing $\dot{Q}_N$ shifts the droplets to smaller size distributions - and thus lower Stokes numbers - where some of the droplets are entrained in the lower, fuel-driven vortex and combust, anchoring the flame as seen in the middle portion of Fig. 5.2. Here, the strengthening of the fuel-driven vortex can be seen with the formation of a local maximum in temperature positioned around 25 mm radially. This increased entrainment, primarily of the portion of the spray which has shifted to smaller droplets, helps to strengthen the flame and increase the temperatures in both the fuel-driven and air-driven recirculation zones.

Further increasing $\dot{Q}_N$ as shown in the lower portion of Fig. 5.2 shifts the droplet size distribution even further. Here, an even greater proportion of the fuel is entrained in the fuel vortex where it is mixed and combusted. Additionally, the overall smaller droplets result in faster evaporation and higher peak temperatures in both the fuel-driven and air-driven vortices.

However, there is a limit to the effectiveness of increasing $\dot{Q}_N$ in improving quality of atomization. As discussed in Section 4.3.2, improvements in quality of atomization experience diminishing returns. This limited improvement in the quality of atom-

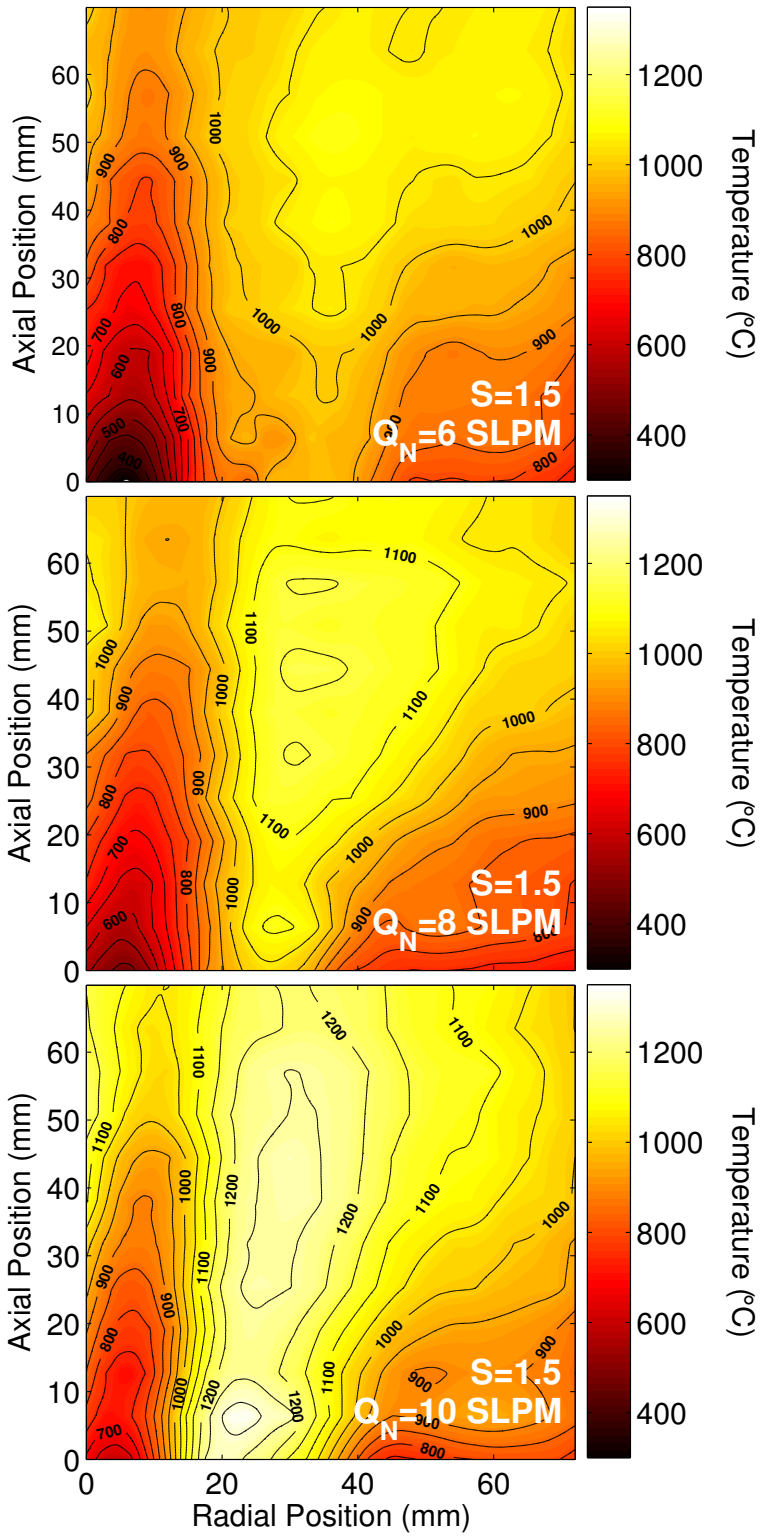

Figure 5.2: Influence of increasing $\dot{Q}_N$ when within the low range of flow rates in a propylene glycol flame.

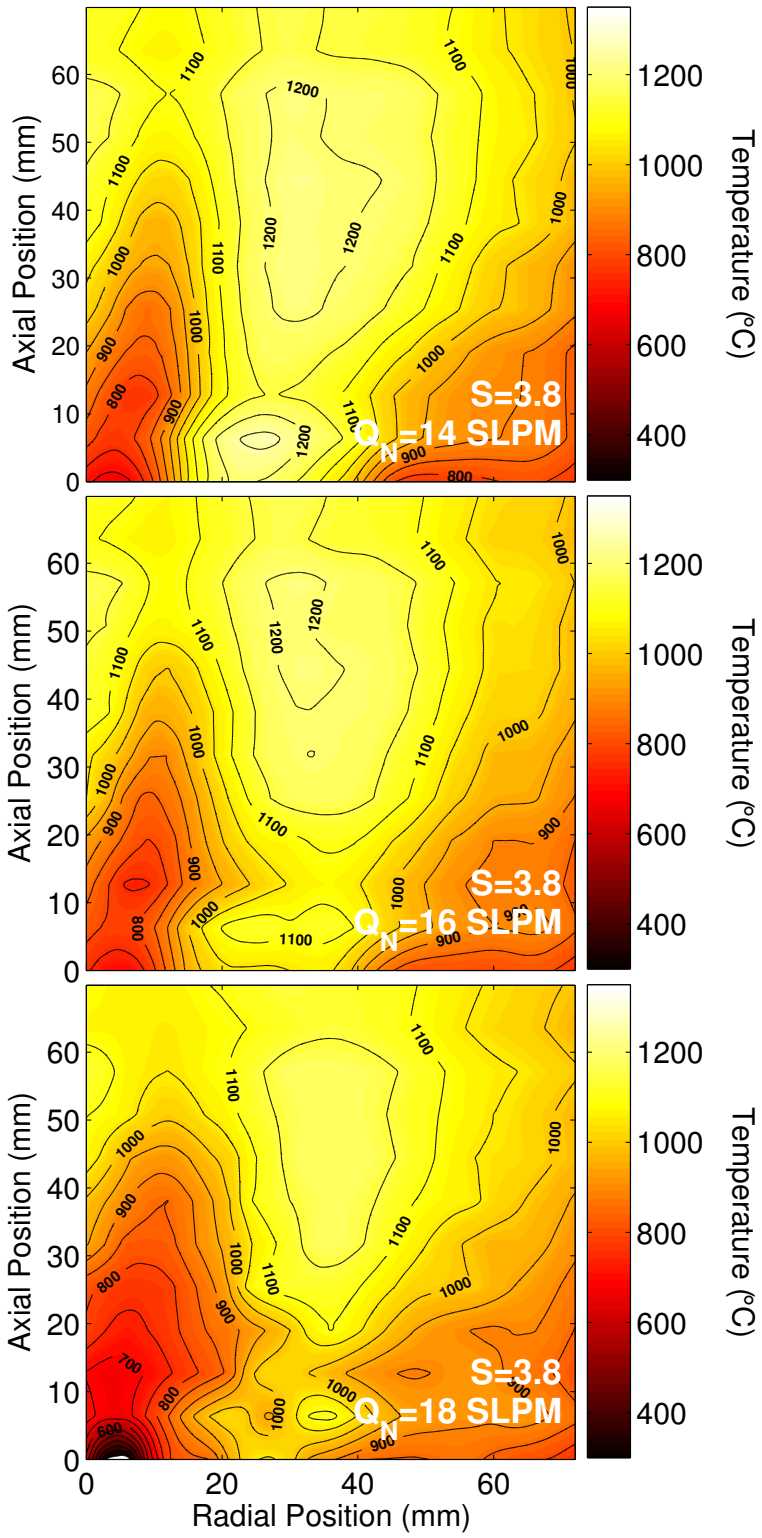

Figure 5.3: Influence of increasing $\dot{Q}_N$ when within the high range of flow rates in a glycerol flame.

ization at the expense of greater air velocities can have significant effects on the flame shape as shown in Fig. 5.3. In this figure, a series of glycerol fueled flames are examined under a relatively high swirl number of $S_g = 3.8$ with increasing $\dot{Q}_N$.

In the upper portion of Fig.5.3, the temperature distribution is qualitatively similar to the lower portion of the preceding figure. Here, the quality of atomization is already relatively high, allowing for entrainment of smaller droplets into the fuel-driven vortex, rapid vaporization, and increased mixing with the remaining droplets resulting in relatively high temperatures in both the fuel-driven and air-driven vortices.

However, due to the diminishing returns in quality of atomization, increasing $\dot{Q}_N$ as shown in the middle portion of Fig. 5.3, does not result in a significant improvement in the droplet size. However, the increased atomizing air flow does impart a greater velocity to the spray. As a consequence, Stokes numbers are increased, reducing entrainment in the fuel-driven vortex and pushing the spray further downstream. This can be seen in the lower temperatures of fuel-driven vortex.

Further increasing $\dot{Q}_N$ as shown in the lower portion of Fig. 5.3 greatly reduces the temperature and entrainment of fuel-driven vortex, pushing the flame to near-blow out. Attempting to increase $\dot{Q}_N$ much further would result in the flame lifting off and either extinguishing or anchoring above the recirculation zones similar to a lifted jet flame.

5.2.2 Effect of swirl number

As was seen in the previous section, increasing $\dot{Q}_N$ yields two separate effects: reductions in the droplet size distribution and increases in the "fuel-jet" momentum of the two-phase spray and air stream. This section is focused on observing the influence of increasing S_g. In Fig. 5.4 adapted from Chen et al. 5.4, the critical momentum ratios at which the flame transitions from the strongly-recirculating flame to a fuel-jet mo-

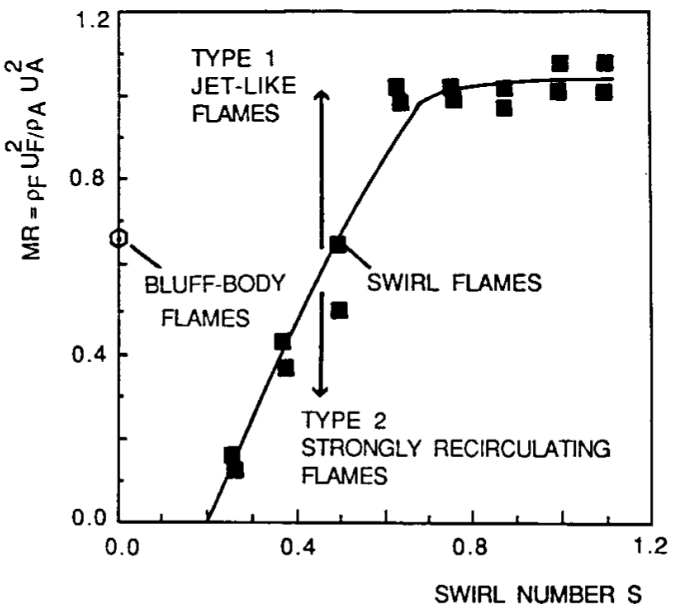

Figure 5.4: Flame shape transitions as a function of swirl number and momentum ratio. Adapted from Chen et al. [110].

mentum dominated flame is plotted. While the flames in Chen's study are not spray flames, a lot can be gleaned from this figure. What one can see is that increasing the swirl number allows for a greater momentum ratio (defined as the ratio of fuel-jet momentum to that of air) and consequently a greater $\dot{Q}_N$ before the flame transitions.

This is particularly important when burning the viscous, low energy density fuels studied here where high $\dot{Q}_N$ are required for atomization with simultaneously strong recirculation for flame stabilization. In comparison of the bottom portion of Fig. 5.2 and the top portion of Fig. 5.3, in which the temperature distributions are qualitatively similar, while $\dot{Q}_N$ and S_g are respectively 10 and 1.5 for propylene glycol and 14 and 3.8 for glycerol. The higher $\dot{Q}_N$ and S_g for glycerol are due to the reduced quality of atomization (and arguably due to higher $\dot{m}_f$ as well).

The influence of increasing S_g from 1.4 to 1.55 in propylene glycol flames under a constant $\dot{Q}_N$ can be observed in Fig. 5.5. As can be seen in the figure, increasing S_g results in a strengthening of the fuel-driven and air-driven recirculation vortices. Consequently, with the strengthening of the vortices (particularly the fuel-driven vor-

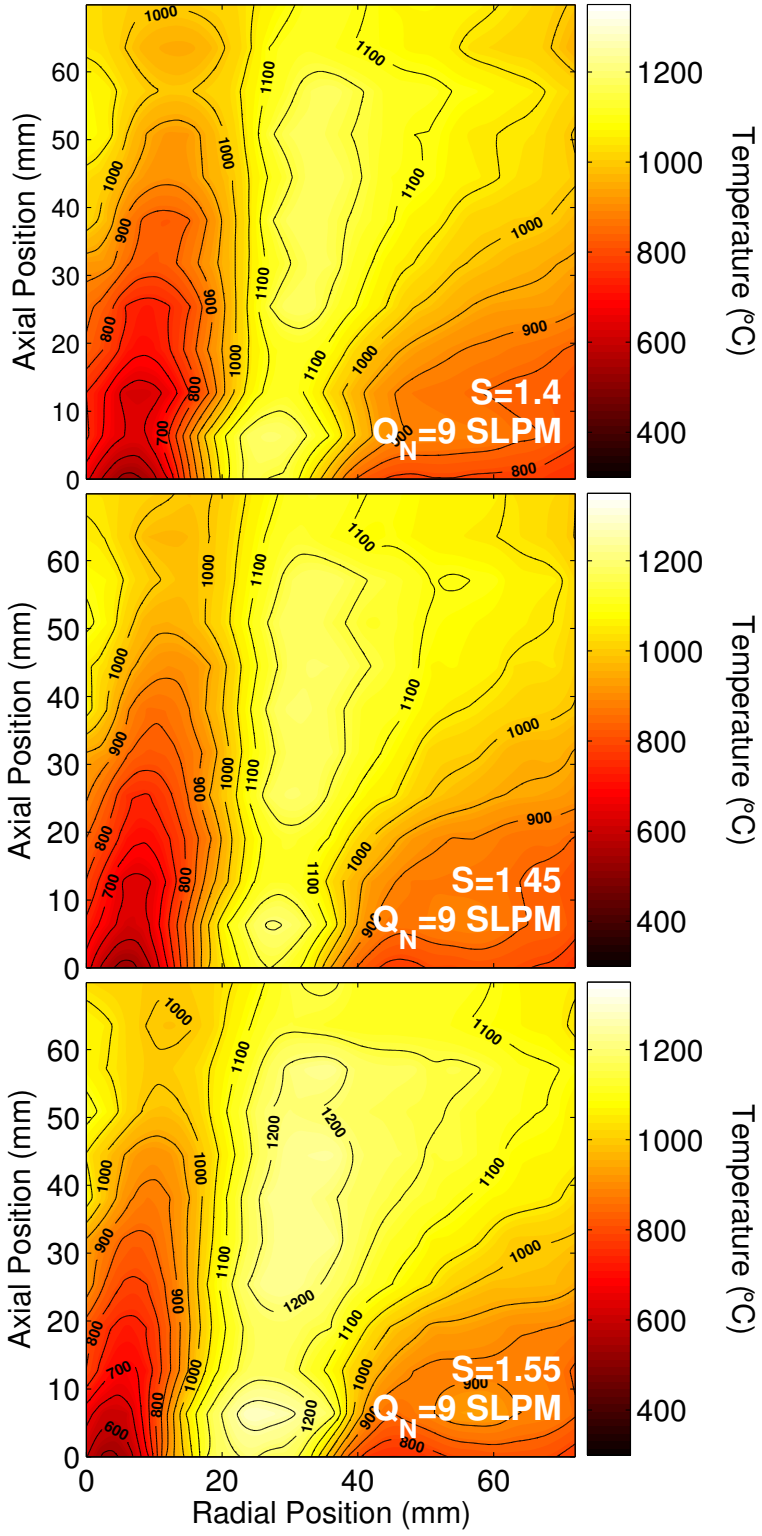

Figure 5.5: Influence of increasing S_g in a propylene glycol flame.

tex), there is greater entrainment of mid- to small- sized droplets anchoring the flame and increasing the size and peak temperature of both vortices. Additionally, stronger vortices result in increased mixing with the hot products and faster fuel vaporization. This effect can be seen in the qualitatively unchanged flame shape, however the peak flame temperatures are increasing with increasing S_g. The strengthened air-driven vortex results in a wider high temperature region near the upper portion of the vortex around 50 mm.

While not well depicted in Fig. 5.5, Hardalupas et al. [184] also observed a centrifuging effect of large droplets away from the central flame due to their higher Stokes numbers. Such effects could be of significance under very high swirl conditions, however the fuel injection and atomization in Hardalupas' work utilized a much higher radial component and poorer atomization in their fuel injection than is used here. It should be much more likely that particularly large droplets should tend to escape in the axial direction.

5.3 Matching of temperature profiles

The objective of the preceding sections has been to gain some fundamental insights into the primary mechanisms which influence the flame shape, particularly the mean flame temperatures. Clearly, the fuel preheat temperature T_f, the atomizing air flow rate $\dot{Q}_N$, and the burner geometric swirl number S_g offer tuning of the combustion dynamics. And while the influence of each parameter is not wholly distinct from the others (i.e. changing $\dot{Q}_N$ influences both droplet size distribution and momentum ratio), a significant amount of control can be exerted over the flame to allow for tailoring of the temperature field.

Therefore, it was possible through an iterative process to approximately match the measured temperature profiles with respect to each other. Thus, it was attempted

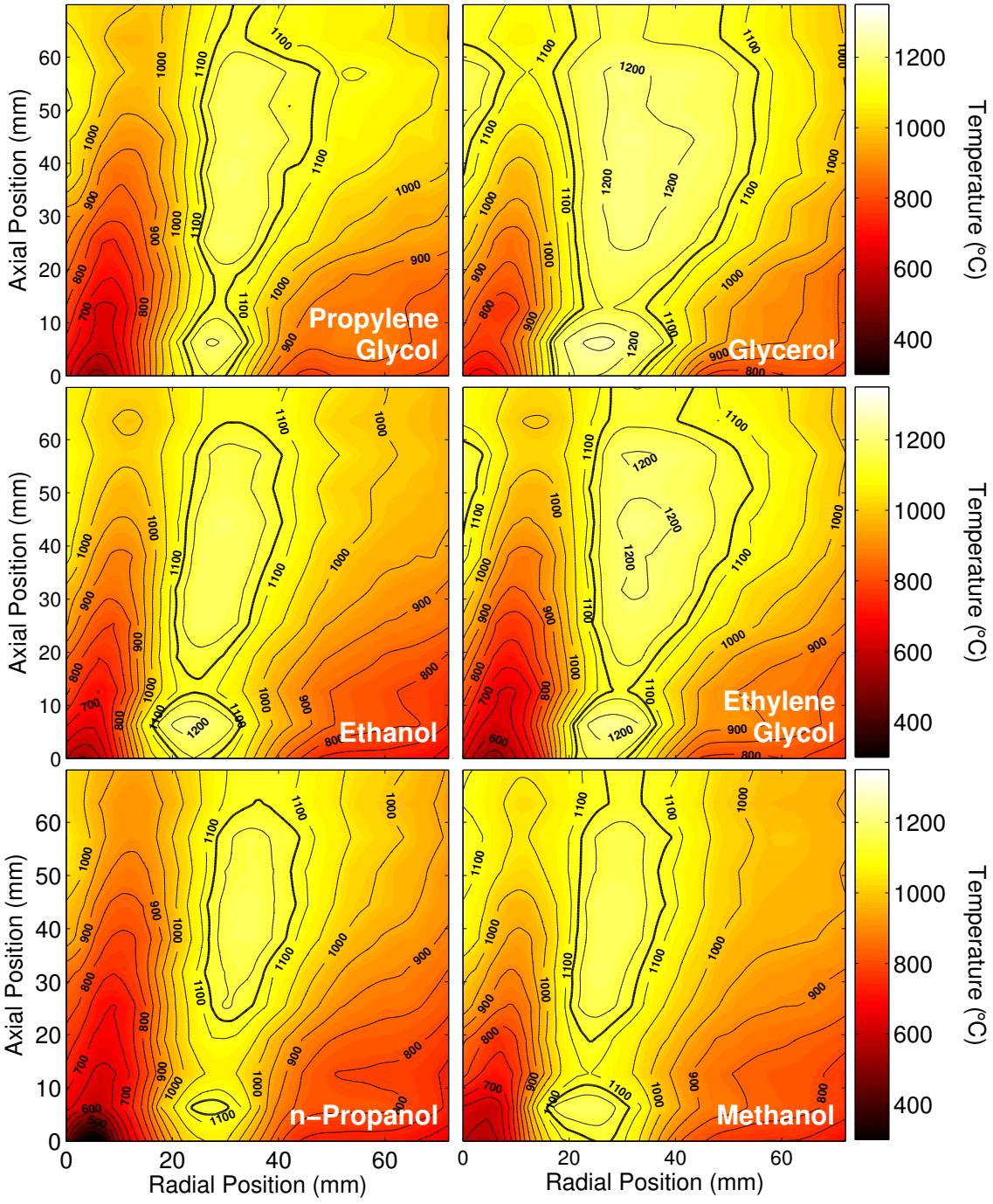

Figure 5.6: Matching temperature profiles for each of the fuels

to approximately match the vaporization rates for each of these very different fuels. Such profiles are shown in Fig. 5.6 where a thickened black contour is drawn at an arbitrary temperature of 1125°C to illustrate the general flame shape. In attempting to analyze these profiles, several additional effects need to be examined.

In requiring the firing rate and the global equivalence ratio to remain constant, the required total air flow $\dot{Q}_T$ must change. However, due to the positive correlation of higher energy densities with lower fuel-bound oxygen concentrations, which are inversely correlated with stoichiometric air/fuel ratios for these fuels, the net effect on total combustion air flow rate is minor. This results in variations of less than 2% (168 SLPM minimum to 174 SLPM maximum). Therefore, the net effect on residence times, velocities, and turbulence levels is ultimately small.

The process for the creation of Fig. 5.6 proceeded simply through an iterative selection of $\dot{Q}_N$ and S_g. The proceeding discussion helped in establishing guidelines for starting conditions for each of the fuels. From there, the two primary parameters were varied and the temperature profiles were compared. As can be seen in Fig. 5.6, the mean temperature profiles in each of the subfigures are very similar, composed of a fuel driven recirculation zone at the base of the measurement area along with an air-driven recirculation zone where the bulk of the combustion occurs. The shape of the three alcohol flames in Fig. 5.6 is remarkably similar due to their similar volatilities. The diol and triol flames have significantly lower volatilities and as a consequence exhibit wider combustion regions. Additionally, because the firing rate was maintained constant, the $\dot{m}_f$ of each of the diols is greater than the alcohols, while the triol mass flux is the highest. Notably, the mass flux of methanol is the highest of the alcohols and between that of the two diols. However, the volatility of methanol is significantly higher than either ethylene glycol of propylene glycol, therefore resulting in the narrower flame shape.

It is difficult to directly qualify how NO formation is influenced by differences

Table 5.4: Average temperature and species measurements (ppm) for conditions with matching temperature profiles

Number of Carbon Atoms		Number of Hydroxyl Groups: 1		2		3	
		n-Propanol		Propylene Glycol		Glycerol	
		T	950	T	1001	T	1068
3		NO	33.6	NO	23.3	NO	10.6
		NO_2	1.0	NO_2	1.2	NO_2	1.0
		CO	14.5	CO	13.9	CO	67.5
		Ethanol		Ethylene Glycol			
		T	996	T	1022		
2		NO	24.9	NO	14.1		
		NO_2	2.2	NO_2	1.5		
		CO	5.4	CO	38.7		
		Methanol					
		T	996				
1		NO	9.2				
		NO_2	1.6				
		CO	32.5				

in the size of the region throughout which the fuel is distributed. Generally, the volatility is inversely correlated with the energy density and mass flux, so while more fuel is spread around a greater area, the stoichiometric mole fraction of air is lower and the local equivalence ratio not as greatly affected.

Average temperatures were calculated over the entire measurement area. Additionally, measurements of NO, NO_2, and CO at the exit of the combustion were conducted. These measurements are included in Table 5.4. One can see that the mean temperatures throughout the measurement regions are reasonably close.

Of more importance, however, are the NO_X concentration measurements. It is clearly seen that the n-propanol flame produces the most NO. Increasing hydroxylation to propylene glycol and then to glycerol results in a reduction in the NO formed. Additionally, moving from n-propanol to the smaller alcohols ethanol and methanol shows the same trend. This also continues in the ethylene glycol flame. These reductions in NO formation are consistent with an increase in the fuel oxygen content as a percentage of fuel mass as shown in Table 5.1. As also shown in Table 5.4, the

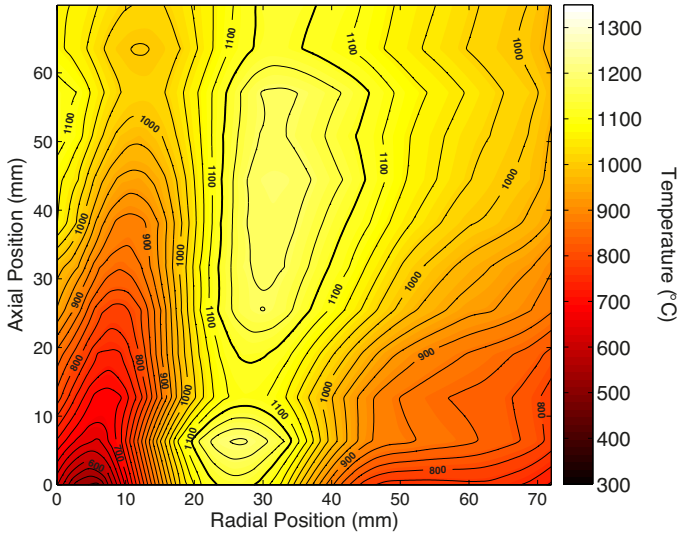

Figure 5.7: Average flame temperature for the matched temperature profiles shown in Fig. 5.6

global NO_2 formation in each of these flames is very small, and varies only slightly with each fuel. CO emissions are also reasonably low, indicating essentially complete combustion due in large part to the high temperature refractory combustion chamber.

While non-neglible global differences in the measured temperature profiles are unavoidable given the complexity of the experiment, the differences are not in opposition to the observed trends. The largest variation in global mean temperatures is from n-propanol to the fuels with OH/C ratios of unity with an absolute difference of 118 K. This trend is in opposition to the trend in NO formation (i.e. the lowest mean temperature produces the highest NO formation), thus the qualitative trend in NO is not weakened. This trend is also consistent in the comparison of fuels with the same number of carbon atoms as well as for the alcohols. However, it is difficult to draw a definitive conclusion within the family of fuels with an OH/C ratio of 1/1 (i.e. methanol, ethylene glycol, and glycerol) as the change in averaged measured temperature with respect to carbon number is non-monotonic. In total, and despite some variance in the average measured temperatures, the qualitative trends in NO formation with respect to fuel characteristics are consistent and clearly observable.

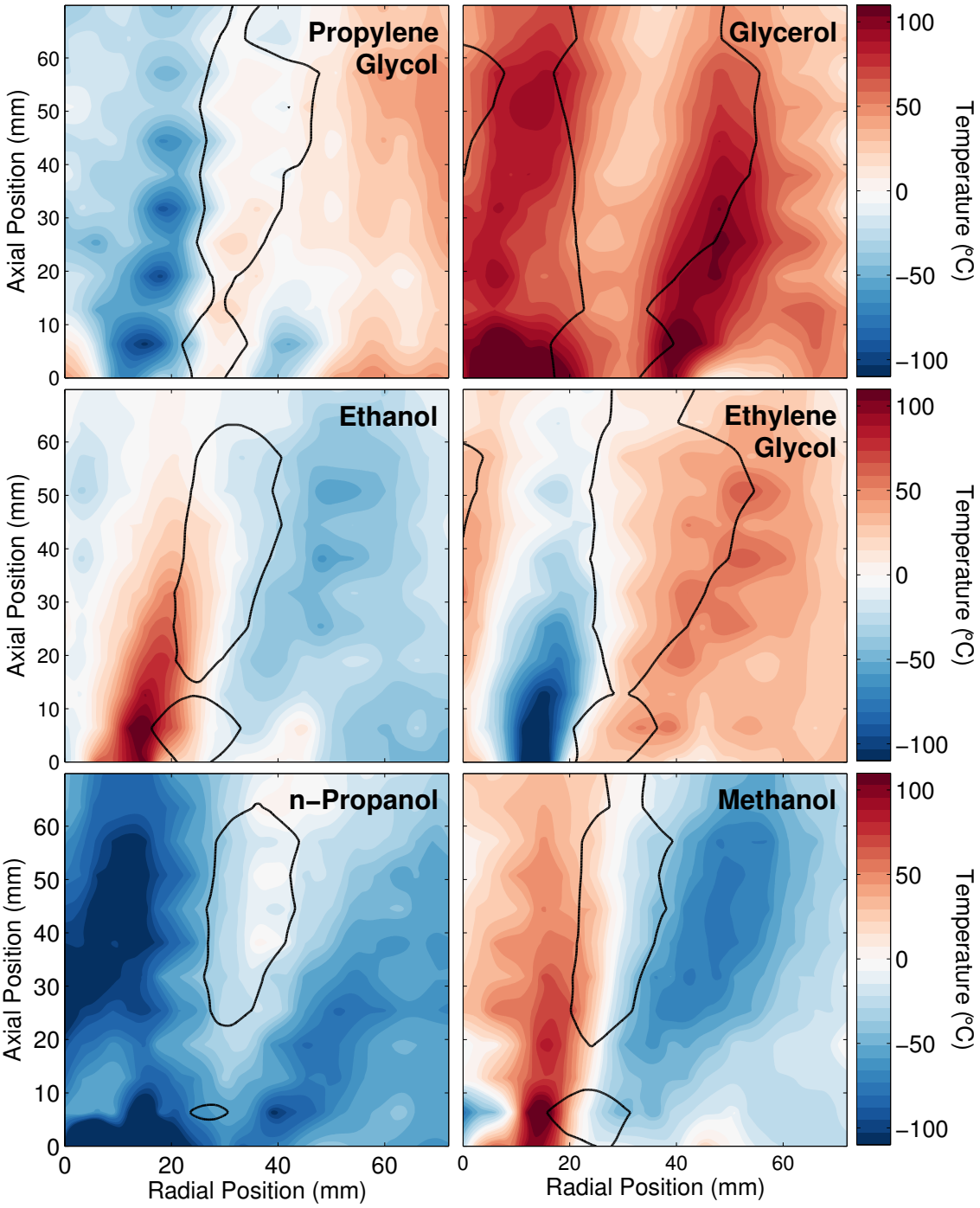

Figure 5.8: Difference from average for each of the fuels

Thus, by matching the mean temperature profiles, it is possible to isolate the effect that non-thermal NO_X formation mechanisms have on the total NO_X formation for the varying fuels.

Figure 5.7 shows the averaged temperature profile from the six fuels (i.e. the six subfigures shown in Fig. 5.6 averaged together). Again, this averaged temperature contour is very similar to the contours for the individual fuels. Further analysis can be done by subtracting the average temperature profile shown in Fig. 5.7 from the individual profiles to determine the regions within the combustor where the temperature deviates from the average. These results are shown in Fig. 5.8. In each subfigure the same high temperature region is indicated with the thick contour line. Regions shaded blue indicate temperatures below the average while regions shaded red are higher than the average. In these figures, the high temperature regions within the contour show only small deviations from the mean. The broader high temperature regions in the polyol flames can be seen in the higher than average temperatures on the outer edge of the contour. Additionally, the lower NO formation in the glycerol and ethylene glycol flames is clearly not due to lower overall temperatures, as the majority of the deviation in temperature is greater than the average indicated by the red regions inside the black contours (indicating regions in excess of 1125°C).

The trends in NO formation with respect to the fuel properties are summarized in Fig. 5.9. This figure illustrates the mean flame temperature across the top. Also included is the fuel bound oxygen concentration and NO concentration, as well as the ratio of OH groups to carbon atoms for each fuel at the top of each bar. It is clear that there is relatively little variation in the mean flame temperature, and that the observed decrease in mean temperatures is in opposition to the increase in NO formation, indicating that the observed trend in reducing non-thermal NO_X formation may be stronger than measured. It can also be seen that there is a monotonic decrease in the measured NO concentrations with respect to the OH/C and a consistent increase in

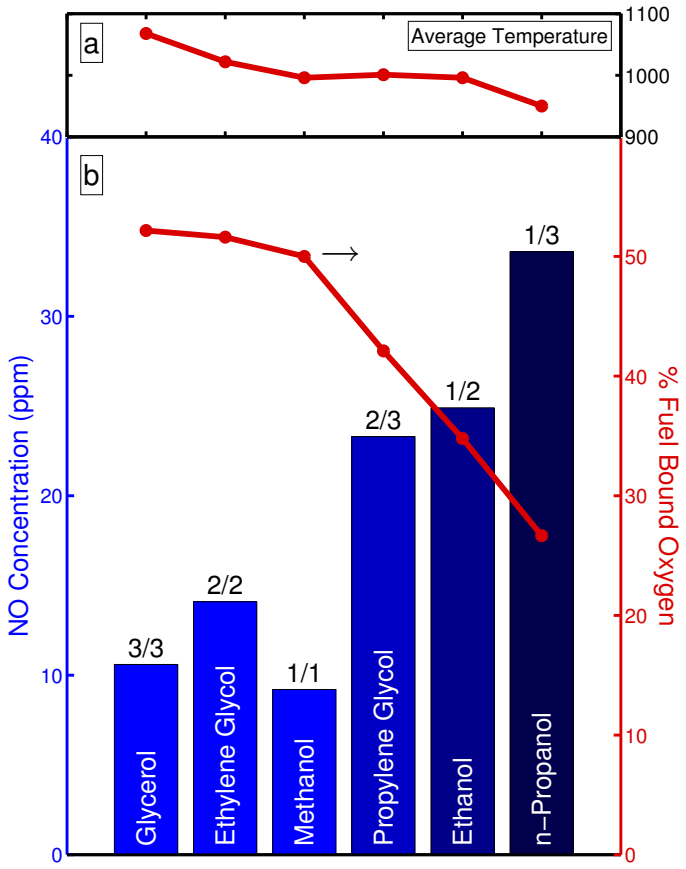

Figure 5.9: Summary of trends in NO formation with fuel properties with a) average temperature and b) NO concentration and fuel bound oxygen concentrations

NO with a decrease in the fuel bound oxygen concentration. There are also consistent trends between families with increasing carbon number corresponding to an increase in NO:

$$[\mathrm{NO}]_{\mathrm{Methanol}} < [\mathrm{NO}]_{\mathrm{Ethanol}} < [\mathrm{NO}]_{\mathrm{n\text{-}Propanol}}$$

$$[\mathrm{NO}]_{\mathrm{Ethylene\ Glycol}} < [\mathrm{NO}]_{\mathrm{Propylene\ Glycol}}$$

This indicates that the structure of the fuel does indeed play a significant role in the formation rates of NO.

5.4 Conclusions

The objective of this chapter was to determine whether an idealized set of conditions could be selected for the comparison of the differences in NO_X formation for these alcohol and poly-alcohol fuels. To achieve this objective, the knowledge gained in Chapter 4 was coupled with a parameter study of the influence of $\dot{Q}_N$ and S_g on flame shape and mean flame temperatures as measured with a translating rake of thermocouples. It was observed that $\dot{Q}_N$ has a strong influence on the flame shape, peak flame temperatures, and prominence of the fuel-driven and air-driven vortices in the flame. It was also observed that S_g has a strong influence on entrainment of droplets in the regions anchoring the flame as well as the maximum $\dot{Q}_N$ flow rates achievable.

It was also observed that, through the careful selection of boundary conditions and implementation of an iterative selection process, it was possible to limit variations in the flame shape and temperature profiles. By effectively matching the temperature distribution throughout the combustion region, the contribution to NO_X through the thermal mechanism was effectively matched for all the fuels, thus allowing comparisons of the fuel's influence on the formation of NO_X through non-thermal mechanisms. It was observed that NO concentrations were strongly dependent on the degree of oxygenation, whereby NO was inversely proportional to fuel bound oxygen concentration. It was also observed that this effect was consistent across constant OH/C ratios, i.e. methanol, ethylene glycol, and glycerol, all of which showed similar NO formation rates. An increase in NO was observed as OH/C was reduced through propylene glycol, ethanol, and n-propanol with OH/C ratios of 2/3, 1/2, and 1/3, respectively.

Chapter 6

Reaction path analysis of poly-alcohol decomposition pathways

In conjunction with the previous chapter, this chapter investigates differences in NO_X formation and fuel decomposition pathways as a function of the fuel molecular structure. The previous chapter showed experimentally that with approximately matched temperature fields - thus approximately matched contributions to thermal NO_X - variations in the non-thermal NO_X mechanisms could be observed. These variations are reasonably attributable to fuel chemistry effects. Therefore, this chapter will attempt to gain further insight into the roles that differing fuel decomposition pathways play in the formation of NO_X through detailed reaction path analyses.

Unfortunately, due to the significant modeling complexity inherent in a swirling, two-phase, turbulent, liquid spray flame it is unfeasible to attempt to replicate these complex physics. Rather, a greatly simplified strategy will be implemented utilizing a 0-D perfectly stirred reaction simulation parameter study spanning the range of temperatures and equivalence ratios expected in the flame, utilizing a comprehensive kinetic model for C1-C3 alcohols which has been extended to include poly-alcohol

Table 6.1: Perfectly Stirred Reactor parameter study

Parameter	(Units)	Values
Temperature	(°C)	1700, 1400, 1100, 800
Equivalence ratio, ϕ_g	(-)	$0.4 \leq \phi \leq 1.5$
Residence Time	(s)	1
Pressure	(atm_g)	1

decomposition pathways through analogy. The objective of this simulation is not to provide quantitative predictions of NO formation, but to allow for qualitative observations of the influence of these parameters on NO_X formation in Section 6.2 and the fuel decomposition pathways in Section 6.3.

6.1 Perfectly stirred reaction simulations

Simulations were conducted in CHEMKIN-Pro [185] utilizing the Perfectly Stirred Reactor module. For each fuel and fixed gas temperature, a transient solver parameter study was conducted until a steady state solution was achieved for a range of equivalence ratios and a fixed residence time as shown in Table 6.1. One second was chosen as a representative residence time based on flow rates, swirl number, temperature, and burner geometry. Mean temperatures in the measurements of Section 5.3 were in the range of 1100°C, therefore simulations were permuted around the mean temperature and at an elevated temperature of 1700°C. The local equivalence ratio throughout the burner is expected to vary widely between extremely lean and extremely rich, therefore simulations were conducted in a fairly wide equivalence ratio range.

6.1.1 Polyalcohol chemical kinetic mechanism

A chemical kinetic model was specifically developed to elucidate the effects of fuel molecule structure on decomposition products and NO_X formation during the com-

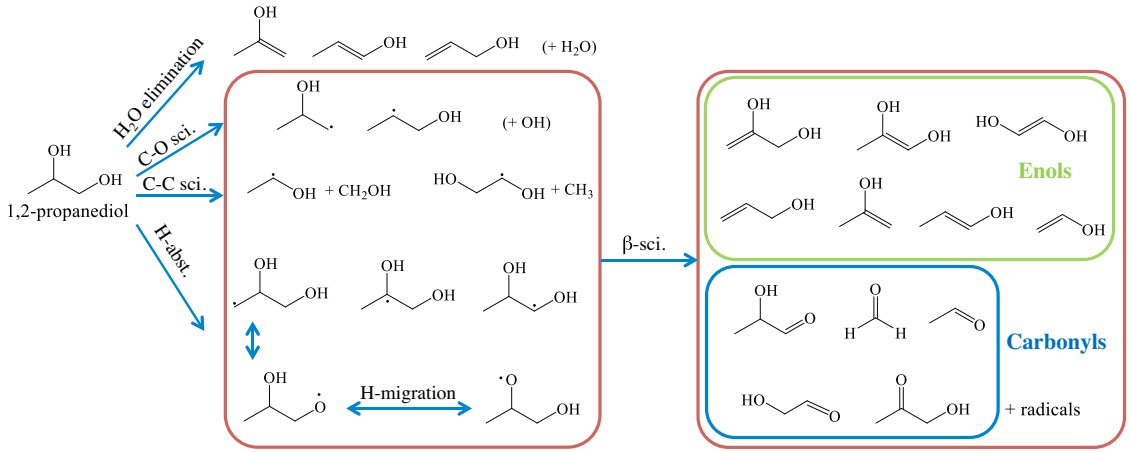

Figure 6.1: Example scheme of 1,2-propanediol high-temperature degradation pathways

bustion of hydroxylated fuels. The primary target of the chemical kinetic model was the accurate prediction of hydrocarbon intermediates that participate in non-thermal NO_X formation reactions. Acknowledgement must be given to Dr. Mariam Al Rashidi for the development of this mechanism.

The model includes high temperature combustion reactions for all the investigated fuels. The basis of the model is the comprehensive chemical kinetic model for the C_1-C_3 alcohols of Sarathy et al. [59], which includes methanol and ethanol submechanisms from Metcalfe et al.'s AramcoMech 1.3 [186]. To this basis, the poly-alcohol combustion reactions developed for this study were added. Following previous work on alcohols [59, 187, 188], the high temperature reaction classes, namely unimolecular decomposition, H-abstraction, H-migration, and β-scission were included for each poly-alcohol.

Figure 6.1 illustrates a sample of the included decomposition pathways for 1,2-propylene glycol. All possible reaction pathways were considered and the rate parameters were estimated based on those of analogous alcohols. As shown in Fig. 6.1, the unimolecular decomposition routes comprise H_2O-elimination, as well as C-O and C-C bond scission reactions, the rates of which were estimated by analogy with ethanol, n-propanol, and iso-propanol. In the case of hydrogen abstraction, H, OH, O_2, HO_2,

and CH_3 were considered as abstracting species, and abstractions from both alkyl and hydroxyl groups were taken into account.

Only 5-membered ring transition state H-migration reactions (i.e., isomerizations) of the alkyl and alkoxy radicals were included. Reactions involving smaller transition state rings have high energy barriers, and thus were neglected; whereas those involving larger rings are not possible for the investigated compounds.

All β-scission pathways for fuel radicals were accounted for in the mechanism, including C-C, C-O, and C-H scissions. These reactions produce enols or carbonyl compounds and were written in the exothermic direction, i.e., radical addition to an unsaturated bond, as describe by Curran et al. [188, 189]. The enols were further degrade via unimolecular decomposition and H-abstraction or addition followed by scission of the radicals. Keto/enol tautomerization and radical-assisted isomerization reactions were also included in the model [59, 187, 188]. Meanwhile, the carbonyls were degraded via H-abstraction, preferably from the aldehydic group when possible, followed by dissociation to CO+alkyl radical.

Thermodynamic properties of the implicated species were determined by group additivity using Ritter and Bozzelli's program THERM [190].

6.1.2 NO_X sub-mechanism

In order to simulate NO_X formation during the combustion of the investigated alcohols and poly-alcohols, thermal and non-thermal NO_X chemistry was incorporated into the reaction mechanism. The NO_X sub-mechanism includes all relevant N-containing reactions of GRI-Mech 3.0 [191], Dagaut et al. [18], and Gimenez-López et al. [192], including mechanisms for: thermal NO, prompt NO, N_2O, NNH, nitro-hydrocarbons, and nitroso-compounds.

The prompt-initiating reaction of Fenimore [10, 13] used in the GRI-Mech 3.0

shown in reaction 6.1 has been shown to be spin forbidden by Moskaleva and Lin [17].

$$CH + N_2 \rightleftharpoons HCN + N \tag{6.1}$$

Therefore reaction 6.1 has been replaced with reaction 6.2, which has been shown to be a more appropriate prompt initiating reaction [18]

$$CH + N_2 \rightleftharpoons NCN + H \tag{6.2}$$

Rates for this reaction and the NCN sub-mechanism are from Gimenez-López et al. [192]. It has been shown that even after replacing the HCN initiating reaction with the NCN reaction, HCN remains a significant contributor to NO formation [18, 22]. A more detailed discussion of the various NO formation and consumption reactions is included in Section 6.2.

6.2 NO formation

The concentration of NO at the exit of the PSR is shown in Fig. 6.2. It is immediately clear that at the highest temperature of 1700°C, NO formation is dominated by the thermal mechanism [6]. The increase in NO formation with decreasing ϕ_g is due to the fixed temperature of the PSR coupled with both the increasing nitrogen content and the increasing availability of O atom concurrent with decreasing equivalence ratios. This also contributes to the steep reduction of NO in the rich region.

At 1400°C and 1100°C, NO peaks around $\phi_g = 1$ and trails off to the rich and lean sides. It is very interesting to note that NO formation predicted between 1100°C and 1400°C is within the same order of magnitude measured for the matching temperature profiles of Section 5.3 and NO in Table 5.4. This does not serve to validate the accuracy of the mechanism or its predictive capability, but it does help to give

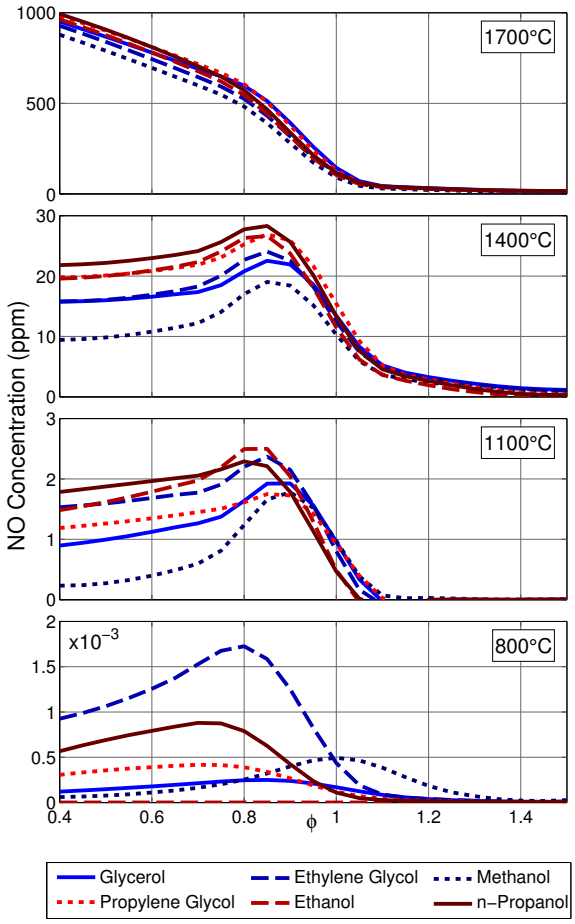

Figure 6.2: NO concentration as a function of ϕ_g and temperature.

credence to the qualitative trends discussed. Additionally, as either the number of carbon atoms increases or the ratio of OH groups to carbon atoms decreases, the NO formation increases, consistent with the results in Fig. 5.9.

Figure 6.3 shows several of the species key to the formation of NO through non-thermal mechanisms. The formation of hydrocarbon radicals CH, CH_2, and CH_3 follow the same fuel specific trends as previous observed, i.e., lower concentrations of the radicals in the more oxygenated fuels. While there are slight differences in trends with respect to fuel structure at the two temperatures, the absolute magnitude of HC concentrations are not greatly affected and are within the same order of magnitude for both temperatures. Fuels with OH/C ratios of unity are separated from those with lower oxygen concentrations, and decreases in both the fuel bound oxygen con-

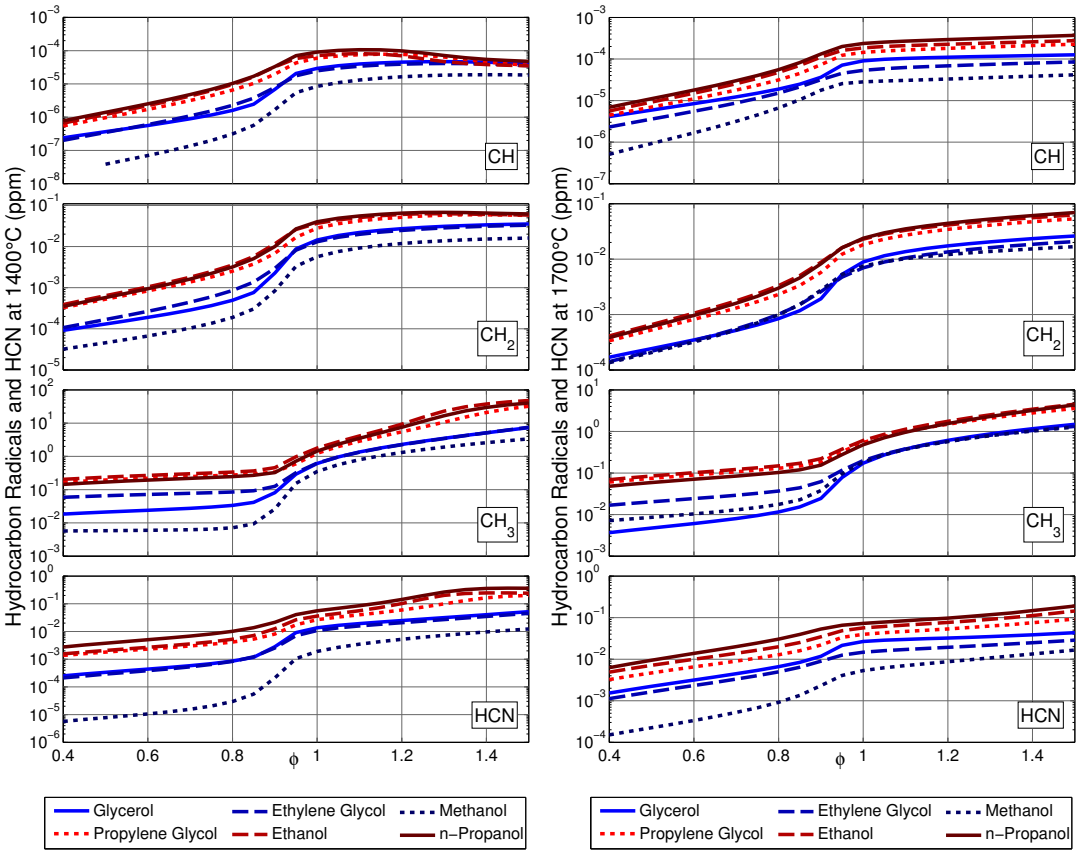

Figure 6.3: Non-thermal NO_X precursors CH, CH_2, and CH_3 and intermediary HCN at 1400°C and 1700°C.

centration and OH/C ratio correspond to increases in HC radicals. Such a result can reasonably be expected due to the greater ratio of C-O to C-H bonds with increasing OH/C ratio. The differences in HC concentrations for methanol, ethylene glycol, and glycerol are due to the ability to enter the C_2H_3OH and acetylene channels as will be described in Section 6.3 for the larger fuels.

The same trend is observed in the formation of HCN. While the formation of prompt NO is largely controlled through the formation of NCN [18, 22], concentrations of NCN are expected to be very low as NCN rapidly converts to HCN, among other species [17, 20, 193]. These trends are also consistent with those observed for the other HC species. Additionally, the increase in HCN, especially in the rich regions, increases potential for NO removal through the NO→HCN→N_2 mechanism [19, 27,

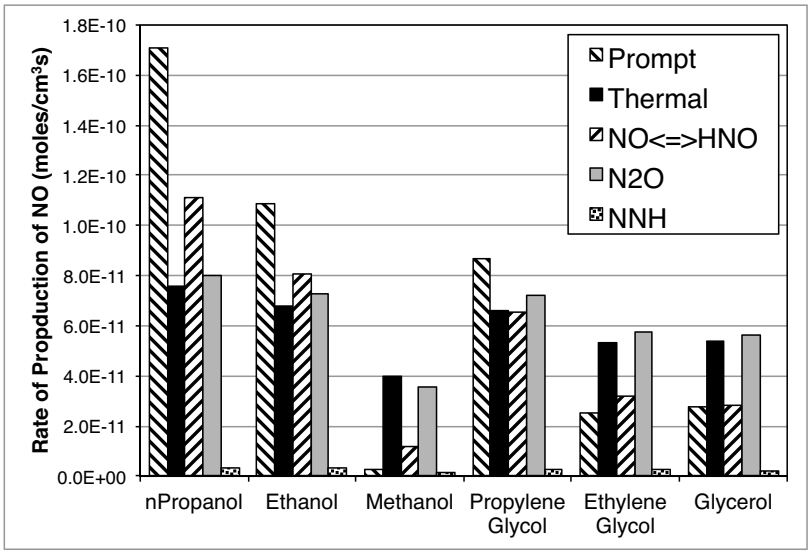

Figure 6.4: Contributions to NO_X formation at $\phi_g = 0.7$ and T = 1400°C.

28, 192, 194, 195].

Analysis of the various NO formation pathways for each of the fuels at $\phi_g = 0.7$ and T = 1400°C is shown in Fig. 6.4. As can be seen the primary differences in NO production are due to reductions in the NO formed through the prompt mechanism. There is a monotonic reduction in prompt NO from n-propanol to methanol, with similar reductions observed from n-propanol to propylene glycol to glycerol.

For n-propanol, prompt NO is formed through two channels. First is through the formation of NCN via reaction 6.2. After NCN is formed, it is rapidly oxidized to form NO along with HCN, CN, and N as shown in reactions 6.3–6.5.

$$NCN + OH \rightleftharpoons HCN + NO \tag{6.3}$$

$$NCN + O \rightleftharpoons CN + NO \tag{6.4}$$

$$NCN + H \rightleftharpoons HCN + N \tag{6.5}$$

The second path to prompt NO is from the oxidation of HCN and CN through NCO

and onto NO as shown in reactions 6.6–6.9.

$$HCN + O \rightleftharpoons NCO + H \tag{6.6}$$

$$CN + O2 \rightleftharpoons NCO + O \tag{6.7}$$

$$NCO + OH \rightleftharpoons NO + H + CO \tag{6.8}$$

$$NCO + O \rightleftharpoons HO + CO \tag{6.9}$$

It was also observed that a significant amount of NO can participate in a recycle loop with HCNO through HCCO, especially when a significant portion of the oxidation pathway is through HCCO, as will be discussed in Section 6.3. Several different groups have also observed that removal of NO can occur through reaction with HCCO and vinyl radical, C_2H_3 [19, 192]. This loop is shown in reactions 6.10–6.14 below:

$$HCCO + NO \rightleftharpoons HCNO + CO \tag{6.10}$$

$$C_2H_3 + NO \rightleftharpoons HCN + CH_2O \tag{6.11}$$

$$HCNO + OH \rightleftharpoons NO + CO + H_2 \tag{6.12}$$

$$HCNO + O \rightleftharpoons HCO + NO \tag{6.13}$$

$$HCNO + OH \rightleftharpoons HCO + HNO \tag{6.14}$$

The contributions to NO through the prompt mechanism are lagely controlled through the CH radical, which in the case of the above fuels, is formed through reactions of CH_2, CH_3, and HCCO all of which are heavily influenced by the varying pathways for fuel decomposition and equivalence ratio.

In addition to the HCNO recycle loop, there is a significant NO recycle loop through HNO [2, 196–198], which is formed through two sources, first through reac-

tion 6.14 and from NH and second through the three-body reaction:

$$H + NO + M \rightleftharpoons HNO + M \tag{6.15}$$

The effect of this loop is a net formation under lean conditions and a net consumption of NO under rich conditions.

In regards to the contribution to NO through the thermal mechanism, the temperature effect is dominant. For high temperatures (not shown), NO formation through the thermal mechanism is much greater than the sum of all other mechanisms. However, at the lower temperature shown in Fig. 6.4, the thermal NO contribution is reduced to approximately the same order as the prompt NO contribution. At this temperature, thermal NO represents approximately 50% of the NO, more or less depending on the variation in prompt NO contribution. At lower temperatures, thermal NO essentially stops completely, and prompt NO is greatly reduced as seen in the low NO concentrations in Fig. 6.2.

Another significant contribution to NO is through the N_2O pathway, in which O atom attacks N_2, after which N_2O forms NO and NH as shown in reactions 6.16–6.18

$$N_2 + O + M \rightleftharpoons N_2O + M \tag{6.16}$$

$$N_2O + H \rightleftharpoons NO + NH \tag{6.17}$$

$$N_2O + O \rightleftharpoons NO + NO \tag{6.18}$$

This mechanism is negligible in the rich regions, but can be significant in the lean regions due to the availability of O atom. Additionally, this pathway does appear to be a weak function of the fuel due to differences in the size of O and H atom radical pools.

Lastly, the NNH and NO_2 mechanisms can be significant sources of NO. However, under these conditions and fuels only a very little contribution to NO is through the

NNH mechanism while the NO_2 mechanism shows a very minor net negative flux from NO to NO_2. While these mechanisms have little influence in this analysis due to the 0-D nature of the PSR simulations, analysis in Chapter 7 of 1-D flames will show that these mechanisms can be significant through the flame.

6.3 Fuel decomposition pathways

The objective now is to investigate differences in the fuel decomposition pathways in order to infer what roles variations in these pathways play in the formation of NO. Clearly, the thermal mechanism is controlled primarily by peak temperatures in the flame, and thus is more sensitive to mixing and flame dynamic effects than fuel decomposition pathways. However, the other mechanisms discussed above are all significantly impacted by the availability of specific radicals, particularly HC and other nitrogen fixing radicals. Therefore, value can be found in investigating the variations fuel decompositions and the effect that these differences have on radical pools.

Fuel decomposition can be broadly classified in this study to four primary categories: H-abstraction, H-abstration via CH_3, water elimination, and unimolecular decomposition. Many more reaction classes are available than will be discussed here, and the author would recommend the review paper of Sarathy et al. [59] for a more thorough discussion, however these classifications provide a handy, although broad, system of classification for reactions observed to be of importance in this study.

Figure 6.5 variations in the relative proportions of these categories for the four temperatures and range of equivalence ratios for each of the fuels. Clearly, at low temperature, fuel decomposition is controlled almost exclusively through H-abstraction, regardless of equivalence ratio. At such low temperatures, it is difficult to overcome the energy barriers necessary for unimolecular decomposition or water elimination

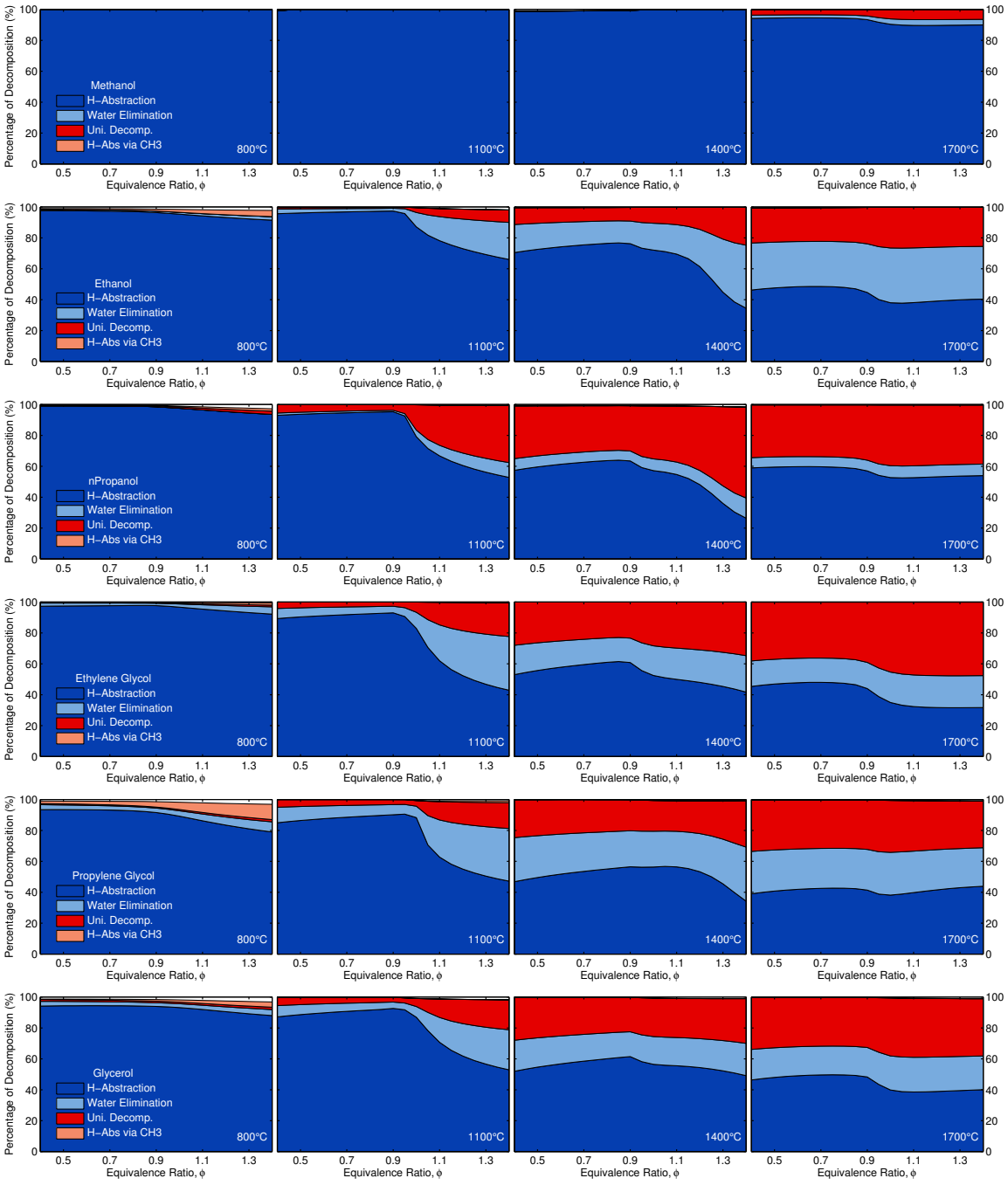

Figure 6.5: Relative proportions of decomposition reaction classes under varying temperatures and equivalence ratios.

reactions, limiting reactions primarily to H-abstractions.

Increasing the temperature to 1100°C sees a rising importance of the other reaction classes, however under lean conditions H-abstraction remains the primary reaction pathway. This is primarily due to the ready availability of the primary abstracting radicals OH and HO_2 at low and intermediate temperature lean conditions [59]. As the equivalence ratio increases, these radicals are supplanted by H radicals, increasing the relative importance of the unimolecular decomposition and water elimination channels.

Above 1400°C and under all equivalence ratios, unimolecular decomposition and water elimination become of increasing importance relative to H-abstraction pathways. Above approximately 1200°C, the preferred reaction paths for alcohols are unimolecular decomposition and water elimination pathways, as can be clearly seen in Fig. 6.5.

It can also be seen from Fig. 6.5 that for the poly-alcohols, these unimolecular and water elimination channels become of greater importance (especially under higher temperatures) than for the alcohols. Heufer et al. [60] showed in calculations for bond dissociation energies (BDE) of pentanol isomers, that the BDE of C-C and C-H bonds involving the carbon adjacent to the hydroxyl group are weakened, while those of the neighboring carbon are stronger. As a result of the increased sites of OH groups in the poly-alcohols, presumably the number of weakened bonds is increased, allowing for a greater proportion of unimolecular decomposition. Additionally, the increased degeneracy of water elimination through the multiple OH moeities results in a further increase in water elimination pathways. However, caution should be exerted in this analysis due to the extension of alcohol reaction rates by analogy to the poly-alcohols. No calculations of bond energies or experimental measurements of reaction rates in poly-alcohols under combustion conditions exists to the author's knowledge. With that said, there can be reasonable confidence in the general trends discussed.

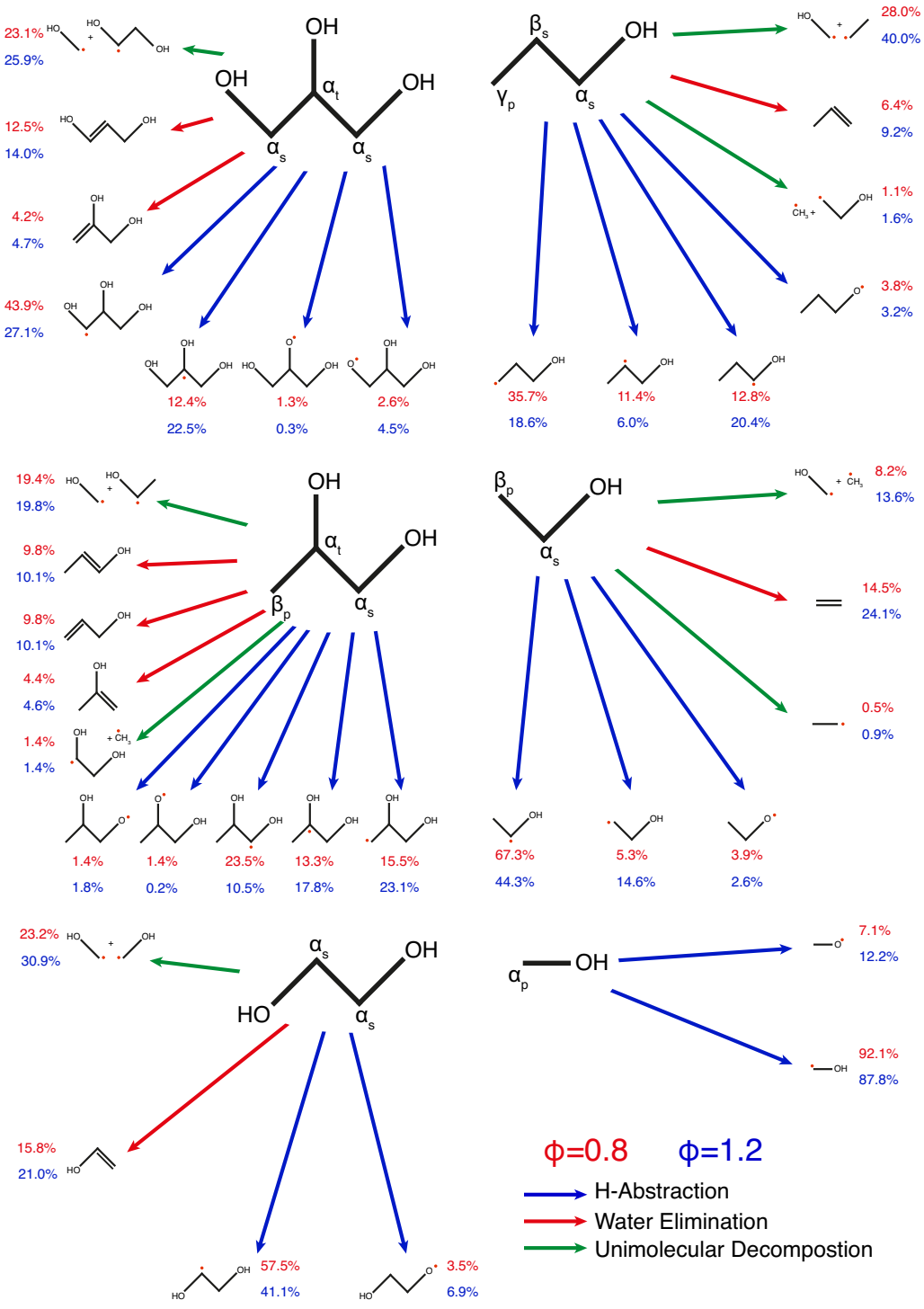

Figure 6.6: Primary initial fuel decomposition reactions at 1400°C and ϕ = 0.8 (red) and 1.2 (blue).

Figure 6.6 details the primary initial fuel decomposition reactions under lean and rich conditions at 1400°C. Each carbon is labeled indicating position relative to an OH group (α, β, and γ sites) and whether the C-H bonds at the site are primary, secondary, or tertiary. As discussed above, the relative position of C-C and C-H bonds to C-O bonds influences the strength of those bonds, yielding variations in decomposition products. Each of the reactions is labeled as one of the reaction classes discussed above, and the percentage of the rate of consumption of the initial fuel molecule is listed for each product under lean and rich conditions in red and blue numbers, respectively.

Beginning with the simplest molecule here, the majority of the fuel proceeds through H-abstraction from the α_p site by OH/O (85/5% of total) under lean conditions and a combination of OH/H under rich (25/60% of total). Xu and Lin [199] predicted by theory that H-abstraction by OH from the α site to be the primary pathway, as is observed. Additionally, Meana-Pañeda et al. [200] calculated rates for abstraction by H with a temperature dependent branching ratio.

The primary reaction paths for ethanol are through H-abstraction from the α site, water elimination, and unimolecular decomposition. H-abstractions of the β site or the oxygen site are of minor importance compared with that of the α, which is reasonable given the BDE discussion above. Unimolecular decomposition through scission of the C-O is neglible due to the significantly higher bond strength compared with the alternative C-C neighboring bond. Shock tube measurements of Sivaramakrishnan et al. [64] show increasing importance for the C-C unimolecular decomposition relative to the water elimination reaction at higher temperatures.

For n-propanol, the primary reaction paths are through a combination of unimolecular decomposition and H-abstraction, with a lower proportion through water elimination than that seen in ethanol. The majority of H-abstraction reactions result in hydroxypropyl radicals, which proceed to form a mix of ethylene, propene,

ethenol, propanal, and formaldehyde through subsequent scission reactions. The primary products of unimolecular decomposition are hydroxymethyl and ethyl radical.

The rates for the remaining poly-alcohols are obtained by analogy with those of alcohols, so care must be taken in analysis of their branching ratios. However, some relative observations can be made about the influence of the multiple OH groups on differences in decomposition pathways. Due to the symmetry of ethylene glycol, the possible decomposition pathways are limited. The major pathways are H-abstraction from one of the two α_s sites and C-C scission into two hydroxymethyl radicals. Water elimination is of approximately equal importance as seen in ethanol, however the resultant decomposition product is ethenol, rather than ethylene.

The decomposition products of propylene glycol are the most diverse of the fuels studied here. H-abstraction from the two α sites are the most significant, followed closely by H-abstraction from the β site and unimolecular decomposition through C-C scission of the α carbons. Water elimination of the α_t hydroxyl is also significant, more so than from the α_s site. A more detailed study of the reaction paths is included in Fig. 6.7, however it can be seen here that one of the consequences of the presence of an additional OH group is the continued presence of oxygen in the decomposition radicals, which will be shown to carry through the remaining reaction scheme.

Finally, glycerol decomposes through unimolecular decomposition and H-abstraction from one of the three α sites. Water elimination occurs at the central α_t site more than either of the α_s sites. Clearly, the additional OH group(s) of the poly-alcohols play a role in the selection of preferred decomposition pathways, but they play an even more prominent role in the structure of the decomposition radical. Specifically, the decomposition products of the poly-alcohols remain oxygenated, shifting a greater proportion of the carbon to oxidize through hydroxymethyl radical to formaldehyde to HCO, effectively by-passing the formation of HC radicals which participate in any nitrogen-fixing reactions.

This effect can be shown more clearly in the analysis of the general decomposition scheme of propylene glycol at T = 1400°C and $\phi = 0.8$ shown in Fig. 6.7. A similar analysis could be conducted for all the fuels, however propylene glycol demonstrates an interesting mix between features of both alcohols and poly-alcohols, so only this case will be shown. The various decomposition pathways can be organized into a few groups that react along similar pathways and have limited cross-reactions of intermediate species. These organized groups are illustrated in the colored boxes in Fig. 6.7. The flux of carbon was followed until each carbon atom reached one of several species which could be considered the final species of consequence for NO_X formation. The most important species considered in this analysis are CH_3 (which ultimately yields the prompt-initiating CH), hydroxymethyl radical CH_2OH (which ultimately functions as an alternative path to carbon oxidation, sidestepping the formation of CH_i radicals), and HCCO (which under certain conditions can function as an NO consuming species through the NO-HCN-reburn mechanism).

The most significant reaction group in Fig. 6.7 is the green group on the left of the figure, composed of the unimolecular decomposition and β site H-abstraction. Every molecule that proceeds down these paths splits off a hydroxymethyl radical within the first two steps, effectively limiting the ability to contribute to prompt NO_X formation. After removing the hydroxymethyl, the remaining fuel fragments form either ethenol or acetaldehyde. The net effect through this group is the significant formation of hydroxymethyl and CO (11% and 7% of all fuel carbon, respectively). However, oxidation of ethenol and acetaldehyde do contribute to CH_3 (7% of all fuel carbon). However, this is where the propylene glycol differs from either glycerol or ethylene glycol, in that the remaining fuel fragments do not contain a secondary carbon free of a C-O bond. As a result, the CH- and OH- scission pathways of the remaining fuel radical ultimately decompose into hydroxymethyl radical and CO, instead of CH_3 and CO. Only a small percentage of the remaining fuel radical of

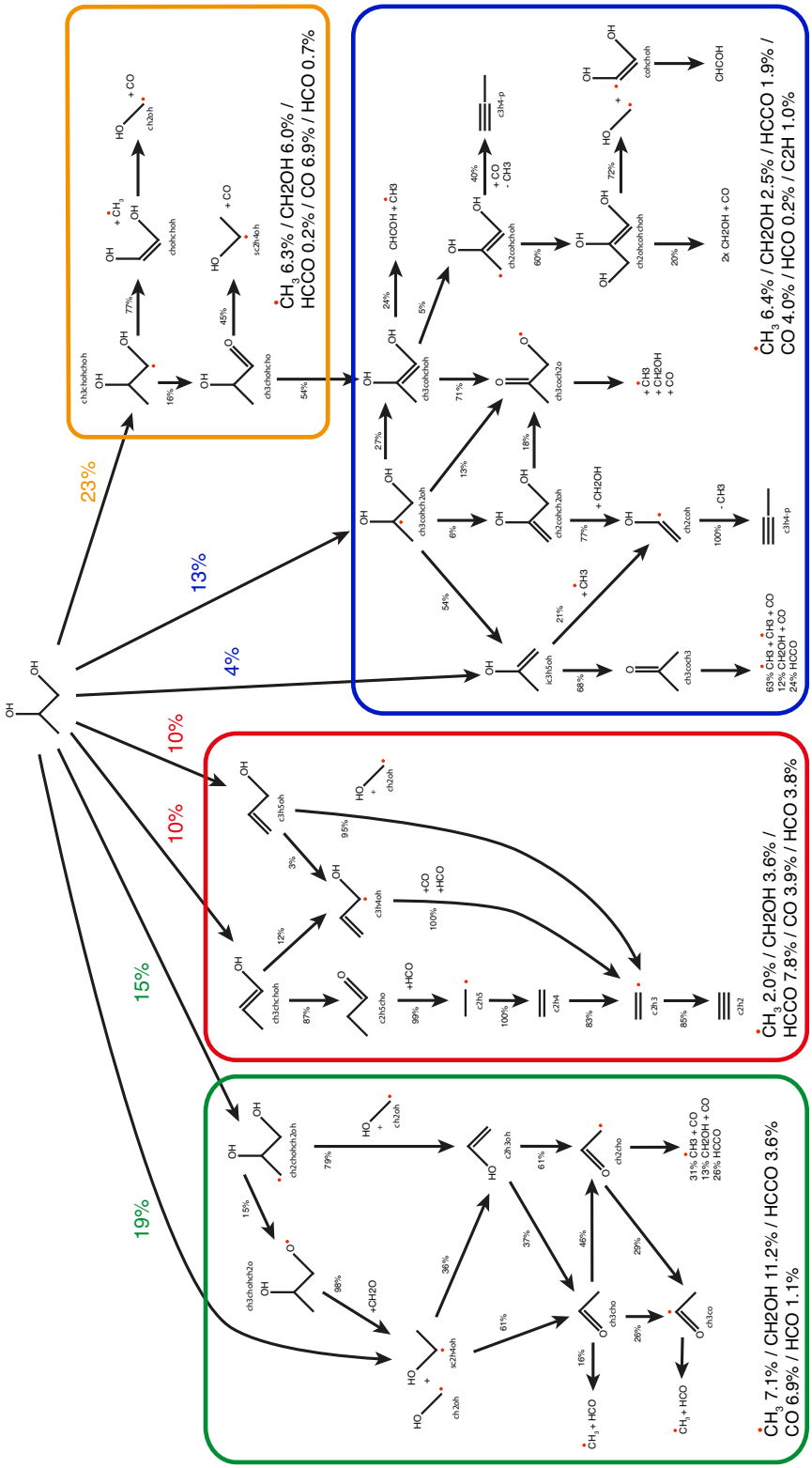

Figure 6.7: Detailed reaction path analysis of propylene glycol at T = 1400°C and $\phi_g = 0.8$.

glycerol unimolecular decomposition follows OH-abstraction or water elimination to form ethenol (C_2H_3OH). Alternatively, a much greater proportion of the n-propanol decomposition follows this channel through ethenol and acetaldehyde. Ultimately, the preference to oxidize through hydroxymethyl and formaldehyde, rather than through this group, becomes the controlling factor in reducing prompt NO formation for the more oxygenated fuels.

The second grouping considered is the products of the water elimination paths shown in red. These decomposition products typically split off either a hydroxymethyl, CO, or HCO group while the remaining fuel fragment moves through ethyl radical, ethylene, vinyl radical, and acetylene. The majority of the carbon entering this channel (and not removed through hydroxymethyl, CO, or HCO) proceeds through acetylene, the products of which are strongly equivalence ratio dependent. For lean conditions HCCO and CO are the primary products, with small contributions to CH_2 and CH_3, whereas under rich conditions there are larger contributions to the CH, CH_2, and CH_3 radical pools.

The third grouping, shown in blue, is largely focused around the product of H-abstraction from the α_t site. Here the decomposition products proceed to form acetone, propyne, and a number of other intermediates. The net result is weighted more toward forming CH_3 than hydroxymethyl, yielding the highest ratio of CH_3-to-hydroxymethyl for any of the groups.

The last major group considered here is through the product of H-abstraction from the α_s site and is shown in yellow. This group ultimately contributes a proportion of the carbon in the fuel fragments to the green and blue groups, however the majority of the carbon directly yields CH_3, hydroxymethyl, and CO, functioning as a sort of middle path between the blue and green paths.

Figure 6.7 shows that there are a number of decomposition pathways, ultimately resulting in a relatively limited set of products. Some of these pathways completely

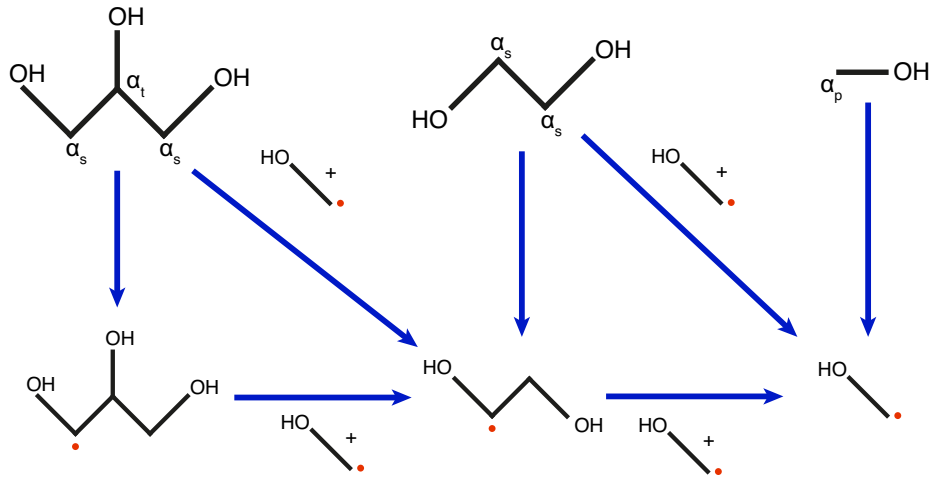

Figure 6.8: The prominent role of hydroxymethyl radical CH_2OH in fuel decomposition pathways for glycerol, ethylene glycol, and methanol and the commonality of the decomposition pathway.

by-pass the formation of CH, CH_2, and CH_3 radicals, effectively limiting the fixation of nitrogen due to the formation of formaldehyde. Other pathways proceed through ketene (CH_2CO), which can contribute to the CH radical pool depending on equivalence ratio. Lastly, as the number of C-O bonds is reduced, a greater proportion can proceed through ethylene and acetylene with greater contributions to CH radical production.

Conversely, increasing the C-O bonds effectively limits available decomposition pathways. Figure 6.8 demonstrates this point through the primary decomposition pathways of the fuels with OH/C ratio of unity. For these fuels, decomposition proceeds through either unimolecular decomposition through C-C scission (due to reduced BDE caused by the proximity of the C-O pair) or through H-abstraction from the α_s site (again due to reduced C-H BDE cause by the proximity of the oxygen). The H-abstraction products then proceed to shed a hydroxymethyl radical. Unimolecular decomposition directly results in the formation of hydroxymethyl radical and a fuel fragment radical which is also the product of the H-abstraction from the fuel molecule with one fewer carbons. The net result is a cascade of shedding hydroxymethyl radicals, all the way down to methanol, resulting in ultimately very similar (and very

low) NO_X formation.

6.4 Conclusions

The objective of this chapter was to investigate the influence of the fuel structure on contributions to NO_X formation and differences in fuel decomposition pathways. It was deemed infeasible to accurately model the complex physics and chemistry of the swirling flame, therefore an alternative approach utilizing a simple zero dimensional model was employed over a wide range of temperatures and equivalence ratios typical of those observed in the flame.

Contributions to NO formation through the various known pathways were analyzed and it was observed that formation of NO through the prompt mechanism was limited by the ability of the fuel to produce HC radicals, as well as recycling of NO through reaction with HCCO and vinyl radical. Clearly, the formation of non-thermal NO is greatly impacted by the availability of these HC radicals to participate in nitrogen fixing reactions and significant differences in the size and distribution of these radical pools were observed in the models.

It was shown that the fuel structure, namely the number and location of C-O bonds, had a profound effect on the decomposition pathways. The presence of these C-O bonds was deterministic in the branching ratios between pathways which proceeded on to formaldehyde, acetylene, or acetaldehyde. Adjacent C-O bonds allowed for a greater proportion of the fuel to decompose through unimolecular dissociation, separating a hydroxymethyl radical from the fuel molecule. Such hydroxymethyl radicals continued almost exclusively to formaldehyde, which oxides irreversibly to HCO, limiting contribution to the HC radical pool. It was also observed that fuels would decompose similarly along family lines, whereby glycerol, ethylene glycol, and methanol exhibited similar branching ratios through formaldehyde while propylene

glycol and ethanol exhibited similar branching ratios through ketene, ethylene, and to a lesser extent formaldehyde.

Chapter 7

Temperature and species concentration measurements and simulations in flat flames

Chapters 5 and 6 examined NO formation in a complicated burner geometry necessitated by the inherent difficulties in the combustion of the poly-alcohol fuels. The objectives of this chapter and those to follow are to investigate the influence of the OH group under more simplified geometries, ultimately allowing for more fundamental studies and comparisons with simulations. This chapter will focus on experimental measurements of the temperature field and NO concentrations in Sections 7.2.1– 7.2.2, as well as probed species measurements when feasible. These temperature measurements will then serve to define the temperature field for simulations of the flame in Section 7.1.3, followed by a detailed reaction path analysis of the various NO formation mechanisms through the flame and the net contributions of each in Section 7.3.

7.1 Experimental setup

The objective of this chapter is to observe the influence of the OH functional group on NO formation. Therefore, a comparative study of the C_1–C_3 alcohols and alkanes was

Table 7.1: Experimental conditions for flat flame experiments

Property	(Units)	Conditions
ϕ		0.8–1.2
Temperature	(°C)	100
Ratio to S_L		0.25
Exit velocity at ϕ=1.0	(cm/s)	
Methane	-	15.1
Ethane	-	16.1
Propane	-	15.9
Methanol	-	19.0
Ethanol	-	17.9
n-Propanol	-	14.8
i-Propanol	-	13.7

selected. Equivalence ratios were varied between 0.8 and 1.2 while the gas temperature was fixed at 373 K. The gas exit velocity was selected for each fuel to be a constant factor of 0.25 times the laminar burning velocity. Laminar burning velocities for each fuel were taken from experimental measurements in the literature: alkanes by Vagelopoulos et al. [115], methanol and ethanol by Gulder [55], and the propanol isomers by Veloo et al. [72]. Corrections for deviations in the initial temperature from that of the experimental data set were conducted utilizing the methodology of Metghalchi and Keck [116, 117]. Table 7.1 summarizes the experimental conditions and provides a sample of gas exit velocities.

7.1.1 Burner apparatus

The experiments in this chapter utilized the burner configuration described in greater detail in Section 2.2.1. Fuel was delivered in the gas phase and premixed with air utilizing the prevaporization system described in Section 2.2. The entire fuel handling and burner apparatus was insulated and heated to ensure the temperature throughout the system was high enough to prevent cold spots and condensation. The porous plug cooling water was replaced with a heated oil recirculation loop to ensure the plug

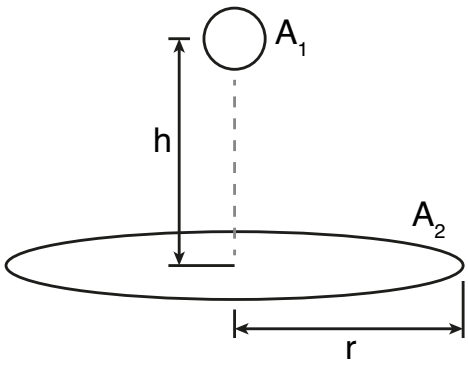

Figure 7.1: View factor for radiation from coaxial sphere to flat disk of finite radius.

temperature was maintained near the desired gas exit temperature.

Measurements of temperature were conducted with two different techniques: 2λ-OH LIF thermometry (described in the next section) and probed thermocouple measurements. The thermocouples used were fine wire, type-R thermocouples (Pt-Pt/Rh 13% sourced from Omega Engineering P13R-005) with a wire diameter of 125 μm. The bead diameter was measured using scanning laser metrology to be 275 μm. The thermocouple junction was coated with silica to reduce catalytic surface effects [168, 201].

Corrections for radiative losses to the burner surface and to the environment were included [168, 169]. Typically, radiative loss corrections are performed assuming an exchange between a gray thermocouple surface and an isothermal environment. However, when the thermocouple bead is in close proximity to the hot burner surface, improvements in the radiative corrections can be achieved by accounting for this geometry. For this configuration, the view factor between the thermocouple bead and the burner surface is shown in Fig. 7.1 with the relation described in equation 7.1.

$$F_{1,2} = \frac{1}{2}\left[1 - \frac{1}{\sqrt{1+\left(\frac{r}{h}\right)^2}}\right] \tag{7.1}$$

The corrected gas temperature is determined by solving the balance of the surface-

area-specific convective-radiative heat transport equation below:

$$h\left(T_g - T_{tc}\right) = \frac{\dot{q}_{1,2} + \dot{q}_{1,\text{surr}}}{A_1} \tag{7.2}$$

where T_g is the gas temperature, T_{tc} is the temperature as read by the thermocouple, and h is the convective heat transfer coefficient, which can be approximated using the Nusselt number empirical correlations for a cylinder:

$$Nu \equiv \frac{hd}{k} \approx 1.8 Re^{0.3} Pr^{0.3} \tag{7.3}$$

where d is the diameter of the wire and k is the thermal conductivity of the bath gas (approximated here as N_2). The heat flux terms $\dot{q}_{1,2}$ and $\dot{q}_{1,\text{surr}}$ are as shown below:

$$\dot{q}_{1,2} = \frac{\sigma\left(T_{tc}^4 - T_b^4\right)}{\dfrac{1-\varepsilon_1}{\varepsilon_1 A_1} + \dfrac{1}{A_1 F_{1,2}} + \dfrac{1-\varepsilon_2}{\varepsilon_2 A_2}} \tag{7.4}$$

$$\dot{q}_{1,\text{surr}} = \frac{\sigma\left(T_{tc}^4 - T_{surr}^4\right)}{\dfrac{1-\varepsilon_1}{\varepsilon_1 A_1} + \dfrac{1}{A_1 F_{1,3}}} \tag{7.5}$$

The emissivity of the Pt/Pt-Rh thermocouple is estimated using the temperature dependent empirical correlation of Hindasageri et al. [169]:

$$\varepsilon_1 \approx 6 \times 10^{-5} T + 0.0138 \tag{7.6}$$

while the emissivity of the burner surface has a negligible impact on the radiation correction. Finally, the gas temperature is solved iteratively using the equation below:

$$T_g = T_{tc} + \frac{\left(\dot{q}_{1,2} + \dot{q}_{1,\text{surr}}\right) d}{A_1 k Nu} \tag{7.7}$$

where the corrective term is updated with each iteration. Figure 7.2 shows a set of

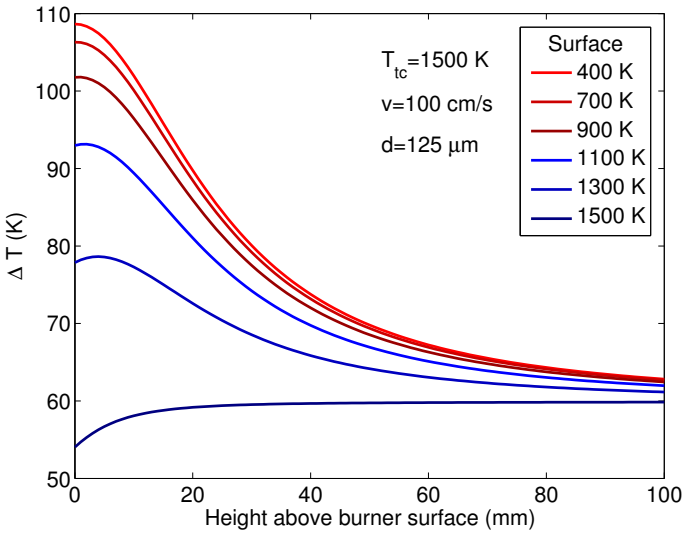

Figure 7.2: Typical temperature corrections for a radiating thermocouple in close proximity to burner surface.

typical radiation correction terms as a function of burner surface temperature and position of the bead relative to burner surface. Clearly in the region near the burner surface it is important to account for this close proximity and to have a reasonable estimate of burner surface temperature. As the bead moves away from the burner surface, the corrections converge to the expected correction for a bead radiating to an isothermal enclosed environment.

Due to the importance of the burner surface temperature to the radiation correction, the porous plug temperature was measured using an IR thermometer for each of the conditions. This measurement also helps to verify that the flame has not advanced into the porous plug, but is instead anchored above the porous plug. These temperatures varied consistently between 100 and 200°C (373-473 K) as a function of equivalence ratio and were relatively constant across fuels at the same equivalence ratio.

Extractive gas samples were collected using an uncooled quartz microprobe with a 250 μm orifice. Sample gases were then cooled, dried, and filtered. After conditioning, sample gases were diluted with argon to increase the sample flow rate to above

the minimum requirement for the California Analytical Instruments CLD NO/NO_2 analyzer. This analyzer was calibrated using a reference NO standard. For the three carbon fuels at $\phi = 1.0$ and 1.2, additional measurements were conducted utilizing the Agilent Refinery Gas Analyzer (RGA) based on an Agilent 7890 GC. This system utilizes a combination of eight columns and three detectors (two TCD and one FID) for the identification of H_2, O_2, N_2, CO, CO_2, and saturated and unsaturated C_1-C_5 hydrocarbons.

The thermocouple and quartz microprobe were mounted on a Newport IMS-V high-load vertical motorized precision translation stage, accurate to 1 μm. This sampling assembly was then translated through the first 5 mm above the burner surface and measurements were logged utilizing an in-house LabView data acquisition system. At each position, 200 temperature measurements were collected at the rate of 10 Hz and averaged. Extractive gas samples were allowed three minutes to purge the sample collection system and analyzer before data collection over two minute intervals.

7.1.2 Laser diagnostic setup

The theory of 2λ-OH LIF thermometry is explained in greater detail in Section 2.3.1, however the details on the experimental set-up of the technique are discussed here. The technique utilizes a 10-Hz Continuum Nd:YAG pumped, frequency doubled Rhodamine dye-laser, with UV output in the neighborhood of 285 nm and approximately 13 mJ per pulse. The selection of a rotational line pair needs to be chosen to account for the sensitivity in the temperature range of interest. The $A^2\Sigma^+ \leftarrow X^2\Pi(1,0)$ band with $P_1(7)$ and $Q_2(11)$ rotational transitions at 285.088 and 285.157 nm, respectively, were selected, yielding a good temperature sensitivity between 1400 and 2000 K [144]. Because the flame in this configuration is steady, the wavelength was retuned between each transition.

Figure 7.3 illustrates a not-to-scale rendering of the optical layout and the ori-

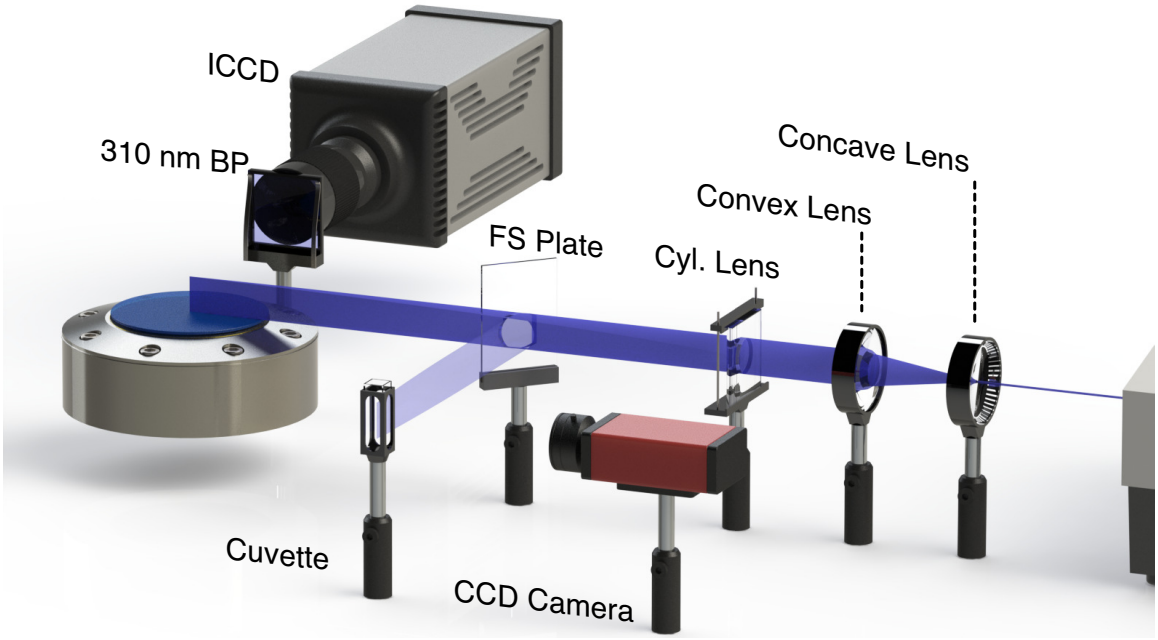

Figure 7.3: Layout of 2λ-OH PLIF thermometry experimental setup.

Table 7.2: Optical elements in 2λ-OH LIF thermometry

Element	Part Number	Unit	Size
Plano-concave lens	CVI PLCC-50.8-51.5-UV	f=-100 mm	⌀50.8mm
Bi-convex lens	CVI BICX-50.0-256.8-UV-248	f=250 mm	⌀50 mm
Cylindrical lens	CVI SCX-50.8-381.4-UV-248	f=750 mm	50.8x50.8 mm
Fused Quartz plate	PGB Custom	(-)	(-)
Bandpass Filter	Asahi Spectra ZBPA310	310 nm, 10 nm FWHM	50.8x50.8 mm
Cuvette	Newport FS Cuvette	(-)	10x10x45 mm
Mirrors (not shown)	CVI TLM1-300-45UNP-1037	R>99%	25.4 mm

entation with respect to the flat flame burner. This figure demonstrates several key features of the setup which should be noted and a more detailed listing of components is included in Table 7.2. Following the path of the beam, the beam exits the dye laser tuned to the desired wavelength approximately 5 mm in diameter. The beam is then expanded and collimated through the telescopic assembly with a magnification ratio of 2.5. The collimated beam is then focused through the cylindrical lens, providing a measurements region 10 mm tall by 300 μm wide.

After focusing through the cylindrical lens, a small fraction of the laser energy

(approximately 4%) is reflected from the fused quartz flat plate to be used for corrections in fluctuations of the laser energy and energy distribution. While the remainder of the energy is focused over the burner surface, this reflected fraction is focused into a coumarin dye in ethanol solution filled cuvette, which is imaged by a triggered CCD camera for each shot. The OH fluorescence is imaged using a gated Princeton Instruments PI-MAX3 blue enhanced ICCD camera. To eliminate spurious sources of fluorescence and laser scatter from being imaged, an Asashi Spectra narrow band pass filter centered at 310 nm with a 10 nm FWHM was installed on the lens.

During post processing, corrections were made to account for fluctuations in the laser shot-to-shot total energy as well as the spatial distribution of energy. These corrections were determined from the correlating correction image from the sample beam for each shot. Operation in the linear regime was verified for both the OH fluorescence and the profile corrections fluorescence. Additionally, corrections were made for non-linearity in the pixel response of the ICCD as well as spatial calibrations utilizing a spatial calibration target. Additional details of these processes are provided in Section 2.3.1.

7.1.3 NO_X simulations

Simulations of the flat flame were conducted in CHEMKIN-Pro, utilizing the fixed gas temperature profiles defined by the merged temperature profiles of the Section 7.2.3. The mechanism selected for this study was based on the AramcoMech1.3 [186], encompassing the C_1 and C_2 alcohol sub-mechanisms. The C_3 alcohol chemistry was provided by the sub-mechanism of Sarathy et al. [187].

A NO_X sub-mechanism is not included among the AramcoMech1.3 base mechanism, so the NO_X chemistry of GDF-Kin3.0_NCN by El Bakali et al. [22] provides the basis of the nitrogen chemistry. This mechanism is primarily composed of rates from Miller [2] and Glarborg [19]. The rate constant for the key prompt initiating

reaction $CH + N_2 \rightleftharpoons NCN + H$ was updated to better reflect more recent predictions of Harding et al. [24] for temperatures less than 2000 K and the shock tube study of Vasudevan et al. [23] for temperatures above 2000 K. Additionally, rates for reactions participating in the NNH formation sub-mechanism for NO were updated to reflect the collection of rates discussed by Klippenstein et al. [47] sourced from [202–204].

7.2 Experimental measurements

For each fuel and equivalence ratio condition, a flame was established on the McKenna flat flame porous plug burner. The primary objective in these experiments is to provide an accurate temperature profile for use in modeling each of these flames in CHEMKIN. Typically, one could solve the gas-energy equation in CHEMKIN without the requirement of a defined temperature profile. However, due to the proximity of the flame to the porous plug and the difficulty inherent in estimating the heat loss to the plug, it was determined to be a better solution to experimentally measure the profile. Additionally, there was interest in determining if species measurements could be conducted using extractive gas samples at positions through the flame. This process was successful in the post flame, however samples extracted near the flame front were less successful due to the difficulty in sampling thin flames at atmospheric pressure and the presence of in-probe reactions and probe wall effects. As a result, only a limited set of results from the extracted samples through the flame are presented. However, Chapter 8 will present non-intrusive experimental measurements of NO through the flame utilizing PLIF.

7.2.1 Probed measurements of temperature and species

Temperature measurements were conducted at a non-uniform spacing through the flame, with concentrated measurements near the flame front. Figure 7.4 shows an

example surface plot of the radiation corrected thermocouple measured temperature profiles for the highest and lowest temperature fuels in this study. Both fuels exhibit similar trends, characterized by a rapid rise in temperature near the burner surface through the preheat zone, followed by a peak in temperature approximately one millimeter over the burner surface. The temperature then decreases to a steady state value due to high temperature gas radiation, primarily driven by H_2O and CO_2.

One of the troubles with this technique is the difficulty in measuring the temperature in the flame region due to the probe intrusive effects and large temperature gradients in this region. While the thermocouple bead is quite small, the gradient in temperature across the diameter of the bead results in artificially high temperatures at the lowest measurement position and difficulty measuring the highest peak temperature. Both features tend to blur, flattening the profiles.

Measurements of the burner porous plug surface temperature using the IR thermometer show plug temperatures within 100 K of the gas exit temperature of 373 K, demonstrating the difficulty in measuring the temperature in the region approximately one bead diameter in width above the burner surface. Additionally, to avoid introduction of additional thermoelectric generated voltages through the Seebeck effect in the contact of the thermocouple bead and the stainless steel porous plug, it was necessary to ensure that the bead remained above the surface and avoid contact, further making measurement in this region difficult.

The measurement of peak temperature in the flame around one millimeter does not suffer from such steep gradients, however it is still difficult to capture the peak temperature well without exceptionally fine thermocouples due to moderate temperature gradients and intrusive probe effects. Both of these regions are very well served in the measurement of temperature via non-intrusive techniques such as the 2λ-OH LIF thermometry in Section 7.2.2. However, temperature measurements via thermocouple are the most accurate in the post-flame regions, from about 1.5 mm and up.

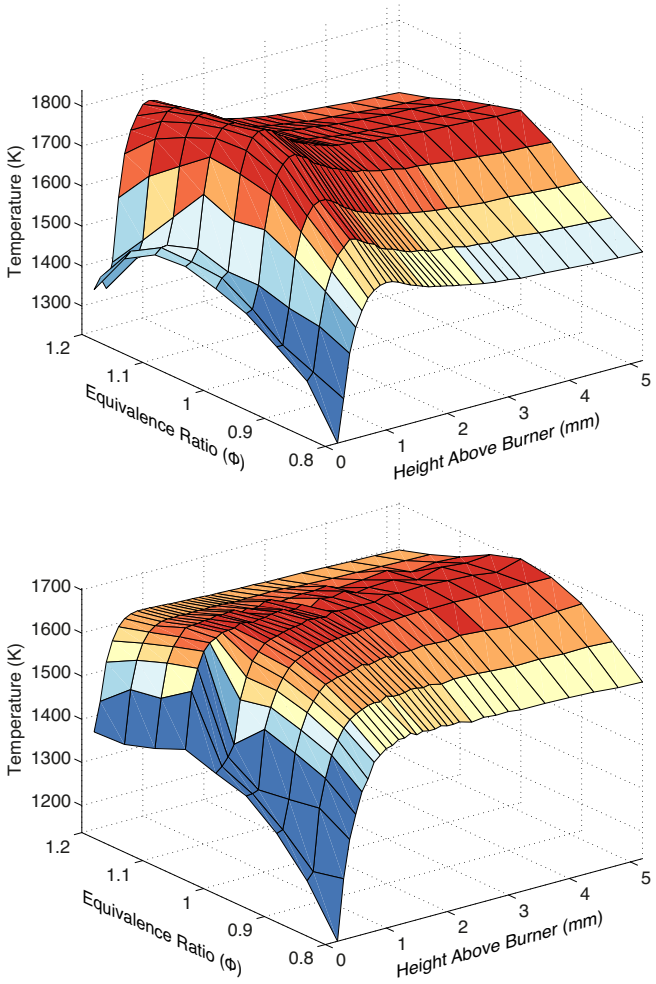

Figure 7.4: Surface contours of the highest and lowest temperature profiles as measured through the flame for $0.8 < \phi < 1.2$ in propane and methanol flames.

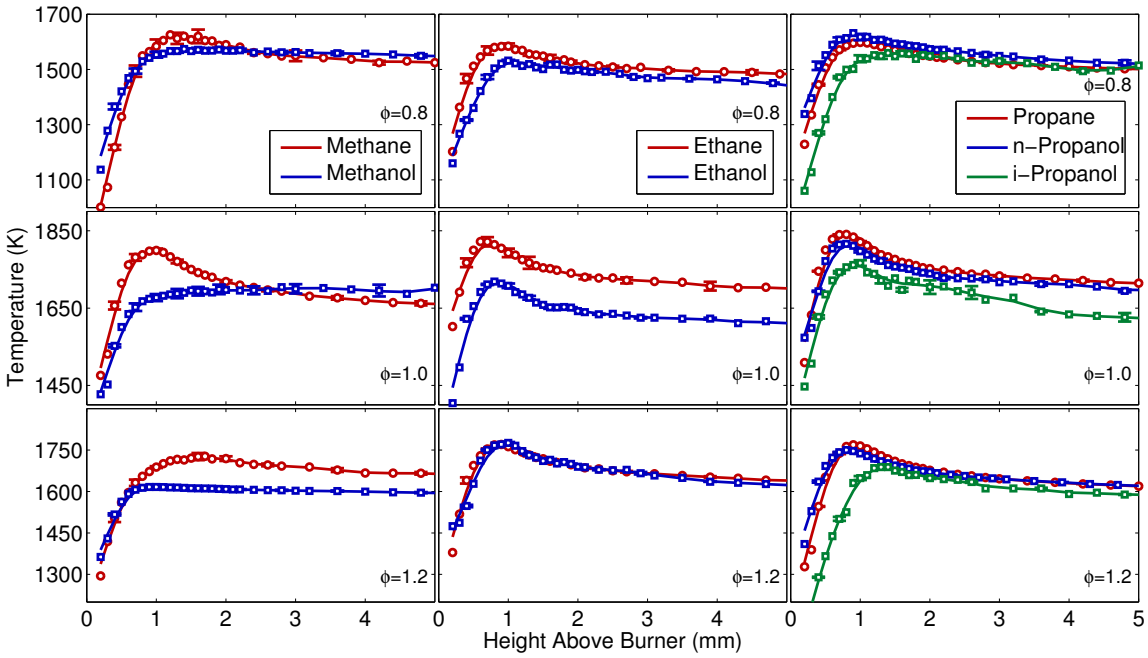

Figure 7.5: Temperature profiles for all fuels under lean, stoichiometric, and rich conditions.

In this region the temperature gradients are the lowest, the fuel chemistry is most complete, and intrusive effects are the least significant.

Figure 7.5 shows a comparison of the temperature profiles for all seven fuels, grouped according to carbon number and equivalence ratio. Examining the C_1 fuel profiles, one can see that the methanol flames are typically lazier, with lower peak temperatures and slower rates of temperature rise. The steady state temperatures higher above the burner surface are typically comparable. The C_2 fuels behave comparably to each other, except around the stoichiometric condition in which the alcohol flame exhibits lower temperatures. Under lean and rich conditions, the alcohol and alkane C_2 flames are more comparable. Meanwhile the C_3 alkane and n-alcohol flames are very similar across all equivalence ratio conditions. However, the C_3 isomer exhibits typically lower peak temperatures and the location of the peak is shifted farther downstream.

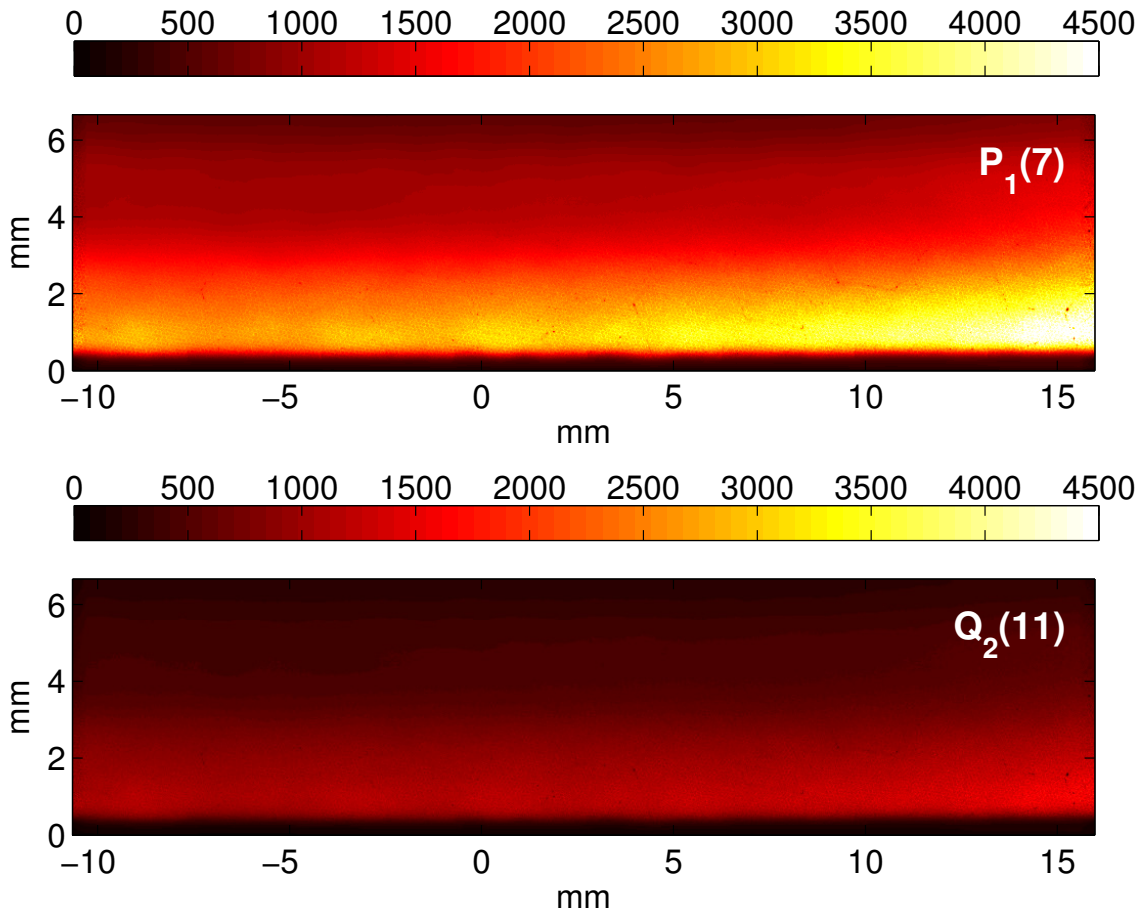

Figure 7.6: OH fluorescence images of the $P_1(7)$ and $Q_2(11)$ rotational lines in a propane flame, $\phi = 1.0$.

7.2.2 2λ-OH LIF thermometry

In order to compliment some of the difficulties in measuring the flame temperature with thermocouples, 2λ-OH LIF thermometry was employed. The technique requires calculating the ratio of OH fluorescence excited from two separate rotational transitions as described below.

$$R = \frac{(\eta BE)_1}{(\eta BE)_2}\frac{g_1}{g_2}\frac{f_1(T)}{f_2(T)}\frac{\Phi_1(T)}{\Phi_2(T)} \tag{7.8}$$

$$R = C\frac{E_1}{E_2}\exp\left(-\Delta\varepsilon_{12}/kT\right) \tag{7.9}$$

where Equation 7.8 in independent of the number density of the absorbing species and its only temperature dependence comes from the relative populations in the absorbing levels through the ratio of Boltzman fractions f_i. While the fluorescent yield Φ_i is weakly temperature dependent, at elevated temperatures the ratio in fluorescent yields between the two excited states is small [144]. Ultimately the ratio can be reduced to Equation 7.9, where the ratio in fluorescent signals is related to an experimentally determined calibration constant C, the laser energy fluence E_i, the difference in excitation energy levels $\Delta\varepsilon_{12}$, and the temperature.

Following the correction and calibration procedure discussed in greater detail in Section 2.3.1, images such as those shown in Fig. 7.6 are captured for each condition. The images in Fig. 7.6 are the result of the average of 150 exposures for each excitation wavelength.

The region of interest in these images is centered around 0 $\pm$ 5 mm, extending approximately 5 mm above the burner surface. The region of interest is limited to the center of the burner to avoid temperature and species gradients near the edge of the burner [119, 205]. Effects such as dilution, entrainment, or non-uniformity in velocity can be seen near the right hand extreme in Fig. 7.6. Near the center of the burner, these effects are minimized and aided by the rotational symmetry of the burner. The OH fluorescence begins approximately 0.25 mm above the burner surface, and peaks around 1 mm above the burner, coinciding with the expected peak temperature and OH concentration.

Figure 7.7 shows the mean temperature profiles in the region of interest as a function of height above burner for both transitions. Peak signal for the $P_1(7)$ and $Q_2(11)$ transitions are approximately 3000 and 1200 counts, with signal-to-noise ratios of 14.4 and 17.6, respectively. Clearly, one benefit of this technique over that of probed thermocouple measurements is that the peak OH fluorescence signal coincides with the region of greatest difficulty for probed techniques.

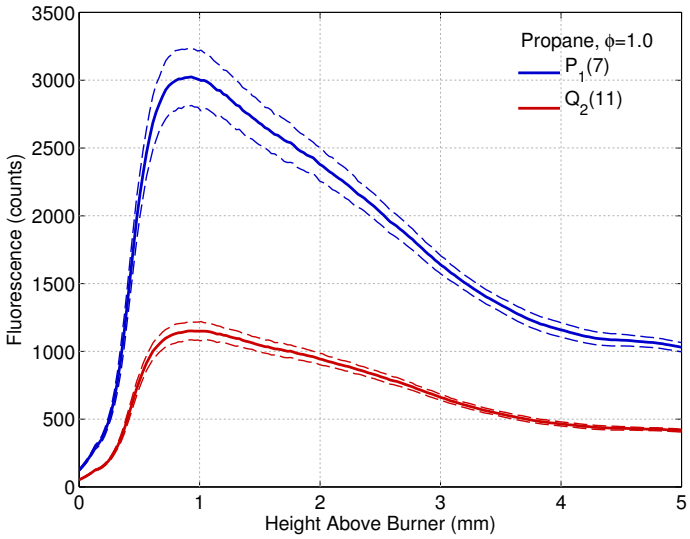

Figure 7.7: Averaged profiles of OH fluorescence signals in a propane flame, $\phi = 1.0$.

Determination of the calibration constant C was made for each fuel and equivalence ratio condition to account for differences in the quenching environment of the upper state as a function of equivalence ratio. This calibration was achieved using the temperature measured via thermocouples from the previous section at a height of 3 mm above the burner surface. At this position, the thermocouple is far enough from the flame front to avoid temperature gradient and probe intrusive effects while still in a region of high OH fluorescence. This calibration constant was then applied to the remainder of the flame and the temperature field was computed.

Figure 7.8 shows an example temperature profile for a stoichiometric propane flame using this technique. The peak temperature stands off of the burner surface approximately 0.75 mm with a peak value of approximately 1900 K. The temperature then declines to a steady value of approximately 1750 K due to heat loss to the porous plug and gas radiation. Below approximately 200 μm above the burner surface, the OH fluorescence signal for both rotational transitions drops significantly as seen in Fig. 7.7, therefore it is difficult to measure the temperature so close to the burner surface. Qualitatively, this technique yields temperature profiles similar to those measured with the thermocouple technique above, however the region of peak

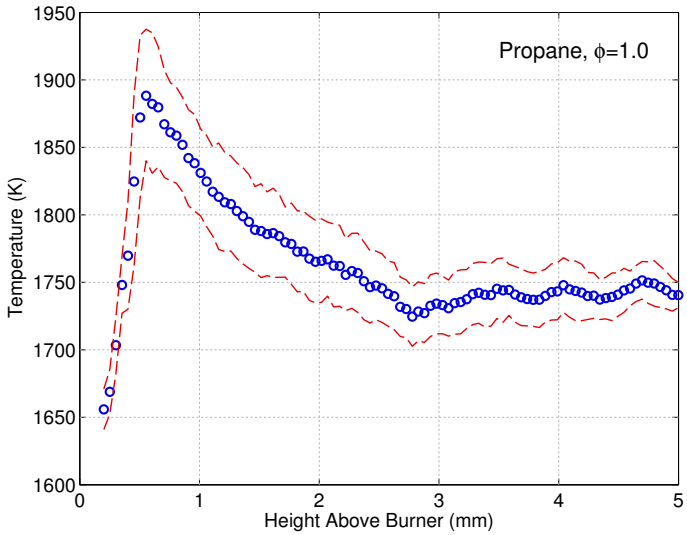

Figure 7.8: Sample temperature profile for stoichiometric propane flame measured using 2λ-OH LIF thermometry.

temperature shows a sharper peak, with a peak temperature approximately 50 K higher.

7.2.3 Merged temperature profiles

The goal is then to utilize the strengths of both techniques and merge the temperature profiles to provide a defined temperature profile for modeling in Section 7.3. Thermocouples typically provide the most accurate temperature measurements in regions where the flow is steady, gradients are low, and interference in the flame is limited. Complimentary to the limitations of thermocouples, 2λ-OH LIF thermometry can provide non-intrusive measurements where the concentration of OH is high, such as the flame zone. The following criteria establish the method for merging the profiles:

1. In low gradient, post-flame regions, thermocouple measurements are chosen. However, because the OH thermometry is calibrated in this region, differences between the two techniques are expected to be relatively small.

2. In steep gradient, high OH concentration regions, such as through the flame

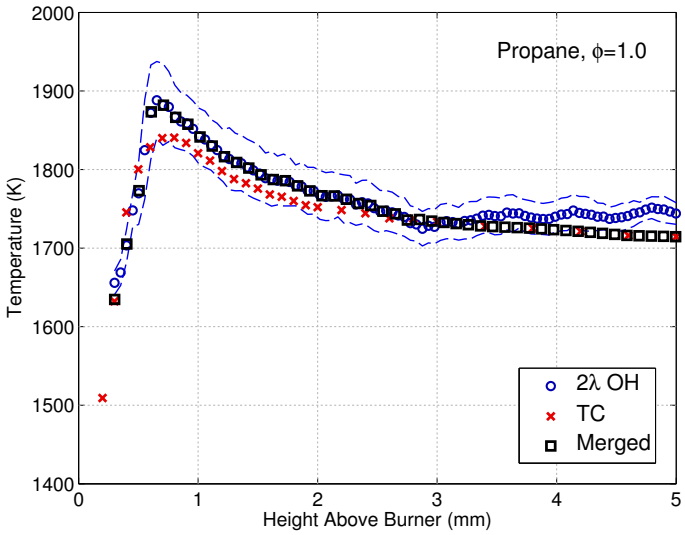

Figure 7.9: Temperature profiles for a stoichiometric propane flame, measured with thermocouples (TC), 2λOH thermometry (2λ OH), and merged techniques.

zone, OH thermometry measurements are chosen.

3. In high gradient, low OH concentration regions, such as very near the burner surface, both techniques are limited. For all cases the burner surface temperature is measured with an IR thermometer and is assumed to be reasonably close to being in thermal equilibrium with the exit gas temperature.

4. Intermediate temperatures near the burner surface are interpolated over the approximately 100–200 μm thick intervening region where the OH LIF signal is low.

Continuing the example with stoichiometric propane, Fig. 7.9 illustrates the merger of the two techniques. It can be seen that initial agreement between the two technique is quite good and the merger yields a reasonable temperature distribution that takes advantage of the strengths of both techniques while minimizing the individual weaknesses. This procedure is repeated for all the conditions and used as the fixed gas temperature profile for modeling the flame in CHEMKIN.

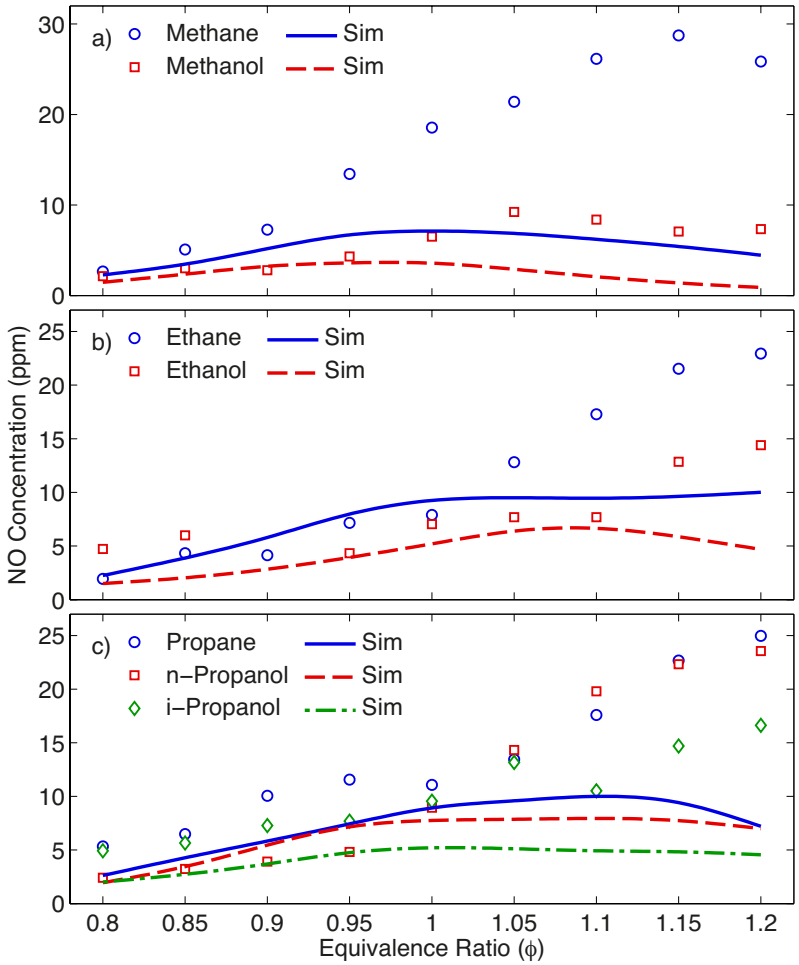

Figure 7.10: Measured and predicted NO concentration profiles for a) C_1, b) C_2, and c) C_3 alcohol and alkane flames at 3 mm above burner.

7.2.4 Measured and predicted NO and HC species concentrations

Concentrations of NO were measured in the post flame region (3 mm above burner surface) and are shown in Fig. 7.10, with predictions from simulations overlayed. For methane and ethane, trends are similar to those observed in Refs. [206, 207] and [208]. Under lean conditions, the model and experiments for the C_1 fuels agree well, however the model significantly underpredicts in the rich regions. For the C_2 and C_3 flames, the model generally underpredicts, especially in the rich region. However, the primary objective in this analysis is to capture qualitative trends with respect to fuel

families.

Measurement uncertainties in this experiment can be induced through probe intrusion effects, probe-wall interactions, and post-quench reactions [209, 210]. However, Konnov [210] showed that for a similar configuration, the intrusive effect of the probe at this position was low. Additionally, Allen [209] showed that prob-wall interactions and post-quench reactions were less prevalent when collected sufficiently far from the flame front. The consequence for these experiments is that any measurement error should be systematic for both the alcohol and alkane fuels, and should not greatly impact the trends observed with regard to the initial fuel. Ultimately, predicted NO concentrations in alcohol flames are consistently lower than in alkane flames and the greatest differences are observed in rich flames. Predicted concentrations in the propane and the n-propanol flames exhibit the least difference, however it appears that n-propanol is over predicted in the lean region.

The accuracy of the NO predictions, especially in these lower temperature flames where Thermal NO formation is minimal, are strongly influenced by the ability of the model to accurately predict hydrocarbon radical concentrations, namely $CH_{i=1,2,3}$ and HCCO, which are key components in the fixation of nitrogen and will be discussed in the following section. Lipardi et al. [211] showed that significant uncertainties in the predicted concentrations of NO can be present when the base and NO_X mechanisms are not tuned to each other; however the interest in this work is a comparative analysis between fuels, not the predictive quality of absolute NO.

While not shown in Fig. 7.10, sensitivity to perturbations in measured temperature profile were also investigated. The temperature profile was shifted up and down by the uncertainty in the merged temperature profile (example in Fig. 7.9), however the resultant shifts in predicted NO concentrations were less than ± 3 ppm at the highest, indicating deviations in measured and predicted NO concentrations were not a result of temperature measurement uncertainty.

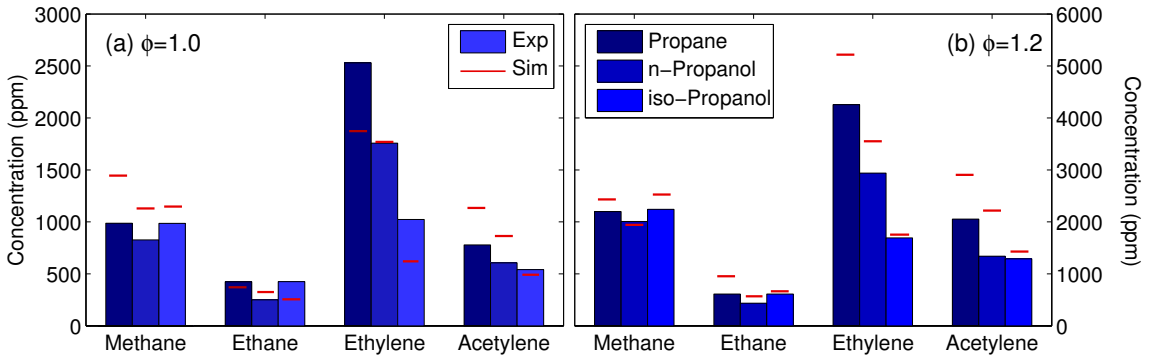

Figure 7.11: Measured and predicted peak C_1 and C_2 saturated and unsaturated HC concentrations for the C_3 fuels at stoichiometric and rich conditions.

Gas samples for stoichiometric and rich C_3 flames were also collected through the flame and analyzed with an Agilent Refinery Gas Analyzer (RGA). This system utilizes a combination of eight columns and three detectors (two TCD and one FID) for the identification of H_2, O_2, N_2, CO, and CO_2, and saturated and unsaturated C_1-C_5 hydrocarbons. Figure 7.11 shows the results of peak saturated and unsaturated HC concentrations and comparisons with predicted peak concentrations. The relative contributions of these species is interesting as a indicator of the preference for decomposition pathways resulting in reduced concentrations of HC radicals, particularly concentrations of the unsaturated HC species such as ethylene and acetylene. Recall from Section 6.3 that the presence of the hydroxyl group(s) leads to a preference for pathways in which these unsaturated hydrocarbons are not readily produced, resulting in lower concentrations of unsaturated intermediates and ultimately lower contributions to CH radical formation.

7.3 Reaction path analysis

Imposing the temperature profiles of Section 7.2.3 on the burner stabilized flat flame module of CHEMKIN-Pro allows for a more detailed investigation of the relative contributions of the various NO formation sub-mechanisms. One approach for conducting

this investigation is to define a set of reactions for the thermal mechanism and a set for the full mechanism and attribute the difference to a prompt or Fenimore mechanism, less contributions from any minor sub-mechanisms under consideration [212]. However, there are limitations to this approach due to the coupling of the thermal mechanism with other sub-mechanisms [213].

Alternatively, a better approach is not to consider the thermal sub-mechanism isolated from the remainder of the nitrogen chemistry, but rather to investigate the NO_X sub-mechanisms in the presence of all other NO_X sub-mechanisms [214]. However, again there are limitations in this approach. As the number of reactions necessary to capture nitrogen chemistry has grown, the simplification in prescribing individual reactions to a single sub-mechanism has not kept pace. Using this technique, individual mechanisms can only be attributed to a single sub-mechanism, regardless of whether the reactions preceding a given step contain contributions from more than one sub-mechanism. Several examples include the second and third reactions of the thermal sub-mechanism, involving the oxidation of N atom:

$$N + O_2 \rightleftharpoons NO + O \tag{7.10}$$

$$N + OH \rightleftharpoons NO + H \tag{7.11}$$

where attribution of these two reactions to the thermal sub-mechanism neglects contributions to the N atom radical pool from other sources, such as those in the early stages of the prompt initiating sub-mechanism:

$$NCN + OH \rightleftharpoons HCN + NO \tag{7.12}$$

$$HCN + O \rightleftharpoons NCO + H \tag{7.13}$$

$$NCO + H \rightleftharpoons NH + CO \tag{7.14}$$

$$NH + H \rightleftharpoons N + H_2 \tag{7.15}$$

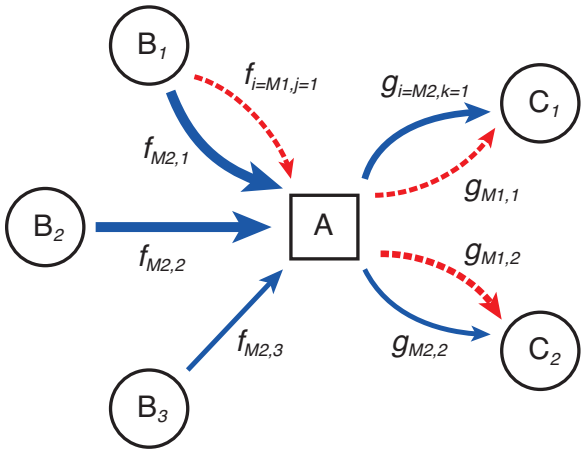

Figure 7.12: Demonstration of nitrogen flux accounting scheme for tracing the flux through species A attributable to mechanisms M1 and M2.

Additionally, reaction 7.15 is also a participant in the NNH and N_2O sub-mechanisms. Clearly, care must be taken in the accounting and attribution of NO_X formation to a particular sub-mechanism.

7.3.1 Nitrogen flux accounting

An alternative approach is to use a variation on this last technique. In contrast to predefining a chemistry subset, this work distinguishes the various NO formation pathways by 'tracing' the flow of nitrogen that has been unfixed from inert molecular nitrogen N_2, utilizing the complete set of nitrogen chemistry so that all reactions proceed in the presence of the others while not limiting attribution of an individual reaction to a single sub-mechanism.

To achieve this objective, the total flux of nitrogen between all nitrogen containing species is calculated at each position in the flames. Each species is then analyzed for all pathways leading to its formation, as well as all the possible products from the reaction of this species. This scheme is illustrated in Fig. 7.12. Here, the objective is to determine the flux from species A to C_1 attributable to mechanism M1, which has been notated as $g_{M1,1}$. Now, the determination of this attribution is dependent

on whether the concentration of species A is locally increasing or locally decreasing. For convenience sake, several terms can be defined in advance. The flow into target species A from a given reactant species B_j attributable to a mechanism M_i is notated as $f_{i,j}$. Meanwhile F_j is sum of all flows into species A from any reactant species B_j attributable to any mechanism. Similarly, $g_{i,k}$ is the flow from species A to any product species C_k attributable to mechanism M_i while G_k is the total flow from A to C_k from all mechanisms.

If the concentration of A is increasing, then the total flux into species A, $F = \sum F_j$, is greater than the total flux out, $G = \sum G_k$ In this situation, a simple accounting of the inflow contributions would result in an over-attribution to the outflow pathways. A similar logic yields the opposite result when the concentration is decreasing. Additionally, since NO sub-mechanisms can be active at different times and positions throughout the flame, it is necessary to account for this flux at the appropriate time. Ultimately, equation 7.16 is used when the concentration of A is increasing and equation 7.17 is used when the concentration of A is decreasing,

$$g_{i,k} = G_k \frac{\sum_j f_{i,j}}{\sum_{i,j} f_{i,j}} \tag{7.16}$$

$$g_{i,k} = f_{i,j} \frac{G_k}{\sum_k G_k} \tag{7.17}$$

where the indices i, j, and k correspond to the sub-mechanism, reactant species, and product species, respectively.

One limitation of this approach is that it is difficult to assess the source(s) of a species whose population is consumed without replenishment. For example, the species HCN accumulates through several mechanisms in the flame zone (such as the Prompt and NO-HCN Reburn mechanisms), but can be consumed relatively slowly when the availability of O atom is limited [35]. This results in the continued flux of nitrogen after the formation of HCN has shut off and HCN continues to be consumed

in the post-flame region. Ultimately, this makes attribution of this flux to a specific sub-mechanism difficult. Therefore, this formulation attributes such consumption of accumulated species to a classification called 'Burnout' in the following analysis.

7.3.2 NO_X sub-mechanism contributions

Having developed a strategy for accounting for the contributions of various NO sub-mechanisms, it is now necessary to define the mechanisms to be investigated. Section 1.1 provides a more detailed survey of the various NO_X mechanisms, however it is convenient to discuss some of the major contributions here as well.

Figure 7.13a shows the Prompt formation pathway, which is controlled by the fixation of nitrogen to carbon, primarily through reaction of N_2 with CH. This initiating reaction in the Prompt NO pathway is sensitive to both the availability of CH and the reaction rate. The resulting NCN then proceeds directly to NO while also forming HCN, CN, and N (which further contribute to NO formation through NCO and $NH_{i=0,1,2}$). Given the relatively low temperatures measured in these flames, it is expected that this mechanism will be one of the primary sources of NO formation.

The NO-HCN Reburn mechanism is shown in Fig. 7.13b. While naturally occurring in these flames, NO reburning has also previously been investigated as an NO control mechanism through the staged addition of fuel [28, 194]. Here, NO is consumed through reaction with ketenyl (HCCO) or methyl radical (CH_3), dependent on the conditions and availability of radicals, resulting in the formation of HCN (either directly or through intermediates HCNO and H_2CN). Under radical rich conditions, additional removal can occur through combination with CH and C to HCN and CN, respectively [14]. HCN can then either reform NO, or proceed to be converted to N_2 through NCO and NH [35].

Shown to be important in lean, low temperature as well as fuel-rich conditions [45, 46, 163, 215], the formation of NO from the combined NNH and N_2O mechanism

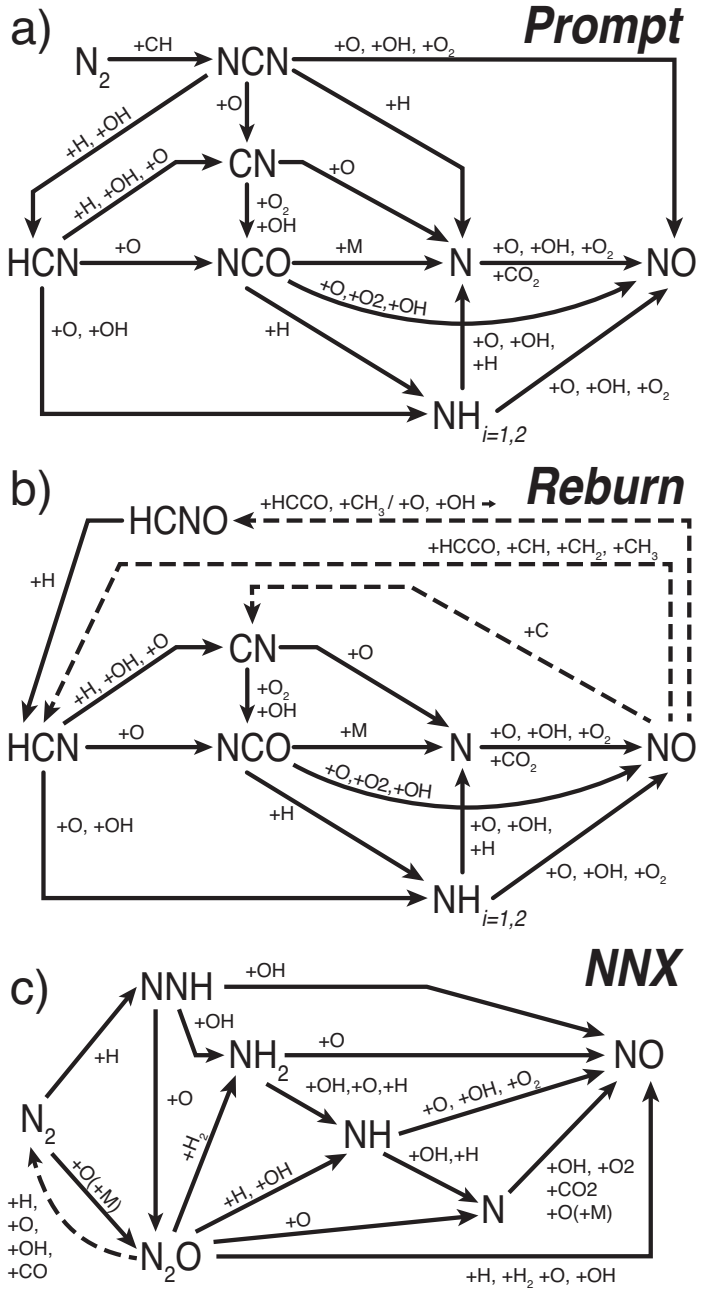

Figure 7.13: Selected NO reaction path diagrams for a) the Prompt mechanism, b) the NO-HCN-Reburn mechanism, and c) the combined NNH and N_2O mechanisms.

(NNX) is shown in Fig. 7.13c. NO formation is initiated through N_2+H to NNH which can form NO and NH_2 through reaction with OH. Additionally, N_2O can form through NNH+O as well as N_2+O(+M), closely coupling both mechanisms.

Not shown in Fig. 7.13, but included in the analysis are the Thermal mechanism, NO_2, and HNO mechanisms. The Thermal mechanism has long been studied and is fairly well understood [2]. Peak temperatures in these flames are relatively low (<1900 K), therefore thermal contributions to NO are limited throughout this analysis, and are not greatly influenced by the initial fuel. Therefore, the majority of the difference in NO formation observed in these flames is due to differences in non-thermal pathways.

The NO_2 mechanism has been shown to result in the rapid transition of NO to NO_2 and back. Formation of NO_2 is achieved through reaction of NO, which has diffused upstream, with HO_2, which is present in high concentrations in the low-temperature regions early in the flame [2]. Later in the flame, NO_2 can rapidly reform NO through reactions with H and O. Finally, NO formation and destruction reactions through HNO are considered, forming HNO through combination with H(+M) and reforming NO through combination with H and CO.

Applying this formulation to an example flame, one can trace the formation of NO through the various pathways in sequence. The predicted total rate of production of NO in a series of lean ($\phi = 0.9$) propane, n-propanol, and i-propanol flames is shown in Fig. 7.14. These flames provide a nice demonstration of all the participating NO mechanisms. By tracing the flux of nitrogen using the formulation above, the contribution to NO formation for each of the considered reaction pathways is overlayed, along with the sum of the contributions of each of the considered mechanisms. The strong match between calculated NO formation rates (black circles) and the sum of the NO formation mechanisms described above (dashed line) is a clear indicator that this formulation adequately captures the total formation of NO.

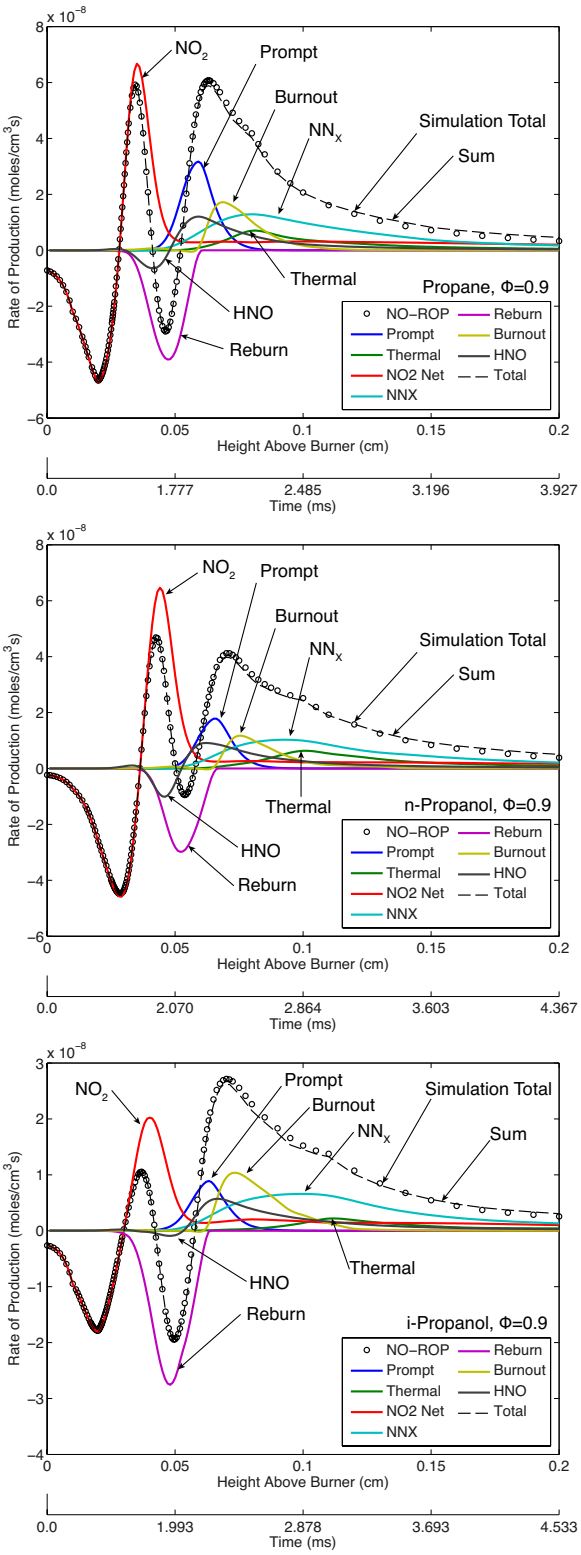

Figure 7.14: Demonstration of total NO rates of production and deconstruction into constituent formation pathways for lean ($\phi = 0.9$) C_3 flames.

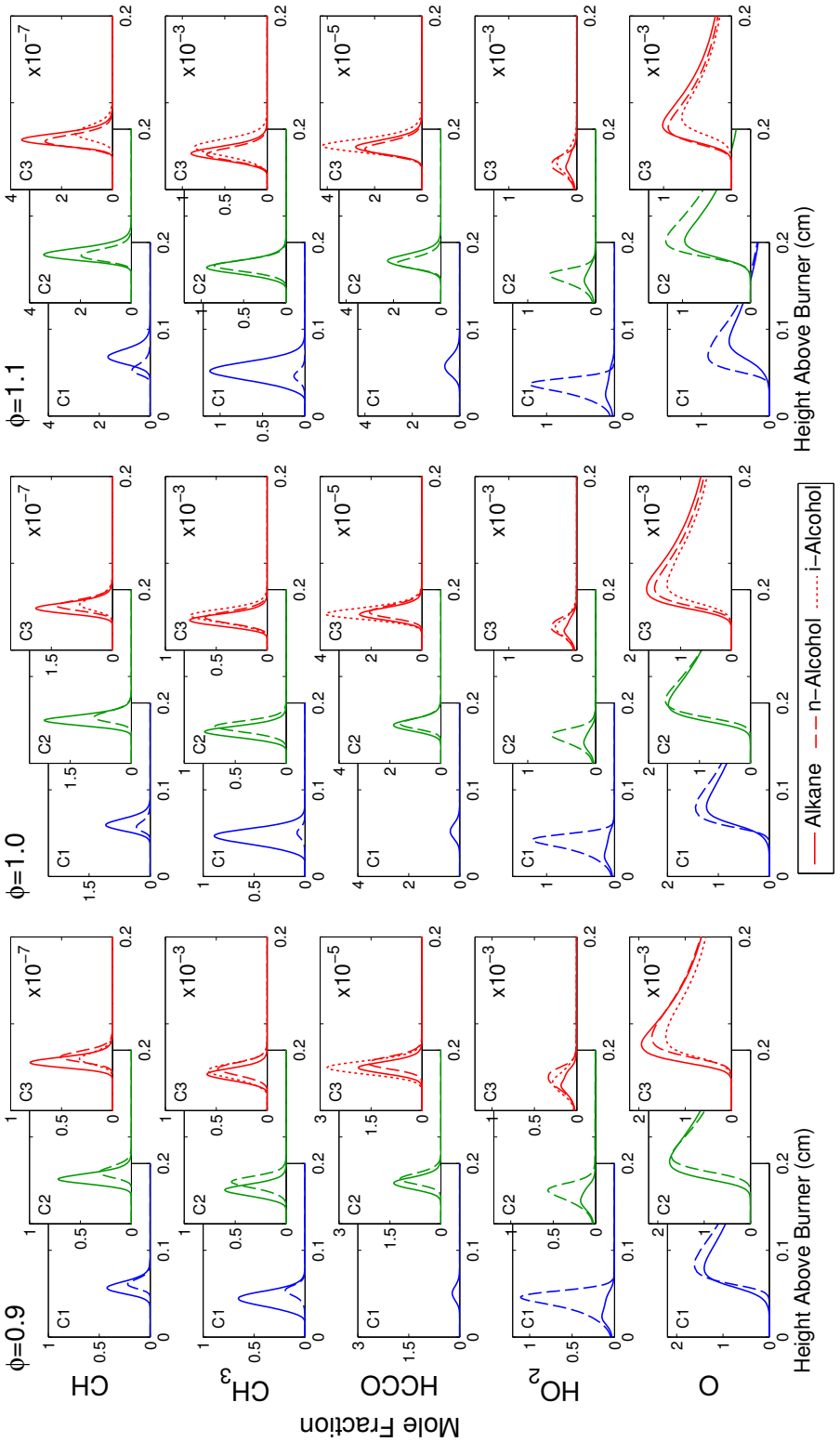

Figure 7.15: Mole fractions of selected species influectial to NO formation.

Marching through the flame, general trends in NO formation can be observed, which are mostly consistent for the fuels studied here. Accompanying the analysis of Fig. 7.14, profiles for several of the important intermediate species are shown in Fig. 7.15. These intermediate species directly influence the formation and consumption of NO through the flame. In the cold, preheat zone, high rates of NO consumption are observed due to high concentrations of hydroperoxyl radical HO_2 reacting with forward diffused NO and forming NO_2. Immediately after forming, NO_2 reforms NO due to the establishment of the O and H radical pools and the instability of NO_2 at high temperatures [216]. A sink for NO is also observed at this position in the flame through the formation of HNO.

Next, coinciding with the formation of HCCO and CH_3, consumption of NO through the NO-HCN Reburn mechanism reaches a peak. While a portion of the consumed NO ultimately returns to NO, a greater proportion remains in the pools of C-N radicals. Overlapping the Reburn mechanism and coinciding with the peak concentration of CH radicals, the Prompt mechanism turns on through the fixing of nitrogen to carbon through $CH+N_2$. Through depletion of HCCO and CH_3, the destruction of NO through the Reburn mechanism then slows, followed by the depletion of CH and the slowing of the Prompt mechanism.

Now the accumulated NO intermediate species HCN, CN, NCO, and N (which have formed primarily through the Prompt and Reburn mechanisms) continue to form NO as shown in the Burnout contribution, either through reaction with O, OH, and O_2 in lean flames or through limited reactions with H in rich flames. Parallel to the C-N mechanisms, the NNX mechanism operates broadly through the post flame zone, beginning prior to the start of Thermal mechanism. Lastly, the Thermal mechanism turns on in the post-flame zone; limited by slow reaction rates and low temperatures, the Thermal mechanism generally contributes only a small proportion of the NO formed in the flames studied here.

Figure 7.16 compares the peak rates of production for several of the mechanisms considered here. Shown in Fig. 7.16a, peak rates of production through the Prompt mechanism are clearly lower in the alcohol flames, compared with the alkanes. All fuels exhibit the greatest rates of formation on the slightly rich side of stoichiometric (where availability of O, OH and O_2 overlap with H and CH and high peak temperatures), falling toward the lean side as CH is reduced and toward the rich side as O, OH, and O_2 become scarce. Generally, the greatest difference is seen in comparison of methane and methanol flames, with a smaller difference in the C_2 flames, and even smaller when comparing propane and n-propanol. Interestingly, iso-propanol is reduced further still. As has been discussed before [18, 22, 193, 207], formation of Prompt NO is inherently linked to the availability of CH, thus lower concentrations of CH in Fig. 7.15 will directly reduce NO. While accurate predictions of CH is difficult and models generally underpredict CH concentrations [217], the important consideration here is the relative contributions in comparison of the alkane and alcohol fuels. Therefore variations in the reaction rates of CH formation are of secondary importance to evaluating trends between fuels.

Figure 7.16b shows the variation in the net rate of NO consumption through the Reburn mechanism. Lower concentrations of NO measured in alcohol flames are often attributed solely to reduced formation of Prompt NO [9, 103, 105, 218]. However, Fig. 7.16 shows that this generalization is complicated through a simultaneous reduction in the rates of consumption of NO through the Reburn mechanism. Lower concentrations of HCCO and CH_3, as shown in Fig. 7.15, result in reduced rates of NO consumption, which partially offset the lower rates of Prompt NO formation. Additionally, recall that the Reburn mechanism generally precedes the Prompt mechanism as shown in Fig. 7.14, directly influencing the forward diffusing NO necessary for the NO_2 mechanism. This competition for forward diffused NO by the Reburn and NO_2 sub-mechanisms is further impacted by the significantly higher concentrations of HO_2

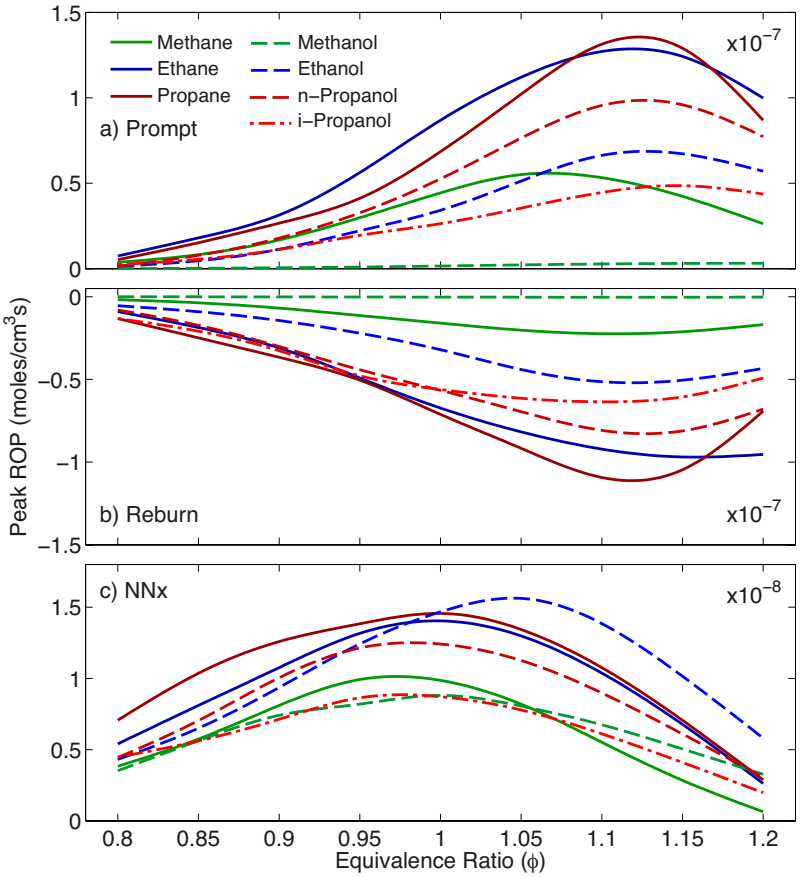

Figure 7.16: Comparison of peak NO rates of production for the a) Prompt, b) NO-HCN Reburn, and c) NNX mechanisms.

(the primary reactant in forming NO_2 from NO) in alcohol flames. Interestingly, rates of consumption for the C_3 fuels demonstrate little difference in the lean region, likely due to higher concentrations of HCCO in the iso-propanol flames. Despite higher concentrations of HCCO, rates of consumption are lower in rich alcohol flames due to the combined effect of reduced overall concentrations of NO and CH_3.

While the peak rates of production shown in Fig. 7.16c for the combined NNX mechanism are lower than those in the Prompt mechanism, the duration over which the NNX mechanism is active indicates that this mechanism can constitute a substantial portion of the NO formation in these low temperature flames. This is especially true in the lean (and to a lesser extent, rich) extremes of this study where contributions form the other formation mechanisms are reduced. Variations in NNX peak

rates for the C_1 fuels are minimal, while rates for the C_2 flames are greater for the alkane flames under lean conditions and the alcohol flames in rich conditions. Availability of O atom becomes the controlling factor in conversion of NNH and N_2 to N_2O and then to NO in the C_3 alcohol flames, which also accounts for the higher rates in the rich ethanol cases.

7.4 Conclusions

The objective of this chapter was to examine the formation of NO in laminar premixed burner-stabilized alkane and alcohol flames. Temperature measurements were utilized as input for modeling the various flames. Then comparisons of experimentally measured NO concentrations and peak intermediate saturated and unsaturated hydrocarbons were compared with the model's predictions. Lastly, a detailed reaction path analysis of the relative contributions of several NO formation pathways were compared.

It was observed that under lean conditions, the predictive capability for concentrations of NO with this mechanism is adequate, however discrepancies were observed for the C_3 alcohols. Additionally, for all fuels, NO was significantly under-predicted in the rich region. These errors are most likely due to the difficulty in accurately predicting hydrocarbon radical concentrations, namely $CH_i = 1, 2, 3$ and HCCO.

It was shown that NO formation in the alcohol flames, which generally exhibit lower temperatures, is greatly influenced by the combination of several intimately coupled mechanisms. This coupling complicates the assessment of a single cause for lower observed NO concentrations in alcohol flames.

Significant rates of consumption of NO through the NO-HCN Reburn mechanism were observed. This mechanism is closely tied to concentrations of HCCO and CH_3. Rates of NO consumption through the Reburn mechanism were predicted to be com-

parable with rates of NO production through the Prompt mechanism, indicating that this mechanism can significantly influence NO concentrations. Additionally, while lower concentrations of NO measured in alcohol flames are often attributed to lower Prompt formation due to lower concentrations of CH, it was shown that consumption of NO through the NO-HCN Reburn was also reduced through variations in the concentrations of CH_3 and HCCO in the alcohol flames, offsetting a portion of the NO reduction attributable to the Prompt mechanism.

'Minor' NO formation pathways, such as the combined NNX, were demonstrated to be of increased importance in these low temperature flames. These pathways represent a greater component of the total NO formed, especially in the alcohol flames, than would traditionally be considered in higher temperature flames.

Chapter 8

NO LIF concentration measurements in alcohol and alkane flames

The objective of this chapter is to further probe the formation of NO in alcohol flames through non-intrusive measurements in the region of the flame front. Intrusive techniques for NO concentrations measurements, such as probed or extractive gas sampling, are not well suited to measurements in regions of flames with fine structures such as the flame front. Rather, in-situ laser diagnostics offer robust techniques for measuring certain species through laser induced fluorescence (LIF) with minimal disturbance to the flame. This chapter will apply quantified NO LIF measurements to the flame front region of the flat flames measured in Chapter 7 as well as Bunsen conical premixed flames. Between these two burner configurations, NO formation under higher and lower temperature fields will be considered. This will allow for the consideration of both thermal and non-thermal contributions. Additionally, the non-intrusive nature of this technique allows for a better measurement of the relatively rapid formation of NO in the flame front as a distinct contribution from the Thermal mechanism.

Table 8.1: Experimental conditions for Bunsen flame experiments

Property	(Units)	Conditions
ϕ		0.8–1.2
Temperature	(°C)	100
Ratio to S_L		2.5
Exit velocity at ϕ=1.0	(cm/s)	
Methane	-	150.8
Ethane	-	160.9
Propane	-	158.9
Methanol	-	190.1
Ethanol	-	178.8
n-Propanol	-	147.5
i-Propanol	-	136.7

8.1 Experimental setup

The experimental setup in this chapter utilizes two flame configurations. The first flame is a Bunsen-type premixed flame. A contoured 10 mm nozzle (described in Section 2.2.2) stabilizes a conical flame with equivalence ratios between 0.8 and 1.2. Table 8.1 shows the experimental conditions, and it can be seen that conditions are similar to those in the flat flame. In order to avoid flash back, the exit velocity was fixed at a constant 2.5 times the laminar burning velocity, which allowed for a relatively constant flame height (within the uncertainty of the extrapolation of laminar burning velocity to the 100°C unburned gas temperature). The second configuration is a burner stabilized flat flame, identical to that described in Chapter 7. The experimental conditions are exactly the same and measurements of the temperature field above the burner surface will be used in the LIF quenching analysis.

8.1.1 Laser diagnostic setup

The measurements in both burner configurations are conducted by laser induced fluorescence of NO in the linear regime. More details on the theory of NO LIF, experimental considerations, and quantification of the stimulated emission is included

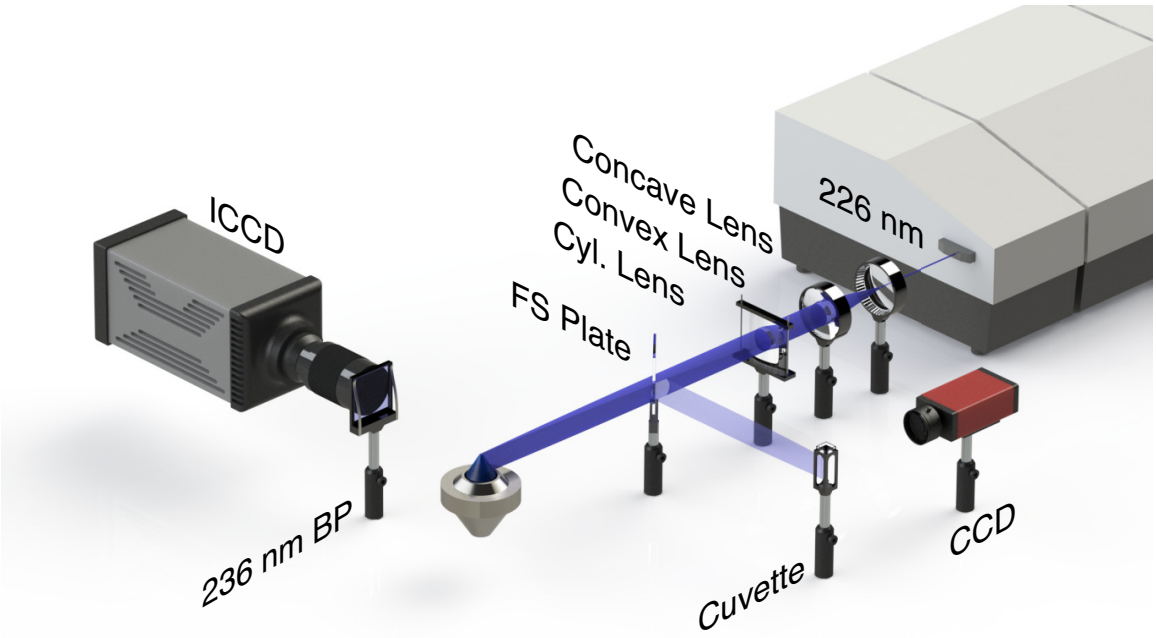

Figure 8.1: Experimental setup for NO LIF with the Bunsen flame.

in Section 2.3.3. This section will focus more closely on the practical aspects of implementing this technique. The optical setup in the flat flame is very similar to that in Fig. 7.3, while the set up for the Bunsen flame is shown in Fig. 8.1.

This technique utilizes a 10-Hz Continuum Nd:YAG pumped, frequency doubled Rhodamine dye-laser with output near 287 nm, which is then mixed with the 1064 nm fundamental output of the Nd:YAG yielding a mixed output in the neighborhood of 226 nm and approximately 1 mJ per pulse. Excitation of the A-X(0,0) band with selection of the $P_1(23.5)$, Q_1+$P_{21}(14.5)$, Q_2+$R_{12}(20.5)$ rotational lines at 225.963 nm (in air) has been shown to maximize signal strength while minimizing interference from molecular oxygen LIF [121, 157, 161]. Emission was detected by a gated Princeton Instruments PI-MAX3 blue-enhanced ICCD. Broadband emission of the A-X(0,1) band was collected with a custom manufactured Asahi Spectra narrow bandpass filter centered at 236 nm with 7.5 nm full width at half maximum. Due to the low concentrations of NO, single shot signals are very low, therefore 200 shots were accumulated on the CCD chip for each condition. The laser was also detuned (shifted 0.011 nm

to the red side) to observe background and O_2 LIF to be included in the correction procedure.

During post processing, corrections were made to account for fluctuations in the shot-to-shot total energy as well as the spatial distribution of energy. Because LIF signals were accumulated on chip, it is not possible to correct for single shot fluctuations, however the energy and spatial distribution of the shots composing a given exposure were averaged and the mean correction was applied. Operation in the linear regime was verified for both the on and off-line exposures and the profile correction fluorescence. Lastly, corrections for non-linearity in the pixel response in the spectral range of 236 nm was applied. Additional details of these processes are provided in Section 2.3.3.

In order to quantify the NO LIF, knowledge of the local temperature and quenching species concentrations (N_2, H_2O, CO_2, CO, O_2, and NO) are necessary. Because experimental measurements of all these parameters is difficult and expensive, it was decided that the best course of action was to model these parameters. A full computational study of a three dimensional axisymmetric flame would also be computationally intensive. However a decent approximation to the three dimensional Bunsen flame front is a one dimensional freely propagating flame. Fristrom [219] showed fairly early on that temperature and density profiles of the three dimensional flame are well reproduced in the near field by the one dimensional model. Later, Nguyen [220] showed with Raman-LIF measurements that major species (including CO, OH, and NO) and temperature were able to be satisfactorily predicted by a one dimensional freely propagating premixed flame model with finite rate chemistry. A number of other studies have indicated good approximations of most of the Bunsen flame surface by one-dimensional flames [124–126, 128, 133]. Therefore, with a greater interest in the differences in NO formation between families of fuels than in the absolute concentrations NO, it was decided to proceed with a one dimensional model utilizing the

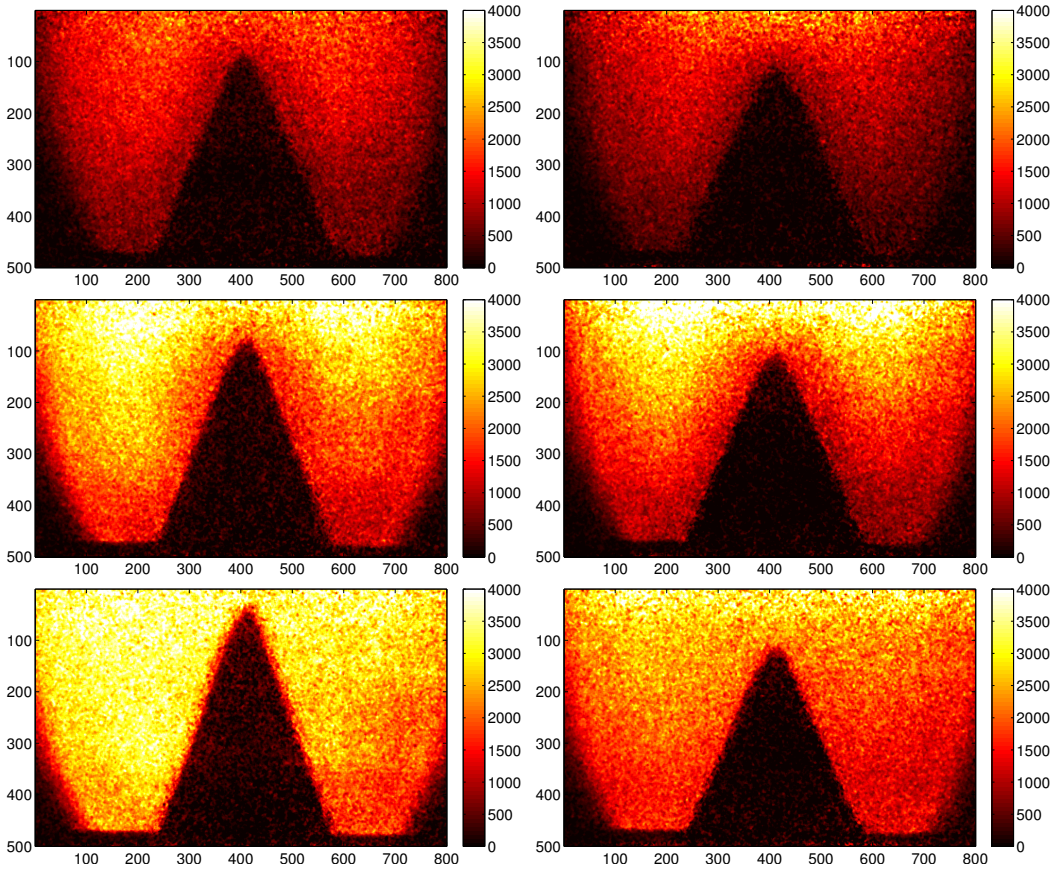

Figure 8.2: NO fluorescence images for propane (left) and n-propanol (right) under lean, stoichiometric, and rich conitions.

chemistry set in Section 7.1.3, and limit the analysis to regions very near the flame front with minimum dilation and buoyancy effects.

8.2 NO LIF in Bunsen flames

The first configuration examined will be the Bunsen flame. After applying the correction scheme for background, dark current, and O_2 LIF, shot-to-shot fluctuations in total energy and energy distribution, pixel linearity, and spatial calibration, images such as those in Fig. 8.2 are produced. Immediately, certain qualitative trends can be observed:

1. Specifying the exit velocity as a constant factor of the laminar burning velocity

does a decent job of controlling the height of the flame, allowing the flame to stay within frame under considerably different exit velocities.

2. The correction process for fluctuations in the energy distribution does a good job of correcting for spatial variations through the vertical axis.

3. Absorption of the excitation beam through the flame results in the slight attenuation of the fluorescence signal when comparing the left and right hand sides of the image.

4. NO LIF fluorescence increases from lean to rich.

5. The flame front is a relatively straight region once sufficiently far from the base of the flame or from the tip of the flame.

6. The region of interest, the area within the first 2 to 3 mm normal to the flame front, is the targeted region for observing the rapid formation of NO through the flame.

7. NO LIF fluorescence in the region of interest for lean flames shows a relatively slow increase in signal normal to the flame, whereas the stoichiometric flames shows a more rapid rise, while the rich flames shows the highest gradient in NO LIF signal.

8.2.1 Determination of flame front and positioning

The objective here is to quantify the NO concentrations through the flame. Toward this objective, it was then necessary to analyze the NO LIF signal in the region of interest, determine a LIF signal normal to the flame front, and apply corrections for collisional quenching. The first step in this process is to identify the flame front in each condition. For this process, the edge is identified by an erosion algorithm for boundary extraction. This algorithm utilizes an arbitrary structuring element (a 5

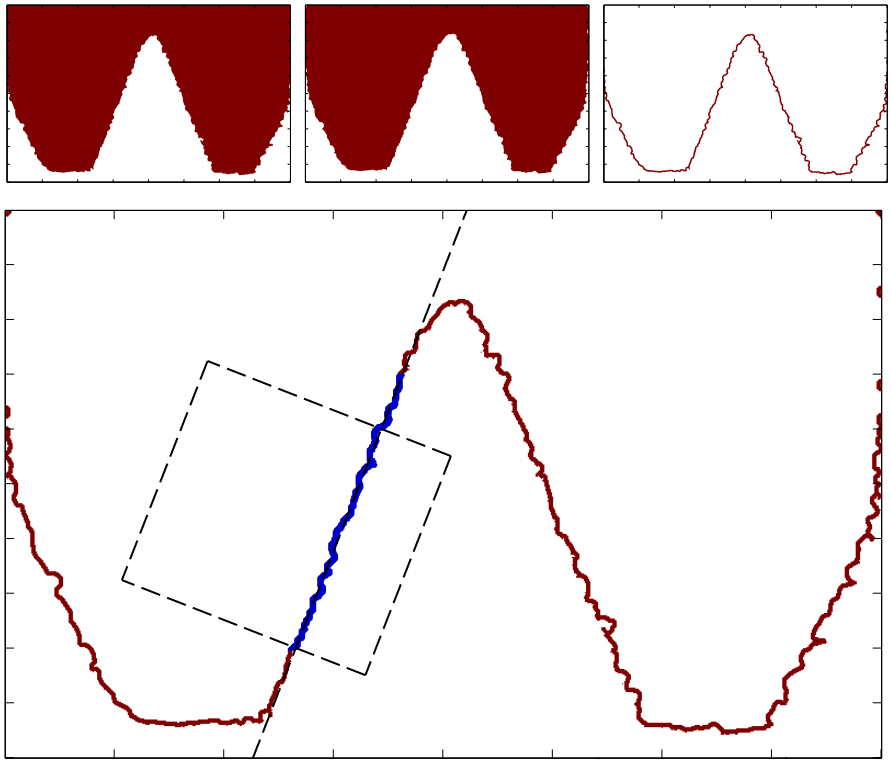

Figure 8.3: Process for edge detection in Bunsen flames.

pixel disk in this case) to erode a binarized image. This eroded image is subtracted from the original binary, resulting in the edge binary. This process can be expressed in equation 8.1

$$\beta\left(A\right) = A - \left(A \ominus B\right) \tag{8.1}$$

where A is the original binarized image, B is the structuring element, and $(A \ominus B)$ is the eroded image, yielding the boundary β. The threshold value for the binarization of the original image is determined as the value at which the LIF signal increases to 1/3 of the spread between the pre-flame and post-flame max fluorescence. An example of this process is included Fig. 8.3 The top three sub-figures show A, $(A \ominus B)$, and the resultant boundary, respectively. One must look very closely to see the difference between the original and eroded images, however careful inspection would show a slight softening of the edges and retraction of the surface due to the structuring element. The very fine details in the original binary image along the edge

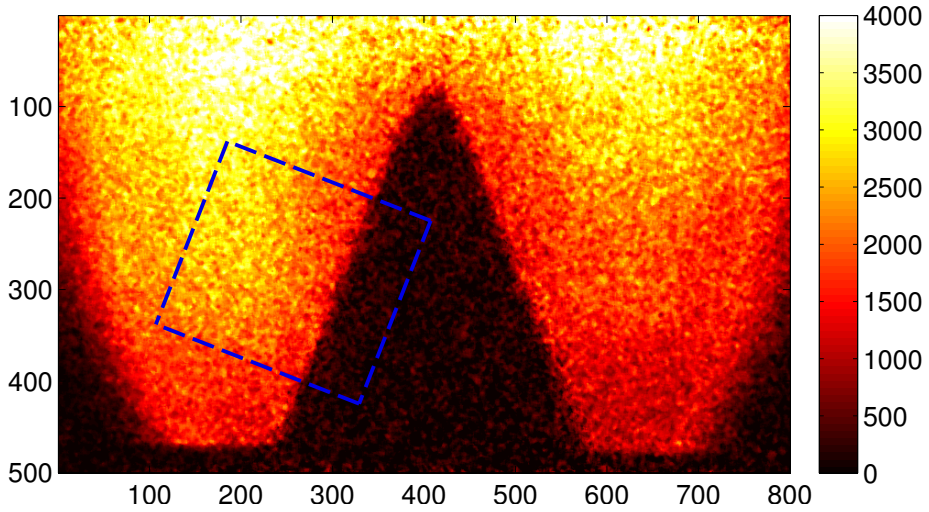

Figure 8.4: Region of interest in stoichiometric propane flame as identified with the flame front detection scheme.

of fluorescence are reduced due to the erosion by the structuring element. Finally, simple subtraction of the two binary images yields a boundary several pixels thick.

After identifying a boundary, it is then necessary to identify the region of interest, particularly to identify a coordinate system normal to the flame surface. This is achieved by fitting a line to the pixels along the flame surface as shown in blue in Fig. 8.3. To improve the quality of fit, and to limit interference from noise which can develop near the base and tip of the flame under conditions with low LIF signal, a Gaussian weighting function was applied to the boundary pixels used in the linear fit. The weighting function was centered in the middle of the flame surface with a standard deviation defined as a quarter of the length of the of flame surface. This distribution gives a greater weight in the fit to the region of the flame least influenced by the tip and base of the flame and yielded a better fit. Using this linear fit, the normal to the flame surface was defined, and a region extending 2 mm into the pre-flame and 5 mm into the post flame was identified as the region of interest as shown in Fig. 8.3.

Then, for each condition, the specific ROI is overlayed to the original LIF image as shown in Fig. 8.4 and data from this region is the objective. Pixel value cross

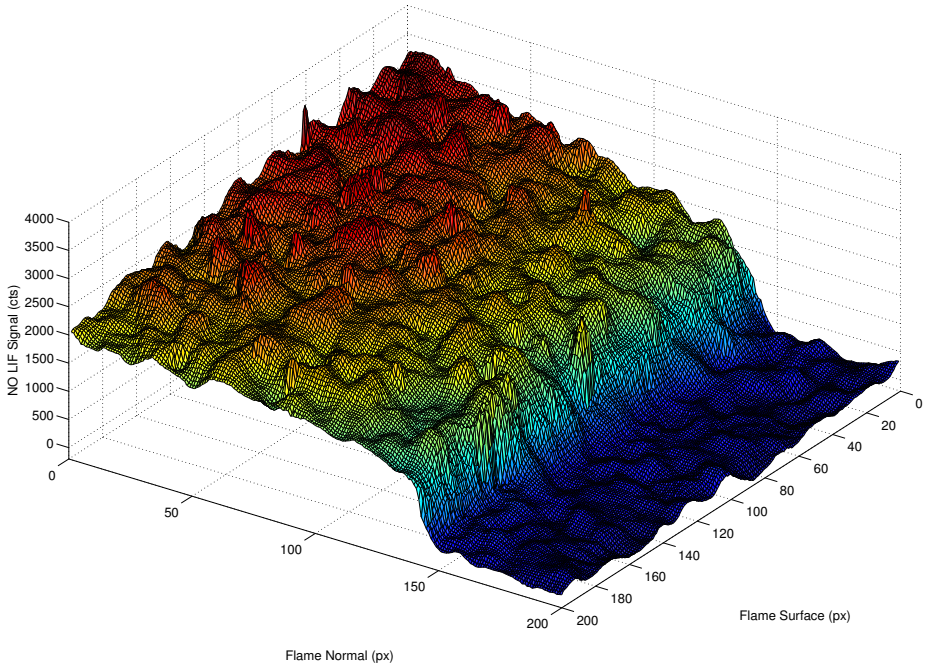

Figure 8.5: Surface plot of NO LIF in region of interest for stoichiometric propane.

sections of the NO LIF signal along segments normal to the flame front are extracted at 200 points along the surface. A surface plot of these profiles are shown for the example stoichiometric propane flame in Fig. 8.4.

This process was also repeated for the right hand side of the flame, however as mentioned above, attenuation of the beam through the flame due to absorption by CO_2 results in asymmetry in the image. It was deemed better to focus only on one side, rather than attempt to correct for this energy attenuation.

The resultant 7 mm wide surface in Fig. 8.5 is typical of the process. Above, it was specified that the ROI would extend 5 mm into the post-flame. This distance is actually much further into the post flame than necessary. The primary focus of this work is on the early stages of NO formation in the flame front, so only regions less than 3 mm are of interest. Beyond about 3 mm, the buoyancy effects, coupled with the continued formation of NO through the thermal mechanism, results in the steady increase of NO LIF signal, increasing toward the furthest corner of Fig. 8.5. However, near the flame front, the Bunsen premixed flame behaves as a freely propagating

premixed flame [220], a fact which will allow for an estimation of the temperature and major quenching species concentrations for the following LIF quantification analysis. Therefore, this analysis is ultimately limited to the near flame region. Finally, the LIF signal was averaged through this ROI.

It should be noted that the exact identification of the 'flame front' discussed above is relatively arbitrary. Based only on the point at which the NO LIF signal increases above an arbitrarily chosen threshold value, increasing or decreasing this threshold value will shift the 'flame front'. However, the line parallel to the flame surface will remain parallel regardless of the threshold value (within reason). Therefore the region of interest remains normal to the flame surface, so with an adequate buffer into the pre-flame and post-flame region, a final alignment of the NO LIF with predicted temperature and species concentrations remains to be done.

For this analysis, the best metric to align the NO LIF with simulations was to identify the point at which the LIF signal (as well as the NO concentration in the simulation) began to increase. This is reasonable given the very rapid formation of NO through the Prompt mechanism serving as a distinct feature in both the LIF and simulation. However, given the somewhat noisy nature of the NO LIF, finding the lift-off point in a systematic fashion presents a challenge. This problem was addressed by analyzing the distribution of pixel intensities through the mean profile, with an example for stoichiometric propane shown in Fig. 8.6.

In this figure, the peak on the left corresponding to low pixel intensities is due to the pre-flame region approaching the flame front. As the Prompt NO mechanism turns on, the LIF signal increases rapidly and a subsequent value in the histogram is observed. Then the rate of increase in LIF signal decreases before leveling off, yielding the two regions on the right hand side of the histogram. The criteria for determining the pixel intensity threshold is based on the difference between the steady, low signal region in the pre-flame and the rapidly increasing region. The threshold count level

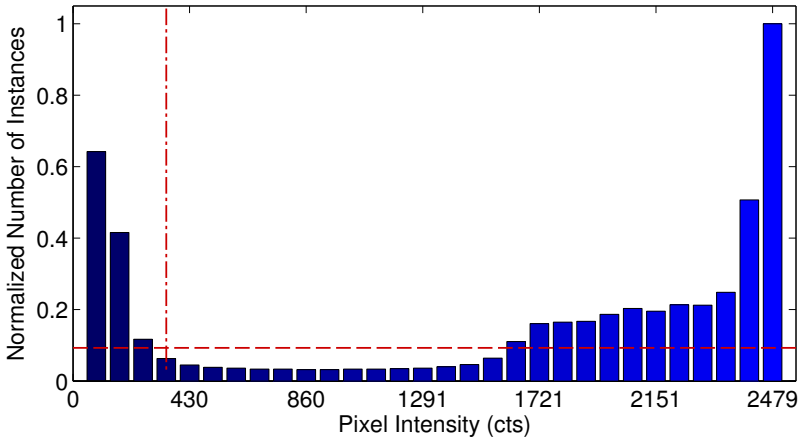

Figure 8.6: Histogram of pixel intensities in stoichiometric propane NO LIF image. The horizontal dashed red line indicates threshold number of instances value and the vertical dash-dot line indicates the corresponding pixel intensity threshold.

is determined as the point at which the number of instances is 5% between the lowest and highest points (corresponding to the region of rapid increase and steady pre-flame region, respectively). This threshold is shown as the dashed red line in Fig. 8.6. The corresponding pixel intensity at this point is then set as the threshold pixel intensity in the LIF profiles indicating lift-off from baseline.

The result of this indexing procedure is a consistent method to determine the point at which the LIF signal begins to increase above the noise and is robust across a wide range of conditions yielding different levels of LIF signal. Figure 8.7 shows lean, stoichiometric, and rich propane flames with the indexing procedure described above applied. This figure shows that this method does a good job of identifying the first point at which the LIF signal increases above the noise, this point is then set as the indexed zero position in the LIF signal. Several features of these profiles can be observed at this point. First, the LIF increases with increasing equivalence ratio. Secondly, two regimes can generally be observed: one rapid rise in the first 0.5 mm, followed by a slower, steady, nearly linear increase in LIF signal. Lastly, beyond approximately 3 mm, the profiles fold over and the noise increases. This is most likely due to the dilation, buoyancy, and entrainment effects as the profiles near

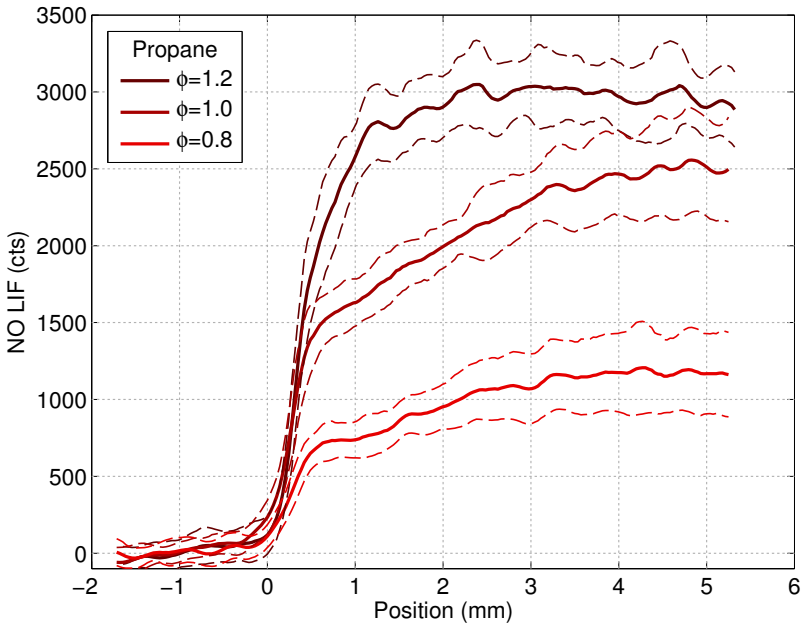

Figure 8.7: Indexed LIF profiles for several propane flames.

the far-field in the flame and helps to demonstrate why the primary region of interest does not extend beyond approximately 3 mm.

8.2.2 Quenching and calibration

Correlation of the NO LIF signal to a local NO concentration requires consideration for a number of factors. When operating in the linear fluorescence regime, the fluorescent signal can be shown to be linearly responsive to the number density of the probed species, however due consideration must be given to temperature and collisional quenching effects which are composition and temperature dependent. Equation 8.2 shows the correlation between measured LIF signal and NO number density:

$$S_{NO} \sim C_{opt}\tau_{\lambda}B_{12}I_{L}f_{b}\Gamma\Phi n^{\circ}_{NO} \tag{8.2}$$

where S_{NO} is the LIF signal, C_{opt} is the collection and calibration constant, τ_{λ} is the transmissivity of the collection optics, B_{12} is the Einstein coefficient for absorption, I_L is the laser irradiance, f_b is the Boltzmann population fraction in the ground state, Γ

Table 8.2: NO LIF quenching a calibration parameters.

Term	(Units)	Function	Constants			
			c_1	c_2	c_3	c_4
B_{12}	$(m^2/(J \cdot s))$		2.38×10^9			
f_b	(-)	$c_1 e^{c_2/T} + c_3 e^{-c_4/T}$	-0.2822	-1799	0.2183	408.4
A_{21}	(1/s)		5.72×10^6			
σ_k						
NO	(Å)	$c_1 e^{c_2/T} + c_3 e^{-c_4/T}$	37.3	11.7	60	0.011
H_2O	(Å)	$c_1(300/T)^{c_2} + c_3 e^{-c_4/T}$	121.2	0.676	100	0.010
CO_2	(Å)	$c_1 e^{c_2/T} + c_3 e^{-c_4/T}$	38.0	173	46	0.0022
O_2	(Å)	$c_1 e^{c_2/T} + c_3 e^{-c_4/T}$	22.0	59.1	4.3	0.00195
CO	(Å)	$c_1 e^{c_2/T} + c_3 e^{-c_4/T}$	4.23	128	17.5	0.00198
N_2	(Å)	$c_1 e^{c_2/T} + c_3 e^{-c_4/T}$	1.88	-2130	84	0.0121

is the laser line overlap integral, Φ is the fluorescent yield, and n°_{NO} is the NO number density.

The optical collection constant and transmissivity, C_{opt} and τ_λ, can be grouped into a single term that is determined empirically and will be discussed shortly. The absorption coefficient B_{12} is a constant for a given species and transition. The laser irrandiance I_L is monitored for shot-to-shot fluctuations and therefore this value is determined experimentally. The Boltzmann fraction in the ground state f_b is temperature dependent, but can be calculated using Boltzmann statistics. The overlap integral Γ is introduced through the spectral width of the exciting laser [165] and is weakly temperature, species, and pressure dependent. However, Γ is primarily influenced through the spectral width of the laser, which remains nearly constant. The fluorescent yield Φ is temperature and composition dependent. Estimations for the quenching rate can be made following the work of Settersten [167]. Finally, the number density n°_{NO} can be relative to the concentration through the ideal gas law to be temperature and pressure dependent.

The quenching terms of interest are shown in Table 8.2. The total quenching rate

can be estimated through the mole fraction weighted sum of the collisional quenching for each species. The relation for individual quenching rates from bath gas species k is shown in equation 8.3:

$$Q_k = \sigma_k \left(\frac{N}{V}\right) \sqrt{\frac{8k_B T}{\pi \mu_k}} \tag{8.3}$$

$$\mu_k = \frac{\mathcal{M}_k \mathcal{M}_{NO}}{\mathcal{M}_k + \mathcal{M}_{NO}} \tag{8.4}$$

where the relation for the total quenching rate for all major bath gas quenching species is shown in equation 8.5.

$$Q_{21} = \sum X_k Q_k \tag{8.5}$$

This relation allows for the correction of the NO LIF signal due to variations in the temperature and species composition through the flame. The quenching rate is introduced into equation 8.2 through the fluorescent yield via equation 8.6:

$$\Phi = \frac{A_{21}}{A_{21} + Q_{21}} \tag{8.6}$$

The next step is to determine the calibration of C_{opt}. The standard procedure for doing this calibration process is to seed known concentrations of NO into the unburned gas mixture of lean flames. The resultant change in NO LIF signal with doped NO concentrations is linear, with the slope of the fit equal to the NO LIF signal response per ppm concentration. This calibration procedure has been utilized by a number of different studies [221–223], with the primary assumption rooted in the need for only minor consumption of NO through the flame front, which is not a terrible approximation under lean conditions [159].

Therefore, a calibration constant was determined for each fuel individually as shown for lean propane in Fig. 8.8, seeding three doped concentrations of NO into

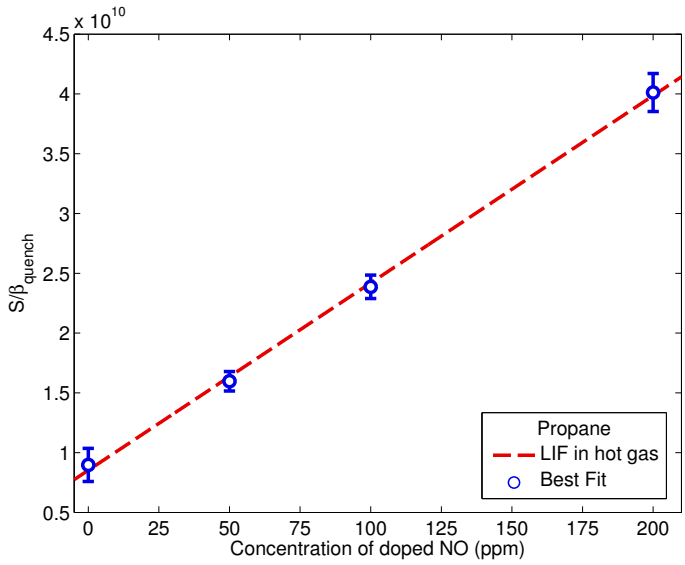

Figure 8.8: Linear response of the quenching corrected LIF signal to increasing doping of NO in the premixed gases.

the $\phi = 0.9$ premixed air stream from a 1000 ppm in N_2 gas standard with make up O_2 to account for the displaced oxygen. The LIF fluorescence at 3 mm for each flame was then corrected for all the temperature and compositionally dependent factors, including collisional quenching using the relation in equation 8.5, the Boltzmann fraction f_b, and correction of number density to mole fraction. These terms were collectively named β_{quench} for the sake of convenience. The remaining constant terms in equation 8.2 were then grouped into the calibration term.

The calibrations for all seven fuels are shown in Fig. 8.9. The slope of each fit is within less than $\pm 10\%$ of the average slope, with the variations introduced through differences in the amount of NO consumed through the flame and differences in the quenching environment.

The final step is to apply corrections for the all the temperature and compositionally dependent quenching rates to all the flames in this study. Figure 8.10 shows an example of the temperature dependence of the LIF correction terms, normalized by the correction at 300 K. The dark blue line indicates the Boltzmann fraction up to 2200 K as calculated using the relation in Table 8.2. A peak in population fraction

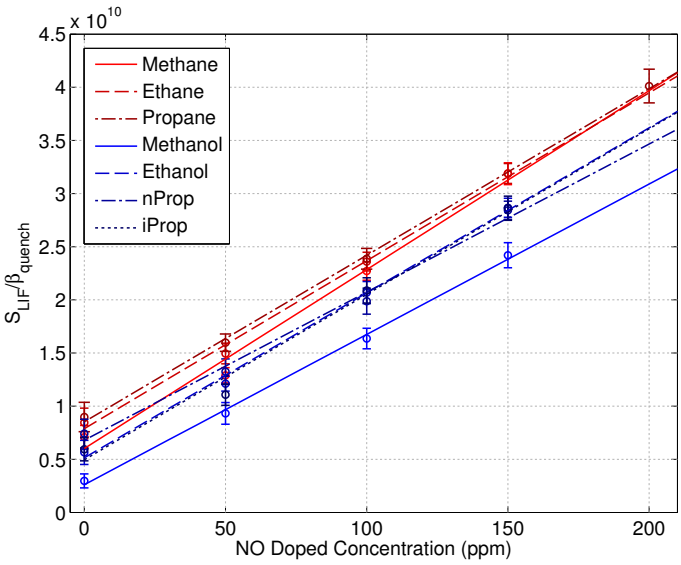

Figure 8.9: Calibration fits to all seven fuels.

can be seen around 800 K, with a nearly linear decay with increasing temperature. Meanwhile, the lighter blue curve shows the correction due to collisional quenching. For this figure, the composition is based on the equilibrium combustion products of stoichiometric methane. The dashed red line indicates the total quenching β_{quench}, including the Boltzmann fraction, quenching rate, and conversion from number density to mole fraction, defined as:

$$\beta_{\text{quench}} = f_b \frac{A_{21}}{A_{21} + Q_{21}} \frac{1}{T} \tag{8.7}$$

Finally, the LIF signal can be correlated to the molar concentration of NO as:

$$S_{NO} = C_{\text{cal}} \cdot \beta_{\text{quench}}\left(T, X_k\right) \cdot X_{NO} \tag{8.8}$$

which accouts for variations in the collisional quenching, Boltzmann population fraction, local temperature and compostion, and ICCD sensor response to LIF emission. This correction can then be applied to all the NO LIF profiles measured for the range of fuels and equivalence ratios.

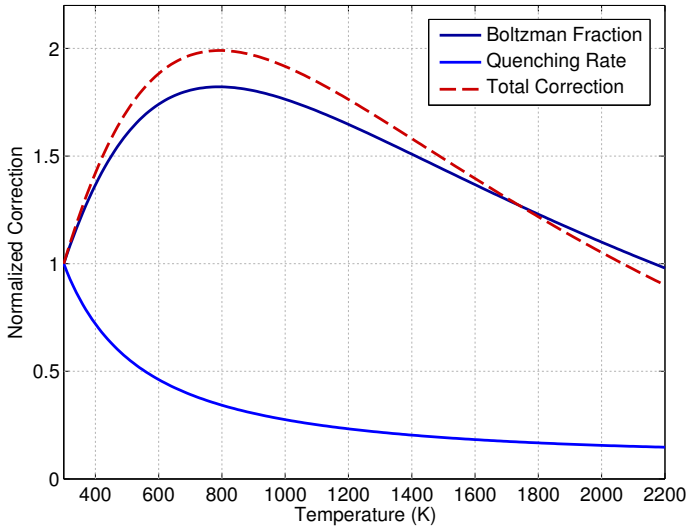

Figure 8.10: Example of normalized temperature and composition dependent corrections to the NO LIF signal. Values are normalized by the correction term at 300 K.

8.2.3 Quantified NO LIF

Using the one-dimensional estimate of a freely propagating flame to provide the temperature and major species profiles, the NO LIF for all the fuels was quantified, yielding profiles such as those for propane shown in Fig. 8.11. Several trends can be identified in these profiles that are consistent for most of the fuels studied here:

1. A fairly steady increase in NO concentrations at 3 mm is observed with increasing equivalence ratio. However, as the flame becomes richer, the increase is diminished, even reaching a peak at equivalence ratios near 1.2.

2. All flames, regardless of equivalence ratio, exhibit a region of very rapid increase in NO concentration within the first 0.5 mm. The extent to which NO increases within this region varies depending on equivalence ratio and fuel.

3. Beyond the region of rapid increase, a region of approximately linear increase in NO concentration exists.

4. However, under increasingly rich conditions, the rate of increase of NO in this

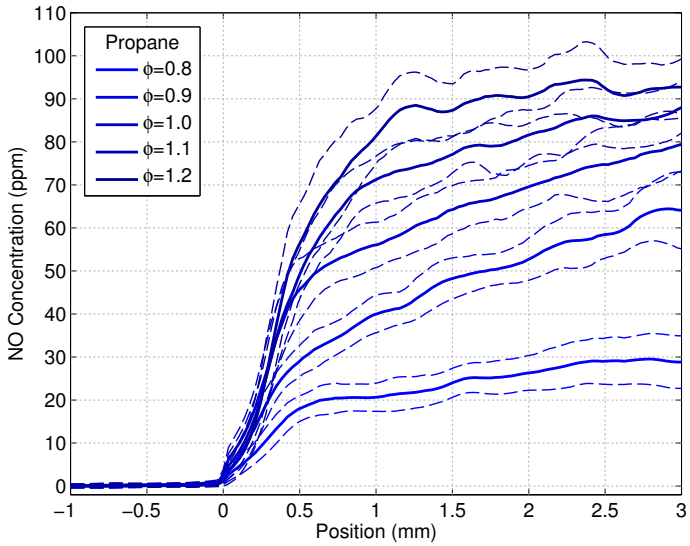

Figure 8.11: Quantified NO concentration profiles in propane fueled Bunsen flames under a range of equivalence ratios.

region is reduced.

5. Similarly, the rate of increase in this linear region is lower under very lean conditions, increasing as the equivalence ratio approaches stoichiometric or very slightly lean.

Comparison of the measured NO concentrations with predicted concentrations by the model for the C_3 fuels is shown in Fig. 8.12. It must be noted at this point that AramcoMech1.3 does not have a NO_X sub-mechanism included in the model, and the NO_X model included in this analysis is adapted from several sources. Additionally, a detailed hierarchical chemistry mechanism for the C_3 fuels which includes detailed NO_X chemistry and Prompt initiation through the NCN path does not currently exist. This is an area with fertile ground for future work.

With that said, in examining the lean flames in Fig. 8.12, the agreement between the experiment and predictions is quite good with regard to steady state values around 3 mm. The model over-predicts NO in the propane flame by about 60%, but the n-propanol and i-propanol are within about 30%. The transition between the two NO formation regimes is not as well defined in the model as in the experiments, however

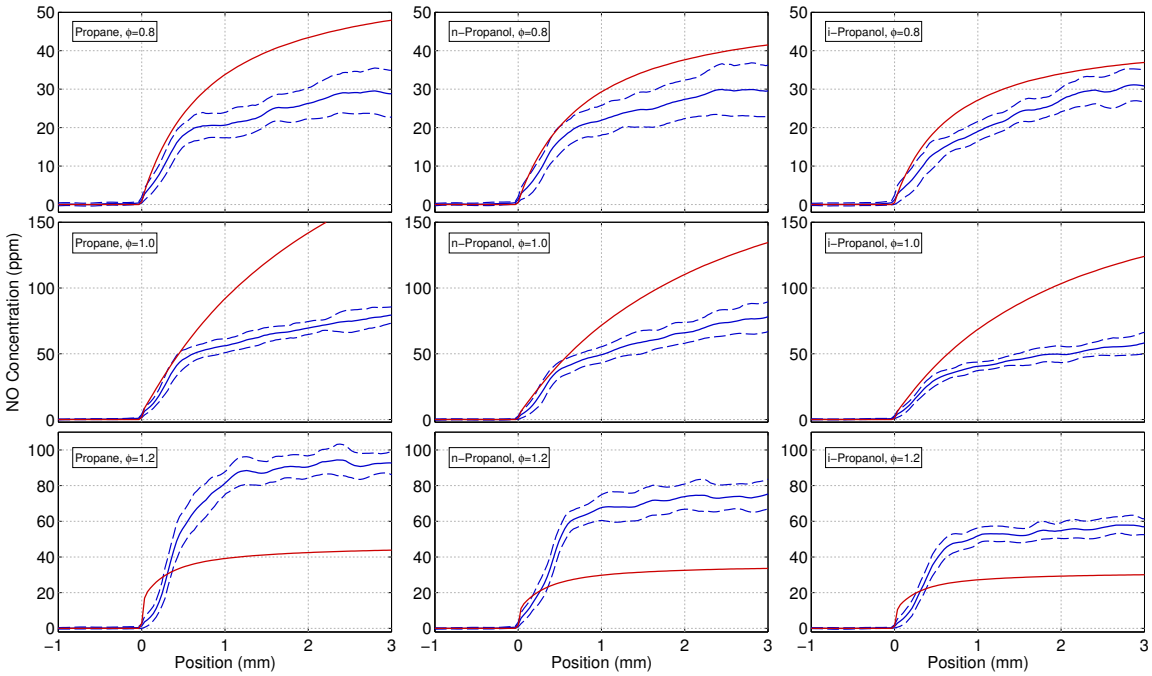

Figure 8.12: Comparison of measured and predicted NO concentration profiles in Bunsen flames for the C_3 fuels under lean, stoichiometric, and rich conditions.

the slope of the linear region composed primarily of the contribution by the Thermal mechanism is fairly well predicted.

The stoichiometric flames are not as well predicted as the lean flames however. Steady state values for NO are greatly over-predicted by the model. The region of rapid NO formation early in the flame appears to be relatively well captured, however the rate of formation later in the post flame appears to be the source of the very large over-prediction. A similar study of NO in stagnating flames by Watson et al. [9] shows a similar over-prediction of NO through the Thermal mechanism. Watson attributes this over-prediction to a discrepancy in the Thermal initiation reaction rate as measured through isolated rate measurements as opposed to measurements within flames. This over-prediction is also apparent in these measurements, indicating that the Thermal initiation reaction rate may be too high.

Agreement with the experiment and prediction suffers the most in the rich flames. NO concentrations under-predict the measured values by approximately 50%. Agree-

ment of the rate of Thermal contribution is pretty good, however this is most likely due to the starvation of O atom necessary for the Thermal initiation rather than accurate prediction of the reaction rate. The model predicts a much faster rate of formation of NO in the flame front than that measured experimentally. It is under these conditions that the difficulty in accurately predicting the non-thermal contributions to NO becomes apparent. The accuracy of these predictions is dependent on the model's ability to capture NO formation through the combination of non-thermal mechanisms that primarily involve interactions with hydrocarbon radicals (such as the Prompt and NO-HCN-Reburn sub-mechanisms) and the non-thermal mechanisms that do not specifically involve interaction with hydrocarbon radicals (such as the N_2O and NNH sub-mechanisms).

For the non-thermal mechanisms involving hydrocarbon radicals, the greatest uncertainties are due to the difficulty in accurate prediction of $CH_{i=1,2,3}$ radicals as well as the branching ratios between the NCN oxidation pathways. Versailles [217] showed that AramcoMech1.3 upon which this mechanism is based consistently underpredicts the concentrations of CH. Additionally, variations between different models were observed with respect to the pathways to which CH is formed which likely further influences a model's ability to predict NO. Versailles also noticed that the thickness of the CH region in the flame was not well predicted by the models in their study under rich conditions. Additionally, uncertainty remains in the Prompt initiating reaction rate for $CH+N_2$ [24].

The non-thermal mechanisms that largely do not involve hydrocarbon radicals appear to exhibit a better predictive capability due to their somewhat simpler chemistry (due to their relative independence from the fuel chemistry). The NNX chemistry in these models is largely based on recently updated reaction rates for NNH chemistry and branching ratios for NH_2 products provided by Klippenstein et al. [47]. However, it is still difficult to provide more than qualitative predictions of contributions to NO

formation through the NNX chemistry.

In order to better understand the differences in fuel effects on non-thermal NO formation between alkane and alcohol fuels, it would be helpful to be able to quantify the contribution to NO through both regimes: the region in the flame front in which NO is formed rapidly (more rapidly than the Thermal mechanism is able to provide a significant contribution) and the region in which NO formation is steady and apparently decoupled from the fuel oxidation. For convenience sake, these two regions will be referred to as non-thermal and thermal contributions, however it should be noted that the thermal sub-mechanism contributes throughout the entire flame region, including the non-thermal region, however the expected contribution in the non-thermal region should be low. Additionally, the NNX mechanism will be shown to slower than the other non-thermal mechanisms (discussed later), and thus will contribute to NO formation in the thermal region as well. However, while slower than the sub-mechanisms related to hydrocarbon intermediates, the NNX is still more rapid than the Thermal sub-mechanism, and the contribution to total NO formation for the NNX occurs mostly in the non-thermal region.

As was discussed in Fig. 8.12, measurements of NO concentrations through the flame yielded two quite distinct regimes. A demarcation between these two regimes is the bend in the NO concentration profile, which will be called the 'knee' for the sake of convenience. The positioning of this knee is specific in each flame due to differences in equivalence ratio, total NO formation, and rate of Thermal NO formation. However, a reliable method for determining the position and concentration of NO at the knee is demonstrated in Fig. 8.13. Here, a chord is drawn between the index previously identified as the beginning of NO LIF signal (essentially 0 ppm NO) and the concentration of NO at 3 mm. Then the distance between any point on the NO concentration curve to the chord can be calculated as the orthogonal projection onto the normal of the chord. The point with the largest distance is then identified as the

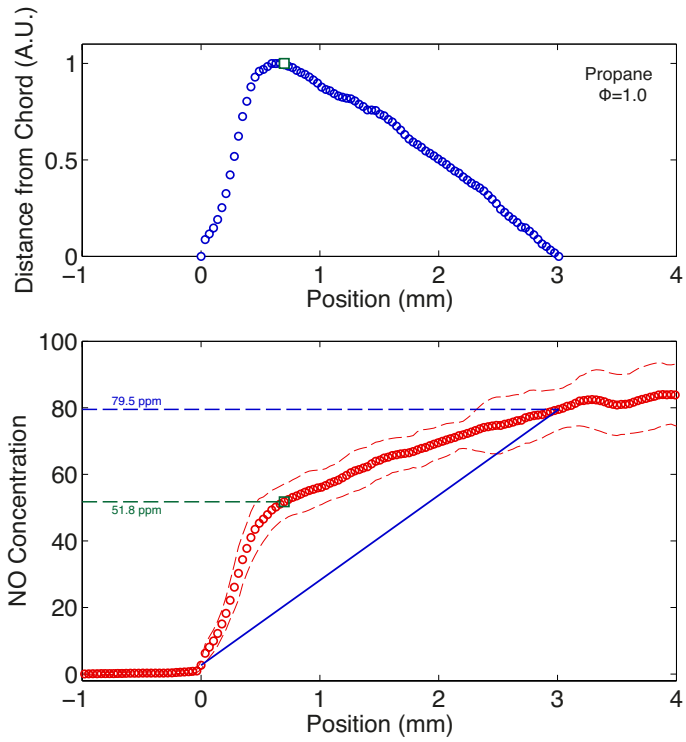

Figure 8.13: Method for determination of demarcation between thermal and non-thermal NO contributions.

knee. The figure on the bottom of Fig. 8.13 shows the overlay of the chord and the top figure shows the normalized distance to the chord. The NO concentration at both the knee and 3 mm are then extracted, with the concentration at the knee largely formed through non-thermal NO contributions and the difference between the concentration at 3 mm and the concentration at the knee due to Thermal NO formation.

The non-thermal contributions for all the fuels are then shown in Fig. 8.14. This is an important figure for the analysis of differences in non-thermal contributions. Clearly, the total contribution to non-thermal NO formation for the alcohols are consistently lower. The C_1 fuels exhibit by far the greatest difference between the alkane and alcohol fuels, especially under the rich conditions where the methanol flames produce very low concentrations of NO. The C_2 fuels exhibit similar trends, more so than the C_1 fuels in that both C_2 fuels demonstrate a consistent increase from $\phi = 0.8$ to $\phi = 1.15$ where a peak in non-thermal contribution is observed. The

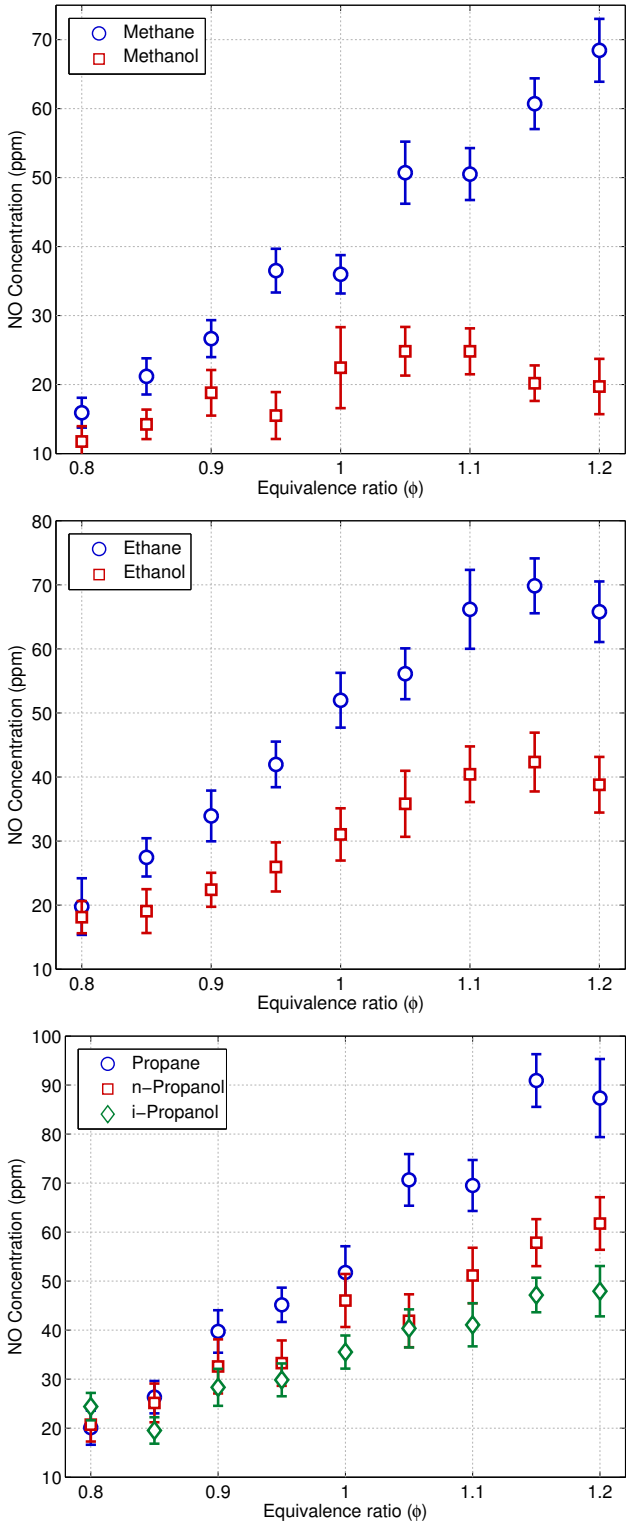

Figure 8.14: Non-thermal NO contributions in Bunsen flames for C_1,C_2, and C_3 fuels.

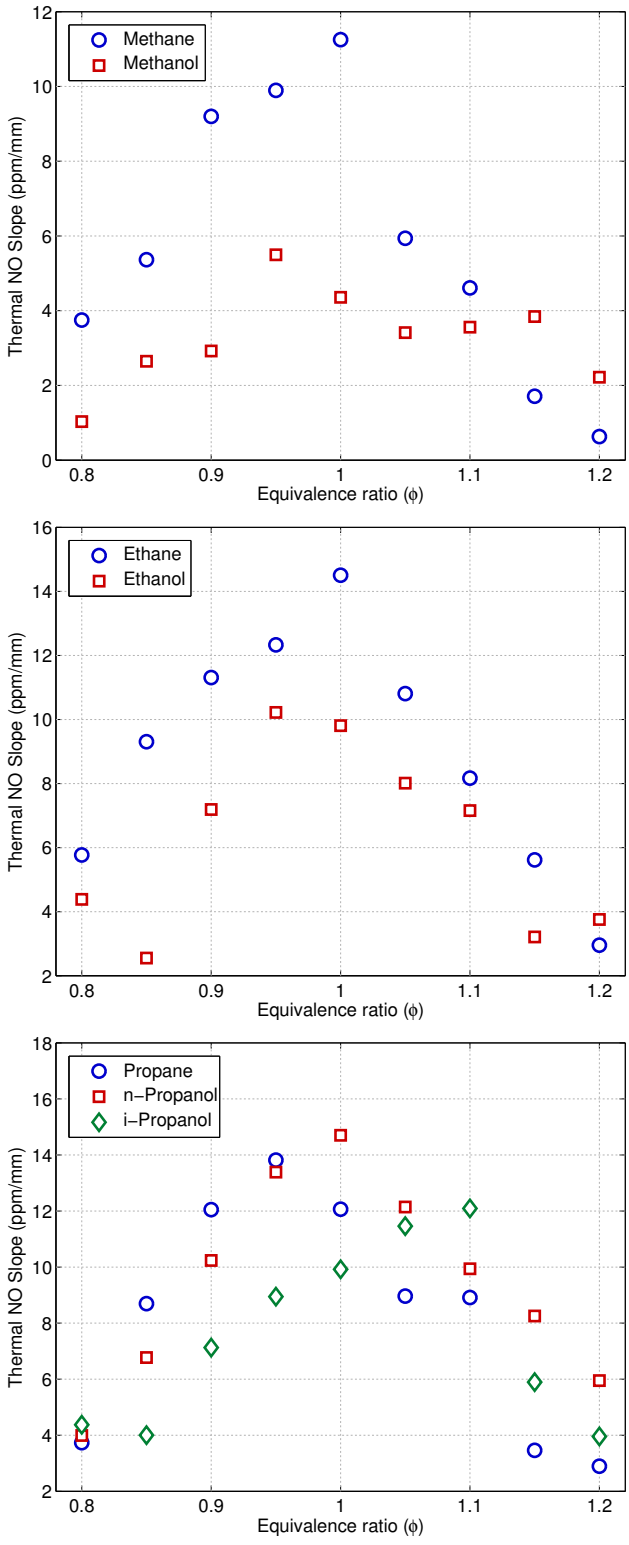

Figure 8.15: Rate of thermal NO contributions in Bunsen flames for C_1,C_2, and C_3 fuels.

C_3 fuels behave similarly to the C_2 fuels, in that there is a consistent increase in non-thermal NO with increasing equivalence ratio, however it appears that non-thermal contributions may peak at higher equivalence ratios. The C_3 alcohols also exhibit a smaller reduction in non-thermal NO than the C_2 fuels, with i-propanol forming less non-thermal NO than n-propanol.

Figure 8.15 shows the rate of Thermal NO contribution of all the fuels. Because equilibrium concentrations of NO at elevated temperatures are exceedingly high, given adequate time the formation of NO through the Thermal mechanism will continue unabated (at least until the availability of oxygen radicals is depleted). Therefore, the values presented in Fig. 8.15 are the spatial rate of thermal NO formation. The greatest difference in the rates of thermal contributions is seen in the C_1 flames due to the lower adiabatic flame temperature for methanol. As the difference in adiabatic flame temperatures decreases, so too do the differences in the contributions through the Thermal mechanism. Additionally, it can be seen that the rate of formation through the thermal mechanism peaks around the stoichiometric conditions. Under rich conditions, the starvation of oxygen radicals begins to rapidly reduce thermal contributions in the post-flame.

8.3 NO LIF in flat flames

A short detour in the analysis of the differences in the non-thermal contributions in alcohols and alkanes will now be taken to complete a very similar analysis in burner stabilized flat flames. These flames operate under lower peak temperatures and will exhibit lower thermal contributions, which will further aid in the current investigation.

The process for quantifying the NO LIF is identical to that described above. The exact same procedure was applied for calibration of the optical collection constant and the LIF signal response to NO concentration. One difference is that experimen-

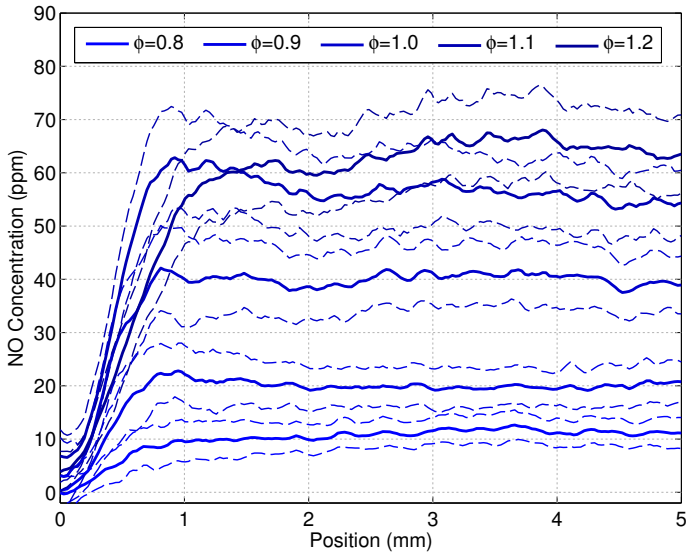

Figure 8.16: Quantified NO concentration profiles in propane fueled flat flames under a range of equivalence ratios.

tally measured temperature profiles for these flames are available from Chapter 2.3.1. These measured temperatures were used, rather than predicted temperatures as in the previous section. Bath gas species were utilized from the predicted species concentrations of the previous chapter as well.

The resultant NO concentration profiles are demonstrated in Fig. 8.16. The shape of the NO concentration profile is quite similar to that observed in the Bunsen flame, characterized by a fairly rapid formation of NO within the first millimeter of the flame. The flat flames however do not exhibit a steady rise in NO concentration in the post flame under any equivalence ratio. This is most reasonably due to the low peak and post-flame temperatures which greatly limit the rate of formation through the Thermal mechanism.

Comparisons with predicted concentrations of NO through the flame front also exhibit similarities to those observed in the Bunsen flames. However, due to the lower temperature and limited contribution to Thermal NO, the agreement between experimental and predicted concentrations is worse than that in the Bunsen flames. This is due to a consistent under-prediction of non-thermal NO contributions and

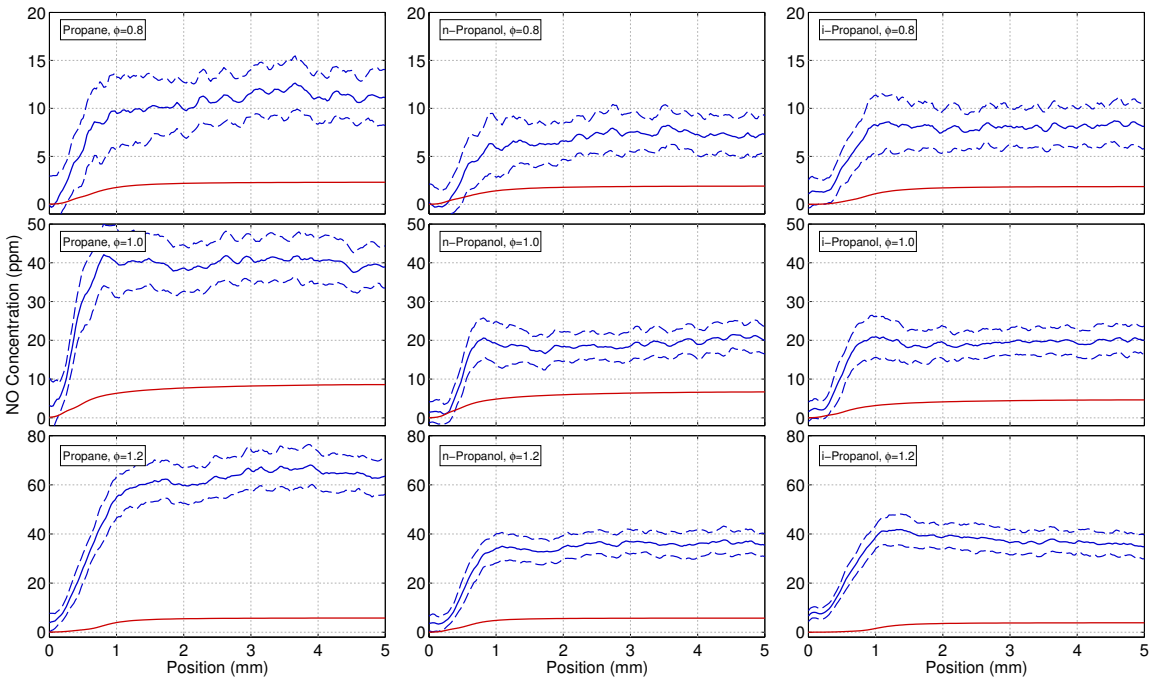

Figure 8.17: Comparison of measured and predicted NO concentration profiles in flat flames for the C_3 fuels under lean, stoichiometric, and rich conditions.

over-predictions of thermal contributions. As a result, conditions in which contributions to total NO formation consist primarily of non-thermal pathways, such as rich Bunsen flames and the full set of these flat flames, concentrations of NO are greatly under-predicted. Whereas, conditions such as the lean and stoichiometric Bunsen flames in which significant contributions to total NO formation come from the Thermal mechanism can show decent agreement due to the combined over-prediction of thermal and under-prediction of non-thermal mechanisms canceling out to a degree. This yields deceptively good agreement.

It can also be seen that the ability of the model to predict non-thermal NO formation in the flat flames is significantly worse, especially under rich conditions, than observed in the Bunsen flames. A possible cause is an even greater difficulty in predicting CH concentrations in relatively low temperatures in which a wide range of fuel decomposition and C/H pathways become activated. These figures reiterate the need for better predictive capability of the CH concentrations, especially under low

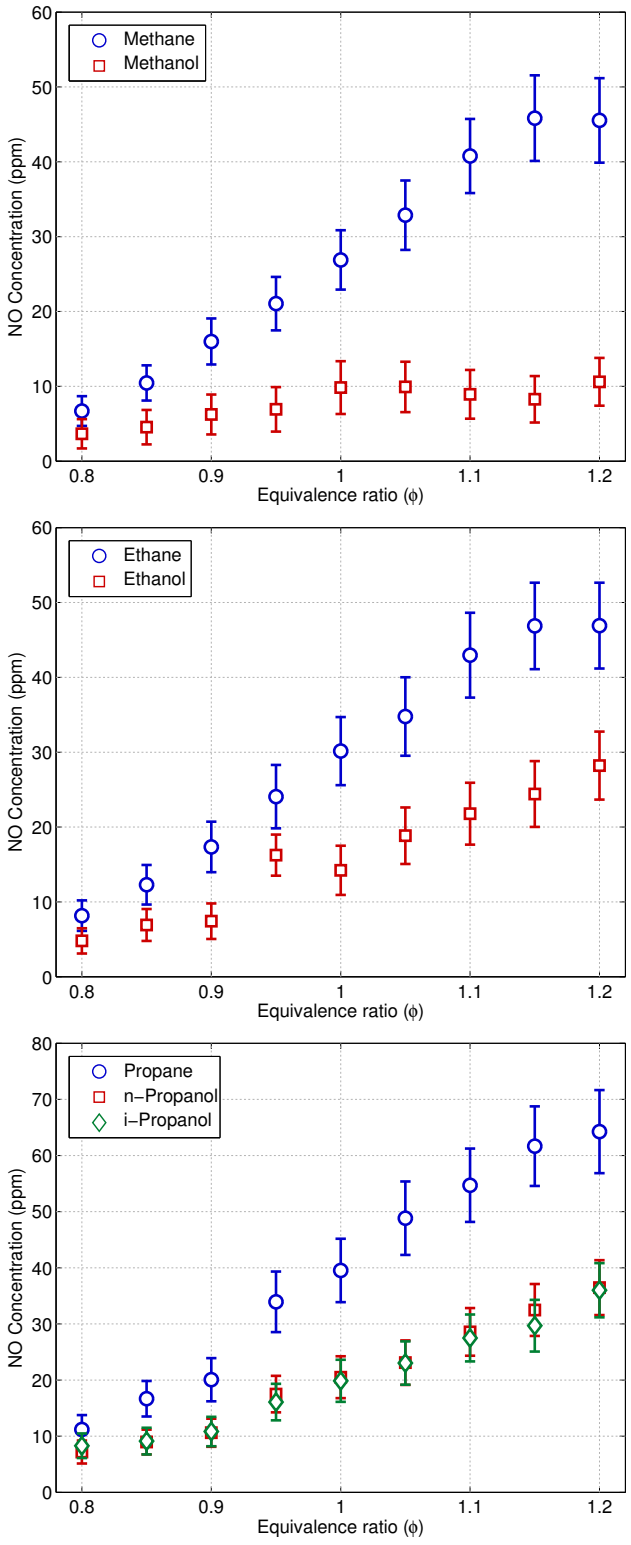

Figure 8.18: Non-thermal NO contributions in flat flames for C_1,C_2, and C_3 fuels.

temperatures.

Figure 8.18 shows a comparison of the non-thermal NO contributions in flat flames for all the fuels. Because it is difficult to identify a region of steady, linear increase in NO concentration in the flat flames similar to what is seen in the Bunsen flames, it is reasonable to conclude that the formation of NO through the Thermal mechanism in the post flame is negligible. Unfortunately, it is not easy to deduce the contribution through the Thermal mechanism in the flame front, however it is also reasonable to assume this contribution is also small, and certainly should be less than that observed in the flame front of the Bunsen flame. Therefore, the non-thermal contribution to NO in the flat flames can be easily identified as the steady state NO concentration in the post-flame region. It is this concentration that is plotted in Fig. 8.18.

It should immediately be apparent that this figure is very similar to that for the Bunsen flames. A consistent increase in NO concentration with increasing equivalence ratio is clearly observed and the alcohol flames produce a fraction of that observed in the alkane flames.

Figure 8.19 shows the relative contributions to non-thermal NO formation in alcohols compared with their cousin alkanes in both burner configurations. In the alcohol-fueled Bunsen flames, increasing the equivalence ratio is generally followed by a subsequent decrease in the formation of non-thermal NO in comparison with alkanes, with a clear trend with respect to carbon number. However, in the flat flames, except for methanol, the ratio to alkanes collapses with a minima around $\phi = 1$. This indicates that, at least for the C_2 and larger alcohols, there may be a limit to the reduction in NO achievable due to reductions in the Prompt mechanism, especially when significant NO contributions through the NNX mechanisms are present. The different behavior of methanol from the other alcohols can most likely be attributed to the somewhat unique decomposition pathways available to methanol and the resultant oxidation through exclusively formaldehyde where a number of other

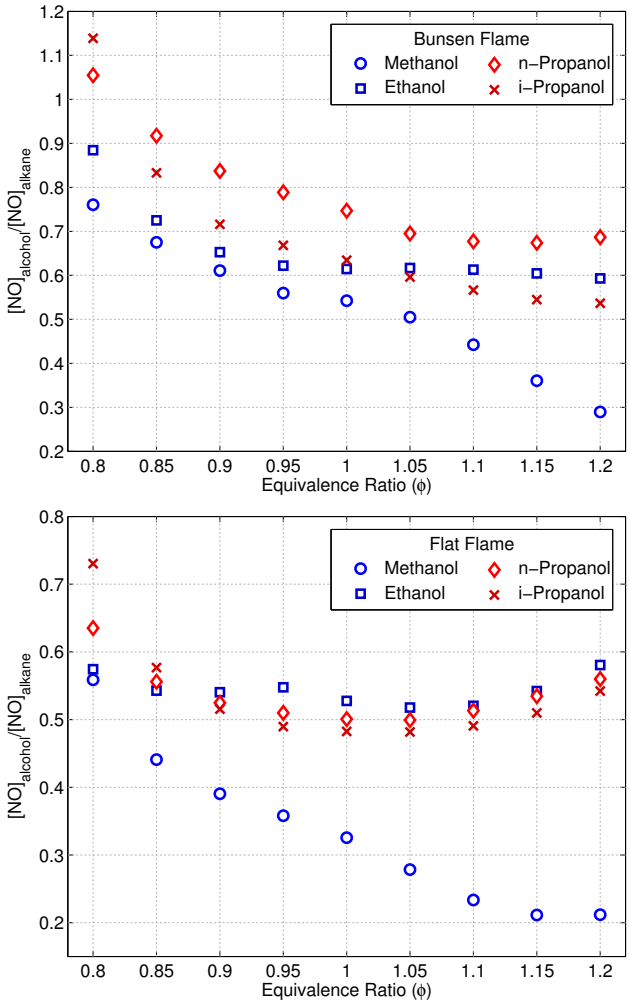

Figure 8.19: Ratio of non-thermal contributions in alcohols to that in alkanes for the C_1,C_2, and C_3 fuels in both burner configurations.

intermediate decomposition products are available to the other alcohols.

8.4 Predicted non-thermal contributions

The same NO_X contribution analysis described in Section 7.2.4 utilizing the nitrogen flux accounting method can be employed here. In the absence of significant Thermal NO contributions, the primary components of total non-thermal NO formation in both flame configurations is composed of the sum of the sub-mechanisms involving the interaction of nitrogen with HC radicals, such as the Prompt and NO-HCN Reburn

mechanisms with the addition of the Burnout contribution described in Section 7.2.4, and the sub-mechanisms which are largely independent of the HC species, such as the N_2O and NNH sub-mechanisms (combined for convenience into the NNX sub-mechanism).

After identifying the rates of production for the various sub-mechanisms, an interesting exercise is to calculate the temporal integral of the rate of production (ROP) to yield an estimate of the number density of the total formation of NO from each sub-mechanism. Combined with an estimation of the total number density, the contribution to NO formation in terms of concentration can be approximated using equation 8.9

$$X_{NO,k} \approx \frac{RuT}{P} \int \mathrm{ROP}_k dt \tag{8.9}$$

There are several caveats to this approach:

1. This analysis does not directly account for diffusion. Diffusion is considered in the CHEMKIN solution, however this post-processing only considers the NO source term, so diffusive effects are neglected. The degree to which this affects the computed NO concentration varies depending on the gas velocity. In the case of the Bunsen flames, the gas velocity is high with a resultant high Péclet number. Consequently the influence of the diffusion of NO should be smaller than in the flat flame with a lower Péclet number.

2. The integrated rate of production should yield a sense of the number of molecules of NO produced through the flame. Therefore, even if disagreements are present in local regions of the flame due to diffusive effects, the result in the post-flame should be indicative of the net contributions of NO through the entire flame.

3. Direct comparisons of the contributions of individual sub-mechanisms with other sub-mechanisms should be done with care. The sub-mechanisms used in this analysis have been shown to be able to capture differences between fuel-

s/equivalence ratios fairly qualitatively, but consistent trends between different sub-mechanisms have not be established. For example, comparisons of NNX formation between methane and methanol have more confidence than comparisons of Prompt and NNX contributions in methane flames.

Figure 8.20 shows a summary of the contributions through the primary non-thermal NO formation pathways in both flame configurations, with Bunsen and flat flames on the left and right, respectively. The NNX mechanism is plotted alongside the combined HC related contributions through the sum of the Prompt, NO-HCN reburn, and Burnout out sub-mechanisms.

Clearly, the contributions for alcohols are lower than for alkanes for both the HC related and non-HC related sub-mechanisms. It appears that the HC-related mechanisms increase with increasing equivalence, as would be expected with the increasing availability of HC radicals. In the Bunsen flames, the increase in fairly steady, while the increase in HC-related NO in the flat flames does not appear to increase significantly until much closer to stoichiometric conditions.

Meanwhile, the NNX mechanism is fairly consistent between both burner configurations, with a peak in contribution around the stoichiometric or slightly lean region, tapering-off toward the lean or rich side. It does appear that the decrease in NNX contributions in alkanes on the very rich side is faster than estimated in the alcohol flames, indicating alcohols may yield a larger NNX contribution in very rich conditions than alkanes.

It is difficult to make definitive statements on absolute concentrations from either mechanism. Recalling from Figs. 8.12 and 8.17, the model generally under-predicts the measured concentrations. With non-thermal contributions originating primarily from these combined mechanisms, it is not clear whether the NNX, Prompt, NO-HCN Reburn, or (more likely) a combination of all of the above is under-predicted. The authors of the sub-mechanisms used here all identify significant uncertainties in the

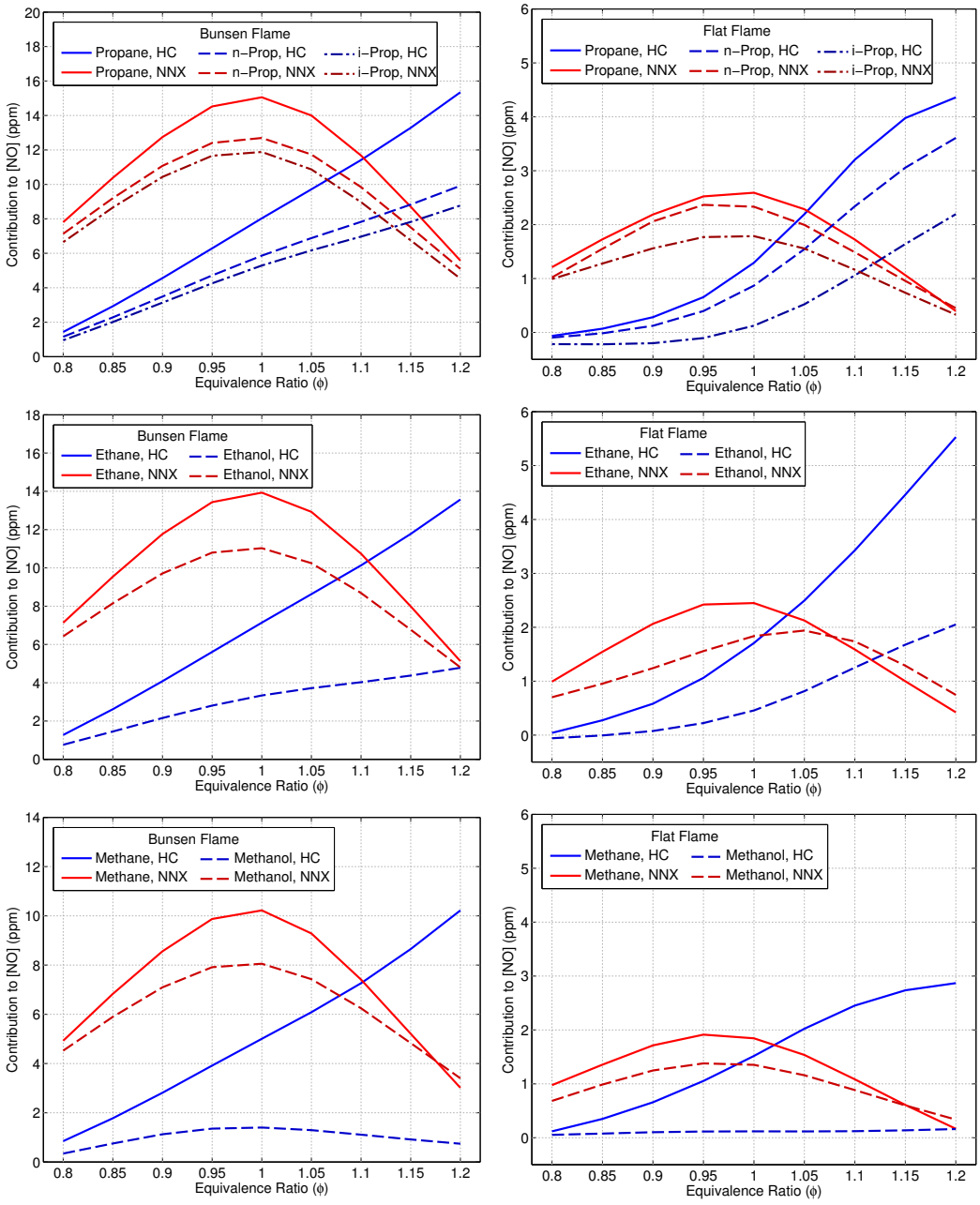

Figure 8.20: Contributions from the non-thermal sub-mechanisms for C_1,C_2, and C_3 fuels in Bunsen (left) and flat (right) flames.

quantitative abilities of their mechanisms, citing: strong coupling to the concentrations of CH, HCCO, CH_3 among other HC species, uncertainty in the reaction rate of CH+N_2, and uncertainty in the branching ratios and reaction rates of NNH+O, NNH+O_2, and NH_2+O_2.

However, it is possible to conclude that NO formation through these non-thermal pathways for alcohols is consistently lower than that for alkanes. Typically, the rule of thumb regarding NO in alcohols has been that lower concentrations are due to lower CH concentrations [103, 105, 107, 224], however contributions through all the non-thermal pathways, N_2O, NNH, Prompt, and NO-HCN Reburn have been shown to be lower in alcohols than alkanes. Clearly then the formation of NO_X through all these pathways is strongly coupled to the fuel chemistry.

8.5 Conclusions

The objective of this chapter was to examine the formation of NO through the flame front of alcohol and alkane flames in a higher temperature Bunsen flame and lower temperature flat flame configurations. This was achieved through a quantitative NO LIF experimental campaign, incorporating careful control of the experimental boundary conditions, including LIF, calibration, and quenching considerations. The result is the ability to observe the formation of NO through the flame front in a non-intrusive manner under temperature fields both with and without significant contributions of Thermal NO.

The experiments identified regions in both flames in which the primary contributions to NO formation were through the non-thermal mechanisms. In the Bunsen flames, this region was identified by a clear delineation in the rates of NO formation. Whereas in the flat flames the contribution to Thermal NO in the post flame was obviously very low or negligible.

Comparisons of the non-thermal contributions under both burner configurations were remarkably similar, with alcohols producing as much as 50% less non-thermal NO than alkanes, with methanol producing less than 20% of the NO observed in methane. Under lean conditions, the observed reduction in non-thermal NO reduced to about 80-90% of that observed in alkanes, however with increasing equivalence ratio the formation of non-thermal NO in alcohol flames was reduced. However, as the equivalence reached the rich region, further increases did not significantly reduce the formation of NO relative to alkanes. Additionally, as the temperature was reduced, the variations in NO formation between the different alcohols was reduced, except for methanol.

Chapter 9

CH_2O LIF concentration measurements in alcohol and alkane flames

In the analysis of the influence of OH groups on fuel decomposition pathways discussed in Section 6.3, it was predicted that the presence of the OH group would shift the selection of decomposition pathways toward those involving hydroxymethyl radical and formaldehyde. Once formed, formaldehyde then directly oxidized through HCO to CO, without providing a significant contribution to the $CH_{i=1,2,3}$ radical pools. As a consequence, formation of NO through the non-thermal mechanisms involving HC radicals were reduced.

In this section, an investigation of the CH_2O concentrations in Bunsen-type premixed flames will be conducted using LIF diagnostics. A description of the experimental approach and alignment of the observed fluorescence with one-dimensional simulations of the flame are presented in Sections 9.1 and 9.2, respectively. Then the CH_2O concentrations utilizing a semi-quantitative approach are presented in Section 9.3.

9.1 Experimental setup

The experimental setup in this chapter is very similar to the measurements in the Bunsen-type flame of the previous chapter. The same burner configuration and exit velocity conditions were used, and a curious reader is directed to Section 8.1 for further details.

As discussed in Section 2.3.2, the light source used in these experiments was a frequency-tripled 10-Hz Nd:YAG around 355 nm. The optical set up, including telescoping lens assembly and beam profile correction apparatus, are also identical to the setup shown in Fig. 8.1, with the substitution of wavelength appropriate mirrors for routing the beam. The CH_2O fluorescence was observed in the broadband between 400 and 500 nm, with background subtraction with the laser off. For each fuel/equivalence ratio condition, 100 exposures were collected.

The process for correcting fluctuations in the total laser energy, the distribution of laser energy as a function of position in the beam, non-linearity of the pixel response of the camera, and spatial calibration were all also identical with the processes for NO LIF and 2λ-OH LIF thermometry as discussed previously. Calibration of the LIF signal to species concentration did follow a different process, however. CH_2O absolute concentrations have previously been calibrated using a LIF reference observed from a reference cell filled with a known concentration of formaldehyde vapor at low pressure [152]. In this work, it was found to be difficult to reliably supply a low pressure reference cell with a known concentration of formaldehyde. Therefore, a semi-quantitative approach was taken to utilize predicted peak CH_2O concentrations in a stoichiometric methane flame as the reference standard for the remaining conditions. Additionally, quenching rates were estimated following the approach of Paul and Najm [149], in which Q_{12} is proportional to T^{α} with $-1 < \alpha < -0.5$. These two limits are preserved in the following analysis, and consistent with observations of others [153, 155], this range of temperature dependence is not very impactful on the

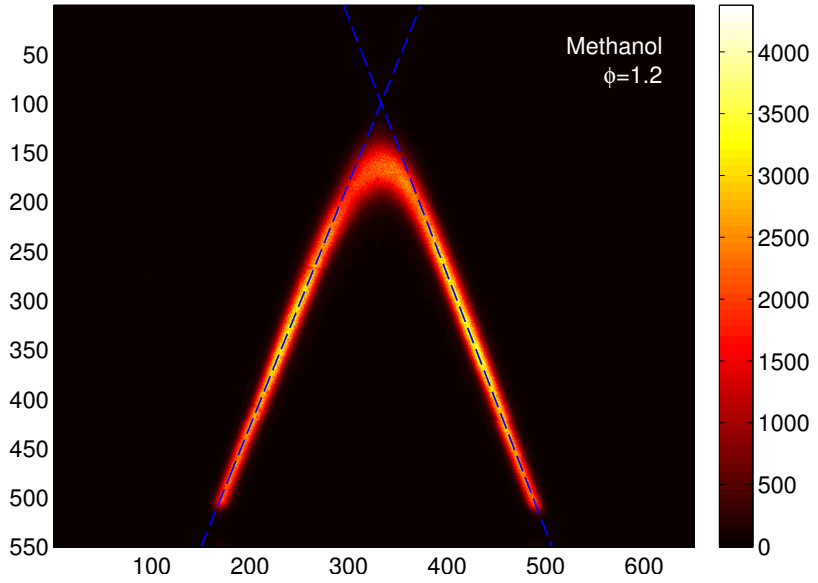

Figure 9.1: CH_2O LIF and edge detection in a methanol, $\phi = 1.2$ bunsen flame.

measured concentrations.

Only measurements in the Bunsen-type flame are reported here. Because the formaldehyde present in the premixed flame exists primarily in the preheat region, with peak concentrations observed to be near 1200 K [155], attempting to measure formaldehyde LIF in the flat flame configuration proved unsuccessful due to the close proximity of the porous plug. Therefore, the focus remained primarily on the conical flames.

9.2 Determination of flame front and positioning

The process for identifying the flame front in the CH_2O LIF images was very similar to that for the NO LIF images in Section 8.2.1. However, the aligning criteria was the peak CH_2O LIF signal. Figure 9.1 shows an example LIF image for a rich methane flame after all of the image processing corrections. Clearly the CH_2O resides in a thin region through the flame and cannot survive into the post-flame in significant quantities.

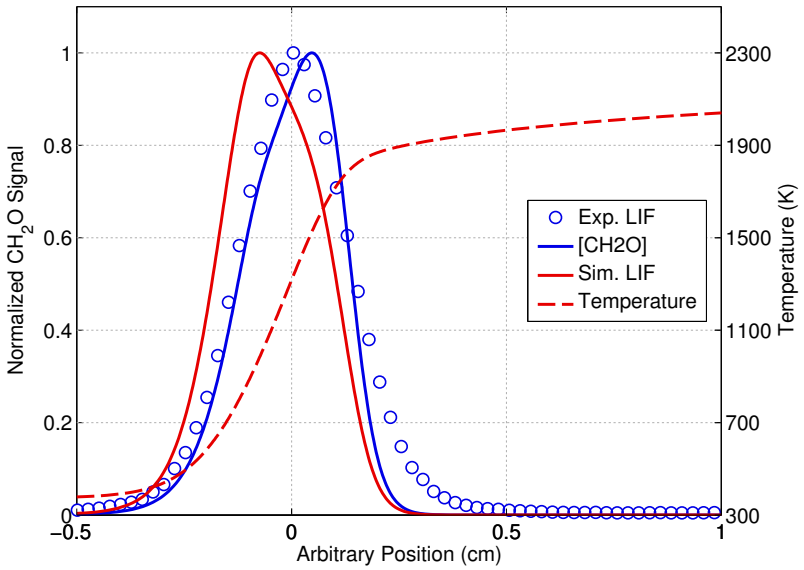

Figure 9.2: Alignment of measured and predicted CH_2O normalized profiles in the stoichiometric reference flame.

It is then necessary to align the LIF profile with the predicted CH_2O concentration profile. However, correction for the temperature dependent quenching and population fraction will shift the location of the peak CH_2O concentration (due to the increasing temperature profile through the CH_2O region). Therefore, rather than align the LIF and predicted CH_2O concentration peak locations, it is actually necessary to align the peak in experimental measurements with the peak in a simulated LIF profile based on the predictions. This is shown in Fig. 9.2. The solid blue line in this figure shows the predicted CH_2O concentration and the solid red line shows what the LIF signal profile would be accounting for the quenching corrections. As can be seen, the peak location shifts approximately 0.2 mm toward the lower temperature region. The experimental measurements are then aligned on this simulation LIF signal, rather than the predicted concentrations.

9.3 CH_2O concentration

After aligning the CH_2O LIF profile with the simulations appropriately, application of the quenching corrections was completed with the following relation:

$$X_{CH_2O} = C \cdot \frac{T}{f_b} \cdot \frac{Q_{21}}{A_{21}} \cdot S_{CH_2O} \tag{9.1}$$

where C is the calibration constant relating pixel intensity to concentration in parts per million, f_b is the population distribution of the ground state as described in equations 2.17–2.20. The fluorescent yield term has been simplified through the assumption that $Q_{21} \gg A_{21}$, which allows for the exponent on the temperature dependence of Q_{21} to be varied between $-1 < \alpha < -0.5$. As mentioned before, the calibration constant C was determined based on the peak predicted concentration of CH_2O in a stoichiometric methane flame. Two calibration constants were calculated based on the extremes of α and were carried over into equation 9.1.

The resulting CH_2O concentrations for $\alpha = -1$ and $\alpha = -0.5$ are shown in Fig. 9.3, indicating a band in which a reasonable quenching rate would result. Figure 9.3 shows comparisons of the measured concentrations with predicted values for the C_1–C_3 fuels, organized in rows, at equivalence ratios of 0.9, 1.0, and 1.1, organized by columns.

Examining the first row, composed of the C_1 fuels, it appears that the model does a good job in predicting the peak height for both fuels. Given that the LIF is calibrated on the middle alkane profile, the peak concentrations are well captured in the lean and rich cases as well. The methanol peak heights are also well captured through the equivalence ratio range. However, while the model does a good job predicting the shape of the methane peak, the predicted methanol peaks are less successful. It appears that the rate of consumption of CH_2O is over-predicted, narrowing the peak.

The C_2 fuels appear to be not well captured in the model's predictive capability.

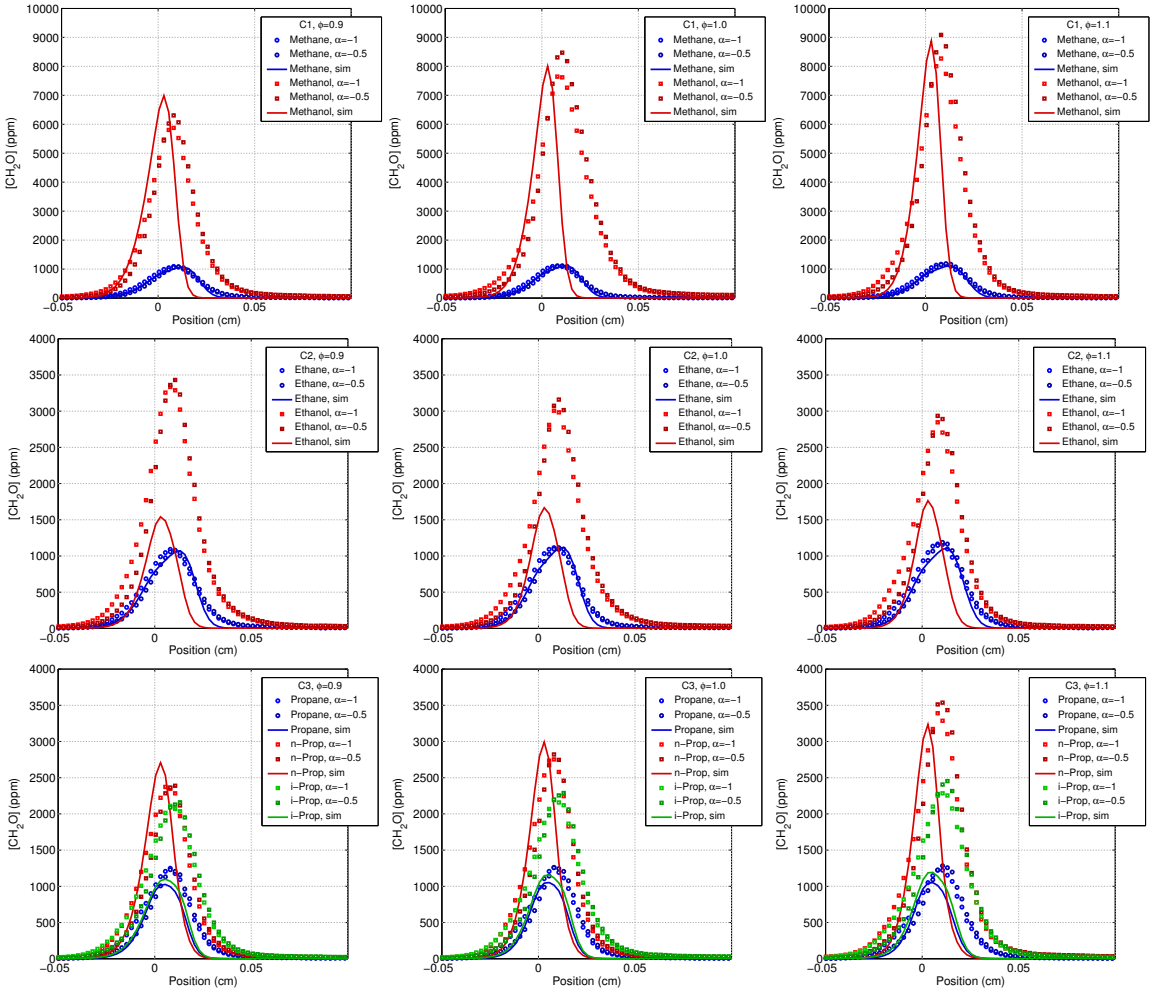

Figure 9.3: CH_2O concentration profiles for lean, stoichiometric, and rich C_1, C_2, and C_3 fuels.

Peak concentration values for the ethane flames are close to the measured values, however the ethanol peaks are greatly under-predicted by about 50%. The ethane peak shape is good on the formation side, and adequate on the consumption side with a slight over-prediction of consumption rate. It is difficult to tell if the ethanol peak would adequately capture the consumption rate due to the significant differences in peak height.

The C_3 alkane shows the worst agreement of all the alkanes. The model under-predicts the peak concentration by approximately 20%. The formation side of the peak is in consistently good agreement, however the consumption also appears to be over-predicted. The C_3 fuels present several interesting trends. It appears that peak n-propanol concentrations are reasonably well predicted while the i-propanol concentrations are off by about 50%. Both alcohols show an increase in peak concentration with equivalence ratio, however the rate of increase for n-propanol is greater than in the i-propanol case. At ϕ=0.9, measured CH_2O for both alcohols are very similar and at ϕ=1.1 the measured i-propanol concentrations were 30% lower than the n-propanol. The model predicts an increase in n-propanol peak concentrations, however the rate of this increase in under-predicted. Meanwhile, the model does not predict a significant increase in the i-propanol flames.

Figure 9.4 provides a summary of the peak concentrations for each of the fuels over the equivalence ratio range in this work. Generally, the summary shows deceptively good agreement in capturing the experimental trends. Predictions in the alkane fuels appear to do a much better job. Poorer prediction in the alcohol fuels is reasonable because different fuel decomposition routes are activated in the alcohol flames. These routes involve a greater proportion of oxygenated intermediates, such a formaldehyde, than has been observed in alkane flames. This is clearly seen in Fig. 9.4 where measured concentrations of formaldehyde in alcohols were approximately 10, 3, and 2 times greater than concentrations in the comparable alkanes. Additionally, peak

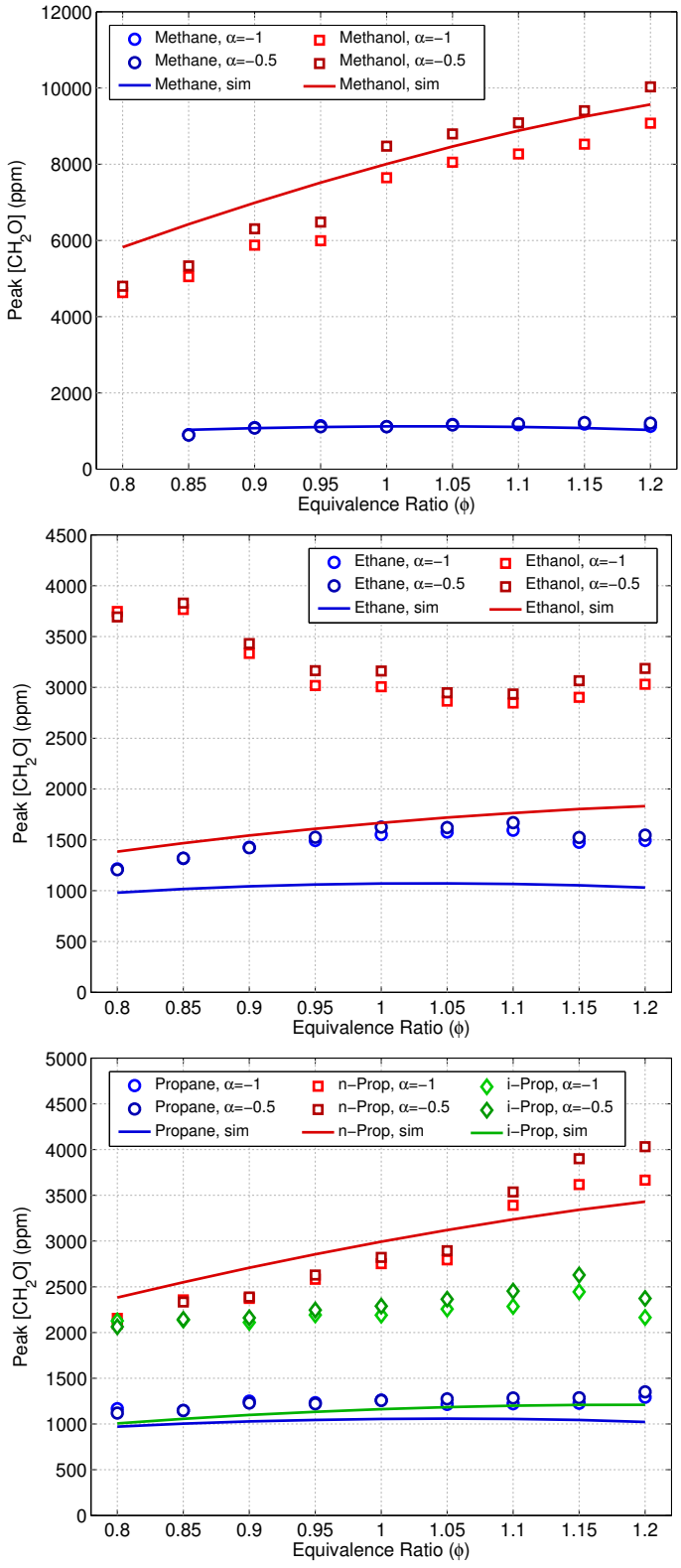

Figure 9.4: CH_2O peak concentrations.

formaldehyde concentrations appear to be a much stronger function of equivalence ratio in the alcohol flames than in the alkane, which further indicates the presence of equivalence ratio sensitive paths in alcohol combustion that are not present in the the alkanes.

The net effect on NO_X formation is difficult to quantify, however the combustion of the alcohol fuels clearly proceeds through a different set of intermediate hydrocarbon and oxygenated hydrocarbon radicals than in comparable alkane flames. These alternative pathways influence the distribution of intermediate species and the result is the reduction of non-thermal NO formation.

9.4 Conclusions

The objective of this chapter was to investigate the concentrations of formaldehyde present in alkane and alcohol flames and compare with the model's predictive capability. Experiments in Bunsen-type premixed flames with CH_2O LIF measurements were conducted and quantified using a semi-quantitative approach to estimating the quenching rate and the LIF calibration. This approach yielded the expected bounds in which a fully quantified CH_2O LIF technique would measure.

It was observed that alcohol flames produced significant greater concentrations of formaldehyde through the flame flame. The peak concentrations in the alcohol flames were up to an order of magnitude greater in the methanol flame than the methane, and approximately a factor of 2 in the n-propanol flame. Generally, the model did a good job of predicting peak CH_2O concentrations (apart from ethanol and i-propanol), however the peak shape was not well predicted. Consumption rates of formaldehyde in the model appear to be much greater than those observed in the experiment, resulting in a curtailing of the CH_2O peak. Under these conditions, it appears that the model could be improved to more accurately match the formaldehyde

distribution. This is especially true as the non-thermal NO_X contributions discussed in Chapter 8 are highly dependent on the distribution of hydrocarbon and oxygenated hydrocarbon radicals.

Chapter 10

Conclusions and Final Comments

In this work, the influence of the OH (hydroxyl) functional group on the suppression of NO_X formation was examined. The primary focus was on attempting to experimentally capture the differences in non-thermal contributions to NO_X formation in the combustion of a relatively wide range of fuels with as many as three hydroxyl groups. Included among these fuels were several practical fuels with significant potential for application on an industrial scale, including the C_1–C_3 alcohols and glycerol, the largest by-product of biodiesel production.

Generally, the conclusions can be summarized as follows. NO_X emissions in flames burning fuels containing one or more OH groups are reduced in proportion to the number of OH groups relative to the number of carbon atoms. The presence of the hydroxyl moiety shifts fuel decomposition pathways away from hydrocarbon intermediates vital for the formation of non-thermal NO toward oxygenated intermediates. In turn, all of the non-thermal NO formation pathways are reduced in alcohol and poly-alcohol flames, with varying degrees of reduction dependent on equivalence ratio. Under lean conditions, H/N/O sub-mechanisms are primarily responsible for lower NO emissions. Under rich conditions, C/N sub-mechanisms are primarily responsible, through the combined effect of reduced Prompt NO formation and an unaffected NO-HCN Reburn NO consumption. However, additional work is necessary to improve the quality of model predictions, both in the formation of HC intermediates and in the

initiation rates for the NO formation sub-mechanisms.

Two different approaches were used in this study. The first was to design and construct a laboratory scale high-swirl burner apparatus with the specific capability to combust difficult to burn fuels. These fuels are characterized by low energy densities, high viscosities, and high boiling points; but the addition of multiple hydroxyl groups to the fuel molecules allowed for a direct comparison of the influence of the substitution of hydroxyl groups. A test matrix of C_1–C_3 fuels with up to three OH groups was established. The second approach was to study pre-vaporized mixtures of alcohols and alkanes under simpler burner configurations with reduced dimensionality. These more fundamental studies allowed for more detailed measurements of NO_X formation in the flame front of a wide range of fuels, both with and without the presence of OH functional groups.

The results of the first approach can be summarized as follows:

- A robust high-swirl combustion apparatus was successfully constructed and characterized for the combustion of glycerol, diesel, and propane fuels. This burner design utilized a high-temperature cast refractory combustion chamber providing rigorous thermal feedback to vaporizing liquid spray achieved with an air atomizing nozzle. Characterization of the burner's operation showed a factor of 20 reduction in NO_X formation in glycerol flames when compared with either glycerol or diesel.

- The influence of the air-atomizing nozzle was investigated for oxygenated liquid fuels. Due to the significant differences in the thermo-physical properties of the liquid fuels, large variations in the quality of atomization could be observed through the range of control parameters available. These variations were investigated in detail for the influence of the nozzle turndown ratio, the atomizing air flow rate, and the liquid preheat temperature. It was observed that the greatest impact on quality of atomization was through the atomizing air flow rate,

followed by the fuel preheat temperature, and then the turndown ratio. It was also observed that through competing effects within the atomization process, careful selection of control parameters could yield a tailoring of the atomization to meet specific objectives.

- A parameter study of the influence of the atomizing air flow rate and the swirl number was conducted, including measurements of the mean flame temperature profiles and stack gas emissions measurements. It was observed that the atomizing air flow rate has a strong influence on the shape of the flame, the peak flame temperatures, and the prominence of the fuel-driven and air-driven vortices anchoring the flame. The swirl number has a strong influence on the entrainment of droplets in the region anchoring the flame as well as the maximum atomizing air flow rates achievable in the burner. Through the careful selection of boundary conditions and an iterative selection process, it was possible to effectively limit variations in global NO_X formations to differences in the non-thermal contributions. It was observed that NO formation through the non-thermal pathways was strongly and inversely dependent on the degree of oxygenation. Additionally, fuels with similar ratios of OH/C exhibited similar NO formation rates, which increased as OH/C decreased.

- A simple zero-dimensional modeling study under a wide range of temperatures and equivalence ratios typical of a swirling liquid spray flame was conducted using detailed chemical kinetics. It was observed that contributions to the non-thermal NO formation through the Prompt mechanisms were indeed limited by the greater sparcity of CH radicals in fuels with higher OH/C ratios. A detailed reaction path analysis for the fuel decomposition pathways identified a preference for carbon atoms adjacent to an OH group to oxidize through hydroxymethyl radicals with subsequent oxidation through formaldehyde. Such

pathways have greatly limited contributions to the hydrocarbon radical pools. These trends were consistent along constant ratios of OH/C, indicating that fuels such as glycerol and ethylene glycol behave very similarly to methanol with regard to HC intermediate species.

The second approach allows for a more detailed investigation of the coupling of the fuel and NO_X chemistry. This approach, however, was limited to fuels that can be premixed relatively easily, which precluded the polyols due to their low saturation pressure. Nonetheless, it was then easy to compare fuels which were structurally similar, with the presence of the OH group as the sole distinction. The results from this part can be summarized as follows:

- A liquid fuel vaporization system was designed and constructed to allow for the controlled evaporation of liquid fuels and premixing with air through a range of equivalence ratios. This pre-vaporization system was then coupled with a pair of fundamental combustion geometries in flat flame and Bunsen-type flame configurations, allowing for comparisons of experimental measurements with model predictions.

- Probed measurements of temperature and selected species were conducted through the flat flame and in the post gases. The low temperatures in the flat flame helped to limit the contribution to NO formation through the Thermal mechanism, allowing non-thermal contributions to provide the greatest distinction between fuels. Despite intrusive effects, lower concentrations of NO formation were observed in alcohol flames than in alkane flames of the same carbon number. This reduction in NO was observed to be greater when the presence of the hydroxyl group had a greater influence in the fuel structure, i.e. methanol and methane flames. Additionally, the difference in NO formation in alcohol and alkane flames increased as the equivalence ratio increased, indicating a strong

coupling of the NO formation to fuel chemistry.

- Non-intrusive measurements of the flame temperature were conducted using 2λ-OH LIF thermometry. Coupled with the probed thermocouple measurements, these two techniques allowed for the simulation of one-dimensional flames with detailed chemistry and the use of the measured temperature profile in the solution. Predictions of NO concentrations in the post flame were shown to generally under-predict the measured concentrations, however the trends with respect to fuel family were consistent.

- NO concentrations were measured in both the flat flame and Bunsen flame configurations using a quantified NO LIF technique. This technique allowed for the investigation of the formation of NO in the flame front which is typically characterized by contributions to NO through non-thermal pathways. The use of the flat flame and Bunsen configurations allowed for the investigations of NO formation in lower and higher temperature flames. For both configurations, the non-thermal NO contributions were significantly lower in the alcohol flames, ranging between 50-80% of the alkane flames. In the higher temperature flames, this difference in non-thermal contributions increased even further as the equivalence ratio increased. However, in the lower temperature flames, the difference in alcohol and alkane flames reached a maximum in the rich region with most of the fuels collapsing at around 50%.

- Simulations for both burner configurations were investigated through detailed reaction path analyses. This analysis allowed for the accounting of nitrogen flux through the flame, leading to the formation of NO. By identification of the different known NO formation pathways, the contributions of each sub-mechanism could be compared. It was observed that formation of NO through all of the NO formation pathways in alcohol flames were lower than in the

alkane flames. This indicates that the lower concentrations of NO resulting from alcohol flames in not due simply to a smaller CH radical pool, but is also due lower concentrations of other hydrocarbon intermediates as well as lower formation through the N_2O and NNH mechanisms.

In conclusion, all these considerations of non-thermal NO formation pathways become increasingly important as advanced NO_X mitigation techniques frequently enter the low temperature regime, shifting the formation of NO primarily from the thermal mechanism to non-thermal mechanisms. Coupled with the increasing role of alcohols and oxygenated fuels globally, understanding of the unique characteristics of one of the most tightly regulated emissions will play an increasingly vital role.

REFERENCES

[1] DIPPR Project 801. Full Version Evaluated Standard Thermophysical Property Values, Design Institute for Physical Properties, Department of Chemical Engineering, Brigham Young University, Provo, UT, 2005.

[2] James A. Miller and Craig T. Bowman. Mechanism and modeling of nitrogen chemistry in combustion. *Prog. Energy Combust. Sci.*, 15(4):287–338, 1989.

[3] Doug Grano. Nitrogen Oxides: Impacts on Public Health and the Environment. *Off. Air Radiat. United States Environ. Prot. Agency*, (August), 1997.

[4] Environmental Protection Agency (EPA). Nitrogen Oxides (NOx), Why and How They Are Controlled. *Epa-456/F-99-006R*, (November):48, 1999.

[5] Ya.B Zeldovich, P.Ya. Sadovnikov, and D.A. Frank-Kamenetskii. Oxidation of nitrogen in combustion, translated by M. Sheref. *Acad. Sci. USSR, Moscow*, 1947.

[6] K.K. Kuo. *Principles of Combustion*. John Wiley & Sons, Hoboken, NJ, 2nd edition, 2005.

[7] J. Warnatz, U. Maas, and R. W. Dibble. *Combustion*. Springer-Verlag, Berlin Heidelberg, New York, 4th edition, 2006.

[8] D. L. Baulch, Craig T. Bowman, C. J. Cobos, R. A. Cox, Th. Just, J. A. Kerr, Michael J. Pilling, D. Stocker, J. Troe, and Ts. Evaluated Kinetic Data for Combustion Modeling: Supplement II. *J. Phys. Chem. Ref. Data*, 34(3):757, jul 2005.

[9] Graeme M. G. Watson, Philippe Versailles, and Jeffrey M. Bergthorson. NO Formation in premixed flames of C1-C3 alkanes and alcohols. *Combust. Flame*, (accepted), 2016.

[10] C.P. Fenimore. Formation of nitric oxide in premixed hydrocarbon flames. *Proc. Combust. Inst.*, 13(1):373–380, 1971.

[11] C.P. Fenimore. Studies of fuel-nitrogen species in rich flame gases. *Seventeenth Symp. Combust.*, 17(1):661–670, 1979.

[12] L S Caretto. MODELING POLLUTANT FORMATION IN COMBUSTION PROCESSES. *Fourteenth Symp. Combust.*, pages 803–817, 1973.

[13] Joanna Blauwens, Bruno Smets, and Jozef Peeters. Mechanism of "Prompt" NO formation in hydrocarbon flames. *Proc. Combust. Inst.*, 16(1):1055–1064, 1977.

[14] James A. Miller, Michael J. Pilling, and Jürgen Troe. Unravelling combustion mechanisms through a quantitative understanding of elementary reactions. *Proc. Combust. Inst.*, 30(1):43–88, 2005.

[15] S.C Hill and L Douglas Smoot. Modeling of nitrogen oxides formation and destruction in combustion systems. *Prog. Energy Combust. Sci.*, 26(4-6):417–458, aug 2000.

[16] A.N. Hayhurst and I.M. Vince. The origin and nature of prompt nitric oxide in flames. *Combust. Flame*, 50:41–57, jan 1983.

[17] L V Moskaleva and M C Lin. The spin-conserved reaction CH+N2H+NCN: A major pathway to prompt no studied by quantum/statistical theory calculations and kinetic modeling of rate constant. *Proc. Combust. Inst.*, 28(2):2393–2401, 2000.

[18] P. Dagaut, Peter Glarborg, and Maria U. Alzueta. The oxidation of hydrogen cyanide and related chemistry. *Prog. Energy Combust. Sci.*, 34(1):1–46, feb 2008.

[19] Peter Glarborg, Maria U. Alzueta, Kim Dam-Johansen, and James A. Miller. Kinetic Modeling of Hydrocarbon/Nitric Oxide Interactions in a Flow Reactor. *Combust. Flame*, 115(1-2):1–27, oct 1998.

[20] R. S. Zhu and M. C. Lin. Ab initio study on the oxidation of NCN by O (3P): Prediction of the total rate constant and product branching ratios. *J. Phys. Chem. A*, 111(29):6766–6771, 2007.

[21] Gregory P Smith. Evidence of NCN as a flame intermediate for prompt NO. *Chem. Phys. Lett.*, 367(5-6):541–548, jan 2003.

[22] A. El-Bakali, L. Pillier, Pascale Desgroux, B. Lefort, Laurent Gasnot, J.F. Pauwels, and I. da Costa. NO prediction in natural gas flames using GDF-Kin®3.0 mechanism NCN and HCN contribution to prompt-NO formation. *Fuel*, 85(7-8):896–909, may 2006.

[23] Venkatesh Vasudevan, Ronald K. Hanson, Craig T Bowman, David M Golden, and David F Davidson. Shock tube study of the reaction of CH with N2: overall rate and branching ratio. *J. Phys. Chem. A*, 111(46):11818–11830, 2007.

[24] Lawrence B. Harding, Stephen J. Klippenstein, and James A. Miller. Kinetics of CH + N 2 Revisited with Multireference Methods. *J. Phys. Chem. A.*, 112: 522–532, 2008.

[25] Nathalie Lamoureux, Hilal El Merhubi, Laure Pillier, Stéphanie de Persis, and Pascale Desgroux. Modeling of NO formation in low pressure premixed flames. *Combust. Flame*, 163:557–575, 2016.

[26] C. Morley. The Formation and Destruction of Hydrogen Cyanide from Atmospheric and Fuel Nitrogen in Rich Atmospheric-Pressure Flames. *Combust. Flame*, 27:189–204, 1976.

[27] Albert L. Myerson. The reduction of nitric oxide in simulated combustion effluents by hydrocarbon-oxygen mixtures. *Proc. Combust. Inst.*, 15(1):1085–1092, 1975.

[28] Jost O L Wendt, C V Sternling, and M A Matovich. Reduction of sulfur trioxide and nitrogen oxide by secondary fuel injection. *Proc. Combust. Inst.*, 14(1):897–904, 1973.

[29] Dieter Stapf and Wolfgang Leuckel. Flow reactor studies and testing of comprehensive mechanisms for NOx reburning. *Symp. Combust.*, 26(2):2083–2090, 1996.

[30] T. Etzkorn, S. Muris, J. Wolfrum, C. Dembny, H. Bockhorn, P.F. Nelson, A. Attia-Shahin, and J. Warnatz. Destruction and formation of no in low pressure stoichiometric CH4/O2 flames. *Symp. Combust.*, 24(1):925–932, jan 1992.

[31] P. Dagaut, F. Lecomte, S. Chevailler, and M. Cathonnet. Experimental and Detailed Kinetic Modeling of Nitric Oxide Reduction by a Natural Gas Blend

in Simulated Reburning Conditions. *Combust. Sci. Technol.*, 139(1):329–363, 1998.

[32] L. PRADA and James A. Miller. Reburning using Several Hydrocarbon Fuels: A Kinetic Modeling Study. *Combust. Sci. Technol.*, 132(1-6):225–250, feb 1998.

[33] Kenneth G. Unfried, Graham P. Glass, and R.F. Curl. Infrared flash kinetic spectroscopy of the ketenyl radical. *Chem. Phys. Lett.*, 177(1):33–38, feb 1991.

[34] Werner Boullart, Minh Tho Nguyen, and Jozef Peeters. Experimental Investigation of the Reaction between Nitric Oxide and Ketenyl Radicals (HCCO + NO): Rate Coefficient at T = 290-670 K and Product Distribution at 700 K. *J. Phys. Chem.*, 98(33):8036–8043, aug 1994.

[35] James A. Miller, Melvyn C Branch, William J Mclean, David W Chandler, Mitchell D. Smooke, and Robert J. Kee. The conversion of hcn to no and n2 in h2 o2 hcn ar flames at low pressure. *Proc. Combust. Inst.*, 20:673–684, 1984.

[36] G M Johnson and M Y Smith. Emissions of Nitrogen Dioxide from a Large Gas-Turbine Power Station. *Combust. Sci. Technol.*, 19(1-2):67–70, 1978.

[37] R.W. Coutant, E.L. Merryman, and A. Levy. Formation of NO2 in range-top burners. *Environ. Int.*, 8(1-6):185–192, jan 1982.

[38] C.P. Fenimore. The ratio NO2NO in fuel-lean flames. *Combust. Flame*, 25: 85–90, aug 1975.

[39] Sanjay M Correa. A Review of NOx Formation Under Gas-Turbine Combustion Conditions. *Combust. Sci. Technol.*, 87(1-6):329–362, 1993.

[40] James a. Miller, M.C. Branch, and Robert J. Kee. A chemical kinetic model for the selective reduction of nitric oxide by ammonia. *Combust. Flame*, 43(0): 81–98, 1981.

[41] James A. Miller and P Glarborg. Modelling the Formation of N 2 0 and N0 2 in the Thermal De-NO x Process. 61(x):318–333, 1996.

[42] Peter Glarborg, Kim Dam-Johansen, and James A. Miller. The reaction of ammonia with nitrogen dioxide in a flow reactor: Implications for the NH2 + NO2 reaction. *Int. J. Chem. Kinet.*, 27(12):1207–1220, dec 1995.

[43] James A. Miller. Theory and modeling in combustion chemistry. *Symp. Combust.*, 26(1):461–480, 1996.

[44] C.C Schmidt and C.T Bowman. Flow reactor study of the effect of pressure on the thermal de-NOx process. *Combust. Flame*, 127(1-2):1958–1970, oct 2001.

[45] Joseph W. Bozzelli and Anthony M. Dean. 0 + NNH: A Possible New Route for NOx formation in flames. *Int. J. Chem. Kinet.*, 27(11):1097–1109, 1995.

[46] Joel E. Harrington, Gregory P. Smith, Pamela A. Berg, Alison R. Noble, Jay B. Jeffries, and David R. Crosley. Evidence for a new no production mechanism in flames. *Proc. Combust. Inst.*, 26(2):2133–2138, 1996.

[47] Stephen J. Klippenstein, Lawrence B. Harding, Peter Glarborg, and James A. Miller. The role of NNH in NO formation and control. *Combust. Flame*, 158 (4):774–789, 2011.

[48] D B Spalding. The combustion of liquid fuels. *Proc. Combust. Inst.*, 4(1): 847–864, 1953.

[49] G A E Godsave. Studies of the combustion of drops in a fuel spray the burning of single drops of fuel. *Proc. Combust. Inst.*, 4(1):818–830, 1953.

[50] H Wise, J Lorell, and B Wood. The effects of chemical and physical parameters on the burning rate of liquid droplets. *Proc. Combust. Inst.*, 5(1):132–141, 1955.

[51] Alan Williams. Combustion of droplets of liquid fuels: A review. *Combust. Flame*, 21:1–31, 1973.

[52] G. M. Faeth. Current status of droplet and liquid combustion. *Prog. Energy Combust. Sci.*, 3:191–224, 1977.

[53] Fokion N. Egolfopoulos, D.X. X Du, and C.K. Law. A study on ethanol oxidation kinetics in laminar premixed flames, flow reactors, and shock tubes. *Twenty-Fourth Symp. Combust.*, 24(1):833–841, jan 1992.

[54] Charles K. Westbrook and Frederick L. Dryer. Prediction of laminar flame properties of methanol-air mixtures. *Combust. Flame*, 37:171–192, jan 1980.

[55] Omer L Gulder. Laminar burning velocities of methanol, ethanol and isooctane-air mixtures. *Proc. Combust. Inst.*, 19:275–281, 1982.

[56] Thomas S. Norton and Frederick L. Dryer. Some New Observations on Methanol Oxidation Chemistry. *Combust. Sci. Technol.*, 63(December 2014):107–129, 1989.

[57] Thomas S. Norton and Frederick L. Dryer. The flow reactor oxidation of C1C4 alcohols and MTBE. *Symp. Combust.*, 23(1):179–185, jan 1991.

[58] Fokion N. Egolfopoulos, D. X. Du, and C. K. Law. A Comprehensive Study of Methanol Kinetics in Freely-Propagating and Burner-Stabilized Flames, Flow and Static Reactors, and Shock Tubes. *Combust. Sci. Technol.*, 83(October 2012):33–75, 1992.

[59] S. Mani Sarathy, Patrick Oßwald, Nils Hansen, and Katharina Kohse-Höinghaus. Alcohol combustion chemistry. *Prog. Energy Combust. Sci.*, 44: 40–102, oct 2014.

[60] K. Alexander Heufer, S. Mani Sarathy, Henry J. Curran, Alexander C. Davis, Charles K. Westbrook, and William J. Pitz. Detailed Kinetic Modeling Study of n -Pentanol Oxidation. *Energy & Fuels*, 26(11):6678–6685, nov 2012.

[61] S. Mani Sarathy, Sungwoo Park, Bryan W. Weber, Weijing Wang, Peter S. Veloo, Alexander C. Davis, Casimir Togbe, Charles K. Westbrook, Okjoo Park, Guillaume Dayma, Zhaoyu Luo, Matthew A. Oehlschlaeger, Fokion N. Egolfopoulos, Tianfeng Lu, William J. Pitz, Chih-Jen Sung, and Philippe Dagaut. A comprehensive experimental and modeling study of iso-pentanol combustion. *Combust. Flame*, 160(12):2712–2728, dec 2013.

[62] Charles K. Westbrook and Frederick L. Dryer. Comprehensive Mechanism for Methanol Oxidation. *Combust. Sci. Technol.*, 20(3-4):125–140, 1979.

[63] US Energy Information Admininstration. Monthly Energy Review. Technical report, US Energy Information Admininstration, 2016.

[64] R. Sivaramakrishnan, M-C C. Su, J. V. Michael, Stephen J. Klippenstein, L. B. Harding, and B. Ruscic. Rate constants for the thermal decomposition of ethanol and its bimolecular reactions with OH and D: Reflected shock tube and theoretical studies. *J. Phys. Chem. A*, 114(35):9425–9439, sep 2010.

[65] J. Park, Z. F. Xu, and M. C. Lin. Thermal decomposition of ethanol. II. A computational study of the kinetics and mechanism for the H+C2H5OH reaction. *J. Chem. Phys.*, 118(22):9990–9996, 2003.

[66] Zhen Feng Xu, Kun Xu, and Ming Chang Lin. Ab initio kinetics for decomposition/isomerization reactions of C 2H5O radicals. *ChemPhysChem*, 10(6): 972–982, 2009.

[67] Juan P. Senosiain, Stephen J. Klippenstein, and James A. Miller. Reaction of ethylene with hydroxyl radicals: A theoretical study. *J. Phys. Chem. A*, 110 (21):6960–6970, jun 2006.

[68] J. A. Barnard. The pyrolysis of isopropanol. *Trans. Faraday Soc.*, 56:72, jan 1960.

[69] Antony B. Trenwith. Thermal decomposition of isopropanol. *J. Chem. Soc. Faraday Trans. 1 Phys. Chem. Condens. Phases*, 71(May):2405, jan 1975.

[70] Yuyang Li, Lixia Wei, Zhenyu Tian, Bin Yang, Jing Wang, Taichang Zhang, and Fei Qi. A comprehensive experimental study of low-pressure premixed C3-oxygenated hydrocarbon flames with tunable synchrotron photoionization. *Combust. Flame*, 152(3):336–359, feb 2008.

[71] T. Kasper, P. Oßwald, U. Struckmeier, K. Kohse-Höinghaus, C.A. Taatjes, J. Wang, T.A. Cool, M.E. Law, A. Morel, and P.R. Westmoreland. Combustion chemistry of the propanol isomers investigated by electron ionization and VUV-photoionization molecular-beam mass spectrometry. *Combust. Flame*, 156(6): 1181–1201, jun 2009.

[72] Peter S. Veloo and Fokion N. Egolfopoulos. Studies of n-propanol, iso-propanol, and propane flames. *Combust. Flame*, 158(3):501–510, mar 2011.

[73] B. Galmiche, C. Togbe, P. Dagaut, F. Halter, and F. Foucher. Experimental and Detailed Kinetic Modeling Study of the Oxidation of 1-Propanol in a Pressurized Jet-Stirred Reactor (JSR) and a Combustion Bomb. *Energy & Fuels*, 25(5):2013–2021, may 2011.

[74] Michael V. Johnson, S. Scott Goldsborough, Zeynep Serinyel, Peter O'Toole, Eoin Larkin, Grainne O'Malley, and Henry J. Curran. A shock tube study of n- and iso-propanol ignition. *Energy and Fuels*, 23(12):5886–5898, dec 2009.

[75] Alessio Frassoldati, Alberto Cuoci, Tiziano Faravelli, Ulrich Niemann, Eliseo Ranzi, Reinhard Seiser, and Kalyanasundaram Seshadri. An experimental and kinetic modeling study of n-propanol and iso-propanol combustion. *Combust. Flame*, 157(1):2–16, jan 2010.

[76] Xingjia Man, Chenglong Tang, Jiaxiang Zhang, Yingjia Zhang, Lun Pan, Zuohua Huang, and Chung K. Law. An experimental and kinetic modeling study of n-propanol and i-propanol ignition at high temperatures. *Combust. Flame*, 161(3):644–656, mar 2014.

[77] S. Mani Sarathy, Stijn Vranckx, Kenji Yasunaga, Marco Mehl, Patrick Oßwald, Wayne K. Metcalfe, Charles K. Westbrook, William J. Pitz, Katharina Kohse-Höinghaus, Ravi X. Fernandes, and Henry J. Curran. A comprehensive chemical kinetic combustion model for the four butanol isomers. *Combust. Flame*, 159 (6):2028–2055, 2012.

[78] James R. Dunlop and Frank P. Tully. Catalytic Dehydration of Alcohols. 2-Propanol: An Intermediate Case. *J. Phys. Chem.*, 97(24):6457–6464, jun 1993.

[79] Emma Barker Hemings, Carlo Cavallotti, Alberto Cuoci, Tiziano Faravelli, and Eliseo Ranzi. A Detailed Kinetic Study of Pyrolysis and Oxidation of Glycerol (Propane-1,2,3-triol). *Combust. Sci. Technol.*, 184(7-8):1164–1178, jul 2012.

[80] Duane T Johnson and Katherine A Taconi. The glycerin glut: Options for the value-added conversion of crude glycerol resulting from biodiesel production. *Environ. Prog.*, 26(4):338–348, 2007.

[81] César A.G. Quispe, Christian J.R. Coronado, and João A. Carvalho Jr. Glycerol: Production, consumption, prices, characterization and new trends in combustion. *Renew. Sustain. Energy Rev.*, 27:475–493, nov 2013.

[82] Mayank Gupta and Naveen Kumar. Scope and opportunities of using glycerol as an energy source. *Renew. Sustain. Energy Rev.*, 16(7):4551–4556, sep 2012.

[83] Hyu-Bum Park, Ho-Jin Kweon, Young-Sik Hong, Si-Joong Kim, and Keon Kim. Preparation of La1-x Srx MnO 3 powders by combustion of poly (ethylene glycol) metal nitrate gel precursors. *J. Mater. Sci.*, 32:57–65, 1997.

[84] Weifan Chen, Fengsheng Li, and Jiyi Yu. Combustion synthesis and characterization of nanocrystalline CeO2-based powders via ethylene glycolnitrate process. *Mater. Lett.*, 60(1):57–62, jan 2006.

[85] Diana Hernández, Jhon J. Fernández, Fanor Mondragón, and Diana López. Production and utilization performance of a glycerol derived additive for diesel engines. *Fuel*, 92(1):130–136, feb 2012.

[86] Carlo Beatrice, Gabriele Di Blasio, Maurizio Lazzaro, Catia Cannilla, Giuseppe Bonura, Francesco Frusteri, Francesco Asdrubali, Giorgio Baldinelli, Andrea Presciutti, Francesco Fantozzi, Gianni Bidini, and Pietro Bartocci. Technologies for energetic exploitation of biodiesel chain derived glycerol: Oxy-fuels production by catalytic conversion. *Appl. Energy*, 102:63–71, feb 2013.

[87] D. Cespi, F. Passarini, G. Mastragostino, I. Vassura, S. Larocca, A. Iaconi, A. Chieregato, J.-L. Dubois, and F. Cavani. Glycerol as feedstock in the synthesis of chemicals: a life cycle analysis for acrolein production. *Green Chem.*, 17(1):343–355, 2014.

[88] R Patzer. Stack emissions evaluation: combustion of crude glycerin and yellow grease in an industrial fire tube boiler. Technical report, Marshall, MN, 2007.

[89] V. Dee and B.D. Shaw. Combustion of propanolglycerol mixture droplets in reduced gravity. *Int. J. Heat Mass Transf.*, 47(22):4857–4867, oct 2004.

[90] Myles D. Bohon and William L. Roberts. *Characertization of Glycerol Combustion and Emissions*. PhD thesis, North Carolina State University, Raleigh, NC, 2010.

[91] Myles D. Bohon, Brian A. Metzger, William P. Linak, Charly J. King, and William L. Roberts. Glycerol combustion and emissions. *Proc. Combust. Inst.*, 33(2):2717–2724, 2011.

[92] Brian A. Metzger and William L. Roberts. *Glycerol Combustion*. PhD thesis, Raleigh, NC, 2007.

[93] William P. Linak, C. Andrew Miller, Joseph P. Wood, Takuya Shinagawa, Jong-Ik Yoo, Dawn a. Santoianni, Charles J. King, Jost O. L. Wendt, and Yong-Chil Seo. High Temperature Interactions Between Residual Oil Ash and Dispersed Kaolinite Powders. *Aerosol Sci. Technol.*, 38(9):900–913, 2004.

[94] Jong-Ik Yoo, Takuya Shinagawa, Joseph P. Wood, William P. Linak, Dawn A. Santoianni, Charles J. King, Yong-Chil Seo, and Jost O. L. Wendt. High-Temperature Sorption of Cesium and Strontium on Dispersed Kaolinite Powders. *Environ. Sci. Technol.*, 39(13):5087–5094, jul 2005.

[95] Scott A Steinmetz, Jason Sandor Herrington, Christopher K Winterrowd, William L. Roberts, Jost O L Wendt, and William P. Linak. Crude glycerol

combustion: Particulate, acrolein, and other volatile organic emissions. *Proc. Combust. Inst.*, 34(2):2749–2757, 2013.

[96] Benjamin M Simmons. Flow and Dropsize Measurements in Glycerol Spray Flames. *New Horizons*, (January):1–9, 2012.

[97] Lulin Jiang and Ajay K. Agrawal. Investigation of Glycerol Atomization in the Near-Field of a Flow-Blurring Injector using Time-Resolved PIV and High-Speed Visualization. *Flow, Turbul. Combust.*, oct 2014.

[98] Lulin Jiang and Ajay K. Agrawal. Combustion of straight glycerol with/without methane using a fuel-flexible, low-emissions burner. *Fuel*, 136:177–184, nov 2014.

[99] Myles D. Bohon and William L. Roberts. NOx emissions from high swirl turbulent spray flames with highly oxygenated fuels. *Proc. Combust. Inst.*, 34(1): 1705–1712, jan 2013.

[100] Myles D. Bohon, Mariam J. Al Rashidi, S. Mani Sarathy, and William L. Roberts. Experiments and simulations of NOx formation in the combustion of hydroxylated fuels. *Combust. Flame*, 162(6):2322–2336, 2015.

[101] John McNeil, Paul Day, and Felix Sirovski. Glycerine from biodiesel: The perfect diesel fuel. *Process Saf. Environ. Prot.*, 90(3):180–188, may 2012.

[102] Scott J. Eaton, George N. Harakas, Richard W. Kimball, Jennifer A. Smith, Kira A. Pilot, Mitch T. Kuflik, and Jeremy M. Bullard. Formulation and Combustion of GlycerolDiesel Fuel Emulsions. *Energy & Fuels*, 28(6):3940–3947, jun 2014.

[103] S C Li and Forman A. Williams. Formation of NOx, CH4, and C2, species in laminar methanol flames. *Proc. Combust. Inst.*, 27:485–493, 1998.

[104] S. C. Li and Forman A. Williams. Experimental and Numerical Studies of NOx Formation in Two-Stage Methane-Air Flames. In *Vol. 3 Coal, Biomass Altern. Fuels; Combust. Fuels; Oil Gas Appl. Cycle Innov.*, page V003T06A001. ASME, jun 1998.

[105] Priyank Saxena and Forman A. Williams. Numerical and experimental studies of ethanol flames. *Proc. Combust. Inst.*, 31(1):1149–1156, jan 2007.

[106] Carla S.T. Marques, Luiz G. Barreta, Maria E. Sbampato, and Alberto M. dos Santos. Laser-saturated fluorescence of nitric oxide and chemiluminescence measurements in premixed ethanol flames. *Exp. Therm. Fluid Sci.*, 34(8):1142–1150, nov 2010.

[107] Gregory A. Chung, Benjamin Akih-Kumgeh, Graeme M. G. Watson, and Jeffrey M. Bergthorson. NOx formation and flame velocity profiles of iso- and n-isomers of butane and butanol. *Proc. Combust. Inst.*, 34(1):831–838, jan 2013.

[108] S. Mani Sarathy, Murrary J. Thomson, C. Togbé, P. Dagaut, F. Halter, and C. Mounaim-Rousselle. An experimental and kinetic modeling study of n-butanol combustion. *Combust. Flame*, 156(4):852–864, apr 2009.

[109] Myles D. Bohon, Thibault F. Guiberti, S Mani Sarathy, and William L. Roberts. Variations in non-thermal NO formation pathways in alcohol flames. *Proc. Combust. Inst.*, 36 (accept, 2016.

[110] Ruey-Hung Chen, James F Driscoll, J Kelly, M Namazian, and R W Schefer. A Comparison of Bluff-Body and Swirl Stabilized Flames. *Combust. Sci. Technol.*, 71:197–217, 1990.

[111] Douglas Feikema, Ruey-Hung Chen, and James F Driscoll. Enhancement of flame blowout limits by use of swirl. *Combust. Flame*, 80:183–195, 1990.

[112] Douglas Feikema, Ruey-Hung Chen, and James F Driscoll. Blowout of Non-premixed Flames- Maximum Coaxial Air Velocities Achievable, with and without Swirl. *Combust. Flame*, 86:347–358, 1991.

[113] M. M. Ribeiro and J. H. Whitelaw. Coaxial jets with and without swirl. *J. Fluid Mech.*, 96(04):769, 1980.

[114] T C Claypole and Nicholas Syred. The Effect of Swirl Burner Aerodynamics on NOx Formation. *Proc. Combust. Inst.*, 18:81–89, 1981.

[115] Christine M. Vagelopoulos and Fokion N. Egolfopoulos. Direct experimental determination of laminar flame speeds. *Proc. Combust. Inst.*, 27:513–519, 1998.

[116] Mohamad Metghalchi and James C. Keck. Laminar burning velocity of propane-air mixtures at high temperature and pressure. *Combust. Flame*, 38:143–154, 1980.

[117] Mohamad Metghalchi and James C. Keck. Burning velocities of mixtures of air with methanol, isooctane, and indolene at high pressure and temperature. *Combust. Flame*, 48:191–210, jan 1982.

[118] S. Prucker, W. Meier, and W. Stricker. A flat flame burner as calibration source for combustion research: Temperatures and species concentrations of premixed H2/air flames. *Rev. Sci. Instrum.*, 65(9):2908–2911, sep 1994.

[119] L.P.H. de Goey, A. van Maaren, and R.M. Quax. Stabilization of adiabatic premixed laminar flames on a flat flame burner. *Combust. Sci. Technol.*, 92: 201–207, 1993.

[120] A. van Maaren, D.S. Thung, and L.P.H. de Goey. Measurement of flame temperature and adiabatic burning velocity of methane/air mixtures. *Combust. Sci. Technol.*, 96:327–344, 1994.

[121] Brett E. Battles and Ronald K. Hanson. Laser-induced fluorescence measurements of NO and OH mole fraction in fuel-lean, high pressure (1-10 atm) methane flames: fluorescence modeling and experimental validation. *J. Quant. Spectrosc. Radiat. Transf.*, 54(3):521–537, 1995.

[122] Laurent Gasnot, Pascale Desgroux, J.F. Pauwels, and L R Sochet. Detailed Analysis of Low-pressure Premixed Flames of CH4+O2+N2: A Study of Prompt-NO. *Combust. Flame*, 117:291–306, 1999.

[123] Lei Deng, Andreas Kempf, Olaf Hasemann, Oleg P. Korobeinichev, and Irenaeus Wlokas. Investigation of the sampling nozzle effect on laminar flat flames. *Combust. Flame*, 162(5):1737–1747, 2014.

[124] G.E. Andrews and D. Bradley. Determination of burning velocities: A critical review. *Combust. Flame*, 18(1):133–153, feb 1972.

[125] D.D.S. Liu and R. MacFarlane. Laminar burning velocities of hydrogen-air and hydrogen-air-steam flames. *Combust. Flame*, 49(1-3):59–71, jan 1983.

[126] Terrance C. Wagner and Colin R. Ferguson. Bunsen flame hydrodynamics. *Combust. Flame*, 59(3):267–272, mar 1985.

[127] Yong He, Zhihua Wang, Li Yang, Ronald Whiddon, Zhongshan Li, Junhu Zhou, and Kefa Cen. Investigation of laminar flame speeds of typical syngas using laser based Bunsen method and kinetic simulation. *Fuel*, 95:206–213, 2012.

[128] Bernard Lewis and Guenther von Elbe. Stability and Structure of Burner Flames. *J. Chem. Phys.*, 11(2):75, 1943.

[129] C K Law, S Ishizuka, and P Cho. On the Opening of Premixed Bunsen Flame Tips. *Combust. Sci. Technol.*, 28(3-4):89–96, 1982.

[130] S.H. Sohrab and C.K. Law. Influence of burner rim aerodynamics on polyhedral flames and flame stabilization. *Combust. Flame*, 62(3):243–254, dec 1985.

[131] M. Mizomoto and H. Yoshida. Effects of Lewis number on the burning intensity of Bunsen flames. *Combust. Flame*, 70(1):47–60, oct 1987.

[132] C.J. Sun, C.J. Sung, and C.K. Law. On adiabatic stabilization and geometry of bunsen flames. *Symp. Combust.*, 25(1):1391–1398, jan 1994.

[133] F.J. Higuera. Aerodynamics of a slender axisymmetric Bunsen flame with large gas expansion. *Combust. Flame*, 156(5):1063–1067, may 2009.

[134] A. Bourehla and F. Baillot. Appearance and Stability of a Laminar Conical Premixed Flame Subjected to an Acoustic Perturbation. *Combust. Flame*, 114 (3-4):303–318, aug 1998.

[135] V.N. Kornilov, K.R.A.M. Schreel, and L.P.H. de Goey. Experimental assessment of the acoustic response of laminar premixed Bunsen flames. *Proc. Combust. Inst.*, 31(1):1239–1246, jan 2007.

[136] Preetham, H. Santosh, and Tim Lieuwen. Dynamics of Laminar Premixed Flames Forced by Harmonic Velocity Disturbances. *J. Propuls. Power*, 24(6): 1390–1402, 2008.

[137] V.N. Kornilov, R. Rook, J.H.M. ten Thije Boonkkamp, and L.P.H. de Goey. Experimental and numerical investigation of the acoustic response of multi-slit Bunsen burners. *Combust. Flame*, 156(10):1957–1970, oct 2009.

[138] L.P.H. de Goey, J.A. van Oijen, V.N. Kornilov, and J.H.M. ten Thije Boonkkamp. Propagation, dynamics and control of laminar premixed flames. *Proc. Combust. Inst.*, 33(1):863–886, 2011.

[139] Alan C. Eckbreth. *Laser Diagnostics for Combustion Temperature and Species*. CRC Press, 1996.

[140] John W. Daily. Laser induced fluorescence spectroscopy in flames. *Prog. Energy Combust. Sci.*, 23(2):133–199, jan 1997.

[141] Normand M. Laurendeau. Temperature measurements by light-scattering methods. *Prog. Energy Combust. Sci.*, 14(2):147–170, jan 1988.

[142] Ronald K. Hanson, Jerry M. Seitzman, and Phillip H. Paul. Planar laser-fluorescence imaging of combustion gases. *Appl. Phys. B Photophysics Laser Chem.*, 50(6):441–454, 1990.

[143] J M Seitzman and Ronald K. Hanson. Two-Line Planar Fluorescence for Temporally Resolved Temperature Imaging in a Reacting Supersonic Flow over a Body. *Appl. Phys. B*, 57:385–391, 1993.

[144] J M Seitzman, Ronald K. Hanson, P A Debarber, and C F Hess. Application of quantitative two-line OH planar laser-induced fluorescence for temporally resolved planar thermometry in reacting flows. *Appl. Opt.*, 33(18):4000–4012, 1994.

[145] B K Mcmillin, J M Seitzman, and Ronald K. Hanson. Comparison of NO and OH Planar Fluorescence Temperature Measurements in Scramjet Model Flowfields. *AIAA J.*, 32(10):1945–1952, 1994.

[146] Wolfgang G Bessler and Christof Schulz. Quantitative multi-line NO-LIF temperature imaging. *Appl. Phys. B*, 78(5):519–533, mar 2004.

[147] B K McMillin, J L Palmer, and R K Hanson. Temporally resolved, two-line fluorescence imaging of NO temperature in a transverse jet in a supersonic cross flow. *Appl. Opt.*, 32(36):7532–45, 1993.

[148] Jorge Luque and David R. Crosley. LIFBASE: Database and Spectral Simulation Program (Version 1.5). *SRI Int. Rep. MP 99-009*, 1999.

[149] Phillip H. Paul and Habib N. Najm. Planar laser-induced fluorescence imaging of flame heat release rate. *Proc. Combust. Inst.*, 27(3):43–50, 1998.

[150] James C. Weisshaar. Quenching, electronic energy transfer, and rotational relaxation of S1 formaldehyde. *J. Chem. Phys.*, 74(1):226, 1981.

[151] Joel E. Harrington and Kermit C. Smyth. Laser-induced fluorescence measurements of formaldehyde in a methane/air diffusion flame. *Chem. Phys. Lett.*, 202(3-4):196–202, 1993.

[152] D I Shin, T Dreier, and J Wolfrum. Spatially resolved absolute concentration and fluorescence-lifetime determination of H[sub 2] CO in atmospheric-pressure CH[sub 4] /air flames. *Appl. Phys. B Lasers Opt.*, 72(2):257–261, 2001.

[153] Dimitrios C. Kyritsis, Vito S. Santoro, and Alessandro Gomez. The effect of temperature correction on the measured thickness of formaldehyde zones in diffusion flames for 355nm excitation. *Exp. Fluids*, 37(5):769–772, 2004.

[154] Y. Yamasaki and a. Tezaki. Non-linear pressure dependence of A-state fluorescence lifetime of formaldehyde. *Appl. Phys. B Lasers Opt.*, 80(7):791–795, 2005.

[155] Robert L. Gordon, Assaad R. Masri, and Epaminondas Mastorakos. Simultaneous Rayleigh temperature, OH- and CH2O-LIF imaging of methane jets in a vitiated coflow. *Combust. Flame*, 155(1-2):181–195, 2008.

[156] D. J. Clouthier and D. A. Ramsay. The spectroscopy of formaldehyde and thioformaldehyde. *Annu. Rev. Phys. Chem.*, 34:31–58, 1983.

[157] Wolfgang G Bessler, Christof Schulz, Tonghun Lee, Jay B Jeffries, and Ronald K. Hanson. Strategies for laser-induced fluorescence detection of nitric oxide in high-pressure flames. I. A-X(0,0) excitation. *Appl. Opt.*, 41(12): 3547–3557, 2002.

[158] Wolfgang G Bessler, Christof Schulz, Tonghun Lee, Jay B Jeffries, and Ronald K. Hanson. Strategies for laser-induced fluorescence detection of nitric oxide in high-pressure flames. II. A-X(0,1) excitation. *Appl. Opt.*, 42(12): 2031–2042, 2003.

[159] Wolfgang G Bessler, Christof Schulz, Tonghun Lee, Jay B Jeffries, and Ronald K. Hanson. Strategies for laser-induced fluorescence detection of nitric oxide in high-pressure flames. III. Comparison of A-X excitation schemes. *Appl. Opt.*, 42(24):4922–4936, 2003.

[160] John R. Reisel and Normand M. Laurendeau. Quantitative LIF measurements and modeling of nitric oxide in high-pressure C2H4/O2/N2 flames. *Combust. Flame*, 101:141–152, 1995.

[161] Michael D. DiRosa, Kurt G. Klavuhn, and Ronald K. Hanson. LIF Spectroscopy of NO and O2 in High-Pressure Flames. *Combust. Sci. Technol.*, 118(4-6):257–283, 1996.

[162] Clayton S. Cooper and Normand M. Laurendeau. Parametric study of no production via quantitative laser-induced fluorescence in high-pressure, swirl-stabilized spray flames. *Proc. Combust. Inst.*, 28(1):287–293, 2000.

[163] D CharlstonGoch, B.L Chadwick, R.J.S Morrison, A Campisi, D.D Thomsen, and Normand M. Laurendeau. Laser-Induced fluorescence measurements and modeling of nitric oxide in premixed flames of CO+H2+CH4 and air at high pressures. *Combust. Flame*, 125(1-2):729–743, apr 2001.

[164] D D Thomsen, F F Kuligowski, and Normand M. Laurendeau. Background corrections for laser-induced-fluorescence measurements of nitric oxide in lean, high-pressure, premixed methane flames. *Appl. Opt.*, 36(15):3244–3252, 1997.

[165] William P Partridge and Normand M. Laurendeau. Formulation of a dimensionless overlap fraction to account for spectrally distributed interactions in fluorescence studies. *Appl. Opt.*, 34(15):2645–2647, 1995.

[166] R. V. Ravikrishna, Sameer Naik, Clayton S. Cooper, and Normand M. Laurendeau. Quantitative Laser-Induced Fluorescence Measurements and Modeling of Nitric Oxide in High-Pressure (6-15 Atm) Counterflow Diffusion Flames. *Combust. Sci. Technol.*, 176(1):1–21, 2004.

[167] Thomas B. Settersten, Brian D. Patterson, and Jeffrey A. Gray. Temperature- and species-dependent quenching of NO AΣ+2(v'=0) probed by two-photon laser-induced fluorescence using a picosecond laser. *J. Chem. Phys.*, 124 (234308):0–14, 2006.

[168] Christopher R Shaddix. Correcting thermocouple measurements for radiation loss: a critical review. In *Proc. 33rd Natl. Heat Transf. Conf.*, pages 1–10, Albuquerque, 1999.

[169] V Hindasageri, R P Vedula, and S V Prabhu. Thermocouple error correction for measuring the flame temperature with determination of emissivity and heat transfer coefficient. *Rev. Sci. Instrum.*, 84(2):024902, feb 2013.

[170] Malvern Instruments Ltd. *Spraytec User Manual*. Number 2. 2006.

[171] Benjamin M Simmons and Ajay K. Agrawal. Spray Characteristics of a Flow-Blurring Atomizer. *At. Sprays*, 20(9):821–835, 2010.

[172] R. Hadef and B. Lenze. Measurements of droplets characteristics in a swirl-stabilized spray flame. *Exp. Therm. Fluid Sci.*, 30(2):117–130, nov 2005.

[173] Y. Hardalupas, A.M.K.P. Taylor, and J. H. Whitelaw. Mass flux, mass fraction and concentration of liquid fuel in a swirl stabilized flame. *Int. J. Multiph. Flow*, 20:233–259, 1994.

[174] A.A. Rizkalla and Arthur H. Lefebvre. Influence of Liquid Properties on Airblast Atomizer Spray Characteristics. *J. Eng. Power*, (April 1975):173–177, 1975.

[175] A A Rizkalla and Arthur H. Lefebvre. The Influence of Air and Liquid Properties on Airblast Atomization. *J. Fluids Eng.*, 97(3):316, 1975.

[176] K.Y. Kim and W.R. Marshall. Drop-size distributions from pneumatic atomizers. *AIChE J.*, 17(3):575–584, 1971.

[177] G. E. Lorenzetto and Arthur H. Lefebvre. Measurements of Drop Size on a Plain-Jet Airblast Atomizer. *AIAA J.*, 15(7):1006–1010, jul 1977.

[178] S.C. Tsai and B. Viers. Airblast atomization of viscous liquids. *Fuel*, 69(11): 1412–1419, nov 1990.

[179] Arthur H. Lefebvre. Airblast atomization. *Prog. Energy Combust. Sci.*, 6(3): 233–261, jan 1980.

[180] LD Wigg. Drop Size Prediction for Twin Fluid Atomizers. *J. Inst. Fuel*, 27: 500–505, 1964.

[181] G. M. Faeth, L. P. Hsiang, and P. K. Wu. Structure and breakup properties of sprays. *Int. J. Multiph. Flow*, 21(Suppl):99–127, 1995.

[182] D. R. Guildenbecher, C. López-Rivera, and P. E. Sojka. Secondary atomization. *Exp. Fluids*, 46(3):371–402, 2009.

[183] B.E. Gelfand. Droplet breakup phenomena in flows with velocity lag. *Prog. Energy Combust. Sci.*, 22(3):201–265, jan 1996.

[184] Y. Hardalupas, A.M.K.P. Taylor, and J. H. Whitelaw. Velocity and size characteristics of liquid-fuelled flames stabilized by a swirl burner. *Proc. R. Soc. London A*, 428:129–155, 1990.

[185] CHEMKIN-PRO 15112, Reaction Design: San Diego, 2011.

[186] Wayne K. Metcalfe, Sinéad M. Burke, Syed S. Ahmed, and Henry J. Curran. A Hierarchical and Comparative Kinetic Modeling Study of C 1 C 2 Hydrocarbon and Oxygenated Fuels. *Int. J. Chem. Kinet.*, 45(10):638–675, oct 2013.

[187] S. Mani Sarathy, Stijn Vranckx, Kenji Yasunaga, Marco Mehl, Patrick Oßwald, Wayne K. Metcalfe, Charles K. Westbrook, William J. Pitz, Katharina Kohse-Höinghaus, Ravi X. Fernandes, and Henry J. Curran. A comprehensive chemical kinetic combustion model for the four butanol isomers. *Combust. Flame*, 159 (6):2028–2055, jun 2012.

[188] Kenji Yasunaga, Takahiro Mikajiri, S. Mani Sarathy, Tohru Koike, Fiona Gillespie, Tibor Nagy, John M. Simmie, and Henry J. Curran. A shock tube and chemical kinetic modeling study of the pyrolysis and oxidation of butanols. *Combust. Flame*, 159(6):2009–2027, jun 2012.

[189] Henry J. Curran. Rate constant estimation for C1 to C4 alkyl and alkoxyl radical decomposition. *Int. J. Chem. Kinet.*, 38(4):250–275, apr 2006.

[190] Edward R. Ritter and Joseph W. Bozzelli. THERM: Thermodynamic property estimation for gas phase radicals and molecules. *Int. J. Chem. Kinet.*, 23(9): 767–778, sep 1991.

[191] Gergory P. Smith, David M. Golden, Michael Frenklach, Nigel W. Moriarty, Boris Eiteneer, Mikhail Goldenberg, Craig T Bowman, Ronald K. Hanson, Soonho Song, William C. Gardiner, Vitali V. Lissianski, and Zhiwei Qin. http://www.me.berkeley.edu/gri_mech/, 2014.

[192] J. Giménez-López, Maria U. Alzueta, C.T. Rasmussen, P. Marshall, and Peter Glarborg. High pressure oxidation of C2H4/NO mixtures. *Proc. Combust. Inst.*, 33(1):449–457, 2011.

[193] A. A. Konnov. Implementation of the NCN pathway of prompt-NO formation in the detailed reaction mechanism. *Combust. Flame*, 156(11):2093–2105, 2009.

[194] Albert L. Myerson, Francis R. Taylor, and Barbara G. Faunce. Ignition limits and products of the multistage flames of propane-nitrogen dioxide mixtures. *Proc. Combust. Inst.*, 6(1):154–163, jan 1957.

[195] Y.H. Song, D.W. Blair, V.J. Siminski, and W. Bartok. Conversion of fixed nitrogen to N2 in rich combustion. *Symp. Combust.*, 18(1):53–63, jan 1981.

[196] D.J. Seery and M.F. Zabielski. Comparisons between flame species measured by probe sampling and optical spectrometry techniques. *Combust. Flame*, 78 (1):169–177, 1989.

[197] Robert J. Cattolica, J A Cavolowsky, and T G Mataga. Laser-fluorescence measurements of nitric oxide in low-pressure h2/o2/no flames. *Twenty-Second Symp. Combust.*, pages 1165–1173, 1988.

[198] Hamid Sarv and Nicholas P. Cernansky. NOx formation from the combustion of monodisperse n-heptane sprays doped with fuel-nitrogen additives. *Combust. Flame*, 76(3-4):265–283, jun 1989.

[199] Shucheng Xu and M. C. Lin. Theoretical study on the kinetics for OH reactions with CH3OH and C2H5OH. *Proc. Combust. Inst.*, 31 I:159–166, 2007.

[200] Rubén Meana-Pañeda, Donald G. Truhlar, and Antonio Fernández-Ramos. High-level direct-dynamics variational transition state theory calculations including multidimensional tunneling of the thermal rate constants, branching ratios, and kinetic isotope effects of the hydrogen abstraction reactions from methanol by atomic hyd. *J. Chem. Phys.*, 134(9), 2011.

[201] W.E. Kaskan. The dependence of flame temperature on mass burning velocity. *Sixth Symp. Combust.*, pages 134–143, 1957.

[202] Oyvind Skreiberg, Pia Kilpinen, and Peter Glarborg. Ammonia chemistry below 1400 K under fuel-rich conditions in a flow reactor. *Combust. Flame*, 136(4): 501–518, 2004.

[203] Zhenyu Tian, Yuyang Li, Lidong Zhang, Peter Glarborg, and Fei Qi. An experimental and kinetic modeling study of premixed NH3/CH4/O2/Ar flames at low pressure. *Combust. Flame*, 156(7):1413–1426, 2009.

[204] Stephen J. Klippenstein, L. B. Harding, B. Ruscic, R. Sivaramakrishnan, N. K. Srinivasan, M. C. Su, and J. V. Michael. Thermal decomposition of NH2OH and subsequent reactions: Ab initiotransition state theory and reflected shock tube experiments. *J. Phys. Chem. A*, 113(38):10241–10259, 2009.

[205] G Hartung, J Hult, and C F Kaminski. A flat flame burner for the calibration of laser thermometry techniques. *Meas. Sci. Technol.*, 17(9):2485–2493, 2006.

[206] Michael C Drake and Richard J Blint. Calculations of NOx Formation Pathways in Propagating Laminar, High Pressure Premixed CH4/Air Flames. *Combust. Sci. Technol.*, 75(4-6):261–285, 1991.

[207] Nathalie Lamoureux, Pascale Desgroux, A El Bakali, and J.F. Pauwels. Experimental and numerical study of the role of NCN in prompt-NO formation in low-pressure CH 4 O 2 N 2 and C 2 H 2 O 2 N 2 flames. *Combust. Flame*, 157(10):1929–1941, 2010.

[208] Michael C Drake, JW Ratcliffe, and RJ Blint. Measurements and modeling of flamefront NO formation and superequilibrium radical concentrations in laminar high-pressure premixed flames. *Proc. Combust. Inst.*, 23:387–395, 1990.

[209] J D Allen. Probe Sampling of Oxides of Nitrogen from Flames. *Combust. Flame*, 24:133–136, 1975.

[210] A. A. Konnov, I. V. Dyakov, and J. De Ruyck. Probe Sampling Measurements and Modeling of Nitric Oxide Formation in Methane-Air Flames. *Combust. Sci. Technol.*, 169(1):127–153, 2001.

[211] Antonio C. A. Lipardi, Jeffrey M. Bergthorson, and Gilles Bourque. NO _x Emissions Modeling and Uncertainty From Exhaust-Gas-Diluted Flames. *J. Eng. Gas Turbines Power*, 138(5):051506, 2015.

[212] Makihito Nishioka, S. Nakagawa, Y. Ishikawa, and T. Takeno. NO emission characteristics of methane-air double flame. *Combust. Flame*, 98(1-2):127–138, jul 1994.

[213] Y G Ju and T Niioka. Computation of NOx emission of a methane-air diffusion flame in a two-dimensional laminar jet with detailed chemistry. *Combust. Theory Model.*, 1(3):243–258, 1997.

[214] Eun-Seong Cho and Suk Ho Chung. Numerical evaluation of NOx mechanisms in methane-air counterflow premixed flames. *J. Mech. Sci. Technol.*, 23(3): 659–666, jun 2009.

[215] G J Rortveit, J E Hustad, S H Li, and Forman A. Williams. Effects of diluents on NOx formation in hydrogen counterflow flames. *Combust. Flame*, 130(x): 48–61, 2002.

[216] Taeko Sano. NO2 Formation in Laminar Flames. *Combust. Sci. Technol.*, 29 (3-6):261–275, 1982.

[217] Philippe Versailles, Graeme M. G. Watson, Antonio C A Lipardi, and Jeffrey M Bergthorson. Quantitative CH measurements in atmospheric-pressure , premixed flames of C 1 C 4 alkanes. *Combust. Flame*, 165:1–6, 2015.

[218] Graeme M. G. Watson, Philippe Versailles, Antonio C. A. Lipardi, and Jeffrey M. Bergthorson. Comparisons of NO formation in premixed flames of C_1 to C_4 alkanes and alcohols. In *Proc. 2014 Spring Tech. Meet. Combust. Institute/Canadian Sect.*, Windsor, 2014.

[219] Robert M. Fristrom. Flame Zone Studies. II. Applicability of One-Dimensional Models to Three-Dimensional Laminar Bunsen Flame Fronts. *J. Chem. Phys.*, 24(4):888, 1956.

[220] Quang Viet Nguyen, R. W. Dibble, C. D. Carter, G. J. Fiechtner, and R. S. Barlow. Raman-LIF measurements of temperature, major species, OH, and NO in a methane-air Bunsen flame. *Combust. Flame*, 105(4):499–510, 1996.

[221] John R. Reisel, Campbell D. Carter, Normand M. Laurendeau, and Michael C Drake. Laser-Saturated Fluorescence Measurements of Nitric Oxide in Laminar, Flat, C 2 H 6 /O 2 /N 2 Flames at Atmospheric Pressure. *Combust. Sci. Technol.*, 91(4-6):271–295, jun 1993.

[222] John R. Reisel, C D Carter, and Normand M. Laurendeau. Measurements and Modeling of OH and NO in Premixed C2H6/O2/N2 flames at atmospheric Pressure. *Energy Fuel*, 11(5):1092–1100, 1997.

[223] William P. Partridge, John R. Reisel, and Normand M. Laurendeau. Laser-saturated fluorescence measurements of nitric oxide in an inverse diffusion flame. *Combust. Flame*, 116(1-2):282–290, 1999.

[224] Carla S.T. Marques, Luiz G. Barreta, Maria E. Sbampato, and Alberto M. dos Santos. Laser-saturated fluorescence of nitric oxide and chemiluminescence measurements in premixed ethanol flames. *Exp. Therm. Fluid Sci.*, 34(8):1142–1150, nov 2010.